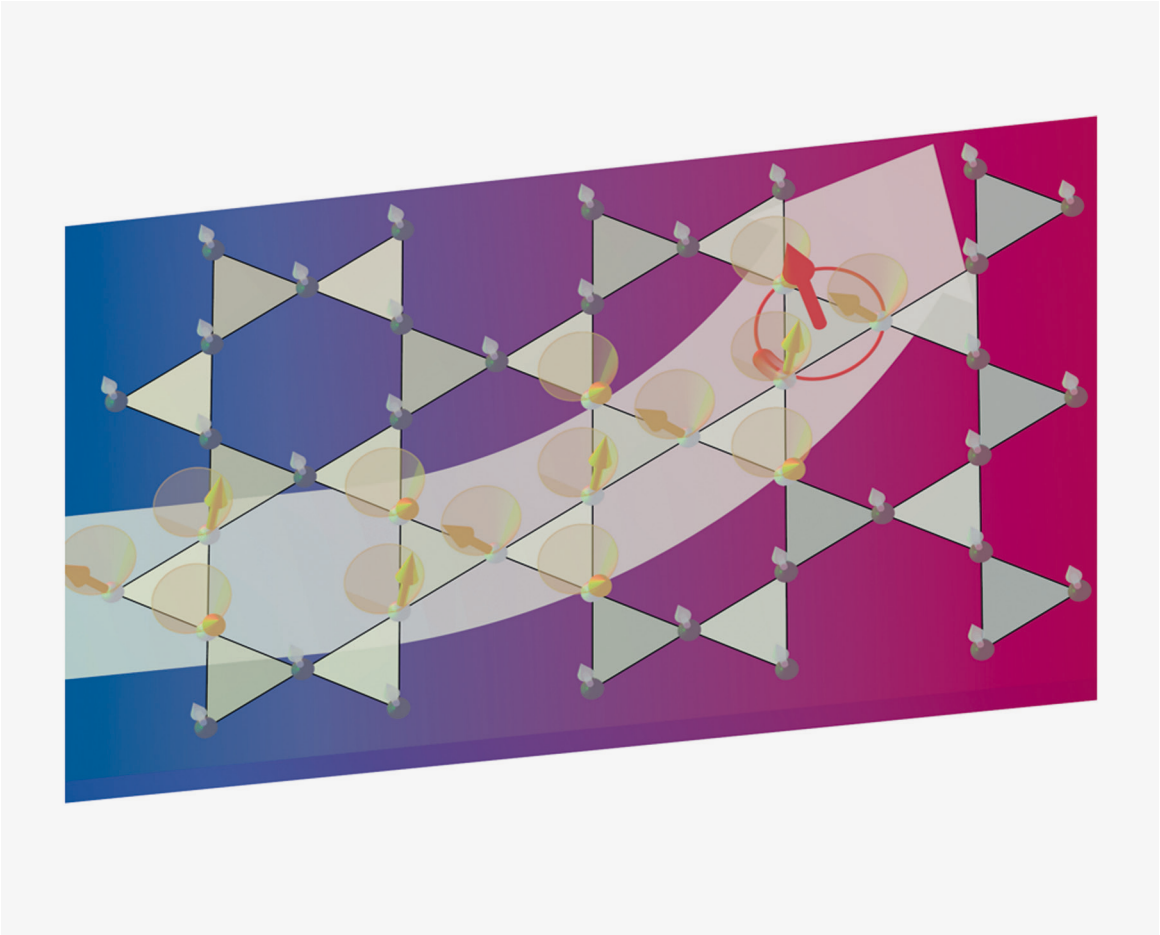

Topological magnonic properties of two-dimensional magnetic materials

Lichuan Zhang

Schlüsseltechnologien / Key Technologies
Band / Volume 253
ISBN 978-3-95806-621-2

Mitglied der Helmholtz-Gemeinschaft

JÜLICH
Forschungszentrum

Schriften des Forschungszentrums Jülich
Reihe Schlüsseltechnologien / Key Technologies Band / Volume 253

Forschungszentrum Jülich GmbH
Peter Grünberg Institut (PGI)
Quanten-Theorie der Materialien (PGI-1/IAS-1)

Topological magnonic properties of two-dimensional magnetic materials

Lichuan Zhang

Schriften des Forschungszentrums Jülich
Reihe Schlüsseltechnologien / Key Technologies Band / Volume 253

ISSN 1866-1807 ISBN 978-3-95806-621-2

Bibliografische Information der Deutschen Nationalbibliothek.
Die Deutsche Nationalbibliothek verzeichnet diese Publikation in der
Deutschen Nationalbibliografie; detaillierte Bibliografische Daten
sind im Internet über http://dnb.d-nb.de abrufbar.

Herausgeber und Vertrieb:	Forschungszentrum Jülich GmbH Zentralbibliothek, Verlag 52425 Jülich Tel.: +49 2461 61-5368 Fax: +49 2461 61-6103 zb-publikation@fz-juelich.de www.fz-juelich.de/zb
Umschlaggestaltung:	Grafische Medien, Forschungszentrum Jülich GmbH
Druck:	Grafische Medien, Forschungszentrum Jülich GmbH
Copyright:	Forschungszentrum Jülich 2022

Schriften des Forschungszentrums Jülich
Reihe Schlüsseltechnologien / Key Technologies, Band / Volume 253

D 82 (Diss. RWTH Aachen University, 2022)

ISSN 1866-1807
ISBN 978-3-95806-621-2

Vollständig frei verfügbar über das Publikationsportal des Forschungszentrums Jülich (JuSER)
unter www.fz-juelich.de/zb/openaccess.

Declaration of Authorship

I, **Lichuan Zhang, M. Sc.**,
declare that this thesis and the work presented in it are my own and has been generated by me as the result of my own original research.
Hiermit erkläre ich an Eides statt / I do solemnly swear that:

1. This work was done wholly or mainly while in candidature for the doctoral degree at this faculty and university;

2. Where any part of this thesis has previously been submitted for a degree or any other qualification at this university or any other institution, this has been clearly stated;

3. Where I have consulted the published work of others or myself, this is always clearly attributed;

4. Where I have quoted from the work of others or myself, the source is always given. This thesis is entirely my own work, with the exception of such quotations;

5. I have acknowledged all major sources of assistance;

6. Where the thesis is based on work done by myself jointly with others, I have made clear exactly what was done by others and what I have contributed myself;

7. Parts of this work have been published before as:

- Chemical Science 10, 10381-10387, 2019
- Phys. Rev. Research 2, 013063, 2020
- Communications Physics 3, 227, 2020
- Physical Review B 103, 134414, 2021
- Science Advance 7(37), eabi7532, 2021

Signed:

Date: March, 2022

The important thing is not to stop questioning. Curiosity has its own reason for existing. One cannot help but be in awe when he contemplates the mysteries of eternity, of life, of the marvelous structure of reality. It is enough if one tries merely to comprehend a little of this mystery every day. Never lose a holy curiosity.

Albert Einstein

Learning without thought is labour lost; thought without learning is perilous.

Confucius

Abstract

Spintronics is based on the transport of information by the spin of electrons rather than charge current so as to avoid the Joule heat. Among it, magnons, as the most elementary excitations in magnetic materials, have emerged as a prominent tool in electrical and thermal manipulation and transport of spin. Importantly, magnonics as a field is considered as one of the pillars of modern spintronics.

In this thesis, the linear spin-wave theory is utilized to explore the magnonic properties based on the effective spin Hamiltonian, parameterized from the first-principles calculations and fitting to experiments. Inspired by the experimental result, a family of two-dimensional metal-organic frameworks with the Shastry-Sutherland lattice are calculated from first-principles, and corresponding applications in spintronics and magnonics are investigated in the thesis. Additionally, combined with inelastic neutron scattering results, the magnonic topological properties are systematically explored in the multiferroic ferrimagnet Cu_2OSeO_3. The experimental magnon dispersions are well fitted, when considering the Heisenberg-Dzyaloshinsky-Moriya interaction model, and the Weyl points are forecasted whose position can be controlled by changing the Dzyaloshinsky-Moriya interaction of the material. Moreover, a measurable thermal Hall conductivity is predicted, which can be associated with the emergence of the Weyl points.

Notably, in realistic two-dimensional materials, *e.g.,* ferromagnetic honeycomb materials, the Dzyloshinskii-Moriya interaction is often accompanied by the Kitaev interaction, which poses a challenge to distinguish their magnitude. In the thesis, we demonstrate that it can be done by accessing magnonic transport properties and rotating the magnetization in the system. By studying honeycomb ferromagnets that exhibit at the same time the Dzyaloshinskii-Moriya interaction and Kitaev interaction, complex magnonic topological properties are revealed accompanied by intricate magnonic transport characteristics represented by thermal Hall and magnon Nernst effects. Moreover, the effect of a in-plane magnetic field is investigated, showing that it can break the symmetry of the system and bring drastic modifications to magnonic topological transport properties, serving as hallmarks of the relative strength for anisotropic exchange interactions. Furthermore, based on our proposed strategy, the spin interactions in $CrSiTe_3$ and $CrGeTe_3$ are predicted and their potential applications in topological magnonics are explored.

In addition to magnonics, orbitronics, which exploits the orbital degree of freedom of electrons rather than the spin, emerges as a powerful platform in efficient design of currents and redistribution of angular momentum in structurally complex materials. In the thesis, we uncover a way to bridge the magnonics and electronic orbital magnetism, originating in the coupling of scalar spin chirality, inherent to magnons, to the orbital degree of freedom in solids. We show that this can lead to efficient generation and transport of electronic orbital angular momentum by magnons, thus opening the door to

combine the functionalities of magnonics and orbitronics. Lastly, the discovery is applied to realistic materials, *e.g.*, Mn_3Ge, to demonstrate the magnon-mediated orbital magnetism.

Zusammenfassung

Die Spintronik verspricht Informationen durch Spins anstelle von Elektronen zu übertragen und so die Entstehung von Joulewärme zu vermeiden. Dabei haben sich Magnonen, die elementarsten Anregungenen magnetischer Materialien, als ein wichtiges Werkzeug zur elektrischen und thermischen Beeinflussing and beim Transport von Spins herausgestellt.

Unter diesen haben sich Magnonen als elementarste Anregungen magnetischer Materialien als herausragendes Werkzeug bei der elektrischen und thermischen Manipulation und beim Transport von Spin herausgestellt. Heutzutage hat sich das Feld der Magnonik eine der zentralen Säulen der Spintronik etabliert.

In dieser Arbeit wird die lineare Spinwellentheorie verwendet, um Magnonen basierend auf einem effektivem Spin-Hamilton-Operator zu untersuchen, der mit Hilfe von ab initio Berechnungen und experimentellen Daten parametrisiert wurde.

Inspiriert vom Experimenten wurde eine Familie zweidimensionaler metallorganischer Systeme mit einem Shastry-Sutherland-Gitter mittels abinitio Berechnungen und die entsprechenden Anwendungen in der Spintronik und Magnonik werden in der vorliegenden Arbeit ebenfalls untersucht. Mit Hilfe der inelastischen Neutronenstreuungsergebnissen werden die topologischen Eigenschaften von Magnonenanregungen im multiferroischen Ferrimagneten Cu_2OSeO_3 systematisch untersucht.

Die experimentellen Magnonendispersionen sind gut geeignet um das Heisenberg-Dzyaloshinsky-Moriya-Interaktionsmodells zu verstehen. Darüber hinaus sagen wir voraus, dass eine messbare thermische Hall-Leitfähigkeit mit dem Auftreten der Weyl-Punkte verbunden ist, deren Position durch Änderungen der Dzyaloshinsky-Moriya-Wechselwirkung des Materials verändert werden kann.

Insbesondere in realistischen zweidimensionalen Materialien wird die Dzyloshinskii-Moriya-Wechselwirkung häufig von der Kitaev-Wechselwirkung begleitet, was es schwierig macht ihre Größe zu unterscheiden. In der vorliegenden Arbeit zeigen wir jedoch, dass dies durch eine Untersuchung der Magnonentransporteigenschaften möglich ist. Indem wir wabenförmige Ferro-magneten untersuchen, die gleichzeitig Dzyaloshinskii-Moriya- und Kitaev-Wechselwirkungen aufweisen, zeigen wir nicht triviale topologische Eigenschaften der Magnonen, die von komplizierten Magnonentransporteigenschaften begleitet werden, wie sie durch thermische Hall- und Magnon-Nernst-Effekte gegeben sind. Darüber hinaus untersuchen wir auch die Wirkung eines Magnetfelds und zeigen, dass es nicht nur die Symmetrie des Systems bricht, sondern auch drastische Modifikationen der topologischen Transporteigenschaften von Magnonen mit sich bringt, die als Kennzeichen für die relative Stärke anisotroper Austauschwechselwirkungen dienen. Basierend auf unserer vorgeschlagenen Strategie werden außerdem die Spin-Wechselwirkungen in $CrSiTe_3$ und $CrGeTe_3$ vorhergesagt und ihre mögliche Anwendungen in der Magnonik untersucht.

Neben der Magnonik stellt sich auch die Orbitronik, die den Orbitalfreiheitsgrad von Elektronen anstelle ihres Spins ausnutzt, als leistungsstarke Plattform für die effiziente Realisierung von Strömen und die Umverteilung des Drehimpulses in strukturell komplexen Materialien heraus. In dieser Arbeit entdecken wir einen Weg, die Welt der Magnonik mit der des elektronischen Orbitalmagnetismus zu verbinden. Wir zeigen, dass dies zu einer effizienten Erzeugung und zum Transport des elektronischen Drehimpulses durch Magnonen führen kann, wodurch die Möglichkeit eröffnet wird, die Funktionen von Magnonik und Orbitronik zum gegenseitigen Nutzen im Bereich der Spintronik-Anwendungen zu kombinieren. Schließlich wenden wir den vorgeschlagenen Mechanismus auch auf realistische Materialien an, hier Mn_3Ge, um seine Magnonenspin- und Orbitaleigenschaften zu demonstrieren.

Contents

List of Abbreviations

FM	**F**erro**m**agnetic
AFM	**A**nti**f**erro**m**agnetic
TM	**T**ransitional **M**etal
PBP	5, 5′-bis (4-pyridyl) (2, 2′- bipirimidine)
TOM	**T**opological **O**rbital **M**oment
LSWT	**L**inear **S**pin-**W**ave **T**heory
DMI	**D**zyaloshinskii-**M**oriya **I**nteraction
SOC	**S**pin-**O**rbit **C**oupling
SSC	**S**calar **S**pin **C**hirality
SSL	**S**hastry-**S**utherland **L**attice
HP	**H**olstein-**P**rimakoff
TB	**T**ight-**B**onding
INS	**I**nelastic **N**eutron **S**cattering
MFT	**M**ean **F**ield **T**heory
MOFs	**M**etal **O**rganic **F**rameworks
2D	**T**wo **D**imensional
3D	**T**hree **D**imensional
DFT	**D**ensity **F**unctional **T**heory
VASP	**V**ienna *Ab initio* **S**imulation **P**ackage
PAW	**P**rojector **A**ugmented **W**ave
LDA	**L**ocalized **D**ensity **A**pproximation
GGA	**G**eneralized **G**radient **A**pproximation
BZ	**B**rillouin **Z**one
ELF	**E**lectron **L**ocal **F**unction

Physical Constants

$$
\begin{aligned}
\pi &= 3.141592653\cdots \\
1\ \text{Å} &= 1 \times 10^{-10}\,\text{m} \\
1\ \text{nm} &= 1 \times 10^{-9}\,\text{m} \\
1\ \text{eV} &= 1.602\,176\,565 \times 10^{-19}\,\text{J} \\
k_\text{B} &= 1.380\,648\,52 \times 10^{-23}\,\text{J}\,\text{K}^{-1} \\
\hbar &= 1.054\,571\,800 \times 10^{-34}\,\text{J}\cdot\text{s} \\
m_\text{e} &= 9.109\,383\,56 \times 10^{-31}\,\text{kg} \\
\text{e} &= 1.602\,176\,620\,9 \times 10^{-19}\,\text{C}
\end{aligned}
$$

List of Symbols

κ_{TH}	-thermal Hall conductivity
κ_{N}	-magnon Nernst conductivity
κ_{ONE}	-orbital Nernst conductivity
T	-absolute temperature
∇T	-temperature gradient
$\mathbf{\Omega}$	-magnonic Berry curvature
C_n	-the Chern number of branch n
g_{e}	-Lande's g-factor
$\mathbf{S}$	-spin angular momentum
$\mathbf{L}$	-angular momentum
$\mathbf{m}$	-magnetic moment
χ	-scalar spin chirality
κ^{TO}	-topological orbital susceptibility
μ_{B}	-Bohr magneton
$\mathbf{q}$	-wave vector
$\mathbf{k}$	-Bloch wave vector of magnon
Φ_k	-wave function of electron
T_{C}	-Curie temperature
$f(E)$	-Fermi-Dirac distribution function
$n_{\mathrm{B}}(E)$	-Bose distribution function
$E(\mathbf{k})$	-eigenvalue of magnon at $\mathbf{k}$
k_{B}	-Boltzmann's constant
e	-electron charge
E	-electric field
$\mathbf{B}$	-magnetic field
$\hbar$	-Planck's constant
m_{e}	-electron mass
M_I	-mass of atom I
V	-volume of unit cell
t	-time
$\mathbf{r}$	-point of electron
$\mathbf{R}_n$	-point of lattice ion n
$\hat{H}$	-Hamiltonian
H	-Effective Hamiltonian of spin
$\hat{D}$	-the dynamical matrix of H
$\mathbf{D}$	-Dzyaloshinskii-Moriya interaction vector
$\mathbf{J}$	-Heisenberg exchange interaction
K	-the strength of Kitaev interaction
A	-the strength of anisotropy energy

V_{L}	-left eigenstate of effective spin Hamiltonian
V_{R}	-right eigenstate of effective spin Hamiltonian
α	-bosonic annihilation operator
$\alpha^{\dagger}$	-bosonic creation operator
$\alpha_{\mathbf{k}}$	-magnon annihilation operator
$\alpha_{\mathbf{k}}^{\dagger}$	-magnon bosonic creation operator

Chapter 1

Introduction

With the development of modern society, energy consumption has increased dramatically, leading to energy issues that are receiving more and more attention from mankind. It is reported that the Information and Communication Technology (ICT) consumption has a one-way causality with electricity consumption, which in turn causes a rise in CO_2 emissions [1]. In order to protect our environment and make full use of energy, *spintronics* is proposed and actively promoted in the past decades.

In spintronics, the information is transported by the spin of electrons rather than electrons themselves so as to avoid the generation of Joule heat. Based on this theory, many applications have been realized. For instance, some logic devices are designed in the data storage field based on the giant magnetoresistance (GMR) [2] effect and tunneling magnetoresistance (TMR) effect [3]. In addition, spintronics also has applications in semiconductors, such as spin-polarized electrical injection and spin-based transistors. Nowadays, it is still a promising topic to search for new candidate materials in spintronics. Notably, half-metal materials can be used efficiently for spin-polarized injection, and semiconductors with high Curie temperature have promising applications in spin-based transistor technology.

Within spintronics, the concept of spin waves, i.e. collective spin excitation, plays an important role. The spin-wave theory was first proposed by Bloch in 1930 [4] and its fingerprints were first observed by Brockhouse [5]. For a magnetic material in the ground state, each spin has its own direction, and magnetic properties can be explained by the spins and their interactions. Out of equilibrium, the behavior of these spins is perceived as an "elastic medium". The perturbation of local magnetization can propagate through the whole material, due to external heat, optical excitation, etc. As this behavior is analogous to the propagation of water waves in the sea, this phenomenon is named spin waves, whose quanta are quasiparticles called magnons. Magnons hold unprecedented potential for various applications in the realm of magnetic phenomena. For instance, the information can be transferred by magnons without any Ohmic losses in magnetic insulators, as there is no directional flow of electrons. Utilizing magnons for information transformation is known as *magnonics*, which is boomed by the experimental discovery of the thermal Hall effect of magnon in $Lu_2V_2O_7$ [6]. In a recent study, it was predicted that the thermal Hall effect of magnons can be aroused by the spin-orbit coupling (SOC) in the form of the Dzyaloshinskii-Moriya interaction (DMI) [7]. Therefore, understanding the nature of spin

interactions in real magnets is a prerequisite for an in-depth study of the topological properties of magnons.

In magnets, the spin interactions are usually dominated by the short-range exchange interactions and long-range magnetic dipole interactions. Besides, the DMI, magnetocrystalline anisotropy, and Kitaev interactions, which originate in the interplay of SOC with crystal symmetry, may exist in magnets. Thus, establishing how to evaluate the contribution of these types of interactions becomes an important research aim. On the one hand, the quantitative parameters of different spin interactions can be obtained through first-principles calculations based on density functional theory (DFT). On the other hand, the spin interactions can be predicted based on a fitting to experimental data. For instance, many experimental techniques to detect magnonic excitations have been developed in the past, such as the angle-dependent ferromagnetic resonance (FMR), Raman scattering, and inelastic neutron scattering (INS). By utilizing these techniques, we can formulate the corresponding effective spin Hamiltonian, which reflects the spatial dependence of the magnetic exchange interactions.

After determining spin interactions in magnets, the magnetic properties can be finally investigated. In addition to an external magnetic field, the combination of interactions mentioned above can produce rich magnetic ground states, such as skyrmions, domain walls, spin spirals, and spin liquids [8, 9, 10]. Besides, the DMI or Kitaev interaction can also bring to the forefront a variety of interesting magnonic topological phenomena and various magnonic topological states, *e.g.*, the Weyl points, explored here for the case of Cu_2OSeO_3. Previously, it has been speculated that both DMI [6] and the Kitaev interaction [11] can generate the thermal Hall effect in layered van der Waals materials with similar magnon dispersion. In my thesis, the interplay of DMI and Kitaev interactions for magnonic transport properties of honeycomb materials is investigated, and the strategies to be applied in real materials to distinguish both interactions are proposed.

In addition to magnonics, *orbitronics* is also attracting more and more attention in recent years. Orbitronics exploits the orbital degree of freedom of electrons rather than their spin, emerging as a powerful platform in efficient design of currents and redistribution of angular momentum in structurally complex materials. The orbital magnetism is aroused from the circulating electric currents, and usually finite orbital moment can be produced from the SOC that naturally breaks the orbital degeneracy. Apart from this, orbital magnetism can also be obtained based on magnetic geometry. In this theory, an effective internal magnetic field is generated to break the orbital degeneracy, which is caused by the electron hopping among non-coplanar spin sites with spin chirality in a frustrated magnet or in a skyrmion. The emergence of such chirality-driven orbital magnetization in various systems has been shown in recent years [12, 13, 14, 15, 16], where the spin chirality normally corresponds to the scalar spin chirality (SSC). By using this approach, not only large orbital magnetic moments can be realized in light materials, but also it inspires us to realize the orbital magnetism through magnonic excitations.

It is clear that the SSC is vanishing in the ground state of collinear magnetic systems, while it can be harvested by magnons excitation, generating the topological orbital magnetism (TOM). In the thesis, combining magnonics and electronic orbital magnetism calculations, we revealed efficient generation and transport characteristics of electronic orbital angular momentum by magnons. Our findings combine the functionalities of magnonics and orbitronics in the realm of spintronics applications, which provide references for future theoretical and experimental studies.

Altogether, this thesis mainly focuses on four aspects: 1) A family of two-dimensional (2D) metal-organic frameworks (MOFs) is investigated to explore possible applications in spintronics and magnonics; 2) In collaboration with experimental partners, spin interactions, and magnonic properties, *e.g.*, magnonic Weyl phases and thermal Hall effect, are investigated in a prototypical skyrmionic material Cu_2OSeO_3; 3) The influence of DMI and Kitaev interactions on magnonic characteristics are explored in van der Waals materials; 4) Orbital properties of magnetic materials are explored through the coupling between SSC and magnons, in which a new mechanism named as the orbital Nernst effect is proposed.

1.1 Outline of the Thesis

The left parts of the thesis are organized as follows:

Chapter 2. In this chapter, we present the origin of magnetism, especially the contribution from the orbital angular momentum. Besides, different types of spin interactions are introduced to constitute the generalized Heisenberg model. Furthermore, we present the concept of spin waves, and a general method is introduced to obtain the magnon eigenvalue and eigenstate via quantum mechanical formalism.

Chapter 3. In this chapter, we introduce the fitting to experimental data and *ab initio* method to achieve the parametrization of the generalized Heisenberg Hamiltonian.

Chapter 4. In this chapter, we present the geometric topology, whose concept is extended from electronic systems to magnonic systems. By utilizing the magnon Berry curvature, we present a magnonic topological phenomenon, the magnonic Weyl point. According to the semiclassical method, the magnonic transport properties in the context of the thermal Hall effect and magnon Nernst effect are introduced.

Chapter 5. Based on the first-principles calculation, we demonstrate the candidate application of 2D-MOFs with the Shastry-Sutherland lattice (SSL) in spintronics. A family of 2D MOFs are studied and Mn-PBP is predicted to be the first ferromagnetic (FM) 2D MOF-SSL with the Curie temperature 105 K. We predict that Mn-PBP would change from semiconductor to half-metal under compressive strain or proper electron/hole doping and a spintronic device based on Mn-PBP has been proposed. Moreover, based on the *ab initio* calculation, the magnon dispersion and the magnonic transport properties of Mn-PBP are investigated to explore its application in magnonics.

Chapter 6. In this chapter, based on the linear spin-wave theory and INS method, we predict the magnonic Weyl points in a multiferroic ferrimagnet Cu_2OSeO_3. The DMI is adopted to successfully explain the experimental magnon dispersion. Further, we observe that a measurable thermal Hall conductivity is associated with the emergence of the Weyl points, the position of which can be tuned by modifying the DMI vector.
Chapter 7. In real materials, the DMI and the Kitaev interaction can coexist, which poses the challenge of distinguishing their magnitude separately. Hereby, we propose that it can be done by accessing magnonic transport properties and magnetic field response. Further, working with collaborators, we predict the spin interactions in $CrSiTe_3$ and $CrGeTe_3$ based on our proposed strategies. The candidate applications in magnonics are also studied in these two materials.
Chapter 8. In this chapter, we propose a new mechanism to establish a link between magnonics and orbitronics. We theoretically reveal the unknown coupling of magnonic excitations to spin chirality in generic classes of spin systems. Relying on the microscopic analysis, we show that a finite spin chirality can be generated by thermally excited magnons even in a collinear spin system. Further, we predict that there is a topological orbital magnetism aroused from the coupling between the magnonic generation of chirality and free electrons. This provides a direct link between the magnonic excitations and the generation of electronic orbital magnetization. Finally, we reveal that driving currents of magnons (*i.e.*, in an applied temperature gradient) can cause a significant magnon drag of the orbital momentum across the system. As such, the discovery demonstrates the potential of orbital electron-magnon coupling for controlling the magnetization properties.
Chapter 9. Based on the theory proposed in Chapter. 8, the magnon-driven orbitronics are investigated in non-collinear systems, *e.g.*, antiferromagnetic Kagome lattice and Mn_3Ge.
Chapter 10. In the last Chapter, we summarize all the results. Parts of this thesis have already been published in Refs [17, 18, 19, 20].

Chapter 2

Spin-wave theory

In this chapter, we discuss the origin of magnetism, in which the generation of orbital magnetism is presented in detail. Then, the concept of interaction between spins is introduced to constitute the Heisenberg model [4]. Furthermore, different types of spin interactions, *e.g.*, Dzyaloshinskii-Moriya interaction, Kitaev interaction, and higher-order interactions are presented to form the generalized Heisenberg model. Lastly, the concept of spin wave is introduced, and a general method is shown to obtain the magnon dispersion (eigenvalue) and magnon wavefunction (eigenvector) through quantum mechanical formalism. In this section, some of the methods are inspired by Ref. [21].

Some results presented in Chapter 2.2 and Chapter 2.3.3 have already been published:
Li-chuan Zhang, et. al., Communications Physics, 3, 227, 2020.
Fengfeng Zhu, Li-chuan Zhang, et. al., Science Advance 7(37), eabi7532, 2021.
Some methods presented in Chapter 2.4 have already been published:
Li-chuan Zhang, et. al., Physical Review B 103, 1344142021, 2021.
Li-chuan Zhang, et. al., Communications Physics, 3, 227, 2020.

2.1 Origin of magnetism

In magnets, the origin of magnetism almost entirely comes from the magnetic moments contributed by electrons. It is provided by two parts, which are the intrinsic spin magnetic moment of electrons and the orbital magnetism generated from the circulating electric currents. Usually, magnetism is dominated by the spin in magnets and its mechanism has been studied over decades, while the contribution of the orbital moment is usually neglected as it is usually much smaller than the spin magnetic moment.

The magnetic moment $\mathbf{m}$ contributed by the spin angular momentum $\mathbf{S}$ can be represented as:

$$\mathbf{m}^{\mathrm{S}} = -\frac{1}{\hbar}\mu_{\mathrm{B}} g_{\mathrm{e}} \mathbf{S}, \tag{2.1}$$

where μ_{B} is Bohr magneton, given by $e\hbar/2m_{\mathrm{e}}$ in SI units with m_{e}, $\hbar$ represent the electron mass and reduced Planck constant separately. The g_{e} is the Lande's g-factor, and usually we assume $g_{\mathrm{e}} = 2$. Similarly, we can calculate

the orbital magnetic moment:

$$\mathbf{m}^{\mathrm{L}} = -\frac{1}{\hbar}\mu_{\mathrm{B}} \sum_{i} \mathbf{L}_i, \tag{2.2}$$

where $\mathbf{L}_i = \mathbf{r}_i \times (m_{\mathrm{e}}\mathbf{v}_i)$ represents the angular momentum of the *i*th electron, and $\mathbf{v}_i$ is the velocity of the *i*th electron. By combining the Eq. (2.1) and Eq. (2.2), the total magnetic moment can be represented as:

$$\mathbf{m} = -\frac{1}{\hbar}\mu_{\mathrm{B}}(\mathbf{L} + g_{\mathrm{e}}\mathbf{S}). \tag{2.3}$$

Next, we discuss the origin of magnetism in real materials. We first start from the isolated atoms according to the Hund's rules. It is easy to understand that the angular momentum is zero for those atoms that have full subshells (such as the noble gases), as each orbital is filled with two opposite spins.

The situation is more complicated except for the noble gases. For instance, in some transition-metal compounds, the electron from the outermost subshells or part of inner subshells may be involved in the formation of chemical bonds, while most of the inner d/f subshells are less susceptible and still follow the Hund's rules. These transition-metal atoms are said to possess localized magnetism, and a similar phenomenon is discussed in Chapter 5. Besides, in some metallic systems, the electrons are itinerant and delocalized, and the density of electrons with spin up different from that of electrons with spin down, leading to the magnetism of the system.

Usually, we just ignore the contribution of orbital magnetism. However, it is revealed that in some materials, it has a significant impact on the system. Besides, the orbital magnetism may originate not only from the spin-orbit coupling. In the next section, we will discuss the features of orbital magnetism in detail.

2.2 Orbital magnetism

2.2.1 The calculation of orbital magnetism from modern theory[1]

As shown in Section 2.1, magnetism is mainly generated by the spin and orbital moment. Except for the intensive study of spin, it is investigated that the orbital magnetism has influence on the spin transport [22, 23], magnetic anisotropy [24] and DMI [25, 26], etc. To study the properties of orbital magnetism, several approaches are proposed. Especially, based on the semiclassical approach [27], the modern theory is a very powerful framework to address and obtain the orbital magnetism.

[1] In my thesis, the shown results calculated with this method are obtained by Dongwook Go.

From the modern theory, we can numerically access the orbital magnetism of the electronic system according to the rigorous expression [28]:

$$\mathbf{L}^{\mathrm{OM}} = \frac{\mathrm{e}}{2\hbar} \sum_{n\mathbf{k}\in \mathrm{occ}} \mathrm{Im}[\langle \partial_{\mathbf{k}} u_{n\mathbf{k}}| \times (\mathcal{H}(\mathbf{k}) + \mathcal{E}_{n\mathbf{k}} - 2\mathcal{E}_{\mathrm{F}})|\partial_{\mathbf{k}} u_{n\mathbf{k}}\rangle], \tag{2.4}$$

where $\mathcal{H}(\mathbf{k})$ is the Hamiltonian for the electronic system. In the calculation it often refers to the effective Wannier-function based Hamiltonian or tight-binding Hamiltonian, $u_{n\mathbf{k}}$ is a periodic part of the Bloch state with band index n at momentum $\mathbf{k}$, its corresponding energy eigenvalue is $\mathcal{E}_{n\mathbf{k}}$. At zero temperature, the summation goes over all occupied states below the Fermi energy $\mathcal{E}_{\mathrm{F}}$.

2.2.2 Topological orbital magnetism

The orbital magnetism can be modulated by the spin-orbit interaction. However, in light materials the orbital magnetism is usually tiny, as the spin-orbit interaction is weak to break the orbital degeneracy. Here, we would like to explore a specific mechanism to realize large orbital magnetism in weak spin-orbit interaction systems. This prompted the presentation of the topological orbital magnetism. When an electron hops among non-coplanar spin sites with spin chirality in frustrated magnets (*i.e.*, skyrmions), it behaves as if it feels an internal magnetic field [29, 30, 12, 15]. Similar to the Zeeman field, the generated effective magnetic field can couple to the orbital degrees of freedom and break the orbital degeneracy, manifesting in the topological orbital moment. The emergence of such chirality-driven orbital magnetization in various systems has been investigated in recent years [30, 12, 13, 14, 15, 16], where the spin chirality normally corresponds to the scalar spin chirality (SSC):

$$\chi_{ijk} = \hat{\mathbf{S}}_i \cdot (\hat{\mathbf{S}}_j \times \hat{\mathbf{S}}_k), \tag{2.5}$$

where $\mathbf{S}_i$, $\mathbf{S}_j$ and $\mathbf{S}_k$ are three neighboring spins forming a triangle, where $\hat{\mathbf{S}}_\alpha$ is the unit vector along $\mathbf{S}_\alpha$ with $\alpha \in (i, j, k)$. The SSC is inherent to skyrmions [8, 31, 14, 15, 32] and frustrated magnets [33, 34, 35], which has been crucial for understanding *i.e.*, topological Hall effect [36, 37].

The topological orbital moment (TOM) at the ith lattice site originates from non-zero SSC of all triangles of spins in which i participates [16]:

$$\mathbf{L}_i^{\mathrm{TOM}} = \kappa^{\mathrm{TO}} \sum_{jk} \chi_{ijk} \hat{\mathbf{e}}_{ijk}, \tag{2.6}$$

where χ_{ijk} represents the SSC between the atoms located at $\mathbf{R}_i$, $\mathbf{R}_j$, and $\mathbf{R}_k$. Here, we focus only on triangles that are formed by atoms which are nearest neighbors. The direction of the TOM is given by the normal vector $\hat{\mathbf{e}}_{ijk} \propto (\mathbf{R}_j - \mathbf{R}_i) \times (\mathbf{R}_k - \mathbf{R}_i)$ of the oriented triangle of spins. The κ^{TO} is called topological orbital susceptibility, and it characterizes the strength of the orbital response of electrons to the SSC.

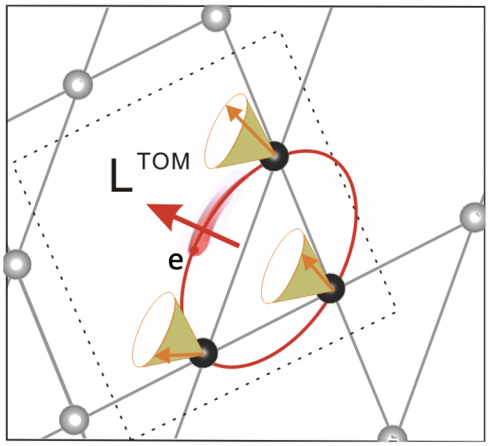

FIGURE 2.1: Schematic diagram of the generation of orbital angular momentum by magnons. An electron hopping among non-collinear triplets of spins gives rise to so-called topological orbital moment (TOM), $\mathbf{L}^{\mathrm{TOM}}$, which points out of the plane of the spins. The electronic TOM is effectively induced by the scalar spin chirality realized for example on a kagome spin lattice, which is shown in an oblique view.

In this thesis, we want to explore whether magnonic excitations themselves can give rise to net SSC, even if it is absent in the ground state. Then we would have a unique mechanism for imprinting electronic orbital angular momentum into the system through generating SSC by magnons. Here, we use a schematic diagram, shown in Figure 2.1, to represent the mechanism, which presents a unique way to obtain orbital angular momentum by magnon excitation. In Chapter 8, the ferromagnetic kagome lattice is selected as an example to explore the coupling between chirality and electronic orbital magnetism.

2.3 Origin of magnetic interactions

The magnetic interaction is the coupling between spins in magnets, and it is the source of magnetic order. The magnetic interactions are mainly generated by electron-electron Coulomb interaction, magnetic dipole-dipole interactions and spin-orbit coupling. Usually, the Coulomb interactions dominate and give rise to the exchange interaction. The dipole-dipole interaction is a long-range interaction, which can create magnetic domains. We don't discuss the dipole-dipole interaction in this thesis, as usually its value is much smaller than the exchange interaction. The spin-orbit interaction also plays an important role in magnets, which can lead to the formation of the domain wall, Dzyaloshinskii-Moriya interaction and magnetic anisotropy energy, etc.

2.3.1 Magnetic exchange interaction

We first discuss the exchange interaction mainly aroused from the Coulomb interactions and the Pauli principle. Following the textbooks [38], we first study the ground state of a two hydrogen atoms system. We here assume two hydrogen atoms at positions $\mathbf{R}_1$ and $\mathbf{R}_2$ and the positions of two electrons are denoted with $\mathbf{r}_1$ and $\mathbf{r}_2$. The corresponding Hamiltonian follows the Schrödinger equation:

$$-\frac{\hbar^2}{2m}(\nabla_1^2+\nabla_2^2)\Phi(\mathbf{r}_1,\mathbf{r}_2)+(V+W)\Phi(\mathbf{r}_1,\mathbf{r}_2)=E\Phi(\mathbf{r}_1,\mathbf{r}_2), \tag{2.7}$$

where V and W represent the potential due to the two protons and electron-electron interaction, separately. According to the Pauli exclusion principle, two electrons can't occupy the same quantum state simultaneously, leading to the fact that the wave function of the system Φ is antisymmetric. In the system, the total spin $\mathbf{S}$ can be selected as $S=1$, which corresponds to symmetric triplet states, and it can be represented with $|S,m_{\mathrm{S}}\rangle$:

$$\begin{aligned}
&|1,1\rangle = |\uparrow\uparrow\rangle\,,\\
&|1,0\rangle = \frac{1}{\sqrt{2}}(|\uparrow\downarrow\rangle+|\downarrow\uparrow\rangle)\,,\\
&|1,-1\rangle = |\downarrow\downarrow\rangle\,,
\end{aligned} \tag{2.8}$$

and $S=0$, which is an antisymmetric singlet state

$$|0,0\rangle = \frac{1}{\sqrt{2}}(|\uparrow\downarrow\rangle-|\downarrow\uparrow\rangle). \tag{2.9}$$

The wavefunction of the system Φ can be indicated by a spin-dependent function $|S,m_{\mathrm{S}}\rangle$ and spin-independent position function $\phi(\mathbf{r})$, which means that singlet and triplet spin states must correspond to symmetric and antisymmetric spin-independent position function $|\phi(\mathbf{r})\rangle^+$ and $|\phi(\mathbf{r})\rangle^-$, separately.

$$\begin{aligned}
&|\Phi_{\mathrm{s}}\rangle = |\phi(\mathbf{r})\rangle^+\,|0,0\rangle\,,\\
&|\Phi_{\mathrm{t}}\rangle = |\phi(\mathbf{r})\rangle^-\,|1,m\rangle\ \ (m=-1,0,1).
\end{aligned} \tag{2.10}$$

From Eq. (2.7), the Hamiltonian is spin-independent, we have

$$\begin{aligned}
&\hat{H}|\Phi_{\mathrm{s}}\rangle = E_{\mathrm{s}}|\Phi_{\mathrm{s}}\rangle = E_{\mathrm{s}}\,|\phi(\mathbf{r})\rangle^+\,|0,0\rangle\,,\\
&\hat{H}|\Phi_{\mathrm{t}}\rangle = E_{\mathrm{t}}|\Phi_{\mathrm{s}}\rangle = E_{\mathrm{t}}\,|\phi(\mathbf{r})\rangle^-\,|1,m\rangle\,,
\end{aligned} \tag{2.11}$$

where the $\hat{H}$ is the Hamiltonian dependent on position, and it has the corresponding eigenvalues E_{s} and E_{t}.

Here, we introduce a new Hamiltonian H, which provides the same eigenvalues but is position-independent, and we assume that H acts exclusively

on the electron spins:

$$\begin{aligned} H|0,0\rangle &= E_{\mathrm{s}}\,|0,0\rangle\,, \\ H|1,m\rangle &= E_{\mathrm{t}}\,|1,m\rangle\,. \end{aligned} \tag{2.12}$$

From quantum mechanics, we know that the expectation value of $\mathbf{S}_i^2$ is given by

$$\mathbf{S}_i^2 = \hbar^2 S(S+1) = \frac{3}{4}\hbar^2, \tag{2.13}$$

where $S = \frac{1}{2}$. The total spin $\mathbf{S} = \mathbf{S}_1 + \mathbf{S}_2$, and we have

$$\mathbf{S}_1 \cdot \mathbf{S}_2 = \frac{1}{2}(\mathbf{S}^2 - \mathbf{S}_1^2 - \mathbf{S}_2^2) = \frac{1}{2}\hbar^2(S(S+1) - \frac{3}{2}). \tag{2.14}$$

From Eq. (2.14), one can show that:

$$H = \frac{1}{4}(E_{\mathrm{s}} + 3E_{\mathrm{t}}) - \frac{1}{\hbar^2}(E_{\mathrm{s}} - E_{\mathrm{t}})\mathbf{S}_1 \cdot \mathbf{S}_2 = J_0 - J_{12}\mathbf{S}_1 \cdot \mathbf{S}_2, \tag{2.15}$$

where we call J_{12} the exchange coupling parameter:

$$J_{12} = \frac{1}{\hbar^2}(E_{\mathrm{s}} - E_{\mathrm{t}}). \tag{2.16}$$

If J_{12} is positive, we say that the spin interaction is ferromagnetic, and the spins tend to align parallel to each other.

To investigate what is the meaning of J_{12}, the Heitler-London approximation is adopted, and the ϕ_{s} and ϕ_{t} are represented as:

$$\begin{aligned} \Phi_{\mathrm{s}} &= \frac{1}{\sqrt{2}}(\varphi_2(\mathbf{r}_1)\varphi_1(\mathbf{r}_2) - \varphi_1(\mathbf{r}_1)\varphi_2(\mathbf{r}_2)), \\ \Phi'_{\mathrm{t}} &= \frac{1}{\sqrt{2}}(\varphi_2(\mathbf{r}_1)\varphi_1(\mathbf{r}_2) + \varphi_1(\mathbf{r}_1)\varphi_2(\mathbf{r}_2)), \end{aligned} \tag{2.17}$$

where φ_i represents the ground state wave function of the isolated atom i. The value of $E_{\mathrm{s}} - E_{\mathrm{t}}$ can be expressed as:

$$E_{\mathrm{s}} - E_{\mathrm{t}} = \frac{\langle\Phi_{\mathrm{s}}|\hat{H}|\Phi_{\mathrm{s}}\rangle}{\langle\Phi_{\mathrm{s}}|\Phi_{\mathrm{s}}\rangle} - \frac{\langle\Phi'_{\mathrm{t}}|\hat{H}|\Phi'_{\mathrm{t}}\rangle}{\langle\Phi'_{\mathrm{t}}|\Phi'_{\mathrm{t}}\rangle}\,. \tag{2.18}$$

From the Heitler-London approximation, in the limit of large separation between the atom 1 and 2, the $E_s - E_t$ is approximately given by:

$$\begin{aligned} E_{\mathrm{s}} - E_{\mathrm{t}} \approx 2 \int \varphi_1(\mathbf{r}_1)\varphi_2(\mathbf{r}_2) \left[\frac{e^2}{|\mathbf{r}_1 - \mathbf{r}_2|} + \frac{e^2}{|\mathbf{R}_1 - \mathbf{R}_2|} - \frac{e^2}{|\mathbf{r}_1 - \mathbf{R}_2|} - \frac{e^2}{|\mathbf{r}_2 - \mathbf{R}_1|}\right] \\ \varphi_2(\mathbf{r}_1)\varphi_1(\mathbf{r}_2) d\mathbf{r}_1 d\mathbf{r}_2. \end{aligned} \tag{2.19}$$

Eq. (2.19) indicates that exchange coupling parameter $J_{12} = \frac{1}{\hbar^2}(E_{\mathrm{s}} - E_{\mathrm{t}})$ is

equal to the matrix element between two states which differ only by coordinate exchange, and that is the reason why we call this interaction the exchange interaction.

This interaction can be promoted from two spin sites to N spins, then we get the Heisenberg exchange interaction:

$$H_{\text{exc}} = -\sum_{ij} J_{ij}\mathbf{S}_i \cdot \mathbf{S}_j. \tag{2.20}$$

To obtain the exchange interaction, two assumptions are made. On the one hand, the interaction is restricted to a certain subset of nondegenerate orbital states. On the other hand, the orbital functions are assumed orthogonal. In fact, in a real system, these two assumptions are not satisfied, and the interactions are very complicated. Regardless, the magnetic exchange interaction successfully describes many observed magnetic phenomena in magnets.

2.3.2 Zeeman coupling

Under the application of homogeneous magnetic field $\mathbf{B}$, the magnetisation $\mathbf{m}$ can couple with $\mathbf{B}$, generating additional energy:

$$H_{\text{Zeeman}} = -\sum_{i} \mathbf{B} \cdot (\mathbf{m}_i^{\text{L}} + \mathbf{m}_i^{\text{S}}), \tag{2.21}$$

where the $\mathbf{m}_i^{\text{L}}$ and $\mathbf{m}_i^{\text{S}}$ are the orbital magnetic moment and spin magnetic moment at site i. Usually, the orbital contribution is too tiny to be ignored. In Chapter 8, we discuss the Zeeman energy generated by the coupling between topological orbital moment and $\mathbf{B}$, which is also named the ring-exchange interaction.

2.3.3 Magnetic interactions caused by spin-orbit coupling

Magnetocrystalline anisotropy

The magnetocrystalline anisotropy (MCA) is mainly due to the spin-orbit coupling (SOC). The orbital motion of the electrons couples with the crystal field, and this coupling energy is dependent on the magnetic moment orientation. If the system has a uniaxial anisotropy, the spin Hamiltonian of magnetocrystalline anisotropy can be written as:

$$H_{\text{MCA}} = -A\sum_{i} (\hat{\mathbf{n}}_i \cdot \mathbf{S}_i)^2. \tag{2.22}$$

Here, A is the anisotropy parameter determined by the energy difference between the magnetic moments along vector $\hat{\mathbf{n}}_i$ and perpendicular to it. If $A > 0$, the direction of $\hat{\mathbf{n}}_i$ is called the easy-axis, and the system has the minimum energy if the spin direction is parallel to $\hat{\mathbf{n}}_i$. If $A < 0$, the minimum energy corresponds to the case when the spin direction is perpendicular to

$\hat{\mathbf{n}}_i$, and the system has an easy-plane. Besides, multi-axis systems exist, but they are too complex for us to consider. In this thesis, all magnetic systems investigated are uniaxial systems.

Dzyaloshinskii-Moriya interaction

The Dzyaloshinskii-Moriya interaction (DMI) [25, 26], also known as an antisymmetric exchange interaction, is an exchange interaction between two neighboring spins due to the SOC. Its spin Hamiltonian in an atomistic description can be written as:

$$H_{\mathrm{DMI}} = -\sum_{ij} \mathbf{D}_{ij} \cdot (\mathbf{S}_i \times \mathbf{S}_j), \tag{2.23}$$

where $\mathbf{D}_{ij} = (D_{ij}^x, D_{ij}^x, D_{ij}^x)$ is a vector which holds antisymmetric: $\mathbf{D}_{ij} = -\mathbf{D}_{ji}$. The DMI only exists in a system with broken inversion symmetry, and the direction of $\mathbf{D}_{ij}$ is determined by the structure, following the Moriya's symmetry rules [26]. To satisfy the symmetry requirement, the DMI usually exists at surfaces, interfaces or bulk materials with low symmetry. In addition, heavy elements are introduced to enhance the SOC.

The DMI is a very important interaction, which greatly promotes the prosperity of magnetic phenomena. It is the origin of spin-spiral magnetic structures, skyrmions and some frustrated magnets. In magnonics, an appropriate DMI can drive the vector spin chirality and nontrivial magnonic topology. The influence of DMI on magnonic phenomena is investigated and the detailed information is shown in Chapter 6.

Kitaev interaction

In addition to DMI, the Kitaev interaction originating from SOC is attracting increasing attention [39, 40, 41, 42, 10]. The Kitaev interaction is not only theoretically studied in the triangular, honeycomb and kagome lattice [43, 42, 44], but is also observed in the honeycomb lattice, experimentally (*e.g.*, A_2IrO_3, $\alpha-RuCl_3$) [45, 42]. The Kitaev interaction plays an important role in spin liquid states [42, 10], Majorana quantization [10], and plenty of topologically ordered phases can be achieved by applying an external magnetic field [46, 47]. The interplay of the Kitaev interaction and DMI for magnonic properties are systematically studied for the honeycomb lattice, as discussed in Chapter 7. The sketch of the honeycomb Kitaev model is shown in Figure 2.2 (a), and the effective spin Hamiltonian of the Kitaev interaction is represented as:

$$H_{\mathrm{K}} = -K \sum_{\langle ij \rangle^\gamma} S_i^\gamma S_j^\gamma \quad (\gamma \in \boldsymbol{x}, \boldsymbol{y}, \boldsymbol{z}), \tag{2.24}$$

where K is called the strength of the Kitaev interaction and γ denotes the component of the spin directed along the bond $\boldsymbol{x}$, $\boldsymbol{y}$ and $\boldsymbol{z}$. In this thesis, S_i^γ is defined as $\mathbf{S}_i \cdot \hat{\gamma}_\alpha$ with $\hat{\gamma}_\alpha$ ($\alpha \in (\boldsymbol{x}, \boldsymbol{y}, \boldsymbol{z})$) being the Kitaev vector and $\mathbf{S}_i$ being the spin vector defined as $\mathbf{S}_i = (S^x, S^y, S^z)$. One kind of definition of the

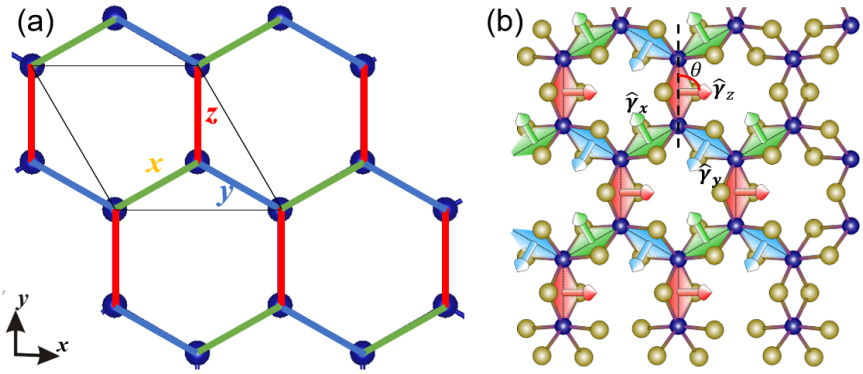

FIGURE 2.2: (a) Sketch of the structure of honeycomb Kitaev model. The unit cell is outlined with a thin black line, where blue balls represent magnetic atoms. The Kitaev bonds x (yellow), y (blue), z (red) are indicated with thick colored lines. (b) The top view of monolayer CrI_3 with the Cr_2I_2 plane colored according to their normal vectors $\hat{\gamma}_x$, $\hat{\gamma}_y$ and $\hat{\gamma}_z$. These normal vectors are called as Kitaev vector and the polar angle of $\hat{\gamma}_z$ is defined as the Kitaev angle.

Kitaev vector is shown in Figure 2.2 (b), where the $\hat{\gamma}_z$ is defined as (sinθ, 0, cosθ) with polar angle θ defined as the Kitaev angle in the thesis, and the $\hat{\gamma}_x$ and $\hat{\gamma}_y$ can be obtained according to the crystal symmetry.

2.3.4 Higher-order spin interactions

The interactions mentioned above are one or two site spin interactions. There are interactions including more than two spins, such as ring exchange interaction [48, 49, 7], spin-chirality interaction, and chirality-chirality interaction [16]. The ring exchange is known as the orbital Zeeman coupling and it is discussed in Chapter 8. Other higher-order interactions are not considered in my thesis.

2.3.5 Generalized Heisenberg Hamiltonian

After considering all interactions mentioned above, we get the generalized Heisenberg Hamiltonian:

$$\begin{aligned} H = &- \sum_{i,j} J_{ij}\mathbf{S}_i \cdot \mathbf{S}_j - \sum_{\langle ij\rangle \in \boldsymbol{x},\boldsymbol{y},\boldsymbol{z}} K S_i^{\gamma} S_j^{\gamma} - \sum_{ij} \mathbf{D}_{ij} \cdot (\mathbf{S}_i \times \mathbf{S}_j) \\ &- A \sum_i (\hat{\mathbf{n}}_i \cdot \mathbf{S}_i)^2 - \mathbf{B} \cdot \mu_{\mathrm{B}} \sum_i (g_{\mathrm{e}} \mathbf{S}_i + \mathbf{L}_i), \end{aligned} \tag{2.25}$$

where the first term is the exchange interaction term, and J_{ij} coefficients mediate the isotropic Heisenberg exchange interaction between spins $\mathbf{S}_i$ and $\mathbf{S}_j$

on sites i and j. The second term is due to the anisotropic Kitaev interaction, where S_i^{γ}= $\mathbf{S}_i \cdot \hat{\gamma}_{ij}$ with $\hat{\gamma}_{ij}$ being the Kitaev vector determined by the sites i and j. The third term is the DMI represented by the DMI vectors $\mathbf{D}_{ij}$. The fourth term is the single-ion anisotropy term with respect to the local easy axis $\hat{\mathbf{n}}_i$, and the last term is the energy of Zeeman coupling to the magnetic field $\mathbf{B}$. Here $\hbar$ is renormalized as "1".

2.3.6 Monte Carlo method

In this section, we discuss how to obtain the classical ground states and Curie temperature with the help of the Monte Carlo method. During the simulation, we first need to build a big system which contains enough sites. The Markov chain is selected and the time-dependence of the probability $P_n(t)$ is given by the master equation [50]:

$$\frac{\partial P_n(t)}{\partial t} = -\sum_{n \neq m} [P_n(t) W_{n\to m} - P_m(t) W_{m\to n}], \tag{2.26}$$

where $W_{n\to m}$ represents the transition rate from state n to m. In equilibrium, the probability obeys $\partial P_n^{\mathrm{eq}}(t)/\partial t = 0$ and $P_n(t) W_{n\to m} = P_m(t) W_{m\to n}$. In a classical system, the probability can be calculated according to:

$$P_n(t) = e^{-\frac{E_n}{k_{\mathrm{B}} T}}/Z, \tag{2.27}$$

where T represents the temperature, k_{B} is the Boltzmann constant, E_n is the energy of state n and Z is the partition function. In many cases, it is impossible to calculate the Z, and it is usually unknown. In fact, we don't need to calculate Z, and only the energy difference $\Delta E = E_n - E_m$ is important. During the process of the Markov chain, if the system is in equilibrium, each configuration is directly generated from the previous one with the equation:

$$\frac{P_n(t)}{P_m(t)} = \frac{W_{m\to n}}{W_{n\to m}} = e^{-\frac{\Delta E}{k_{\mathrm{B}} T}}, \tag{2.28}$$

In our calculation, the most widely used form is adopted:

$$W_{m\to n} = \begin{cases} e^{-\frac{\Delta E}{k_{\mathrm{B}} T}} & (\Delta E > 0), \\ 1 & (\Delta E < 0). \end{cases} \tag{2.29}$$

We carry out the simulation from a given classical spin configuration $\{S\}_n$ with energy E_n. Then, we randomly give an updated spin at site i, *e.g.* we change the spin $S_i \to -S_i$ in an Ising model. Then, the new energy E_{n+1} can be calculated according to the Hamiltonian. If the new energy is lower than the old one ($E_{n+1} < E_n$), we always accept the update, which is the new configuration $\{S\}_{n+1}$. If $E_{n+1} > E_n$, whether we accept it or not depends on the probability

$$q = e^{-\frac{E_{n+1} - E_n}{k_{\mathrm{B}} T}} \tag{2.30}$$

We generate a random number $r \in (0, 1)$, and we compare the value of r and q to determine whether we accept the new configuration or not. If $r < q$, we accept the step, otherwise, it is rejected. We repeat this routine many times, until the system is in equilibrium, which corresponds to the classical magnetic ground state under the given temperature.

The Curie temperature of a ferromagnet or the Néel temperature of an antiferromagnet can be estimated through counting the variation of the average magnetic moment with temperature. For instance, the Curie temperature of magnets can be determined by locating the second-order phase transition point of the magnetic moment. In Chapter 5, the Monte Carlo method is used to obtain the Curie temperature of Mn-PBP.

2.3.7 Introduction to spin wave

As mentioned above, we introduced all kinds of spin interactions to build the generalized Heisenberg Hamiltonian. In the following sections, we discuss the spin dynamics with localized magnetic moments. Firstly, we discuss it from the perspective of mean-field theory.

To simplify the analysis, in our Hamiltonian, we only select the Heisenberg exchange interaction and we set $J_{ij} > 0$ to ensure that its ground state is ferromagnetic:

$$H = -\sum_{i,j} J_{ij} \mathbf{S}_i \cdot \mathbf{S}_j. \tag{2.31}$$

We introduce the effective field from the mean-field theory:

$$H = -\mathbf{B}_{\text{eff}} \cdot \sum_i \mathbf{S}_i, \tag{2.32}$$

where the effective magnetic field is expressed as:

$$\mathbf{B}_{\text{eff}} = 2 \sum_j J_{ij} \mathbf{S}_j. \tag{2.33}$$

Here the factor '2' is introduced as each pair of neighbors is calculated twice. Then we can study the motion of each spin through calculating the spin torque according to:

$$\begin{aligned} \tau_i = \hbar \frac{d\mathbf{S}_i}{dt} &= -\mathbf{S}_i \times \mathbf{B}_{\text{eff}} \\ &= -2 \sum_j J_{ij} \mathbf{S}_i \times \mathbf{S}_j. \end{aligned} \tag{2.34}$$

The spin operators can be expressed as $\mathbf{S}_i = (S_i^x, S_i^y, S_i^z)$ with the length S for all i. Then, the Eq. (2.34) can be expressed as:

$$\begin{aligned}
\hbar\frac{dS_i^x}{dt} &= -2\sum_j J_{ij}(S_i^y S_j^z - S_j^y S_i^z),\\
\hbar\frac{dS_i^y}{dt} &= -2\sum_j J_{ij}(S_i^z S_j^x - S_j^z S_i^x),\\
\hbar\frac{dS_i^z}{dt} &= -2\sum_j J_{ij}(S_i^y S_j^x - S_j^y S_i^x).
\end{aligned} \tag{2.35}$$

As the ground state is ferromagnetic, we can assume the direction of magnetization points along the z axis and the motion of the spin is consisted of a small movement around the z axis. Then, we can assume that $S^z \approx S$ and treat S^x and S^y as higher-order terms. Then, only the first two equations of Eq. (2.35) are left, as $S_i^x S_j^y$ and $S_i^y S_j^x$ are disregarded:

$$\begin{aligned}
\hbar\frac{dS_i^x}{dt} &= -2S\sum_j J_{ij}(S_i^y - S_j^y),\\
\hbar\frac{dS_i^y}{dt} &= -2S\sum_j J_{ij}(S_j^x - S_i^x).
\end{aligned} \tag{2.36}$$

It is clear from Eq. (2.36), the spin dynamics of S^x is related to S^y, and vice-versa. To decouple these, the following transformation is introduced:

$$S^{\pm} = S^x \pm \mathrm{i}S^y. \tag{2.37}$$

Here, the $S^{\pm}$ are named as the ladder operators. The S^+ and S^- correspond to an increase and a decrease in the S^z quantum number. The ladder operators follow the following commutation relations:

$$\begin{aligned}
[S_i^+, S_j^-] &= 2S_i^z\delta_{ij},\\
[S_i^z, S_j^{\pm}] &= \pm 2S_i^{\pm}\delta_{ij}.
\end{aligned} \tag{2.38}$$

Then Eq. (2.36) can be transformed to:

$$\hbar\frac{dS_i^{\pm}}{dt} = \mp 2S\sum_j J_{ij}(S_i^{\pm} - S_j^{\pm}). \tag{2.39}$$

To simplify the analysis, we can assume that the spin system is in Bravais lattice with only one spin i in each unit cell. Then we can make use of the Fourier transform:

$$\begin{aligned}
S_{\mathbf{k}}^{\pm}(t) &= \frac{1}{\sqrt{N}}\sum_i e^{-\mathrm{i}\mathbf{k}\mathbf{R}_\mathbf{i}} S_i^{\pm}(t),\\
S_i^{\pm}(t) &= \frac{1}{\sqrt{N}}\sum_{\mathbf{k}} e^{\mathrm{i}\mathbf{k}\mathbf{R}_\mathbf{i}} S_{\mathbf{k}}^{\pm}(t),
\end{aligned} \tag{2.40}$$

where $\mathbf{R}_i$ is the position vector of the site i and $\mathbf{k}$ is the wave vector of the spin wave. Then Eq. (2.39) turns into:

$$\hbar\frac{dS_{\mathbf{k}}^{\pm}(t)}{dt} = \mp \mathrm{i}2S(J_0 - J_{\mathbf{k}})S_{\mathbf{k}}^{\pm}(t), \tag{2.41}$$

with $J_0 = \sum_i J_{ij}$, $J_{\mathbf{k}} = \sum_i e^{-\mathrm{i}\mathbf{k}\Delta\mathbf{R}_{ij}} J_{ij}$ and $\Delta\mathbf{R}_{ij} = \mathbf{R}_i - \mathbf{R}_j$. Then, Eq. (2.41) can be solved with the ansatz solution: $S_{\mathbf{k}}^{\pm}(t) = S_{\mathbf{k}}^{\pm} e^{\mp \mathrm{i}\omega_{\mathbf{k}}^{\pm} t}$:

$$\hbar\omega_{\mathbf{k}}^{\pm} = \mp 2S(J_0 - J_{\mathbf{k}}). \tag{2.42}$$

Let's focus on S_i^- and $S_{\mathbf{k}}^-$, as the corresponding eigenvalue is positive. From the Heisenberg picture or commutation relation, we have:

$$\frac{dS_{\mathbf{k}}^-}{dt} = \frac{\mathrm{i}}{\hbar}[H, S_{\mathbf{k}}^-]. \tag{2.43}$$

Then, we have $\hbar\omega_{\mathbf{k}}^- S_{\mathbf{k}}^- = [H, S_{\mathbf{k}}^-]$. If we define a fully polarized ground state $|\Phi\rangle$ and we apply $S_{\mathbf{k}}^-$ to it, then we get:

$$\hbar\omega_{\mathbf{k}}^- S_{\mathbf{k}}^- |\Phi\rangle = [H, S_{\mathbf{k}}^-]|\Phi\rangle = HS_{\mathbf{k}}^-|\Phi\rangle - S_{\mathbf{k}}^- E_0|\Phi\rangle \tag{2.44}$$

where E_0 is the ground state energy. We thus find:

$$HS_{\mathbf{k}}^-|\Phi\rangle = (E_0 + \hbar\omega_{\mathbf{k}}^-)S_{\mathbf{k}}^-|\Phi\rangle. \tag{2.45}$$

In Eq. (2.45), $S_{\mathbf{k}}^-|\Phi\rangle$ is a new eigenstate of Hamiltonian H. The $S_{\mathbf{k}}^-$ creates one quantum of the spin wave with the energy $\hbar\omega_{\mathbf{k}}^-$, and we call this quantized spin wave as magnon.

2.4 Quantum theory of spin waves

2.4.1 Magnon dispersion with quantum theory method

In this part, we first present a simple Hamiltonian to discuss its ground state; then the Holstein-Primakoff transformation is introduced to transfer the Hamiltonian from spin operator to bosonic creation and annihilation operators. Finally, we discuss how to obtain the magnon dispersion from the perspective of quantum theory.

Ground state of the ferromagnetic Heisenberg Hamiltonian

Here, we consider a simple ferromagnetic Heisenberg Hamiltonian:

$$H = -\sum_{i,j} J_{ij}\mathbf{S}_i \cdot \mathbf{S}_j - g_{\mathrm{e}}\mu_{\mathrm{B}}\mathbf{B}\sum_i \mathbf{S}_i, \tag{2.46}$$

with $J_{ij} > 0$, $\mathbf{B}$ is the magnetic field along z direction $(0, 0, B_z)$. We can prove that its exact ground state has the following formula:

$$|\Phi_{\mathrm{GS}}\rangle = \prod_i |S\rangle_i. \tag{2.47}$$

We update the Eq. (2.46) with Eq. (2.37)

$$H = -\sum_{i,j} J_{ij} S_i^z S_j^z - \sum_{i,j} J_{ij} S_i^+ S_j^- - g_{\mathrm{e}}\mu_{\mathrm{B}}\mathbf{B}\sum_i S_i^z. \tag{2.48}$$

As introduced in the Eq. (2.37), we introduce the lowering and raising operators, and they satisfy:

$$S_i^{\pm}|S^z\rangle_i = \sqrt{(S \mp S^z)(S + 1 \pm S^z)}|S^z \pm 1\rangle_i. \tag{2.49}$$

Then, we have

$$S_i^+|S^z = S\rangle_i = 0, \tag{2.50}$$

which means that $S^z = S$ is the maximal quantum number. From Eq. (2.46), we have:

$$H|\Phi_{\mathrm{GS}}\rangle = E_0|\Phi_{\mathrm{GS}}\rangle, \tag{2.51}$$

with $E_0 = -S^2\sum_{ij} J_{ij} - g_{\mathrm{e}}\mu_{\mathrm{B}}B_z\sum_i S_i^z$. Therefore, $|\Phi_{\mathrm{GS}}\rangle$ is an eigenstate of H. As other states with a non-maximal S^z quantum number for one of the lattice sites have larger energy than E_0, it has to be the ground state.

Holstein-Primakoff transformation

Next, we introduce the Holstein-Primakoff (HP) transformation [51]. From quantum mechanics, we are familiar with the bosonic creation operator $\alpha^\dagger$ and annihilation operator α, which satisfy the following equation:

$$\begin{aligned} \alpha_g|...n_g...\rangle &= \sqrt{n_g}|...n_g - 1...\rangle, \\ \alpha_g^\dagger|...n_g...\rangle &= \sqrt{n_g + 1}|...n_g + 1...\rangle, \end{aligned} \tag{2.52}$$

where g represents a generic quantum state and n_g is the corresponding occupation number. The $\alpha^\dagger$ and α follow the bosonic commutation relations:

$$\begin{aligned} [\alpha_i^\dagger, \alpha_i^\dagger] &= [\alpha_i, \alpha_i] = 0, \\ [\alpha_i, \alpha_j^\dagger] &= \delta_{ij}. \end{aligned} \tag{2.53}$$

Here, we can treat the occupation number n_i as the spin-deviation operator given by the equation:

$$n_i = S_i - S_i^z = \alpha_i^\dagger\alpha_i. \tag{2.54}$$

Then, we have

$$\begin{aligned}\alpha_i^\dagger|S^z\rangle_i &= \alpha_i^\dagger|n = S - S^z\rangle_i = \sqrt{S - S_i^z + 1}|n = S - S^z + 1\rangle_i \\ &= \sqrt{S - S_i^z + 1}|S^z - 1\rangle_i, \\ \alpha_i|S^z\rangle_i &= \alpha_i|n = S - S^z\rangle_i = \sqrt{S - S_i^z}|n = S - S^z - 1\rangle_i \\ &= \sqrt{S - S_i^z}|S^z + 1\rangle_i.\end{aligned} \tag{2.55}$$

Combining the Eq. (2.49) and Eq. (2.55), we have

$$\begin{aligned}S_i^-|S^z\rangle_i = \alpha_i^\dagger\sqrt{S + S_i^z}|S^z\rangle_i &= \sqrt{2S}\alpha_i^\dagger\sqrt{1 - \frac{S - S_i^z}{2S}}|S^z\rangle_i \\ &= \sqrt{2S}\alpha_i^\dagger\sqrt{1 - \frac{\alpha_i^\dagger\alpha_i}{2S}}|S^z\rangle_i,\end{aligned} \tag{2.56}$$

$$\begin{aligned}S_i^+|S^z\rangle_i = \sqrt{S + S_i^z + 1}\alpha_i|S^z\rangle_i &= \sqrt{2S}\sqrt{1 - \frac{S - S_i^z - 1}{2S}}\alpha_i|S^z\rangle_i \\ &= \sqrt{2S}\sqrt{1 - \frac{\alpha_i^\dagger\alpha_i}{2S}}\alpha_i|S^z\rangle_i,\end{aligned} \tag{2.57}$$

which yields:

$$\begin{aligned}S_i^- &= \sqrt{2S}\alpha_i^\dagger\sqrt{1 - \frac{\alpha_i^\dagger\alpha_i}{2S}}, \\ S_i^+ &= \sqrt{2S}\sqrt{1 - \frac{\alpha_i^\dagger\alpha_i}{2S}}\alpha_i.\end{aligned} \tag{2.58}$$

We name Eq. (2.58) as the HP transformation. We immediately conclude that $n_i < 2S$, from the Eq. (2.58) and Eq. (2.54). Usually, the spin deviations are very small at low temperature, and we can assume $n_i \ll 2S$. Then, the Eq. (2.58) transforms into:

$$\begin{aligned}S_i^- &= \sqrt{2S}\alpha_i^\dagger, \\ S_i^+ &= \sqrt{2S}\alpha_i, \\ S_i^z &= S - a_i^\dagger a_i = S - n_i.\end{aligned} \tag{2.59}$$

In the linear spin-wave theory, we usually use Eq. 2.59 to perform the HP transformation.

Let us come back to the ferromagnetic Heisenberg Hamiltonian as given by Eq. (2.46). Its ground state corresponds to $S = S^z$, and Eq. (2.55) changes to:

$$\begin{aligned}\alpha_i^\dagger|S^z\rangle_i &= |S^z - 1\rangle_i, \\ \alpha_i|S^z\rangle_i &= 0.\end{aligned} \tag{2.60}$$

Eq. (2.60) indicates that $\alpha_i^\dagger|S^z\rangle_i$ generates one deviation state, and the whole spin is less by 1 than the original state. If we perform the Fourier transformation on $\alpha_i^\dagger$ and α_i, we get the magnon creation and magnon annihilation operators, respectively:

$$\begin{aligned} a_{\mathbf{k}} &= \frac{1}{\sqrt{N}} \sum_{\mathbf{k}} e^{-\mathrm{i}\mathbf{k}\cdot\mathbf{R_i}} \alpha_i, \\ a_{\mathbf{k}}^\dagger &= \frac{1}{\sqrt{N}} \sum_{\mathbf{k}} e^{\mathrm{i}\mathbf{k}\cdot\mathbf{R_i}} \alpha_i^\dagger, \end{aligned} \tag{2.61}$$

The magnon annihilation $a_{\mathbf{k}}$ and magnon creation operator $a_{\mathbf{k}}^\dagger$ have special meaning. For instance, in the ferromagnetic ground state with spin length S, $a_{\mathbf{k}}^\dagger|\Phi_{\mathrm{GS}}\rangle$ corresponds to the total magnetization of $NS-1$, which means that $a_{\mathbf{k}}^\dagger$ creates one quantum of spin wave at momentum $\mathbf{k}$, which is one magnon.

Magnon dispersion

To get the magnon dispersion, we first rewrite the Hamiltonian according to Eq. (2.46) and Eq. (2.59). Then, the Hamiltonian is represented in terms of bosonic operators and we only keep the terms of quadratic order. This is because the higher-order interactions refer to the magnon-magnon interaction and the first-order terms vanish. The Hamiltonian is updated as:

$$H = -S\sum_{ij} J_{ij}(a_i a_j^\dagger + a_i^\dagger a_j - a_i^\dagger a_i - a_j^\dagger a_j) - g_{\mathrm{e}}\mu_{\mathrm{B}} S B_z \sum_i a_i^\dagger a_i + E_0, \tag{2.62}$$

where E_0 is the constant energy and it corresponds to the ground state energy: $E_0 = -S^2\sum_{ij} J_{ij} - g_{\mathrm{e}}\mu_{\mathrm{B}} B_z \sum_i S_i^z$. Then, we can do Fourier transformation on Eq. (2.62) to transform it from real space to momentum space according to Eq. (2.61). Here we assume that each unit cell contains only one spin and we finally obtain:

$$H = \sum_{\mathbf{k}} \epsilon_{\mathbf{k}} a_{\mathbf{k}}^\dagger a_{\mathbf{k}} + E_0, \tag{2.63}$$

and the energy of a magnon at vector $\mathbf{k}$ is represented as:

$$\epsilon_k = S\left(\sum_{ij} J_{ij} - \sum_{ij} J_{ij} e^{\mathrm{i}\mathbf{k}\Delta\mathbf{R}_{ij}}\right) + g_{\mathrm{e}} B_z \mu_{\mathrm{B}} S, \tag{2.64}$$

with $\Delta\mathbf{R}_{ij} = \mathbf{R}_i - \mathbf{R}_j$. As $J_{ij} > 0$, we get $\epsilon_{\mathbf{k}} \geq 0$, indicating that magnons correspond to excitation states. The minimum of $\epsilon_{\mathbf{k}}$ happens at $\mathbf{k} = 0$, which is also the classical ground state. As the method is based on the HP transformation, and we only keep terms up to the quadratic order of the creation and annihilation operators, this method is called the linear spin-wave theory (LSWT) [52, 53].

If the number of spin sites $n > 1$ in one unit cell, the system has n magnon branches. Then, Eq. (2.63) can be changed into the matrix format:

$$H = \left(\begin{array}{c} a^{\dagger}_{\mathbf{k},1} \cdots a^{\dagger}_{\mathbf{k},n} \end{array} \right) H_{\mathbf{k}} \left(\begin{array}{c} a_{\mathbf{k},1} \\ \vdots \\ a_{\mathbf{k},n} \end{array} \right), \tag{2.65}$$

where

$$H_{\mathbf{k}} = \left(\begin{array}{c} H^{11}_{\mathbf{k}} \cdots H^{1n}_{\mathbf{k}} \\ \vdots \ddots \vdots \\ H^{n1}_{\mathbf{k}} \cdots H^{nn}_{\mathbf{k}} \end{array} \right). \tag{2.66}$$

where $H^{ii}_{\mathbf{k}} = \sum_j SJ_{ij} + g_e B_z \mu_B S$ and $H^{ij}_{\mathbf{k}} = -\sum_{\Delta \mathbf{R}_{ij}} SJ_{ij} e^{\mathrm{i}\mathbf{k}\Delta\mathbf{R}_{ij}}$ with $\Delta\mathbf{R}_{ij} = \mathbf{R}_i - \mathbf{R}_j$ for the whole system. We can do the matrix diagonalization of the linear spin-wave matrix $H_{\mathbf{k}}$ to obtain the corresponding magnon dispersion.

Low T spontaneous magnetization

For a given low temperature, the total spin magnetization per unit cell can be derived as:

$$\begin{aligned} M(T) &= g_{\mathrm{e}}\mu_{\mathrm{B}} \sum_i (S - \langle a^{\dagger}_i a_i \rangle_{\mathrm{T}}) \\ &= N g_{\mathrm{e}}\mu_{\mathrm{B}} S - g_{\mathrm{e}}\mu_{\mathrm{B}} \sum_{\mathbf{k}} (\langle b^{\dagger}_{\mathbf{k}} b_{\mathbf{k}} \rangle_{\mathrm{T}}) \\ &= M(0) \left[1 - \frac{1}{NS} \sum_{\mathbf{k}} \langle \hat{n}_{\mathbf{k}} \rangle_{\mathrm{T}} \right] \\ &= M(0) \left[1 - \frac{V}{NS(2\pi)^3} \int_{BZ} \frac{d\mathbf{k}}{e^{\epsilon_{\mathbf{k}}/k_{\mathrm{B}}T} - 1} \right], \end{aligned} \tag{2.67}$$

where $M(0) = N g_e \mu_B S$ is the saturation magnetization. If we ignore the magnetic field, the eigenvalue of magnons can be obtained based on the Eq. (2.64):

$$\epsilon(\mathbf{k}) = 2S \sum_{\triangle \mathbf{R}} J(\triangle \mathbf{R}) \sin^2(\frac{\mathbf{k} \cdot \triangle \mathbf{R}}{2}). \tag{2.68}$$

Usually, the exchange interactions decay rapidly as we increase $\triangle\mathbf{R}$ in magnets. At low temperature, $\epsilon_{\mathbf{k}} \gg k_B T$ and only magnons with small $\mathbf{k}$ contribute to $M(T)$, causing that $\mathbf{k} \cdot \triangle\mathbf{R} \ll 2$. Then, the Eq. (2.68) changes into:

$$\epsilon(\mathbf{k}) \approx \frac{S}{2} \sum_{\triangle\mathbf{R}} J(\triangle\mathbf{R})(\mathbf{k} \cdot \triangle\mathbf{R})^2. \tag{2.69}$$

If we update Eq. (2.69) to Eq. (2.67) and utilize certain approximations, we can arrive at $M(T)$ with the following expression:

$$M(T) = M(0)\left[1 - \left(\frac{T}{T_{\mathrm{C}}}\right)^{\frac{3}{2}}\right], \tag{2.70}$$

where T_{C} is the Curie temperature of the ferromagnet. The Eq. (2.70) is consistent with low-temperature experiments on ferromagnets, which is also known as Bloch $T^{\frac{3}{2}}$ law. In Chapter 8, we present the temperature-dependent magnetization of TOM, which holds different characteristics.

2.4.2 Spin waves with generalized Heisenberg Hamiltonian

In this section, we present a generic approach to get the eigenvalue and eigenstate in complex systems from the generalized Heisenberg Hamiltonian with linear spin-wave theory [52, 53]. We start from the following Hamiltonian:

$$\begin{aligned} H = &- \sum_{i,j} J_{ij}\mathbf{S}_i \cdot \mathbf{S}_j - K \sum_{\langle ij \rangle^{\gamma}} S_i^{\gamma} S_j^{\gamma} - \sum_{ij} \mathbf{D}_{ij} \cdot (\mathbf{S}_i \times \mathbf{S}_j) \\ &- A \sum_i (\hat{\mathbf{n}}_i \cdot \mathbf{S}_i)^2 - g_e \mu_B \mathbf{B} \sum_i \mathbf{S}_i, \end{aligned} \tag{2.71}$$

where the meaning of each term has been discussed above, and $\hbar$ is set to 1.

Spin waves with ferromagnetic ground state

We first focus on the ferromagnetic ground state, where all spins point in the z direction. We can transform the Hamiltonian into the matrix form, and the resulting Hamiltonian is shown as:

$$H = -\sum_{\langle ij \rangle} \mathbf{S}_i^{\dagger} \hat{J}_{ij} \mathbf{S}_j - \sum_{\langle ij \rangle} \mathbf{S}_i^{\dagger} \hat{D}_{ij} \mathbf{S}_j - \sum_{\langle ij \rangle} \mathbf{S}_i^{\dagger} \hat{A} \mathbf{S}_j - \mu_B g_e \sum_i \mathbf{B} \cdot \mathbf{S}_i, \tag{2.72}$$

where the spin operators $S_i^{\dagger}$ are regarded as the column vectors with $S_i^{\dagger} = (S_i^x, S_i^y, S_i^z)$. $\hat{J}_{ij}$ is the new exchange matrix tensor introduced to represent the anisotropic exchange interaction between the atom i and j, containing the Kitaev interaction and isotropic exchange interaction. The $\hat{D}_{ij}$ and $\hat{A}$ represent the antisymmetric off-diagonal DMI tensor and the single-ion magnetic

anisotropy energy tensor caused by the spin-orbit coupling:

$$\hat{D}_{ij} = \begin{pmatrix} 0 & D_{ij}^{z} & -D_{ij}^{y} \\ -D_{ij}^{z} & 0 & D_{ij}^{x} \\ D_{ij}^{y} & -D_{ij}^{x} & 0 \end{pmatrix}, \ \hat{A}_i = \begin{pmatrix} 0 & 0 & 0 \\ 0 & 0 & 0 \\ 0 & 0 & A \end{pmatrix}. \tag{2.73}$$

We introduce anisotropic exchange interaction represented by the Kitaev interaction. Here, we put both Kitaev interaction and the isotropic exchange interaction together to form the new exchange matrix $\hat{J}_{ij}$:

$$\hat{J}_{ij} = \begin{pmatrix} J_{ij}^{xx} & J_{ij}^{xy} & J_{ij}^{xz} \\ J_{ij}^{yx} & J_{ij}^{yy} & J_{ij}^{yz} \\ J_{ij}^{zx} & J_{ij}^{zy} & J_{ij}^{zz} \end{pmatrix} = J_{ij}\mathbb{1} + K\hat{\gamma}_\alpha \otimes \hat{\gamma}_\alpha. \tag{2.74}$$

Here, J_{ij} is the isotropic exchange interaction and $\hat{J}_{ij}$ regards the interaction between site i and j (*e.g.*, $\boldsymbol{x}$, $\boldsymbol{y}$, $\boldsymbol{z}$ in Figure. 2.2) with $\hat{\gamma}_\alpha$ ($\alpha \in (\boldsymbol{x}, \boldsymbol{y}, \boldsymbol{z})$) the Kitaev vector[2]. Based on the symmetry, there are three different Kitaev vectors in the honeycomb lattice (also in the triangle and kagome lattice). Acoording to the definitation of $\hat{\gamma}_z$ discussed in Chapter 2.3.3, $\hat{\gamma}_x$ and $\hat{\gamma}_y$ can be obtained according to the symmetry of the system with

$$\hat{R}_{\theta^i} = \begin{pmatrix} \cos\theta^i & -\sin\theta^i & 0 \\ \sin\theta^i & \cos\theta^i & 0 \\ 0 & 0 & 1 \end{pmatrix}, \tag{2.75}$$

where $i \in (x, y)$ and the $\hat{\gamma}_x = \hat{\gamma}_z\hat{R}_{\theta^x}^{\mathbf{T}}$, $\hat{\gamma}_y = \hat{\gamma}_z\hat{R}_{\theta^y}^{\mathbf{T}}$ with the $\theta^x = 120^\circ$ and $\theta^y = 240^\circ$.

According to Eq. (2.59), the HP transformation [51] is adopted to change from spin operators to creation and annihilation spin-wave operators. We can represent it with matrix format: $\mathbf{S}_i = \hat{M}_i\mathbf{a_i}$ with

$$\hat{M}_i = \frac{\sqrt{2S}}{2}\begin{pmatrix} 1 & 1 & 0 \\ -i & i & 0 \\ 0 & 0 & \sqrt{\frac{2}{S}} \end{pmatrix}, \ \mathbf{a}_i = \begin{pmatrix} \alpha_i \\ \alpha_i^\dagger \\ S_i - \alpha_i^\dagger\alpha_i \end{pmatrix}. \tag{2.76}$$

Finally, we get the Hamiltonian with matrix format and each matrix element holds different order of the creation/annihilation operators and here we only keep the quadratic order. A Fourier transformation of the bosonic operators is used by

$$\mathbf{a}_i(\mathbf{k}) = \begin{pmatrix} \alpha_i(\mathbf{k}) \\ \alpha_i^\dagger(-\mathbf{k}) \end{pmatrix} = \frac{1}{\sqrt{N}}\sum_i e^{-\mathbf{i}\mathbf{k}\mathbf{R_i}}\begin{pmatrix} \alpha_i \\ \alpha_i^\dagger \end{pmatrix}, \tag{2.77}$$

where N is the number of the unit cells, and $\mathbf{k}$ is the vector in the reciprocal k-space of magnons. The Fourier-transformed Hamiltonian with quadratic

[2]If including the symmetric off-diagonal anisotropy, the new exchange matrix $\hat{J}_{ij}$ follows the equation: $\hat{J}_{ij} = J_{ij}\mathbb{1} + K\hat{\gamma}_\alpha\otimes\hat{\gamma}_\alpha + \Gamma(\hat{\gamma}_\beta\otimes\hat{\gamma}_\gamma + \hat{\gamma}_\gamma\otimes\hat{\gamma}_\beta)$ with $\alpha, \beta, \gamma \in (\boldsymbol{x}, \boldsymbol{y}, \boldsymbol{z},)$ in Figure. 2.2 and Γ represents the symmetric off-diagonal anisotropy[54].

terms, denoted as H_2, becomes a $2n \times 2n$ matrix, where n is the number of spins.

The H_2 contains the number-nonconserving terms (*e.g.*, $\alpha_i\alpha_j$, and $\alpha_i^\dagger\alpha_j^\dagger$), and we can use bosonic Bogoliubov transformation to obtain the eigenvalue. Numerically, we can diagonalize the dynamical matrix of H_2, which is calculated based on the commutation relation:

$$\mathrm{i}\frac{\mathrm{d}\Phi(\mathbf{k})}{\mathrm{d}t} = [\Phi(\mathbf{k}), H_2(\mathbf{k})] = \hat{D}\Phi(\mathbf{k}), \tag{2.78}$$

where the dynamical matrix is given by $\hat{D} = \hat{g}H_2$ with $\hat{g} = [(\mathbb{1}, 0), (0, -\mathbb{1})]$. The $\mathbb{1}$ is the $n \times n$ identity matrix, and one basis of $\Phi(\mathbf{k})$ is chosen as $\Phi(\mathbf{k}) = [a_{1k}, \ldots\ a_{nk},\ a_{1-k}^\dagger, \ldots\ a_{n-k}^\dagger]^T$. The positive real eigenvalues of the dynamical matrix $\hat{D}$ correspond to the magnon excitation spectrum in the system. The stability of the system is confirmed when there are n non-negative eigenvalues for each vector $\mathbf{k}$. The left and right eigenvectors of $\hat{D}$, denoted as V_L and V_R, may differ since $\hat{D}$ is not necessarily hermitian. The relationship between them is given by $V_\mathrm{L} = \hat{g}V_\mathrm{R}^\dagger\hat{g}$.

Spin waves with non-collinear ground state

If the classical ground state of magnets is not ferromagnetic, every spin in the unit cell needs to be represented in its local reference frame. To deal with the problem, the rotation matrix $\hat{R}(\theta_s, \phi_s)$ is introduced. In non-collinear systems, the spin $\mathbf{S}_i$ can be represented as $\mathbf{S}_i = \hat{R}_i(\theta_s, \phi_s)\mathbf{S}_i'$, with

$$\hat{R}_i(\theta_s, \phi_s) = \begin{pmatrix} \cos\theta_s\cos\phi_s & -\sin\phi_s & \cos\phi_s\sin\theta_s \\ \sin\phi_s\cos\theta_s & \cos\phi_s & \sin\theta_s\sin\phi_s \\ -\sin\theta_s & 0 & \cos\theta_s \end{pmatrix} \tag{2.79}$$

where the θ_s and ϕ_s represent the polar angle and azimuthal angle, respectively. The $\mathbf{S}_i'$ represents the pseudospin at site i along z axis, and the length is the same as $\mathbf{S}_i$.

Then, the Hamiltonian Eq. (2.72) is transformed into:

$$\begin{aligned} H = &-\sum_{\langle ij\rangle}\mathbf{S}_i'^\dagger\hat{R}_i(\theta_s,\phi_s)^T\hat{J}_{ij}\hat{R}_j(\theta_s,\phi_s)\mathbf{S}_j' - \sum_{\langle ij\rangle}\mathbf{S}_i'^\dagger\hat{R}_i(\theta_s,\phi_s)^T\hat{D}_{ij}\hat{R}_j(\theta_s,\phi_s)\mathbf{S}_j' \\ &-\sum_{\langle ij\rangle}\mathbf{S}_i'^\dagger\hat{R}_i(\theta_s,\phi_s)^T\hat{A}\hat{R}_j(\theta_s,\phi_s)\mathbf{S}_j' - \mu_B g_e\sum_i \mathbf{B}\hat{R}_i(\theta_s,\phi_s)\cdot\mathbf{S}_i' \end{aligned} \tag{2.80}$$

where $\mathbf{S}_i'$ can be transformed according to Eq. (2.76) with the format $\mathbf{S}_i' = \hat{M}_i\mathbf{a_i}$. Finally, the eigenvalues and eigenvectors can be obtained easily according to the method mentioned above.

Spin waves with higher-order interactions

The Hamiltonian of the orbital Zeeman coupling, also called as the ring-exchange interaction, is investigated in this thesis. Although the Hamiltonian contains three-spin interaction, only the quadratic order terms are kept during the HP transformation. More detailed information is discussed in Chapter 8.

2.5 Magnon-phonon coupling

The magnons and phonons are both bosons, and the hybridized excitation of magnons and phonons with the name of magnetoelastic has been observed [55]. This magnon and phonon hybridization can realize nonzero Berry curvature and nontrivial topology. This is an interesting topic, but is not considered in this thesis.

2.6 Summary

In this chapter, the Heisenberg exchange interaction, DMI, Kitaev interaction, Zeeman coupling and higher-order interactions are introduced to explore the effective spin Hamiltonian of magnets. Besides, we introduced the concept of spin wave and discussed how to obtain the magnon dispersion based on the LSWT. These basic theories are used to investigate the magnonic properties in the later chapters.

Chapter 3

The parametrization of effective spin Hamiltonian

As discussed in Chapter 2, a generalized Heisenberg Hamiltonian is utilized to describe the effective spin-spin interaction in magnets with localized magnetic moments. Within the adiabatic approximation, rich magnetic properties (*e.g.*, Curie temperature and spin-wave), can be obtained based on the atomistic Heisenberg Hamiltonian. However, in realistic materials, the specified parameters are required to measure the strength of spin interactions.

In this chapter, we first introduce the fitting to experimental data method to achieve the parametrization of effective spin Hamiltonian, while discussing its strengths and weaknesses. Then, the first-principles method is presented to obtain the quantitative parameters.

3.1 The parametrization of effective spin Hamiltonian through fitting to experimental data

Using experimental data to fit the model parameters is a traditional but powerful method. In this thesis, this method is utilized to explain the experimental magnons dispersion and investigate the magnon properties in Cu_2OSeO_3, $CrSiTe_3$, $CrGeTe_3$ and Mn_3Ge. All fittings are done by selecting the representative data points of the magnon dispersion obtained from the inelastic neutron scattering experiment, and then parameters are fitted with the Broyden – Fletcher – Goldfarb – Shanno method [56].

In order to do the fitting more efficiently, it is desirable to identify the interactions in the materials. For instance, it has been shown that in skyrmion cluster Cu_2OSeO_3, the spin-spin interaction is dominated by the exchange interaction and may be accompanied by Dzyaloshinskii-Moriya interaction (DMI) [57, 58, 59]. We then build the effective model to fit the experimental data, which is illustrated in Section 6.2.2. In the thesis, the fitting method is also used to investigate the types of interactions in magnets. In Chapter 7, we compare the fitting of a Heisenberg-Kitaev model with a Heisenberg-DMI model in order to settle the question over the existence of Kitaev interactions or DMI in $CrSiTe_3$ and $CrGeTe_3$. Although both models fit the experimental magnons spectrum very well, we conclude that the interactions are dominated by Heisenberg-DMI in $CrSiTe_3$ and $CrGeTe_3$.

While fitting to the experimental result is a straightforward method to obtain the required parameters, it has some drawbacks. It is difficult to do fitting in a material in which we lack experimental data. What's worse, despite the fact that we can obtain detailed experimental data, sometimes it is still a challenge to fit the parameters well, as too many degrees of freedom need to be considered. To deal with this problem, we can relay on the first-principles calculations to realize the parametrization of Hamiltonian.

3.2 The parametrization of effective spin Hamiltonian based on the first-principles calculation

First-principles calculation provides a reliable approach to describe quantum-mechanical behaviors of electrons and atomic nuclei in a large number of situations. In other words, we can understand the properties of any material based on first-principles calculation, where properties can be predicted by solving the Schrödinger equation in any structure without the need for free parameters. However, the exact solution of the Schrödinger equation requires an exponential amount of memory and is therefore only feasible for very small systems. To deal with this problem, it is necessary to introduce some approximations.

3.2.1 The Hamiltonian of many-body systems

The system we investigate is a many-body system, containing multi-electron and multi-atomic-nuclei. Here, the Hamiltonian can be written as:

$$\begin{aligned}\hat{\mathrm{H}} = &-\frac{\hbar^2}{2m_e}\sum_i \nabla_i^2 - \sum_{i,I}\frac{Z_I e^2}{|\mathbf{r}_i - \mathbf{R}_I|} + \frac{1}{2}\sum_{i\neq j}\frac{e^2}{|\mathbf{r}_i - \mathbf{r}_j|} - \frac{\hbar^2}{2M_I}\sum_I \nabla_I^2 \\ &+ \frac{1}{2}\sum_{I\neq J}\frac{Z_I Z_J e^2}{|\mathbf{R}_I - \mathbf{R}_J|},\end{aligned} \tag{3.1}$$

where m_e represents the mass of electron and M_I represents the mass of nuclei marked as I with charge number Z_I, respectively. The position vector $\mathbf{r}_i$ and $\mathbf{R}_I$ denote the position of electron i and nuclei I. The total Hamiltonian $\hat{\mathrm{H}}$ consists of the electron kinetic, nuclear-electron interaction, electron-electron interaction, nuclear kinetic, and nuclear-nucleus interaction, which are represented by the first, second, third, fourth, and fifth terms, respectively. As it is impossible to solve the many-body Schrödinger equations, we need to simplify the problem.

3.2.2 Born-Oppenheimer approximation

According to the conservation of momentum, the velocity of the light electrons is much larger than that of the nuclei, which are at least a thousand times heavier. Therefore, we can assume that the nucleus is stationary when

we study the motion of electrons, as the velocity of the nucleus is very small. Thus, the motion of the electron only depends on the position of the nucleus without considering the velocity of the nucleus, and we can separate the motion of the electron from that of the nucleus. This is called the Born-Oppenheimer approximation [60] or the *adiabatic* approximation, because the electrons are treated to be adiabatic with respect to the motion of the nucleus. This approximation suggests that the total wave function is the product of the electron wave function and the nucleus wave function, where two of them are independent of each other. Then, the Hamiltonian of electron and nucleus can be expressed separately. The electronic Hamiltonian can be written as:

$$\hat{\mathrm{H}}_e = -\frac{\hbar^2}{2m_e}\sum_i \nabla_i^2 + \frac{1}{2}\sum_{i\neq j}\frac{e^2}{|\mathbf{r}_i - \mathbf{r}_j|} + \sum_{i,I} V(\mathbf{R}_I - \mathbf{r}_i), \tag{3.2}$$

where the third term of Eq. (3.2) is the effective potential which includes the nuclear electrostatic potential. After the Born-Oppenheimer approximation, the electron-nucleus interaction is simplified to an external effective potential, and the main problem is the electron-electron interaction.

3.2.3 Hartree-Fock Approximation

To solve the Eq. (3.2), the main difficulty is the Coulomb interactions among the electrons, which refers to electron-electron interactions. In Hartree-Fock approximation, we assume the wave function of the many-body system can be expressed as the Slater determinant of the single-electron wave function, which has a wide range of applications in quantum chemistry.

Hartree equation

We first introduce the Hartree equation, which is proposed by Hartree in 1928. To deal with the electron-electron interactions, the mean-field theory (MFT) method is introduced to transform the multi-electrons interactions into the single electron motion equation problem. The wave function of the many-body system is expressed as Hartree wave function:

$$\Phi(\mathbf{r}) = \phi_1(\mathbf{r}_1)\phi_2(\mathbf{r}_2)\cdots\phi_i(\mathbf{r}_i)\cdots\phi_N(\mathbf{r}_N). \tag{3.3}$$

Eq. (3.3) consists of the product of every single electron wave function, and each of them only depends on its own spatial coordinate position. We can obtain the Hartree equation, which is a Schrödinger equation for the single electron wave function:

$$\left[-\frac{\hbar^2}{2m_e}\nabla^2 + \sum_{j\neq i} e^2\int d\mathbf{r}'\frac{|\phi_j(\mathbf{r}')|^2}{|\mathbf{r}-\mathbf{r}'|} + \sum_I V(\mathbf{r}-\mathbf{R}_I)\right]\phi_i(\mathbf{r}) = \varepsilon_i\phi_i(\mathbf{r}). \tag{3.4}$$

The Hartree equation treats every single electron in an effective potential consisting of the nuclear electrostatic potential and mean-field Coulomb potential from all electrons.

Hartree-Fock Equation

Since the electrons are fermions, which obey the Pauli exclusion principle, the wave function of the system has to be antisymmetric when exchanging two electrons. Therefore, the product of every single electron wave function should obey antisymmetricity . To fulfill this rule, the Slater determinant is proposed:

$$\Phi(\mathbf{r}) = \frac{1}{\sqrt{N!}} \begin{vmatrix} \phi_1(\mathbf{r}_1,\sigma_1) & \phi_2(\mathbf{r}_1,\sigma_2) & \cdots & \phi_N(\mathbf{r}_1,\sigma_N) \\ \phi_1(\mathbf{r}_2,\sigma_1) & \phi_2(\mathbf{r}_2,\sigma_2) & \cdots & \phi_N(\mathbf{r}_2,\sigma_N) \\ \vdots & \vdots & \ddots & \vdots \\ \phi_1(\mathbf{r}_N,\sigma_1) & \phi_1(\mathbf{r}_N,\sigma_2) & \cdots & \phi_N(\mathbf{r}_N,\sigma_N) \end{vmatrix}, \tag{3.5}$$

where the σ_i represents the spin of electron i. As shown in Eq. (3.5), obviously, exchanging two electrons corresponds to exchange two columns or two rows of the determinant. If we use the Slater determinant as the wave function, we can get the Hartree-Fock equation:

$$\begin{aligned} &\left[-\frac{\hbar^2}{2m_e}\nabla^2 + \sum_{j\neq i,\sigma'} e^2 \int d\mathbf{r}' \frac{|\phi_j^{\sigma'}(\mathbf{r}')|^2}{|\mathbf{r}-\mathbf{r}'|} + \sum_I V(\mathbf{r}-\mathbf{R}_I)\right]\phi_i^\sigma(\mathbf{r}) \\ &- \sum_{j\neq i,\sigma'} \delta_{\sigma\sigma'} e^2 \int d\mathbf{r}' \frac{\phi_j^{\sigma'*}(\mathbf{r}')\phi_i^\sigma(\mathbf{r}')}{|\mathbf{r}-\mathbf{r}'|}\phi_j^{\sigma'}(\mathbf{r}) = \varepsilon_i^\sigma \phi_i^\sigma(\mathbf{r}). \end{aligned} \tag{3.6}$$

Compared to Eq. (3.4), a new item is added, and it is called the exchange term, where $\delta_{\sigma\sigma'}$ indicates that exchange term favors states having the same spin. Besides, as shown in Eq. (3.4) and Eq. (3.6), the wave function is contained in the effective Hamiltonian. To obtain the eigenvalue and eigenstate of the Hamiltonian, we need to do self-consistent calculations, which is called as "self-consistent field method".

Based on the Hartree-Fock approximation, we expand the many-body wavefunction in Slater determinant that describes the electron wave function. However, it neglects the electron correlation, thus the approximation results usually have large deviations from experimental results. An alternative solution is to use density functional theory, which contains both exchange and correlation energy of the system.

3.2.4 Density Functional Theory

The main idea of density functional theory (DFT) is to utilize the charge density instead of the electronic wave functions as the basic quantity. Without considering spin, the degree of freedom of the system changes from $3N$ (N

is an electron number) to 3 (spatial variables), which is more convenient to solve the problem.

Hohenberg-Kohn Theorems

The Hohenberg-Kohn theorems were proposed by Hohenberg and Kohn in 1960 [61], which contains two parts:
Theorem 1 In a electronic Hamiltonian as shown in Eq. (3.2), for the Hamiltonians with non-degenerate ground states, there is a one-to-one mapping among the external potential $V(\mathbf{r})$, the normalized ground-state wave function Φ and the ground state charge density $\rho_{\mathrm{GS}}(\mathbf{r})$, where the $\rho_{\mathrm{GS}}(\mathbf{r})$ can be represented as:

$$\rho_{\mathrm{GS}}(\mathbf{r}) = N \int d^3\mathbf{r}_2 \cdots \int d^3\mathbf{r}_N \Phi^*(\mathbf{r}, \mathbf{r}_2, \cdots, \mathbf{r}_N)\Phi(\mathbf{r}, \mathbf{r}_2, \cdots, \mathbf{r}_N). \tag{3.7}$$

In other words, all the ground-state properties can be derived from the ρ_{GS}.
Theorem 2 In a many-body system, the number of electrons is a constant, and the minimum value of the total energy of the charge density functional $E[\rho(\mathbf{r})]$ is the ground state energy of the system, and the corresponding $\rho(\mathbf{r})$ is the ground state charge density of the system. Then, the energy functional of the ground state can be expressed as:

$$E_{\mathrm{GS}}[\rho(\mathbf{r})] = T[\rho(\mathbf{r})] + E_{\mathrm{int}}[\rho(\mathbf{r})] + \int d\mathbf{r} V_{\mathrm{ext}}(\mathbf{r})\rho(\mathbf{r}), \tag{3.8}$$

where the $T[\rho(\mathbf{r})]$, $E_{\mathrm{int}}[\rho(\mathbf{r})]$, and $\int d\mathbf{r} V_{\mathrm{ext}}(\mathbf{r})\rho(\mathbf{r})$ refer to the functional of kinetic, electron-electron interaction and electron-potential interaction, separately.

According to the constraint of the constant electron number, we have $\int d\mathbf{r}\rho(\mathbf{r}) = N$. The nonmagnetic calculations can be extended to magnetic calculations, after including the spin degree to the system.

Kohn-Sham equation

The Hohenberg-Kohn theorems help us to derive the ground state properties of the multi-electrons system using the ground state charge density rather than wave function as the basic variable. However, it is still a big challenge to solve the many-body problem. In 1965, Kohn and Sham put forward the approximation to change the many-body question into the single electron problem [62]. They proved that for every interacting system, there exists an effective single-electron potential V_{eff}, such that the ground state density of H_{eff} is equal to that of the interacting system. In a word, the system is assumed to satisfy the Kohn-Sham equation:

$$\left[-\frac{\hbar^2}{2m_e}\nabla^2 + V_{\mathrm{eff}}[\rho(\mathbf{r})]\right]\phi_i(\mathbf{r}) = \varepsilon_i\phi_i(\mathbf{r}), \tag{3.9}$$

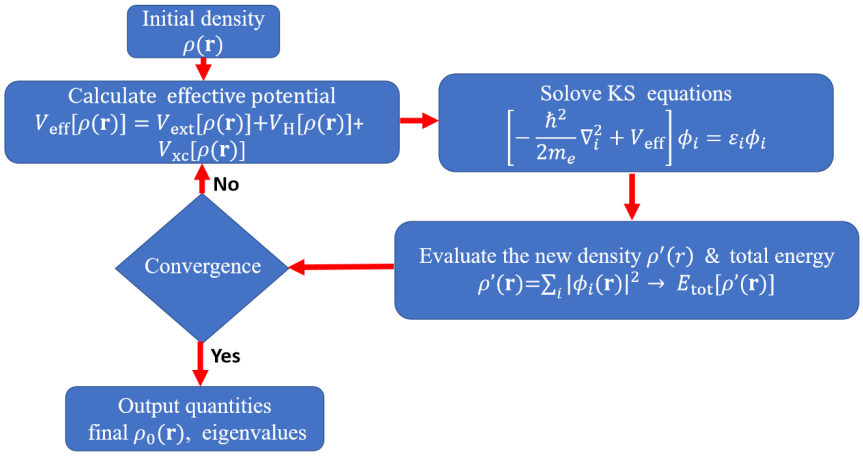

FIGURE 3.1: A flow chart of the self-consistency circle of the DFT calculation.

which holds the same form as the single-particle Schrödinger equation. Then, the exact charge density of the interacting system can be calculated using the formula $\rho(\mathbf{r}) = \sum_{i=1}^{\text{occ}} |\phi_i(\mathbf{r})|^2$. Since the density $\rho(r)$ is calculated from the wavefunction $\phi_i(\mathbf{r})$, the Eq. (3.9) needs to be calculated in a self-consistent manner (as shown in Figure 3.1). The potential $V_{\text{eff}}[\rho(\mathbf{r})]$ is split into $V_{\text{eff}}[\rho(\mathbf{r})] = V_{\text{ext}}[\rho(\mathbf{r})] + V_{\text{H}}[\rho(\mathbf{r})] + V_{\text{xc}}[\rho(\mathbf{r})]$, where the V_{ext} is the nuclear electrostatic potentials, V_{H} is the Hartree potential, and V_{xc} is called the exchange-correlation potential, which is unknown but assumes to be small.

Therefore, V_{xc} is defined as:

$$V_{\text{xc}}[\rho(\mathbf{r})] = V_{\text{eff}}[\rho(\mathbf{r})] - V_{\text{ext}}[\rho(\mathbf{r})] - V_{\text{H}}[\rho(\mathbf{r})]. \tag{3.10}$$

The V_{xc} is defined as the difference between the potential of the many-body system and the Hartree-approximation potential.

Finally, Eq. (3.8) can be rewritten as:

$$E_{\text{KS}}[\rho(\mathbf{r})] = T_{\text{s}}[\rho(\mathbf{r})] + E_{\text{ext}}[\rho(\mathbf{r})] + E_{\text{H}}[\rho(\mathbf{r})] + E_{\text{xc}}[\rho(\mathbf{r})]. \tag{3.11}$$

where the $T_{\text{s}}[\rho(\mathbf{r})]$ is the total noninteracting kinetic energy of the occupied Kohn-Sham orbitals:

$$T_{\text{s}}[\rho(\mathbf{r})] = -\frac{\hbar^2}{2m_e}\sum_i^{\text{occ}}\langle\phi_i^*(\mathbf{r})|\nabla^2|\phi_i(\mathbf{r})\rangle. \tag{3.12}$$

The $E_{\text{H}}[\rho(\mathbf{r})]$ is the Hartree term, which describes the Coulomb interaction between electrons:

$$E_{\text{H}}[\rho(\mathbf{r})] = \iint d\mathbf{r}d\mathbf{r}'\frac{\rho(\mathbf{r})\rho(\mathbf{r}')}{|\mathbf{r}-\mathbf{r}'|}. \tag{3.13}$$

The $E_{\mathrm{xc}}[\rho(\mathbf{r})]$ is the exchange-correlation energy, and it is still unknown. It has the relation with $V_{\mathrm{xc}}[\rho(\mathbf{r})]$:

$$V_{\mathrm{xc}}[\rho(\mathbf{r})] = \frac{\delta E_{\mathrm{xc}}[\rho(\mathbf{r})]}{\delta \rho(\mathbf{r})}|_{\rho(\mathbf{r})=\rho_{\mathrm{GS}}(\mathbf{r})}. \tag{3.14}$$

Exchange-correlation energy

As the exchange-correlation energy $E_{\mathrm{xc}}[\rho(\mathbf{r})]$ is still unknown, one of the biggest challenges is selecting approximations to accurately predict properties in materials with a limited amount of computational resources.

Local density approximation

The local density approximation (LDA) [62] is the simplest approximation. In LDA, we assume the electronic system changes slowly, and the whole system can be divided into many small element $d\mathbf{r}$, in which we treat the electrons as the interacting homogeneous electron gas. In other words, the LDA only takes the density at $\mathbf{r}$ into account and not of the surrounding areas.

$$E_{\mathrm{xc}}^{\mathrm{LDA}}[\rho(\mathbf{r})] = \int d\mathbf{r}\rho(\mathbf{r})\epsilon_{\mathrm{xc}}[\rho(\mathbf{r})], \tag{3.15}$$

where the $\epsilon_{\mathrm{xc}}(\rho(\mathbf{r}))$ is the exchange-correlation energy density of the interacting homogeneous electron gas with the density of $\rho(\mathbf{r})$.

Similarly, for a magnetic system, we have local spin density approximation (LSDA):

$$E_{\mathrm{xc}}^{\mathrm{LDA}}[\rho(\mathbf{r})] = \int d\mathbf{r}\rho(\mathbf{r})\epsilon_{\mathrm{xc}}[\rho_\alpha(\mathbf{r}), \rho_\beta(\mathbf{r})], \tag{3.16}$$

where the $\rho_\alpha(\mathbf{r})$ and $\rho_\beta(\mathbf{r})$ represent local spin up density and local spin down density, and the total density is often expressed as $\rho(\mathbf{r}) = \rho_\alpha(\mathbf{r}) + \rho_\beta(\mathbf{r})$.

Even though the LDA is a very basic approximation, it works surprisingly well and is used in many calculations.

Generalized gradient approximation

In a real system, the charge density is not homogeneous, the correlation energy calculated by LDA is usually larger than the exact value. The generalized gradient approximation (GGA) [63] is introduced to reduce the error caused by the inhomogeneous charge density distribution in space. In GGA, we consider the contribution of the electron density gradient in the energy density functional to reflect the inhomogeneity of the real system. If taking the spin into account, the most commonly used exchange-correlation potential energy from GGA is:

$$E_{\mathrm{xc}}^{\mathrm{GGA}}[\rho(\mathbf{r})] = \int d\mathbf{r}\rho(\mathbf{r})\epsilon_{\mathrm{xc}}[\rho_\alpha(\mathbf{r}), \rho_\beta(\mathbf{r}), \nabla\rho_\alpha(\mathbf{r}), \nabla\rho_\beta(\mathbf{r})]. \tag{3.17}$$

The LDA and GGA are widely used to describe the electronic properties in DFT calculation, especially when the system is dominated by s and p shell electrons. However, in transition-metal systems, the strongly correlated electrons in d and f orbitals are localized. It leads to a large deviation from the experimental results, such as the underestimation of the band gap

in transition-metal sulfides[64]. To deal with this issue, one method is to introduce a strong interaction in the energy expression, which is generated from the inner electron shell of the atom. As this is similar to the form in the Hubbard model, we call this method as LDA(GGA)+*U*.

Choice of Basis Sets

In DFT calculations, an appropriate basis set is needed to expand the Kohn-Sham wave function. The basis needs to be as small as possible to reduce the amount of computation, and as complete as possible to avoid any missing information of the original wave functions after we expand the wave function. The two most commonly used basis are the plane-wave basis set and atomic orbital basis set.

The plane-wave basis set makes it easy to construct the Hamiltonian. The plane-wave basis is often combined with the pseudopotential, and to improve the convergence and efficiency a lot of DFT codes are built according to the plane-wave basis set, *e.g.*, Vienna *ab initio* simulation package (VASP) [65], Quantum Expresso [66]. Besides, standing for the fully linearized augmented plane waves, the FLEUR code is developed (https://www.flapw.de), which has wide applications in electronic structure and magnetic properties calculations.

3.2.5 LDA(GGA)+U

As mentioned above, the LDA(GGA)+U method is widely used to calculate the system containing d and f shell electrons. The U is also called the Hubbard U, and its value can be estimated based on the experimental result or calculated according to linear response theory (LRT) [67]. From the perspective of DFT, the U can be obtained according to Eq. (3.18):

$$U_i = (\chi_0^{-1} - \chi^{-1})_i = \frac{\partial \alpha_i^{\mathrm{no-int}}}{\partial q_i} - \frac{\partial \alpha_i^{\mathrm{int}}}{\partial q_i}, \tag{3.18}$$

where the U_i is the Hubbard U at atom i, and q_i represents the localized orbital state occupations in i atom. χ_0 and χ represent the non-interaction and interaction density response functions of the system with respect to the localized potential shift α_i, respectively. The non-interaction and interaction localized perturbation potential are calculated:

$$\alpha_i^{int} = -\frac{\partial E[\{q_i\}]}{\partial q_i}; \quad \alpha_i^{\mathrm{no-int}} = -\frac{\partial E^{\mathrm{no-int}}[\{q_i\}]}{\partial q_i}, \tag{3.19}$$

where the $E[\{q_i\}]$ and $E^{\mathrm{no-int}}[\{q_i\}]$ denote the occupation-dependent energy function and the occupation-dependent energy function required for the self-consistent solution of the non-interacting Kohn-Sham equations, separately. The LRT is utilized to obtain the Hubbard U in Chapter 5.

3.2.6 The parametrization of the generalized Heisenberg model

As discussed in Chapter 2.3.5, the generalized Heisenberg Hamiltonian can be expressed with localized magnetic moments:

$$\begin{aligned} H = &- \sum_{i,j} J_{ij}\mathbf{S}_i \cdot \mathbf{S}_j - K\sum_{\langle ij\rangle^\gamma} S_i^\gamma S_j^\gamma - \sum_{ij} \mathbf{D}_{ij} \cdot (\mathbf{S}_i \times \mathbf{S}_j) \\ &- A\sum_i (\hat{\mathbf{n}}_i \cdot \mathbf{S}_i)^2 - \mathbf{B} \cdot \mu_B \sum_i (g_e \mathbf{S}_i + \mathbf{L}_i), \end{aligned} \tag{3.20}$$

where the first term represents the isotropic exchange interaction, the second term denotes the Kitaev interaction, third term refers to the Dzyaloshinskii-Moriya interaction (DMI), the fourth and fifth term are the single-ion anisotropy energy and the Zeeman energy, separately. Many methods have been proposed to calculate these interaction parameters, such as the magnetic force theorem method [68], the Berry curvature method [69] and spin-spiral, etc. In this section, we present the parameterization of these interactions with the straightforward method based on the *ab initio* calculation [70].

Exchange interaction

We first discuss the exchange interaction, which contains the isotropic exchange interaction and the Kitaev interacton.

$$H_{\text{exc}} = -\sum_{i,j} J_{ij}\mathbf{S}_i \cdot \mathbf{S}_j - K\sum_{\langle ij\rangle^\gamma} S_i^\gamma S_j^\gamma, \tag{3.21}$$

And it can be transformed to:

$$H_{\text{exc}} = -\sum_{\langle ij\rangle} \mathbf{S}_i^\dagger \hat{J}_{ij} \mathbf{S}_j = -\sum_{\langle ij\rangle} \mathbf{S}_i^\dagger \begin{pmatrix} J_{ij}^{xx} & J_{ij}^{xy} & J_{ij}^{xz} \\ J_{ij}^{yx} & J_{ij}^{yy} & J_{ij}^{yz} \\ J_{ij}^{zx} & J_{ij}^{zy} & J_{ij}^{zz} \end{pmatrix} \mathbf{S}_j, \tag{3.22}$$

with $\mathbf{S}_i^\dagger = (S_i^x, S_i^y, S_z^z)$. To determine the elements of matrix $\hat{J}_{ij}$, we can compare the energy difference between different states with local spin flips.

If we want to investigate the interaction between the spin i and j, we can flip the spin direction of site i and j to calculate the corresponding energy based on the first-principles calculation. In this case, the total energy can be divided as: $E_i = E_{\text{exc1}} + C$, and E_{exc1} donates the interaction between the site i and site j. Then the energy difference between different spin flips lies in the exchange interaction.

Taking J_{ij}^{xx} as an example: to calculate the J_{ij}^{xx}, we can set four states, and the J_{ij}^{xx} can be expressed as:

$$J_{ij}^{xx} = \frac{E_1 - E_2 - E_3 + E_4}{4}, \tag{3.23}$$

state	site i	site j	other sites
1	$S(1,0,0)$	$S(1,0,0)$	Experimental structure
2	$S(1,0,0)$	$S(-1,0,0)$	Experimental structure
3	$S(-1,0,0)$	$S(1,0,0)$	Experimental structure
4	$S(-1,0,0)$	$S(-1,0,0)$	Experimental structure

where E_1, E_2, E_3 and E_4 are total energy calculated with collinear spin configurations, shown below.

Dzyaloshinskii-Moriya interaction

Similar to exchange interactions, the DMI can be calculated. The effective atomic Hamiltonian of DMI can be transformed to matrix format:

$$H_{\mathrm{DMI}} = -\sum_{\langle ij\rangle} \mathbf{S}_i^{\dagger} \hat{D}_{ij} \mathbf{S}_j = -\sum_{\langle ij\rangle} \mathbf{S}_i^{\dagger} \begin{pmatrix} 0 & D_{ij}^{z} & -D_{ij}^{y} \\ -D_{ij}^{z} & 0 & D_{ij}^{x} \\ D_{ij}^{y} & -D_{ij}^{x} & 0 \end{pmatrix} \mathbf{S}_j. \tag{3.24}$$

Comparing Eq. (3.22) and Eq. (3.24), we find that they have similar matrix formulas, and total Hamiltonian of exchange interaction and Dzyaloshinskii-Moriya interaction can be expressed as:

$$H = -\sum_{\langle ij\rangle} \mathbf{S}_i^{\dagger} \begin{pmatrix} J_{ij}^{xx} & J_{ij}^{xy} + D_{ij}^{z} & J_{ij}^{xz} - D_{ij}^{y} \\ J_{ij}^{yx} - D_{ij}^{z} & J_{ij}^{yy} & J_{ij}^{yz} + D_{ij}^{x} \\ J_{ij}^{zx} + D_{ij}^{y} & J_{ij}^{zy} - D_{ij}^{x} & J_{ij}^{zz} \end{pmatrix} \mathbf{S}_j. \tag{3.25}$$

Here, we take J_{ij}^{xy} and D_{ij}^{z} as examples to reveal how to obtain the DMI and anisotropic exchange interaction. We set the following states

state	site i	site j	other sites
1	$S(1,0,0)$	$S(0,1,0)$	Experimental structure
2	$S(1,0,0)$	$S(0,-1,0)$	Experimental structure
3	$S(-1,0,0)$	$S(0,1,0)$	Experimental structure
4	$S(-1,0,0)$	$S(0,-1,0)$	Experimental structure
5	$S(0,1,0)$	$S(1,0,0)$	Experimental structure
6	$S(0,-1,0)$	$S(1,0,0)$	Experimental structure
7	$S(0,1,0)$	$S(-1,0,0)$	Experimental structure
8	$\mathbf{S(0,}$ $-1,0)$	$S(-1,0,0)$	Experimental structure

and we have relation:

$$\begin{aligned} J_{ij}^{xy} - D_{ij}^{xy} &= \frac{E_1 + E_4 - E_2 - E_3}{4}, \\ J_{ij}^{yx} + D_{ij}^{xy} &= \frac{E_5 + E_6 - E_7 - E_8}{4}. \end{aligned} \tag{3.26}$$

We can obtain the elements of DMI and anisotropic exchange interaction easily (here, we have $J_{ij}^{xy} = J_{ij}^{yx}$), according to Eq. (3.26).

Single-ion anisotropy energy

If the system has the easy-axis or easy-plane anisotropy, the single-ion anisotropy energy A can be easily obtained. For instance, if the easy-axis is along with z direction, we can set four states with site i: 1, $S(0,0,1)$; 2, $S(0,0,-1)$; 3, $S(1,0,0)$; 4, $S(-1,0,0)$. and A is calculated according to:

$$A = \frac{E_1 + E_2 - E_3 - E_4}{4}. \tag{3.27}$$

Zeeman energy

To determine the Zeeman energy, we need to know the magnetic moment of each site. In the thesis, we consider the contributions of spin and orbital angular momentum to the magnetic moment. From the DFT calculation, we can obtain the magnetic moment of spin directly, and the orbital angular momentum can be calculated based on the modern theory [28], shown in Chapter 2.

3.3 Conclusion

In the thesis, we discuss the parametrization of the effective spin Heisenberg model with fitting to the experimental data and DFT calculation. According to the experimental data offered from our collaborators, the fitting method is adopted to identify the effective spin interaction Hamiltonian in magnetic materials: Cu_2OSeO_3, $CrSiTe_3$, $CrGeTe_3$ and Mn_3Ge. The DFT method is used to study a family of two-dimensional (2D) metal-organic frameworks (MOFs) with the Shastry-Sutherland magnetic lattice, which is discussed in Chapter 5.

Chapter 4

Magnonic topology and transport

The magnon is a quasiparticle evoked from the collective excitation in magnets, which has promising candidate applications in spintronics [71, 72]. In the field of spintronics, the study of magnons has led to a boom in magnonics, which aims to explore new approaches to carry information using the collections of spins instead of the charge of electrons to avoid the dissipation of Joule heating [73, 74].

In this chapter, analogous to the electronic topology and electronic Berry curvature in momentum space [75], the magnonic topology is presented. By utilizing the magnon Berry curvature, we present a magnonic topological phenomenon, the magnonic Weyl point. Based on the semiclassical method, the magnonic transport properties in the context of the thermal Hall effect and magnon Nernst effect are introduced [76, 6, 77, 78].

4.1 The Berry Phase and Berry curvature

To demonstrate the topological nature, we first introduce the concept of the Berry phase in a quantum mechanical system, which was originally introduced by Berry [75]. We assume that the system described by a Hamiltonian $H(\mathbf{X})$ depends on a set of parameters $\mathbf{X} = (X_1, X_2, ...)$ following the adiabatic evolution, as the parameters are valid. Then, the instantaneous basis of the Hilbert space of $H(\mathbf{X})$ obeys the Schrödinger equation:

$$H(\mathbf{X})|n\mathbf{X}\rangle = \varepsilon_n(\mathbf{X})|n\mathbf{X}\rangle\,, \tag{4.1}$$

where $|n\mathbf{X}\rangle$ are eigenstates of Hamiltonian $H(\mathbf{X})$ with the eigenvalue $\varepsilon_n(\mathbf{X})$.

If we assume the $\varepsilon_n(\mathbf{X})$ are nondegenerate, then the time evolution of the system in the eigenstate $|\,\psi(t)\rangle$ follows the time-dependent Schrödinger equation:

$$H(\mathbf{X}(t))|\psi(t)\rangle = \mathrm{i}\hbar\partial_t|\psi(t)\rangle\,. \tag{4.2}$$

Here, the solution of Eq. (4.2) can be expanded with the instantaneous basis $|\psi(t)\rangle = \sum_m c_m(t)|m\mathbf{X}(t)\rangle$, in which the time-dependent expansion coefficient is marked as $c_m(t)$. If we substitute the new basis to Eq. (4.2) and

multiply $\langle n\mathbf{X}(t)\mid$ from the left side, then we can get the equation:

$$\begin{aligned}\partial_t c_n(t) = &-\mathrm{i}\frac{1}{\hbar}\varepsilon_n(\mathbf{X}(t))c_n(t) - c_n(t)\langle n\mathbf{X}(t)|\partial_t|n\mathbf{X}(t)\rangle \\ &-\sum_{m\neq n} c_m(t)\langle n\mathbf{X}(t)|\partial_t|m\mathbf{X}(t)\rangle ,\end{aligned} \tag{4.3}$$

and the last term of Eq. 4.3 corresponds to the transition rate between the state $|n\mathbf{X}(t)\rangle$ and $|m\mathbf{X}(t)\rangle$. Here, the $\varepsilon_n(\mathbf{X})$ are nondegenerate, and we can set $C_n(0) = 1$ and $C_m(0) = 0(m \neq n)$. Then, the state $|\psi(t)\rangle$ can be represented as $c_n(t)|m\mathbf{X}(t)\rangle$ under the adiabatic evolution, and Eq. (4.3) can be solved directly by integration:

$$\begin{aligned}c_n(t) &= e^{-\frac{\mathrm{i}}{\hbar}\int_0^t \varepsilon_n(\tau)d\tau} e^{\mathrm{i}\int_0^t \mathrm{i}\langle n\mathbf{X}(\tau)|\partial_t|n\mathbf{X}(\tau)\rangle d\tau} \\ &= e^{-\mathrm{i}\alpha_{dyn}(t)} e^{\mathrm{i}\gamma_n(t)},\end{aligned} \tag{4.4}$$

where the $\alpha_{dyn}(t)$ represents the dynamical phase, and for a closed path the $\gamma_n(t)$ refers to the geometric, or Berry phase:

$$\gamma_n(t) = \int_0^t \mathrm{i}\langle n\mathbf{X}(\tau)|\partial_t|n\mathbf{X}(\tau)\rangle d\tau = \oint_C \mathrm{i}\langle n\mathbf{X}|\nabla_{\mathbf{X}}|n\mathbf{X}\rangle d\mathbf{X} = \oint_C \mathbf{A}^n(\mathbf{X})d\mathbf{X}, \tag{4.5}$$

where C is a closed loop in parameter space. Since the basis states are normalized, the $\gamma_n(t)$ is a real number modulo 2π. We call the integrand $\mathbf{A}^n(\mathbf{X})$ Berry connection, which describes the vector potential $\mathbf{A}^n$ along with the path C.

From the Stokes' theorem, the Eq. (4.5) can be rewritten from the integral along with closed path C to the integral over the surface S

$$\gamma_n(t) = \oint_C \mathbf{A}^n(\mathbf{X})d\mathbf{X} = \int_S \mathbf{\Omega}_n(\mathbf{X})\cdot d\mathbf{S}, \tag{4.6}$$

where $\mathbf{\Omega}_n = \nabla_{\mathbf{X}} \times \mathbf{A}^n$. Analogous to the magnetic vector potential and the magnetic field, here $\mathbf{\Omega}_n$ is an effective "magnetic field" and we call it Berry curvature.

Next, we discuss how to obtain the Berry curvature from the eigenvalue and eigenvector. From the Eq. (4.5), we already know that $\mathbf{\Omega}_n = \nabla_{\mathbf{X}} \times \mathbf{A}^n = \mathrm{i}\langle\nabla_{\mathbf{X}} n\mathbf{X}|\times|\nabla_{\mathbf{X}} n\mathbf{X}\rangle$, and it can be adapted with the completeness relation $1 = \sum_m |m(\mathbf{X})\rangle\langle m(\mathbf{X})|$:

$$\mathbf{\Omega}_n = \sum_m \mathrm{i}\langle\nabla_{\mathbf{X}} n\mathbf{X}|m(\mathbf{X})\rangle \times \langle m(\mathbf{X})|\nabla_{\mathbf{X}} n\mathbf{X}\rangle . \tag{4.7}$$

In the adiabatic system, we assume the eigenvalues are nondegenerate, we have relation:

$$\langle m(\mathbf{X})|\nabla_{\mathbf{X}} n\mathbf{X}\rangle = \frac{\langle m(\mathbf{X})|\nabla_{\mathbf{X}} H|n(\mathbf{X})\rangle}{\varepsilon_n(\mathbf{X}) - \varepsilon_m(\mathbf{X})}. \tag{4.8}$$

Then the Berry curvature becomes:

$$\mathbf{\Omega}_n(\mathbf{X}) = \mathrm{i}\sum_{m\neq n}\frac{\langle n(\mathbf{X})\left|\nabla_{\mathbf{X}}H\right|m(\mathbf{X})\rangle\times\langle m(\mathbf{X})\left|\nabla_{\mathbf{X}}H\right|n(\mathbf{k})\rangle}{(\varepsilon_n(\mathbf{X})-\varepsilon_m(\mathbf{X}))^2}, \tag{4.9}$$

with $n \neq m$.

4.2 The Berry curvature in magnonic systems

In this section, we introduce the magnon Berry phase in periodic magnonic systems. As we discussed before, the magnon is used to describe the collective vibration of spins in a magnetic crystal lattice. The Hamiltonian with parameters $\mathbf{X} = (X_1, X_2, ...)$ is used to describe the magnon's behavior with the periodic potential in momentum space $\mathbf{k}$. As crystalline materials have translational symmetry, the eigenstate of magnons $\psi_{n,\mathbf{k}}(\mathbf{r})$ at $\mathbf{k}$ with the band index n follows the Bloch theorem [79].

$$\psi_{n,\mathbf{k}}(\mathbf{r}) = e^{\mathrm{i}\mathbf{k}\cdot\mathbf{r}}u_{n,\mathbf{k}}(\mathbf{r}), \tag{4.10}$$

where the $u_{n,\mathbf{k}}(\mathbf{r})$ is a periodic function. Then, the Hamiltonian of magnon H has

$$H\psi_{n,\mathbf{k}}(\mathbf{r}) = \varepsilon_{n,\mathbf{k}}\psi_{n,\mathbf{k}}(\mathbf{r}), \tag{4.11}$$

which can be rewritten:

$$H_{\mathbf{k}}u_{n,\mathbf{k}}(\mathbf{r}) = \varepsilon_{n,\mathbf{k}}u_{n,\mathbf{k}}(\mathbf{r}), \tag{4.12}$$

where $H_{\mathbf{k}} = e^{-\mathrm{i}\mathbf{k}\cdot\mathbf{r}}\cdot H\cdot e^{\mathrm{i}\mathbf{k}\cdot\mathbf{r}}$ represents the magnon Hamiltonian in momentum representation. The Berry curvature of magnon band n can be obtained by replacing $\mathbf{X}$ with $\mathbf{k}$ in Eq. (4.9).

$$\mathbf{\Omega}_n(\mathbf{k}) = \mathrm{i}\sum_{m\neq n}\frac{\langle u_{n,\mathbf{k}}\left|\nabla_{\mathbf{k}}H\right|u_{m,\mathbf{k}}\rangle\times\langle u_{m,\mathbf{k}}\left|\nabla_{\mathbf{k}}H\right|u_{n,\mathbf{k}}\rangle}{(\varepsilon_{n,\mathbf{k}}-\varepsilon_{m,\mathbf{k}})^2}. \tag{4.13}$$

Besides, in a two-dimensional (2D) system, the Berry curvature tensor only has non-zero value along z direction:

$$\Omega_n^{xy}(\mathbf{k}) = -2\,\mathrm{Im}\sum_{m\neq n}\frac{\left\langle\psi_{n\mathbf{k}}|\frac{\partial H(\mathbf{k})}{\partial k_x}|\psi_{m\mathbf{k}}\right\rangle\left\langle\psi_{m\mathbf{k}}|\frac{\partial H(\mathbf{k})}{\partial k_y}|\psi_{n\mathbf{k}}\right\rangle}{(\varepsilon_{n\mathbf{k}}-\varepsilon_{m\mathbf{k}})^2}. \tag{4.14}$$

Unlike the pure electronic Hamiltonian, sometimes the magnon Hamiltonian H contains number-nonconserving terms (*e.g.*, $\alpha_i\alpha_j$, and $\alpha_i^\dagger\alpha_j^\dagger$), where the α_i and $\alpha_i^\dagger$ represent the creation and annihilation spin-wave operators. As discussed in Chapter 2, we can diagonalize the dynamical matrix $\hat{D}$ instead of the Hamiltonian matrix to get the eigenvalue and eigenvector. Then, in 2D

Symmetry	TR	SI
Eigenvalue	$\mathbf{E}(\mathbf{k}) = \mathbf{E}(-\mathbf{k})$	$\mathbf{E}(\mathbf{k}) = \mathbf{E}(-\mathbf{k})$
Berry curvature	$\mathbf{\Omega}_n(-\mathbf{k}) = -\mathbf{\Omega}_n(\mathbf{k})$	$\mathbf{\Omega}_n(-\mathbf{k}) = \mathbf{\Omega}_n(\mathbf{k})$
Approach	DMI, spin length, field, etc.	spin interaction, DMI, etc.

TABLE 4.1: Comparison of time-reversal(TR) symmetry and space inversion (SI) symmetry in magnonic system. Several approaches are listed to break TR symmetry and SI symmetry in magnonic systems.

system, the Eq. (4.14) becomes into:

$$\Omega_n^{xy}(\mathbf{k}) = -2\,\mathrm{Im}\sum_{m\neq n}\frac{\left\langle\psi_{n\mathbf{k}}|\frac{\partial\hat{D}(\mathbf{k})}{\partial k_x}|\psi_{m\mathbf{k}}\right\rangle\left\langle\psi_{m\mathbf{k}}|\frac{\partial\hat{D}(\mathbf{k})}{\partial k_y}|\psi_{n\mathbf{k}}\right\rangle}{(\varepsilon_{n\mathbf{k}}-\varepsilon_{m\mathbf{k}})^2}, \tag{4.15}$$

where the $\hat{D}(\mathbf{k})$ represents the dynamical matrix in the momentum representation which is discussed in Chapter 2. We need to note that since $\hat{D}(\mathbf{k})$ is not a hermitian matrix, the left and right eigenvector $\langle\psi_{n,\mathbf{k}}|$ and $|\psi_{n,\mathbf{k}}\rangle$ may not hermitian.

Lastly, we briefly discuss the symmetry properties of the magnon Berry curvature in momentum space. There are two major symmetries in the system, time-reversal (TR) symmetry and space inversion (SI) symmetry, and their properties are shown in Table 4.1. If one system fulfills both TR and TR symmetry, the corresponding Berry curvature satisfies both $\mathbf{\Omega}_n(-\mathbf{k}) = -\mathbf{\Omega}_n(\mathbf{k})$ and $\mathbf{\Omega}_n(-\mathbf{k}) = \mathbf{\Omega}_n(\mathbf{k})$. This means the Berry curvature at every $\mathbf{k}$ point is zero. To obtain non-trivial Berry curvature, either TR or SI symmetry should be broken. In electronic systems, the SI or TR can be broken through introducing *e.g.*, non-zero electric polarization or spin-orbit coupling. Here, we briefly list some methods to break the SI or TR symmetry in magnonic systems. On the one hand, the TR symmetry can be broken by introducing some appropriate interaction, such as Dzyaloshinskii-Moriya interaction (DMI), Kitaev interaction and magnon-phonon coupling. On the other hand, the SI symmetry can be destroyed by introducing some anisotropy interaction or changing the spin moment length or direction, etc. This symmetry analysis is applied in Chapter 6.

4.3 Weyl Semimetal in magnonic systems

In this section, we introduce the concept of the Weyl semimetal. First, the concept of Chern number is presented. From Eq. (4.6), we know the Berry

phase:

$$\gamma_n(t) = \oint_C \mathbf{A}^n(\mathbf{X}) d\mathbf{X} = \int_S \mathbf{\Omega}_n(\mathbf{X}) \cdot d\mathbf{S} = \int_{S'} \mathbf{\Omega}_n(\mathbf{X}) \cdot d\mathbf{S} + 2\pi n. \tag{4.16}$$

Here, S and S' are non-overlapping surfaces with the same boundary path C, and we define the closed surface $\boldsymbol{S}$ which is constituted by S and S' with the seam C. As the Berry phase is the modulo of 2π, the n is an integer. If we calculate the integral of Berry curvature over $\boldsymbol{S}$, we get the concept of Chern number:

$$C_n = \frac{1}{2\pi} \int_{\boldsymbol{S}} \mathbf{\Omega}_n(\mathbf{X}) \cdot d\mathbf{S} = \frac{1}{2\pi} \left(\int_S \mathbf{\Omega}_n(\mathbf{X}) \cdot d\mathbf{S} - \int_{S'} \mathbf{\Omega}_n(\mathbf{X}) \cdot d\mathbf{S} \right) = n. \tag{4.17}$$

Here, the C_n is called the first Chern number of the nth-eigenstate. In a non-degenerate system, the C_n is always an integer and it separates out different topological phases from topologically trivial phases. In 2D systems, the Brillouin zone (BZ) is a closed surface because of the periodicity in momentum space, then, the C_n can be calculated based on Eq. (4.18):

$$C_n = \frac{1}{2\pi} \int_{\mathrm{BZ}} \Omega_n^{xy}(\mathbf{k}) dk_x dk_y. \tag{4.18}$$

As shown in Figure 4.1, the C_n is calculated for a given closed surface $\boldsymbol{S}$ and the value of C_n is related to the monopoles inside. In order to generate the monopole, conditions need to be satisfied, which include two aspects: 1) either TR or SI symmetry (or both) should be broken to make the Berry curvature nonzero, 2) there are crossing points that are also called Dirac point, appearing between two nearby bands. The charge of a monopole, which is also called topological charge, can be calculated with an infinitesimal sphere S_i surrounding the crossing point:

$$Q_i = \frac{1}{2\pi} \int_{S_i} \mathbf{\Omega}(\mathbf{k}) \cdot \mathbf{n} \, dS_i, \tag{4.19}$$

where $\mathbf{n}$ is the surface normal. If these crossing points have non-zero topological charge, we call these points Weyl points [80], and the system with Weyl points are also called the Weyl semimetal system, such as TaAs [81], which have been observed in experiments. Besides, the Weyl point not only exists in the electronic system [80, 81], but also in bosonic systems, *e.g.*, photonic [82], magnonic [83, 84, 85] or phononic system [86].

The example of Weyl points is shown in Figure 4.1, where the Weyl points appear in pairs with opposite topological charges. Berry curvature vector field starts from one Weyl point and finally converges to another partner Weyl point, and each pair is connected by an arc on the surface. The appearance of Weyl points is protected by the symmetry of the system, which is stable and can be kept with slight variations of the parameters in the Hamiltonian. There is at least one pair of Weyl points presented in a system, and the number of Weyl points in Weyl semimetal systems can be estimated based on

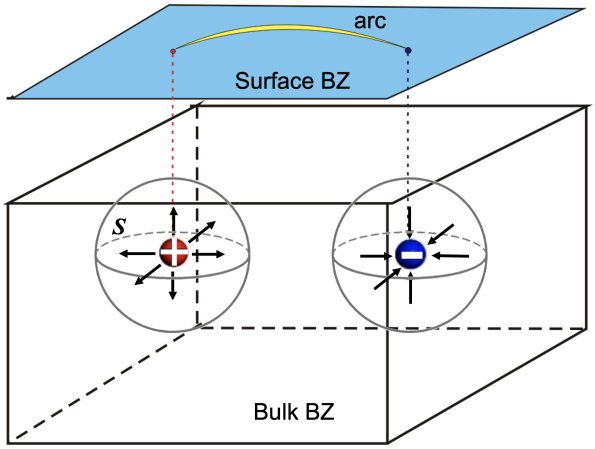

FIGURE 4.1: Weyl points and arc. The red and blue ball represent the Weyl points of two bulk bands with the topological charge $+1$ and -1, which are the source or sink of the Berry curvature vector field. The spherical surface refers to the closed surface $\boldsymbol{S}$ and the Chern number C_n is $+1$ for the left sphere. The projections of Weyl points onto surface are shown with red and blue points and they are connected by an arc. In electronic system, this arc crossing the Fermi level is called the Fermi arc.

the symmetry. As discussed in Section 4.2, the eigenvalue and Berry curvature need to fulfill some rules if the system holds TR or SI symmetry. For instance, when only TR symmetry is broken, the minimal number of Weyl points is two, which locate at $\mathbf{k}$ and $-\mathbf{k}$ point with topological charge q and $-q$ separately. If the SI symmetry is broken and TR symmetry is kept, there are at least two Weyl points with the same topological charge at $\mathbf{k}$ and $-\mathbf{k}$, which means there are at least four Weyl points in the BZ.

In this thesis, we focus on the study of magnonic Weyl points. The appearance of Weyl points and their relationship with symmetry is systematically explored in the material Cu_2OSeO_3, and the detailed information is revealed in Chapter 6.

4.4 Magnonic transport based on the semiclassical theory

The magnon thermal Hall effect and magnon Nernst effect[1] are discussed in this part, according to the semiclassical theory, and both of them are transverse transport caused by non-trivial magnonic topology.

[1]The magnon Nernst effect discussed in the thesis refers to the "magnon spin Nernst effect" discussed in Ref. [77, 78].

The Hall effect refers to the production of a voltage difference across an electrical conductor in a magnetic field, which was discovered by E. Hall [87]. Relevantly, the direction of the generated voltage is transverse to an electric current and applied magnetic field which is perpendicular to the current. Unlike the Hall effect that is formed by the movement of an electronic current, the thermal Hall effect describes the thermal current carried by electron[88], phonon [89], magnon [6], etc. In this section, we focus on discussing the thermal Hall effect via magnons, which is driven by the magnon Berry curvature in momentum space. The Nernst effect is a thermoelectric effect, which refers to a sample, *e.g.*, semiconductor, subjected to a magnetic field and a temperature gradient, will be induced an electric field, where the magnetic field, temperature gradient and electric field are perpendicular with each other. And the magnon Nernst effect indicates a spin currents generated from temperature gradients in a magnonic system.

The Berry curvature refers to the wave function changes and is associated with the band structure, which can drive various Hall effects or Nernst effects in momentum space. We first discuss the Berry curvature dynamics in an electronic system, which was developed by Sundaram and Niu [90] to introduce an "anomalous velocity" [91] to explain the anomalous Hall effect. In both $\mathbf{k}$ (momentum space) and $\mathbf{r}$ space (real space), the electronic wave function dynamics can be described by the motion in a semiclassical way [92, 90]:

$$\begin{aligned} \dot{\mathbf{r}} &= \frac{1}{\hbar}\frac{\partial \varepsilon_n(\mathbf{k})}{\partial \mathbf{k}} - \dot{\mathbf{k}} \times \mathbf{\Omega}_n(\mathbf{k}), \\ \hbar\dot{\mathbf{k}} &= q\mathbf{E} + q\dot{\mathbf{r}} \times \mathbf{B}, \end{aligned} \tag{4.20}$$

where q is the electron charge (here we set it equal to $-e$), $\mathbf{E}$ is an electric field and $\mathbf{B}$ is the magnetic field. The $\frac{1}{\hbar}\frac{\partial \varepsilon_n(\mathbf{k})}{\partial \mathbf{k}}$ represents the group velocity $\mathbf{V}_n(\mathbf{k})$, and the $-\dot{\mathbf{k}} \times \mathbf{\Omega}_n(\mathbf{k})$ is the anomalous velocity, which gives rise to the transverse transport and its direction is perpendicular to the applied electric field and magnetic field. In 2D systems, the electronic wave function motion is restricted to the xy plane and we can obtain its transverse conductivity based on the Boltzmann equation [93]:

$$\delta_{xy} = -\frac{e^2}{(2\pi)^2\hbar}\sum_n \int_{BZ} \Omega_n^{xy}(\mathbf{k})\rho_F(\varepsilon_n(\mathbf{k}))d^2\mathbf{k}, \tag{4.21}$$

where $\rho_F(\varepsilon_n(\mathbf{k}))$ is the Fermi distribution function. At zero temperature, $\rho_F(\varepsilon_n(\mathbf{k}))$ simplifies into a step function at the Fermi energy level. If the Fermi energy is within the m-th band gap, the integral over Berry curvature is an integer w_m which is called the winding number. And the corresponding transverse conductivity can be expressed as:

$$\delta_{xy} = -\frac{e^2}{\pi\hbar}\sum_{n\leq m} C_n = -\frac{e^2}{\pi\hbar}w_m. \tag{4.22}$$

Here, C_n is the Chern number of band n and the m represents the index of the

first band below the Fermi level. Eq. (4.22) indicates that the transverse electrical conductivity is quantized, which corresponds to the integer quantum Hall effect (QHE) [94].

In this thesis, the magnonic transport properties are investigated with a semiclassical method[95]. Analogously to the study of the integer Hall effect, we utilize the magnon Berry curvature to explore the thermal Hall effect of magnon. The thermal Hall effect of magnon is generated by breaking the TR or SI symmetry in the system through introducing *e.g.,* DMI, Kitaev interaction to get a nonzero Berry curvature, which has been observed in the insulating ferromagnet $Lu_2V_2O_7$ [6] . Similar to Eq. (4.20), the motion for magnons in semiclassical way can be written as [96, 95]:

$$\begin{aligned} \dot{\mathbf{r}} &= \frac{1}{\hbar}\frac{\partial \varepsilon_n(\mathbf{k})}{\partial \mathbf{k}} - \dot{\mathbf{k}} \times \mathbf{\Omega}_n(\mathbf{k}), \\ \hbar\dot{\mathbf{k}} &= -\nabla U(\mathbf{r}), \end{aligned} \tag{4.23}$$

where the $\varepsilon_n(\mathbf{k})$ is the eigenvalue of the nth magnonic band, $\mathbf{\Omega}_n(\mathbf{k})$ is the magnonic Berry curvature in $\mathbf{k}$ space, and the $\nabla U(\mathbf{r})$ is the potential for magnons. The equilibrium situation is selected as a starting point. To confine the magnon transport within the magnet, the potential gradient $\nabla U(\mathbf{r})$ is needed. The potential $U(\mathbf{r})$ changes from 0 to infinity value as the position $\mathbf{r}$ changes from the inside of the magnet to the outside, leading to the vector $\dot{\mathbf{k}}$ pointing inward near the edge area of the magnet. Similar to the motion in the electronic system, the $-\dot{\mathbf{k}} \times \mathbf{\Omega}_n(\mathbf{k})$ offers an anomalous velocity along with the edge direction. As a result, there is an edge current of magnons, and the magnon edge current I and the magnon edge energy current I_E can be expressed as:

$$\begin{aligned} I &= -\frac{1}{\hbar V}\sum_{n,\mathbf{k}} \int_{\varepsilon_n(\mathbf{k})}^{\infty} \Omega_n^{xy}(\mathbf{k}) n_B(\varepsilon) d\varepsilon, \\ I_{\mathrm{E}} &= -\frac{1}{\hbar V}\sum_{n,\mathbf{k}} \int_{\varepsilon_n(\mathbf{k})}^{\infty} \Omega_n^{xy}(\mathbf{k}) \varepsilon n_B(\varepsilon) d\varepsilon, \end{aligned} \tag{4.24}$$

where V is the volume of the magnet, the $n_{\mathrm{B}}(\varepsilon)$ is the Bose distribution function and it follows the $n_{\mathrm{B}}(\varepsilon) = (e^{\frac{\varepsilon-\mu}{k_{\mathrm{B}}T}} - 1)^{-1}$ with μ representing the chemical potential. When the temperature gradient is applied, it gives rise to the spatial variation of magnon density. As shown in Figure 4.2, each magnon edge currents in the small regions do not offset each other, resulting in finite thermal Hall current along with the transverse direction. Then, the transverse magnon current density and energy current density of magnon aroused by the edge current can be expressed as: $\mathbf{j} = -\nabla \times I$, $\mathbf{j}_{\mathrm{E}} = -\nabla \times I_{\mathrm{E}}$, and the transverse transport conductivity can be obtained based on the relationship between the magnon current and the heat current.

We take an example of the temperature gradient along y direction, and the magnon current density $(j)_x^{\nabla T}$ and energy current density $(j_{\mathrm{E}})_x^{\nabla T}$ of magnon

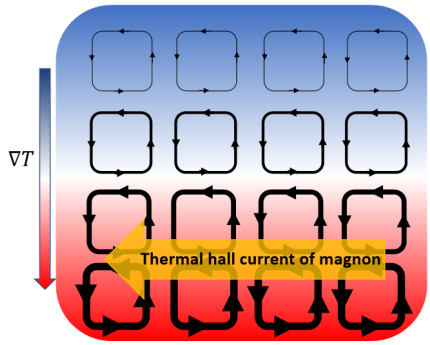

FIGURE 4.2: The magnon transport under the temperature gradient. Each small rectangular box represents the magnon edge currents in the small regions and they do not offset each other along the transverse direction. This leads to the appearance of the transverse thermal hall current of magnon.

along x direction are written as:

$$\begin{aligned}(j)_x^{\nabla T} &= -\frac{T}{\hbar V}\partial_y\left(\frac{1}{T}\right)\sum_{n,\mathbf{k}}\int_{\varepsilon_n(\mathbf{k})}^{\infty}\Omega_n^{xy}(\mathbf{k})(\varepsilon-\mu)\left(\frac{dn_{\mathrm{B}}(\varepsilon)}{d\varepsilon}\right)d\varepsilon,\\ (j_{\mathrm{E}})_x^{\nabla T} &= -\frac{T}{\hbar V}\partial_y\left(\frac{1}{T}\right)\sum_{n,\mathbf{k}}\int_{\varepsilon_n(\mathbf{k})}^{\infty}\Omega_n^{xy}(\mathbf{k})\varepsilon(\varepsilon-\mu)\left(\frac{dn_{\mathrm{B}}(\varepsilon)}{d\varepsilon}\right)d\varepsilon.\end{aligned} \tag{4.25}$$

Here, the μ represents the magnon chemical potential. We select the heat current rather than magnon number current, which is due to the fact that it is not easy to measure the magnon number current experimentally. On the one hand, the magnon is not conserved due to the fact that H contains number-nonconserving terms (*e.g.*, $\alpha_i\alpha_j$, and $\alpha_i^\dagger\alpha_j^\dagger$). On the other hand, the magnon – magnon interactions will produce or annihilate magnons.

Under a temperature gradient, the magnon current density and energy current density holds the relationship:

$$\begin{aligned}j_x^{\nabla T} &= \kappa_{\mathrm{MN}}^{xy}(\nabla T)_y\\ (j_{\mathrm{E}})_x^{\nabla T} &= \kappa_{\mathrm{TH}}^{xy}(\nabla T)_y.\end{aligned} \tag{4.26}$$

Then, we can obtain the transverse thermal Hall conductivity $\kappa_{\mathrm{TH}}^{xy}$ and "pure magnon Nernst conductivity" $\kappa_{\mathrm{MN}}^{xy}$, straightforwardly. Here, we can put $\kappa_{\mathrm{TH}}^{xy}$ and $\kappa_{\mathrm{MN}}^{xy}$ to the transport tensor L, and the transverse transport coefficients L_{ij}^{xy} holds:

$$L_{ij}^{xy} = -\frac{(k_{\mathrm{B}}T)^q}{\hbar V}\sum_{n,\mathbf{k}}\Omega_n^{xy}(\mathbf{k})c_q(n_{\mathrm{B}}(\varepsilon)), \tag{4.27}$$

where $c_q(n_{\mathrm{B}}(\varepsilon)) = \int_{\varepsilon_n(\mathbf{k})}^{\infty}(\varepsilon-\mu)^q(-\frac{dn_{\mathrm{B}}(\varepsilon)}{d\varepsilon})d\varepsilon = (k_{\mathrm{B}}T)^q\int_0^{n_{\mathrm{B}}(\varepsilon)}(\log(1+t^{-1}))^q dt$ with $q = i+j-2$ (i, j correspond to 1 or 2), and $\log(1+t^{-1})$ is the inverse of

the Bose distribution function.

If the $i = j = 2$, the L_{22}^{xy} corresponds to the thermal Hall effect, and the transverse thermal Hall conductivity $\kappa_{\mathrm{TH}}^{xy}$ can be expressed as:

$$\kappa_{\mathrm{TH}}^{xy} = -\frac{k_{\mathrm{B}}^2 T}{(2\pi)^3 \hbar} \sum_n \int_{\mathrm{BZ}} c_2(n_{\mathrm{B}}(\varepsilon))\, \Omega_n^{xy}(\mathbf{k})\, d\mathbf{k}, \tag{4.28}$$

where $c_2(\tau) = (1+\tau)\ln^2[(1+\tau)/\tau] - \ln^2\tau - 2\mathrm{Li}_2(-\tau)$, and Li_2 denotes the polylogarithm function. Similarly, we can obtain the magnon Nernst conductivity κ_{N}^{xy}:

$$\kappa_{\mathrm{N}}^{xy} = -\frac{k_{\mathrm{B}}}{(2\pi)^3} \sum_n \int_{\mathrm{BZ}} c_1(n_{\mathrm{B}}(\varepsilon))\, \Omega_n^{xy}(\mathbf{k})\, d\mathbf{k}, \tag{4.29}$$

where $c_1(\tau) = \int_0^\tau \ln[(1+t)/t]dt = (1+\tau)\ln(1+\tau) - \tau\ln\tau$. Here, the κ_{N}^{xy} refers to the spin Nernst effect of magnon, as each magnon carries the angular momentum $-\hbar$. In the thesis, we call this "spin Nernst effect of magnon" as magnon Nernst effect.

For two-dimensional systems, the thermal Hall conductivity and magnon Nernst conductivity can be expressed as:

$$\begin{aligned} \kappa_{\mathrm{TH}}^{xy} &= -\frac{k_{\mathrm{B}}^2 T}{(2\pi)^2 \hbar} \sum_n \int c_2(n_{\mathrm{B}}(\varepsilon))\, \Omega_n^{xy}(\mathbf{k})\, d\mathbf{k}, \\ \kappa_{\mathrm{N}}^{xy} &= -\frac{k_{\mathrm{B}}}{(2\pi)^2} \sum_n \int c_1(n_{\mathrm{B}}(\varepsilon))\, \Omega_n^{xy}(\mathbf{k})\, d\mathbf{k}, \end{aligned} \tag{4.30}$$

Both thermal Hall conductivity and magnon Nernst conductivity have their high-temperature limit. We here take the thermal Hall conductivity as an example to briefly demonstrate the feature. According to Eq. (4.28), we get:

$$\kappa_{\substack{\mathrm{TH} \\ T\to\infty}}^{xy} = -\frac{k_{\mathrm{B}}^2 T}{(2\pi)^3 \hbar} \lim_{T\to\infty} \sum_n \int_{\mathrm{BZ}} c_2(n_{\mathrm{B}}(\varepsilon))\, \Omega_n^{xy}(\mathbf{k})\, d\mathbf{k}. \tag{4.31}$$

According to the L'Hospital's rule, Eq. (4.31) can be rewritten as:

$$\kappa_{\substack{\mathrm{TH} \\ T\to\infty}}^{xy} = \lim_{T\to\infty} \frac{\frac{\kappa_{\mathrm{TH}}^{xy}}{T}}{\frac{1}{T}} = \lim_{T\to\infty} \frac{\partial \frac{\kappa_{\mathrm{TH}}^{xy}}{T}}{\partial \frac{1}{T}} = \lim_{T\to\infty} \left(-T^2 \frac{\partial}{\partial T} \frac{\kappa_{\mathrm{TH}}^{xy}(T)}{T} \right). \tag{4.32}$$

Then, the high-temperature limit of thermal Hall conductivity can be represented as:

$$\begin{aligned} \kappa_{\substack{\mathrm{TH} \\ T\to\infty}}^{xy} &= -\frac{k_{\mathrm{B}}^2}{(2\pi)^3 \hbar} \lim_{T\to\infty} \sum_n \int_{\mathrm{BZ}} T^2 \frac{c_2(n_{\mathrm{B}}(\varepsilon))}{\partial T}\, \Omega_n^{xy}(\mathbf{k})\, d\mathbf{k} \\ &= -\frac{k_{\mathrm{B}}}{(2\pi)^3 \hbar} \sum_n \int_{\mathrm{BZ}} \varepsilon_n(\mathbf{k}) \Omega_n^{xy}(\mathbf{k})\, d\mathbf{k}. \end{aligned} \tag{4.33}$$

If we assume both bands are flat, and simplify the system into two bands

model, honeycomb lattice for instance, then the Eq. (4.33) can be updated into:

$$\underset{T\to\infty}{\kappa_{\mathrm{TH}}^{xy}} = -\frac{k_{\mathrm{B}}}{(2\pi)^3\hbar}\sum_n \varepsilon_n \int_{\mathrm{BZ}} \Omega_n^{xy}(\mathbf{k})\, d\mathbf{k} = \frac{k_{\mathrm{B}}}{(2\pi)^2\hbar}\triangle C_1. \tag{4.34}$$

where the $\triangle$ represents the effective band gap and C_1 is the Chern number of the first magnon branch. Then, we get the conclusion that the high-temperature limit of thermal Hall conductivity is a constant, which is determined by the band gap $\triangle$ and the Chern number.

4.5 Summary

In this chapter, the topological properties are extended from electronic systems to magnonic systems, where the magnon Berry curvature is introduced and some magnonic topological phenomenon is explored, the magnonic Weyl point. The magnonic transport properties in the context of the thermal Hall effect and magnon Nernst effect were introduced according to the semiclassical method.

Chapter 5

Two-dimensional metal-organic frameworks with Shastry-Sutherland lattice

In this chapter, inspired by the successful synthesis of Fe/Cu-5, 5′-bis (4-pyridyl) (2, 2′- bipirimidine) (PBP) [97, 98], we systematically investigated a family of two-dimensional (2D) metal-organic frameworks (MOFs) with the Shastry-Sutherland lattice (SSL), i.e., transition-metal (TM)-PBP (TM = Cr, Mn, Fe, Co, Ni, Cu, Zn) by means of first-principles density functional theory calculations and Monte Carlo simulation discussed in Chapter 2 and Chapter 3. Mn-PBP is discovered to be the first ferromagnetic (FM) 2D MOF with SSL and the Curie temperature is predicted to be about 105 K, while Fe-PBP, TM-PBP (TM = Cr, Co, Ni) and TM-PBP (TM = Cu, Zn) are found to be antiferromagnetic (AFM), dimerized (AFM dimer) and nonmagnetic, respectively. The electronic structure calculations reveal that TM-PBP are semiconductors with band gaps ranging from 0.12 eV to 0.85 eV, which could be easily modulated by various methods. Particularly, Mn-PBP would exhibit half-metallic behavior under compressive strain or proper electron/hole doping and a Mn-PBP based spintronic device has been proposed. Moreover, the magnon dispersion and the magnonic transport properties of Mn-PBP are studied to explore its candidate application in magnonics.

Some results presented in this chapter have already been published:
Li-chuan Zhang, et. al., Chemical Science 10, 10381-10387 2019.

5.1 Introduction of two-dimensional metal-organic frameworks with Shastry-Sutherland lattice

In recent years, the two-dimensional (2D) metal-organic frameworks (MOFs) formed by metal atoms and polar organic molecules [99, 100, 101] have stimulated wide interest for researchers [102, 103] due to the advantage of low cost, chemical tenability, easy fabrication, and mechanical flexibility. It has

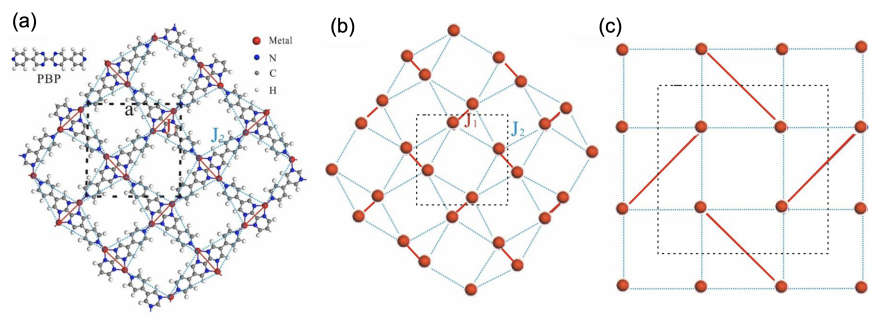

FIGURE 5.1: (a) The schematic structure of transition-metal (TM)−PBP. The red balls indicate the TM atoms. The black dashed lines outline the unit cell of the TM-PBP system and the lattice parameter is marked as **a**. (b) The abstraction of (a) by focusing on TM atoms. The red dot lines ($\mathbf{J}_1$) and blue dashed lines ($\mathbf{J}_2$) represent the interactions between the nearest TM atoms and the second nearest TM atoms, respectively. (c) The conventional standard Shastry-Sutherland lattice, which is topologically equivalent to (b).

been proved that there are a lot of novel physical properties in 2D MOFs systems, such as ferromagnetic/antiferromagnetic ground states [104], superconductors [105], and topological insulators [106, 107]. By choosing transition-metal atoms, the magnetic 2D MOFs can be easily obtained, and the magnetic structure can be modulated by the polar organic molecules. According to the geometrical structure, the magnetic 2D MOFs can be classified into hexagonal lattice [106, 107], square lattice [104], and Kagome lattice [108, 109], etc.

Here, we want to introduce a special magnetic lattice, which is called Shastry-Sutherland lattice (SSL) [110]. The SSL was introduced by Shastry and Sutherland in 1981 [110], and it is a special type of distorted square lattice. It attracts a great variety of attentions, especially on the properties of magnetic order and fractional magnetization plateaus at low temperature in the materials $SrCu_2(BO_3)_2$ [111, 112] and rare-earth-metal tetraborides RB_4 (R= La−Lu) [113, 114]. Besides, several SSL in 2D MOFs have also been synthesized, such as the Cu-5, 5′-bis(4-pyridyl) (2, 2′ -bipirimidine) (PBP) [98] and the Fe−PBP [97]. The schematic structure of Cu/Fe−PBP is shown in Figure 5.1 (a) and the black dashed lines outlined the unit cell. The framework of metal atoms can be abstracted to a deformed square lattice, which is topologically equivalent to the standard SSL (see Figure 5.1 (b, c)). Inspired by the synthesis of Cu/Fe-PBP, we want to explore whether some other candidate TM elements can form MOFs with PBP. We also want to investigate is there novel electronic and magnetic properties of this SSL in 2D MOFs materials. These motivate us to do intensive theoretical research to extend the frontier of the 2D MOF field.

5.2 Stability and ground state in TM−PBP

5.2.1 Bonding Energy

Firstly, we relaxed the structure of TM-PBP to obtain the geometric parameters of 2D-MOFs frameworks, where the Vienna *ab initio* simulation package (VASP)[65] is used with the generalized gradient approximation (GGA) of Perdew–Burke–Ernzerhof (PBE)[63] for the exchange–correlation potential. To explore the stability of the TM-PBP, the binding energy between TM atoms and PBP molecules is introduced to represent the corresponding bonding strength in different TM-PBP system according to:

$$E_{\mathrm{binding}} = (2E_{\mathrm{PBP}} + 4E_{\mathrm{TM}} - E_{\mathrm{TM-PBP}})/4, \tag{5.1}$$

where the $E_{\mathrm{TM-PBP}}$ represents the total energy of TM−PBP unit cell, which contains 2 PBP molecules and 4 TM atoms. The E_{binding} is the binding energy between PBP molecules and TM atoms. As shown in Table 5.1, the binding energy is generally about 3 to 4 eV per TM atom for most TM-PBP except that of Zn-PBP, which is only about 1 eV. Considering the fact that Cu/Fe-PBP has already been successfully synthesized, TM-PBP (TM=Cr, Mn, Co, Ni) is very likely to be obtained experimentally.

5.2.2 Exchange interaction and 2D Ising model

To identify the magnetic ground states of 2D TM-PBP frameworks, we propose three different typical magnetic configurations, i.e., ferromagnetic (FM), Néel antiferromagnetic (AFM) and stripe AFM (see Figure 5.2), and the corresponding total energy of them are calculated, separately. As shown in Table 5.1, all TM-PBP frameworks hold semiconductors and magnetic moments of these systems are mainly localized in transition-metal atoms, which means the exchange interactions are localized and we can choose the exchange interaction between metal atoms to simplify the analysis of spin interactions. In our model, only up to the second-nearest-neighbor exchange interaction is selected. The 2D Ising model for SSL [115] is selected to study the magnetic ground state of TM-PBP frameworks:

$$E_{\mathrm{total}} = E_0 + E_{\mathrm{mag}} = E_0 + \sum_{\langle ij \rangle} J_1 \mathbf{S}_i \cdot \mathbf{S}_j + \sum_{\langle l,m \rangle} J_2 \mathbf{S}_l \cdot \mathbf{S}_m, \tag{5.2}$$

where the E_{mag} and E_0 represent the energy of effective spin interactions and the total energy without the magnetic interactions, separately. J_1 and J_2 stand for the exchange interaction coupling constants of the nearest-neighbor and second-nearest-neighbor metal atoms, $\mathbf{S}_i$, $\mathbf{S}_j$ and $\mathbf{S}_l$, $\mathbf{S}_m$ indicate the spin operators at nearest site i and j (second nearest site l and m) respectively. The out-of-plane magnetic anisotropic energy is calculated with the value of 0.034 meV. In our model, the magnetic anisotropic energy term is neglected because of its tiny value.

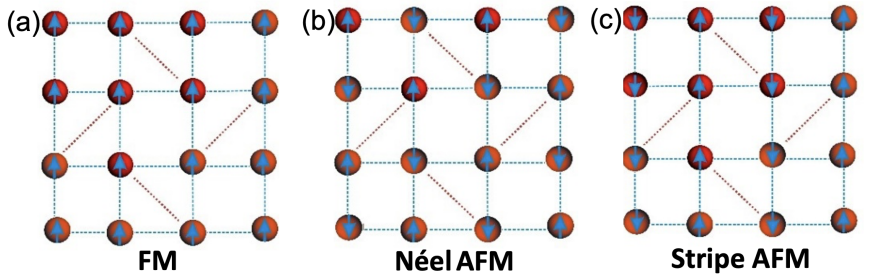

FIGURE 5.2: Magnetic configurations of ferromagnetic (FM) (a), Néel antiferromagnetic (Néel AFM) (b) and stripe antiferromagnetic (Stripe AFM) (c) types in the form of conventional standard Shastry-Sutherland lattice, respectively.

The value of J_1 and J_2 can be obtained by calculating three different typical magnetic states mentioned above. There are four TM atoms in each unit cell, and the total energy per unit cell with different magnetic configurations can be expressed as follows according to the Hamiltonian in Eq. (5.2):

$$\begin{aligned} E_{\mathrm{FM}} &= E_0 + 2J_1S^2 + 8J_2S^2, \\ E_{\mathrm{AFM_{N\acute{e}el}}} &= E_0 + 2J_1S^2 - 8J_2S^2, \\ E_{\mathrm{AFM_{Stripe}}} &= E_0 - 2J_1S^2, \end{aligned} \tag{5.3}$$

then the coupling constants J_1 and J_2 can be derived as

$$\begin{aligned} J_1 &= (E_{\mathrm{FM}} + E_{\mathrm{AFM_{N\acute{e}el}}} - 2E_{\mathrm{AFM_{Stripe}}})/8S^2, \\ J_2 &= (E_{\mathrm{FM}} - E_{\mathrm{AFM_{N\acute{e}el}}})/16S^2, \end{aligned} \tag{5.4}$$

where the S is the spin moment of the system. According to the total energy of the TM-PBP frameworks with different magnetic configurations from the DFT calculation, we calculate the value of coupling constants J_1 and J_2, and the results are listed in Table 5.1. The first-principles calculations were performed using the Vienna *ab initio* simulation package (VASP) [65] with the generalized gradient approximation (GGA) of Perdew-Burke-Ernzerhof (PBE) [63] for the exchange-correlation potential. The interaction between the electron and nuclei was expressed with the projector-augmented wave (PAW) method [116]. 800 eV was selected as the plane wave function kinetic energy cutoff and 10^{-6} eV was set as the energy convergence threshold. The Brillouin zone was sampled with 5×5×1 Gamma-centered Monkhorst−Pack grids [117]. The shape and volume for each cell were fully optimized and the maximum force for each atom was less than 0.01 eV/Å. To obtain accurate results in MT-PBP, the GGA+*U* method is adopted and more details are discussed in Section 5.3.1.

In TM-PBP frameworks, the second nearest neighboring distances of TM atoms (d_2) are much longer than the nearest neighboring distance of TM

	a	d_1	d_2	E_b	E_g	M	M_{cell}	J_1	J_2	Magnetic
Cr	18.17	5.91	10.33	3.4	0.73	4.36	0	0.1	-3.3×10^{-5}	Dimerized
Mn	17.79	5.50	10.21	3.5	0.12	4.33	16	-1.86	-0.31	FM
Fe	17.76	5.43	10.15	4.2	0.16	3.12	0	2.5	0.7	Stripe AFM
Go	17.62	5.46	10.11	4.4	0.53	1.96	0	0.4	-3.5×10^{-2}	Dimerized
Ni	17.49	5.33	10.06	4.3	0.73	0.96	0	0.9	-2×10^{-2}	Dimerized
Cu	17.55	5.44	10.07	3.6	0.85	0	0	–	–	Nomagnetic
Zn	17.34	5.17	10.01	1.0	0.13	0	0	–	–	Nonmagnetic

TABLE 5.1: The structural, electronic, and exchange interaction parameters in MT-PBP frameworks. a (Å): lattice parameter; d_1 (Å) and d_2 (Å): distances between the nearest TM atoms and second-nearest TM atoms; E_b (eV): binding energy between TM atoms and PBP molecules; E_g (eV): energy band gap in the electronic band structure; M (μ_B) and M_{cell} (μ_B/cell): magnetic moment per TM atom and per unit cell, respectively; J_1 (meV) and J_2 (meV): magnetic coupling constants for the nearest neighboring TM atoms and second-nearest neighboring TM atoms, respectively.

atoms (d_1). Considering all frameworks are semiconductors, the nearest neighboring magnetic exchange interactions should be much stronger than the second-nearest neighboring interactions. Significantly, Mn-PBP, Fe-PBP, TM-PBP (TM=Cr, Co, Ni) and TM-PBP (TM=Cu, Zn) are proved to be FM, AFM, dimerized (AFM dimer) and NM, respectively. The calculated results indicate that the first exchange coupling constants of Mn-PBP and Fe-PBP are much larger than that of others. For Mn-PBP, exchange interaction coupling constants J_1 (-1.86 meV) and J_2 (-0.31 meV) are both negative, which manifests the magnetic exchange interactions between nearest and second-nearest TM atoms are both FM, and the whole system also exhibits FM behavior. For Fe-PBP, the value of J_1 (2.5 meV) and J_2 (0.7 meV) are both positive, implying AFM interactions between neighboring Fe atoms and a Stripe AFM ground state of the system. When it comes to TM-PBP (TM=Cr, Co, Ni), all of J_1 are positive, illustrating AFM interactions between the nearest neighboring TM atoms. However, all of J_2 are lesser than J_1 at least two orders of magnitude. Thus, we deduce that the magnetic ground state of TM-PBP (TM=Cr, Co, Ni) should be dimer phase, in which the nearest TM atoms bonded as AFM dimers and the whole system do not exhibit macro magnetic order. From the previous study, we know that the SSL systems normally display AFM ground states [113, 114], the FM ground state founded in Mn-PBP provides a novel example of FM Shastry-Sutherland spin lattice.

5.2.3 Curie temperature of Mn-PBP

Based on the Ising model mentioned above, the thermodynamical magnetic properties of Mn-PBP framework are simulated according to the Monte Carlo

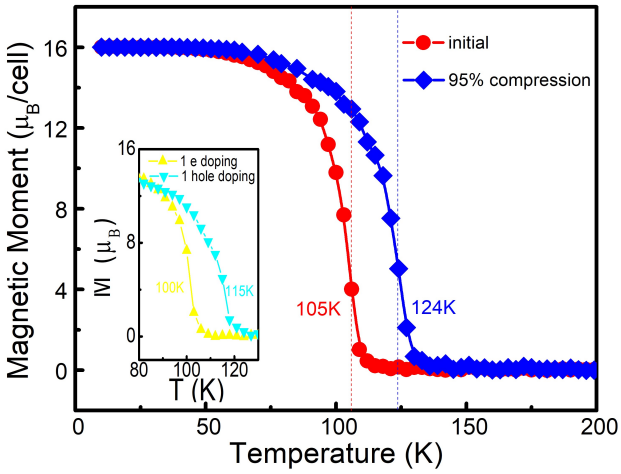

FIGURE 5.3: The variation of the average magnetic moment of unit cell with respect to the temperature for Mn-PBP, the red and blue line correspond to the results simulated with optimized structure and 95% biaxial compression, respectively. The left inset indicates the results with 1 electron/hole doping in each unit cell.

method [118, 119], and the Curie temperature of Mn-PBP is predicted.

With the method discussed in Section 2.3.6, we carry out a Mento Carlo simulation. The simulation is carried out on a 200×200 2D SSL and the simulation steps are up to 10^9 for each temperature. The 100×100 2D SSL with 10^8 steps is also calculated, and almost the same results are obtained, verifying the simulation has converged. As shown in Figure 5.3, with the evolution of temperature, the total magnetic moment per unit cell starts to drop gradually from 16 μ_B at about 60 K, and it becomes 0 μ_B until at about 110 K. The Curie temperature (T_C) can be determined through locating the second-order phase transition point, which locates at about 105 K. This means the magnetic ground state of Mn-PBP changes from FM to paramagnetic when the temperature rises above 105 K. Compared to recent popular 2D FM materials, *e.g.*, PTC−Fe (2D MOF) [120] and CrI_3 [121], this material holds higher T_C from our calculation. Therefore, it's likely that the predicted result can be confirmed by experiments, although the Curie temperature could be overestimated from the Ising model.

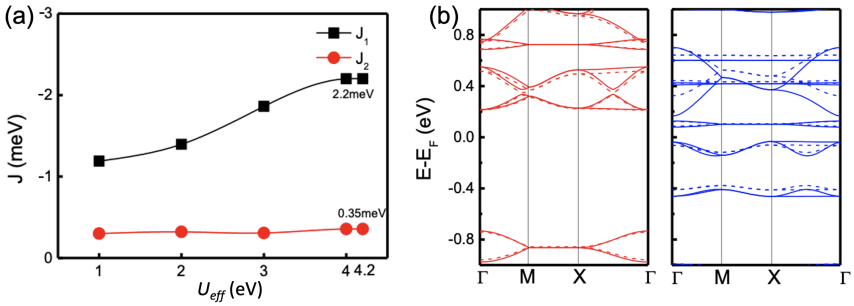

FIGURE 5.4: (a) The exchange interaction J of PBP−Mn as a function of the effective U. The black line represents the value of J_1, and the red line represents J_2. (b) Band structures of Mn−PBP. Left panel: spin-down bands (red); Right panel: spin-up bands (blue). The solid lines and dotted lines represent the band structure with U_{eff} = 3 eV and U_{eff} = 4.2 eV, respectively.

5.3 The Hubbard U and substrate effect on the magnetic properties

5.3.1 The influence of Hubbard U

The calculated electronic and magnetic properties in this Chapter are obtained from the first-principles calculation. The DFT +U method proposed by Dudarev, *et al.* [122, 123] is adopted to obtain accurate electronic properties, where only the effective $U_{\text{eff}} = U$ (correlation energy) $- J$ (exchange energy) value is meaningful. In our calculation, U_{eff} is selected as 3 eV for all TM-PBP frameworks, referring to previous works on other 2D MOFs [124, 125, 104]. Besides, the linear response theory method developed by Cococcioni [67] is employed (shown in Section 3.2.5) to evaluate U_{eff} and the predicted value is 4.2 eV, which does not affect the qualitative result, shown in Figure 5.4. The calculated T_{C} is 115 K when the U_{eff} is chosen as 4.2 eV, demonstrating that the magnitude of effective U_{eff} is appropriate. To confirm the FM ground state of Mn-PBP, we further check the effect of U_{eff} value on magnetic properties. A series of U_{eff} values ranging from 1.0 eV to 4.2 eV have been tested, and the ground state of Mn-PBP is always FM as shown in Figure 5.4 (a). Thus, the predicted FM ground state of Mn-PBP is reliable.

5.3.2 Substrate effect on Mn-PBP

Experimentally, the 2D MOFs are synthesized on the surface of the substrate, and the compression of 2D material is usually realized through applying compression to its substrate. Therefore, it is necessary for us to investigate the effect of the substrate on the magnetic properties of Mn-PBP.

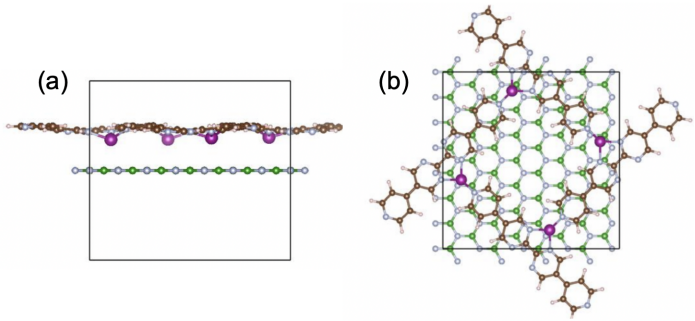

FIGURE 5.5: The relaxed structure of Mn-PBP and monolayer BN which is selected as the substrate. The side view (a) and top view (b) are shown respectively.

As monolayer BN is a stable insulator, we utilize it as the substrate of Mn-PBP. The optimized result of Mn-PBP with the substrate is shown in Figure 5.5, where both with or without 95% compression are investigated. Interestingly, a slight buckling is observed in the structure, and we find that all the Mn atoms move downward to approach the BN monolayer, implying that the BN layer has attractiveness to Mn atoms. However, this buckling will not influence the magnetic ground state of Mn-PBP. After comparing the total energy of different magnetic configurations, we conclude that the ground state of Mn-PBP is still FM.

5.4 Bonding analysis and electronic properties

The bonding analysis is done on the Mn-PBP framework according to the Bader charge analysis [126, 127] and the electron localization function (ELF) analysis [128].

In Bader charge analysis, a zero flux surface is introduced to divide atoms to determine the Bader volume. For instance, the zero flux surface is a 2D surface on which the charge density is a minimum perpendicular to the surface, *i.e.*, the vertical surface of A-A bond for A_2 molecule. Then, the total electronic charge of an atom is approximately calculated based on the charge enclosed within the Bader volume. Based on this method, we can quantify the difference of charge on selected atoms and provide some information to classify the corresponding chemical bonds. Migrations of charge in Mn-PBP are calculated based on the Bader charge analysis, and the result is shown in Figure 5.6 (a). It is evaluated that the charge transfers from each Mn atom to whole PBP molecules with about 1.19 e. We classify the PBP molecules around each Mn atom into several groups, *i.e.*, N1 group and N2/N3 group. Each N1, N2/N3 atoms accept about 0.13 e, 0.12 e from nearby Mn atoms, and charges transferred from each Mn atom to N1 group and N2/N3 group are 0.51 e and 0.68 e, respectively.

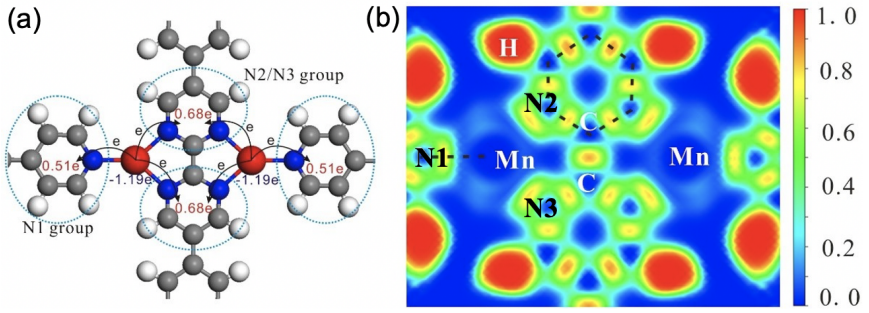

FIGURE 5.6: (a) The values of charge transfers from Mn to nearby PBP through Bader charge analysis. (b) The electron localization function of Mn-PBP on the plane crossing all Mn atoms.

The ELF is a measurement to quantify the extent of spatial localization of electron and it can be used to determine the type of chemical bonds. The ELF value ranges from 0 to 1, and 1 means the electrons are localized which refers to the covalent bond. If the ELF equals 0.5, it corresponds to electron gas, and that is a metallic bond. The ELF analysis of Mn-PBP is shown in Figure 5.6 (b). A high ELF area is found at C-C, C-N covalent bonds. Besides, high ELF area is also found among the bond between N and Mn atoms, which is apparently different from C-C, C-N bond and should correspond to the N-Mn coordinated bond caused by the electron pair donation from N atom to its nearby Mn atom. Moreover, low ELF area also exist in the bridge-like area between neighboring N1, N2 and N3 atoms, which may imply that neighboring N atoms can interact with each other directly.

Electronic structures of TM-PBP frameworks have been investigated, and we here show the band structure and projected density of states (PDOS) of Mn-PBP in Figure 5.7. Meanwhile, the band structure of TM-PBP (TM=Cr, Fe, Co, Ni, Cu, Zn) is shown in Figure 5.8. All TM-PBP frameworks are found to be semiconductors and the corresponding band gaps range from 0.12 eV to 0.85 eV, as listed in Table 5.1. Among them, Cu-PBP has the largest energy gap, while Mn-PBP has the smallest gaps. Only Mn-PBP has the FM ground state, which makes the spin-up and spin-down energy bands deviate from each other as indicated in Figure 5.7. The Mn-PBP framework is a FM semiconductor with a tiny band gap, where the spin-up electrons hold the semiconducting behavior with the band gap of 0.12 eV and the spin-down electrons hold almost 1 eV band gap. This means that the 100% spin-polarized carriers could be realized under optical, thermal or electrical gating excitation or strain. To further uncover the electronic properties of Mn-PBP, the PDOS is calculated and shown in the right side of Figure 5.7, revealing that there is a strong hybridization of p_z orbital from C and N atoms and d_{xz}, d_{yz} orbitals from Mn atoms near the Fermi level. However, s, d_{xy}, d_{z^2} and $d_{x^2-y^2}$

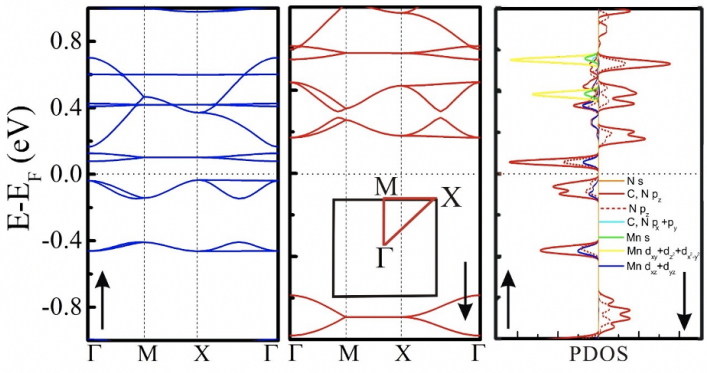

FIGURE 5.7: Electronic structure of Mn-PBP. Left panel: spin-up bands (blue lines); middle panel: spin-down bands (red lines); Right panel: spin-up and spin-down PDOS. The insert of the middle panel indicates the first Brillouin zone.

orbitals of Mn atoms are located about 0.5 eV above Fermi level and they correspond to the flat bands, implying that they are localized states with higher energy.

The novel electronic properties of Mn-PBP can be explained in terms of the symmetry of the system and the type of bonding. As shown in Figure 5.9, there are three Mn-N bonds around the same Mn atom, and the distance between Mn and N1 atom is 2.01 Å, while the distance between Mn and N2/N3 atom is 2.06 Å. Besides, the angle of N2−Mn−N3, N1−Mn−N2 is 83.64° and 138.18°, respectively. The diverse bond lengths and angles reveal that three Mn-N bonds around Mn atom don't hold C_3 symmetry. The asymmetric Mn−N coordinating bonds lead the non−equilateral triangle crystal field contributed by neighboring N atoms, causing the split of Mn d orbitals, where d_{xz}, d_{yz} orbitals shift down and d_{xy}, d_{z^2} and $d_{x^2-y^2}$ orbitals shift up. Among them, Mn d_{xz}, d_{yz} orbitals locate around Fermi level and hybrid with p_z orbitals provided from C and N atoms in PBP, which is responsible for the bonding between Mn and PBP molecules. We also try to investigate the electronic and spin polarization properties from the aspect of real space and we show the result in Figure 5.9. The partial charge density of Mn−PBP around the Fermi level is shown in Figure 5.9 (a), indicating that the partial charge density mainly locates around Mn atoms and its neighboring N atom. The result is consistent with the above deduction that d orbitals (d_{xz}, d_{yz} of Mn) strongly hybrid with p_z (N and C atoms) orbitals. The spin−polarized charge density of Mn−PBP is shown in Figure 5.9 (b), and it is clear that the majority spin locates on Mn atoms, which should be provided by the localized d orbitals from Mn atoms. Meanwhile, the minority spin is mainly polarized in PBP molecules. Among them, N atoms adjacent to Mn atoms are oppositely polarized compared to Mn atoms, and the polarization of N1 atom is much stronger than N2/N3 atoms. Interestingly, the phenomena similar to

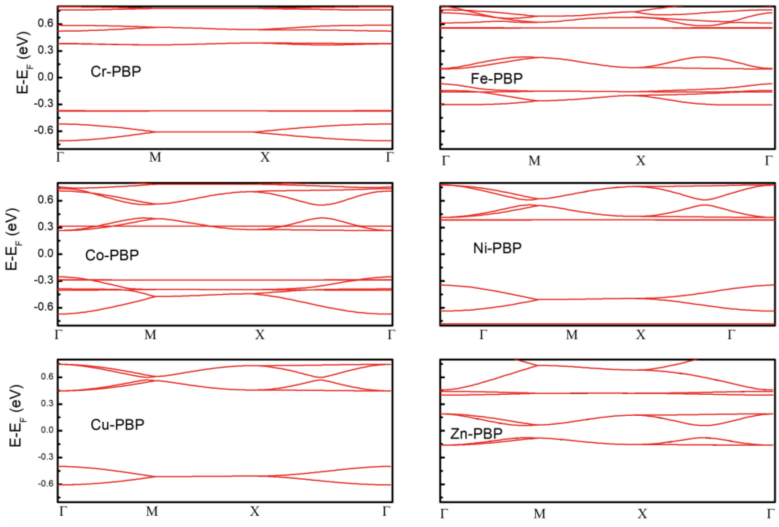

FIGURE 5.8: Band structures of TM-PBP (TM=Cr, Fe, Co, Ni, Cu, Zn). In AFM TM-PBP (TM=Cr, Fe, Co, Ni), the energy band of spin-up and spin-down are identical to each other as here the spin-orbit coupling is ignored in the calculation. The GGA+U method is used and the value of U_{eff} is 3 eV in all calculations. Some similar band structures are obtained in different frameworks according to the symmetry of the system.

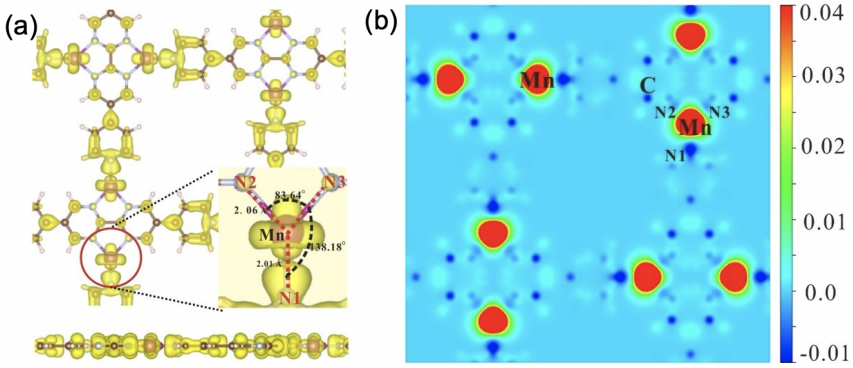

FIGURE 5.9: (a) Top and side views of partial charge density in Mn-PBP framework. The energy range was chosen around the Fermi level: -0.2 to 0.2 eV, and isosurface value is 0.002 e/Bohr^3. The inset enlarges the area around Mn atom, where three neighboring N atoms of Mn were marked as N1, N2 and N3. (b) The spin-polarized charge density of Mn-PBP on the plane crossing all Mn atoms. The unit of the color map is e/Bohr^3.

RKKY exchange mechanism [129] is observed in PBP molecules, where carbon atoms in PBP molecules are alternately polarized. Besides, we find that this is not an isolated case in MOFs, as a similar phenomenon is also be found in some other MOFs [130].

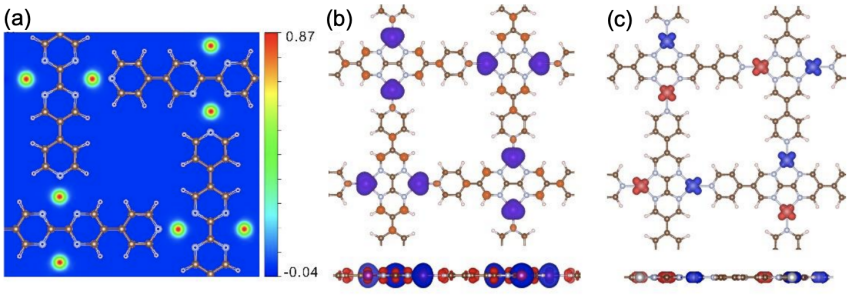

FIGURE 5.10: (a) The spin-polarized charge density distribution of Mn-PBP on the plane crossing the Mn atoms. The scale bar unit is e/bohr^3. The range is from -0.04 e/bohr^3 to 0.87 e/bohr^3 , which is different from Figure 5.9. Top and side view of spin-polarized charge density distribution of (b) FM Mn-PBP. Top and side view of spin-polarized charge density distribution of (c) AFM Fe-PBP. The purple and red colors represent major and minor spin, respectively and the isosurface value is 0.01 e/Å^3.

We should note that although there are some kind of RKKY exchange mechanism in Mn-PBP, the polarized spin is mainly localized at metal atoms, as shown in Figure 5.10 (a), which explains why we can use the atomic model to describe the effective spin interaction. We also compared the difference of spin polarization between the FM Mn-PBP and Stripe AFM Fe-PBP, and the results are shown in Figure 5.10 (b, c).

5.5 The influence of strain and chemical doping for Mn-PBP

Strain is a common way to regulate the electronic and magnetic properties of systems, and the modulation on the band structure of Mn-PBP is shown in Figure 5.11. The result shows that Mn-PBP changes from a ferromagnetic semiconductor to a semimetal when about 95% biaxial strain is applied. Besides, the strain can change the distance between Mn atoms and affect the exchange coupling constants, thus changing the Curie temperature. As shown in Figure 5.3, a 95% biaxial compressive strain can raise the Curie temperature from 105 K to 125 K.

The effect of electron and hole doping on the electronic structure of Mn-PBP is also investigated. As shown in Figure 5.12 (b), there is a tiny band gap with the spin-up polarized states below and above Fermi level, while the spin-down polarized states hold about 1 eV band gap. When the system is

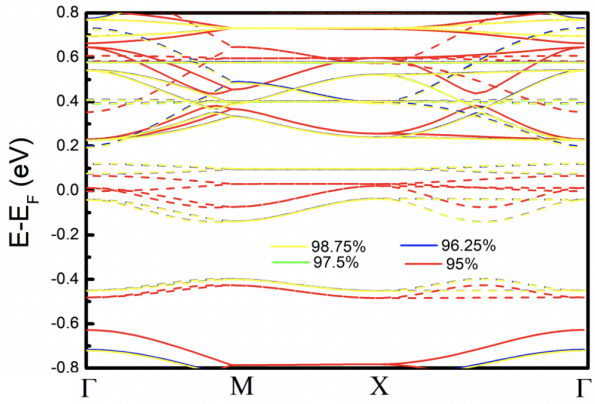

FIGURE 5.11: The band structures of Mn-PBP under different biaxial strains. The solid and dotted lines represent the spin-up and spin-down bands, separately. The corresponding lattice parameters are varying from 98.75% to 95% of the original lattice parameter, and they are represented with different colors. Obviously, 95% compression could close the band gap and turn Mn-PBP into a half metal.

doped with 1 hole/electron per unit cell (Figure 5.12 (c, d)), the Fermi level declines/rise and crosses the spin-polarized energy band. This gives rise to the half metal, in which spin-up electrons behavior as metal, while spin-down electrons act like semiconductor. According to this analysis, we proposed a spin-field-effect transistor (SFET) based on the Mn-PBP framework, and its schematic structure is declared in Figure 5.12 (a). Since electron/hole doping can be controlled by the substrate materials and gate voltage V_{gs}, controllable spin ON/OFF switch can be realized in Mn−PBP SFET and 100% spin−polarization carriers could be observed. While we acknowledge that the concept of SFET has been proposed more than 30 years ago [131], it's still complicated to realize the functional SFET for information processing. Therefore, the Mn-PBP is a promising material for future spintronic devices.

Besides, the electron and hole doping also influence the magnetic properties, and its increase on Curie temperature of Mn-PBP is shown in the inset of Figure 5.3.

5.6 Magnonic properties of Mn-PBP

In the field of spintronics, magnons play an important role. In this section, we investigate the candidate application of Mn-PBP in magnonics, which is considered as one of the pillars in modern spintronics. The linear spin-wave theory (LSWT) [52, 53] introduced in Chapter 2 is selected to calculate the magnon dispersion and magnonic transport properties. The Heisenberg-Dzyaloshinskii-Moriya interaction (DMI) model is utilized to describe the

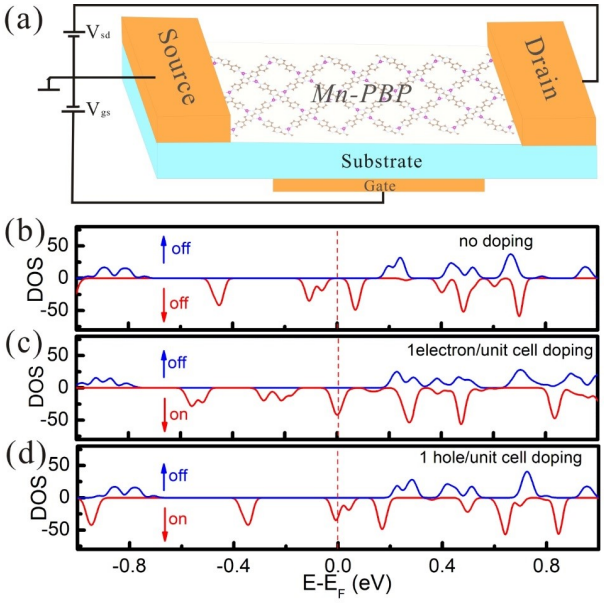

FIGURE 5.12: (a) The schematic of spin-field-effect transistor device based on Mn-PBP. (b) The total DOS of spin-up and spin-down electrons without electron/hole doping. The total spin-up and spin-down DOS with one (c) electron or (d) hole doping in one unit cell.

spin interactions in SSL, which has already been studied [132, 133]. The effective Hamiltonian is given as:

$$E_{\mathrm{mag}} = \sum_{\langle ij \rangle} J_1 \mathbf{S}_i \cdot \mathbf{S}_j + \sum_{\langle l,m \rangle} J_2 \mathbf{S}_l \cdot \mathbf{S}_m + \sum_{\langle lm \rangle} \mathbf{D}_{lm} \cdot (\mathbf{S}_l \times \mathbf{S}_m), \tag{5.5}$$

where J_1 and J_2 represent exchange interactions and we here select the same parameters obtained from our *ab initio* calculations based on the Ising model in Mn-PBP. The DMI is introduced in our Hamiltonian, which is represented by $\mathbf{D}_{lm}$ between the site l and m.

In our *ab initio* calculations, the spin-orbit coupling is ignored to simplify calculations, causing that the DMI is always zero. However, as shown in Figure 5.13 (a), the second-nearest-neighbor DMI can exist in Mn-PBP according to the symmetry of the structure. Inspired by the Ref. [132], the DMI vector is selected as out-of-plane (along the z-axis) with the clockwise chirality. The calculated magnon dispersion is shown in Figure 5.13 (b), where different colors correspond to different DMI magnitude values represented by D. We find that only the top two bands of the magnon spectrum are strongly influenced by the D value. Besides, compared to the electronic band structure

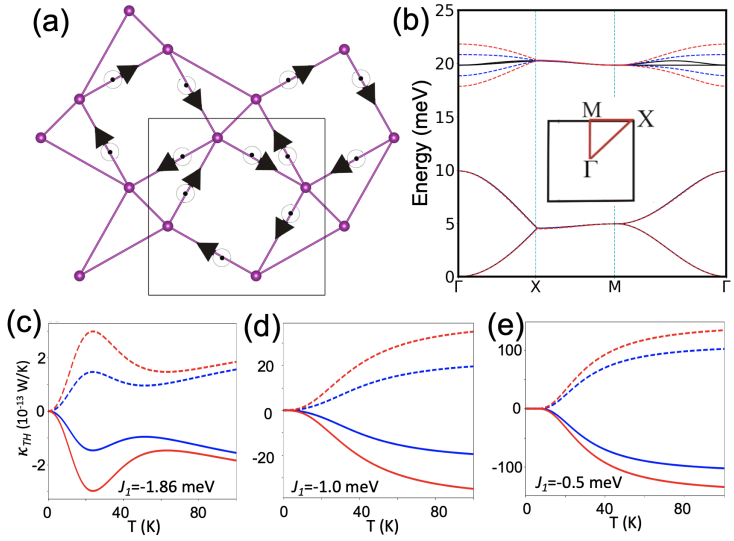

FIGURE 5.13: (a) The illustration of 2D Shastry-Sutherland lattice, where the Dzyaloshinskii-Moriya interactions (DMI) of the second nearest neighbor interaction is introduced. The DMI vector direction is out-of-plane with the clockwise chirality. (b) The spin-wave dispersion of Mn-PBP based on the linear spin-wave theory (LSWT). The exchange interaction J_1 and J_2 are chosen from the DFT calculation. The black, blue dotted, and red dotted line represent the results with DMI value D = $0J_2$, $0.2J_2$ and $0.4J_2$, separately. (c-e) The thermal Hall conductivity with the function of temperature, in which the influence of J_1 and DMI value on thermal Hall conductivity are compared. The blue dotted and red dotted line represent the result with DMI value $0.2J_2$ and $0.4J_2$, which are the same as parameters shown in (b), and here solid lines represent the result with opposite DMI value. In (c-e) the J_2 is chosen as -0.31 meV and J_1 is set with different values shown in the panel (c-e).

shown in Section 5.4, the magnon dispersion has a similar shape, which is due to the symmetry of the SSL.

The transverse 2D thermal Hall effect is investigated in Mn-PBP, and the calculated 2D thermal Hall conductivity κ_{TH} is shown in Figure 5.13 (c-e) according to Eq. (4.30). In Figure 5.13 (c-e), we show the relationship between κ_{TH} and temperature T, where the T is limited to 100 K referring to the calculated Curie temperature. We observe that the κ_{TH} is zero when the D is zero, and non-zero κ_{TH} can be realized by introducing a non-zero chirality provided by the second-nearest neighbor DMI. Additionally, through comparing the influence of DMI and J_1 on κ_{TH}, the κ_{TH} is strongly affected by the DMI and the exchange interaction. As displayed in Figure 5.13 (c-e), the κ_{TH} increases with the increasing of DMI or the reduction of J_1. We have demonstrated that the electronic properties can be modulated by the strain

or doping, which suggests that the exchange interaction can be controlled, leading to the modulation of magnonic transport properties. Furthermore, the corresponding 3D κ_{TH} can be obtained when choosing an effective thickness of 2D SSL based on the formula $\kappa_{\mathrm{TH}}^{xy} = \kappa_{\mathrm{TH}}/l$, in which l corresponds to the effective thickness and $\kappa_{\mathrm{TH}}^{xy}$ represents the transverse 3D thermal Hall conductivity. For instance, the estimated transverse 3D thermal Hall conductivity is about 10^{-3} W/mK when the l is selected as 5 Å, which is about the same order of magnitude in $Lu_2V_2O_7$[6].

5.7 Discussion

A family of 2D TM-PBP (TM= Cr, Mn, Fe, Co, Ni, Cu, Zn) MOFs with the SSL have been systematically studied by means of first-principles calculations and Monte Carlo simulations. It is observed that each TM atoms bond with its nearby three N atoms with asymmetric coordination bonds in the TM-PBP frameworks. Different magnetic arrangements have been investigated in TM-PBP frameworks, where the Mn-PBP framework holds the FM ground state with the Curie temperature of about 105 K which can be regulated by strain or chemical doping. Besides, TM-PBP (TM= Cr, Fe, Co, Ni) holds stripe AFM ground state, and TM-PBP (TM= Cu, Zn) possesses nonmagnetic properties. The band gap of TM-PBP ranges from 0.12eV to 0.87 eV. The Mn-PBP framework is found to be a half semiconductor with the band gap of less than 0.15 eV, caused by the novel low-symmetry coordination bonds with the hybridization of p_z orbital from C and N atoms in PBP molecules and d_{xz}, d_{yz} orbitals from Mn atoms. It is demonstrated that both strain and electron/hole doping can modulate the electronic properties of Mn-PBP, that can be transited from semiconductor to metal. The magnonic transport properties of Mn-PBP is investigated, indicating that the system holds non-trivial topological properties in the aspect of magnons. Moreover, as Cu-PBP and Fe-PBP systems have already been successfully synthesized, it will be promising to synthesize Mn-PBP and other 2D MOF TM-PBP in the near future. These novel properties indicate that TM-PBP frameworks have candidate applications in electronic devices, especially the Mn-PBP framework with the first predicted FM ground state with SSL in MOFs.

Chapter 6

Magnonic Weyl states in Cu_2OSeO_3

The Cu_2OSeO_3 is a multiferroic ferrimagnet with the ground state of helical spin order. Based on the linear spin-wave theory discussed in Chapter 2 and magnonic topology theory presented in Chapter 4, the best fit of the experimental magnons dispersion of Cu_2OSeO_3 is done in the presence of Dzyaloshinskii-Moriya interaction (DMI). It is predicted that two pairs of degenerate Weyl nodes with opposite topological charge are located at the high-symmetry points in the reciprocal space in the absence of DMI terms. However, the degeneracy of these Weyl nodes are lifted when considering the non-vanishing effect of the DMI in this material, and positions of Weyl points sensitively depend on the direction and magnitude of the DMI vector. Besides, the topologically protected magnon surface states are investigated and the magnonic contribution to the thermal Hall conductivity is estimated, which are strongly influenced by the DMI.

Results presented in this chapter have already been published:
Li-chuan Zhang, et. al., Phys. Rev. Research 2, 013063 2020.

6.1 Introduction of Cu_2OSeO_3

The cubic copper(II)-oxoselenite Cu_2OSeO_3 is a multiferroic ferrimagnet with a chiral crystal structure that attracts more and more researchers' attention due to the emergence of skyrmion order [134, 135, 136, 137, 138]. Its crystal structure is cubic (space group $P2_13$) with the lattice constant $a = 8.925$ Å [139]. As shown in Figure 6.1, each unit cell of Cu_2OSeO_3 has 16 magnetic Cu^{2+} ions, and the magnetic structure can be approximated as a distorted breathing-pyrochlore lattice, which is consisted of slightly deformed tetrahedral Cu_4 clusters in a face-centered cubic (fcc) arrangement [59]. Magnetic interactions within the tetrahedron lead to a ferrimagnetic ground state, in which one of the Cu^{2+} spins is antiparallel to the other three, resulting in the total spin $S = 1$ of the tetrahedron [140, 141]. Below the Curie temperature $T_C \approx 57$ K, the helical spin order is observed with a wave number $q \approx 0.01$ Å^{-1}, which corresponds to a modulation period of approximately 63 nm in the [001] direction [135].

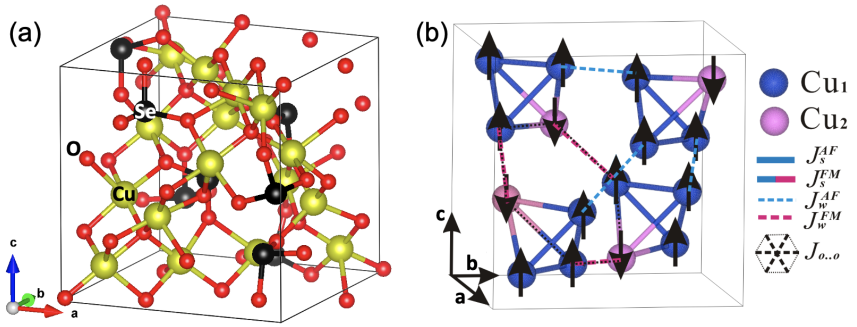

FIGURE 6.1: (a) The geometric structure of Cu_2OSeO_3 in the unit cell with Cu, Se, and O elements represented by yellow, black and red ball. (b) The magnetic structure of ferrimagnetic Cu_2OSeO_3 is shown together with five different interactions, marked by J_s^{FM}, J_s^{AFM}, J_w^{FM}, J_w^{AFM} and $J_{O..O}$, where $J_{O..O}$ represents the antiferromagnetic long-range interaction.

As shown in Figure 6.1 (b), every Cu^{2+} ion occupies two structurally nonequivalent positions, so that every Cu_4 tetrahedral cluster consists of one Cu(2) ion on the 4*a* Wyckoff site and three Cu(1) ions on the 12*b* site [139, 142]. The exchange interactions in Cu_2OSeO_3 have been systematically studied and up to 5 different interactions are considered [140, 57, 141, 143]. The proposed model is used to describe the inelastic neutron scattering (INS) spectrum of spin-wave excitations in a broad energy range and in the whole reciprocal space [59], as well as electron spin resonance (ESR) that probes spin-wave excitations at the zone center [144].

In more details, the strong superexchange coupling J_s^{FM} between the Cu(1) ions within the cluster are ferromagnetic (FM), whereas the Cu(1) and Cu(2) spins within the same tetrahedron are coupled antiferromagnetically with a coupling constant J_s^{AFM}. These exchange constants constitute the dominant magnetic interactions that lead to a ferrimagnetic spin arrangement within the cluster: three Cu(1) spins align ferromagnetically, and the Cu(2) spin is pointing in the opposite direction [145]. The intercluster interactions are considerably weaker, given by the FM superexchange J_w^{FM} between the nearest Cu(1) ions of neighboring clusters, the weak AFM coupling J_w^{AFM} between Cu(1) and Cu(2), and a longer-range exchange $J_{O..O}^{AFM}$ that connects Cu(1) and Cu(2) sites across the diagonals of alternating Cu(1)–Cu(2) hexagon loops [57].

The model, involving five different Heisenberg exchange interactions, provides a qualitatively good fit to the experimental spin-wave dispersion over the entire Brillouin zone (BZ) [59] with the exception of the zone corner (**R** point), where the magnon bands remain degenerate for any values of the exchange parameters. Tucker *et al.* [58] recently showed that this degeneracy is removed by Dzyaloshinskii-Moriya interaction (DMI), leading to a clearly resolved spin gap of ∼1.6 meV in the magnon spectrum, which they observed by neutron spectroscopy. These observations are a strong indication for the existence of topological magnon states in Cu_2OSeO_3, which motivated our

investigation in this chapter.

6.2 Magnon dispersion and model establishment of Cu_2OSeO_3

6.2.1 Experimental result and effective Hamiltonian

New accuracy experimental INS results are offered from Prof. Dmytro S. Inosov's group in TU Dresden, and more detailed measurements were utilized with cold-neutron triple-axis spectrometer PANDA [146] and the time-of-flight (TOF) spectrometer MAPS [147]. From the experimental result shown in Figure 6.2 (a, b), it is very clear that at $\mathbf{R}$ point there is a band gap of about 1.6 eV. The magnon spectrum of Cu_2OSeO_3 has been analyzed in several previous works, where similar parameters of exchange interactions are adopted and the DMI is ignored [57, 58, 59]. In this section, we use linear spin-wave theory (LSWT) [52, 53] to calculate the magnon spectrum of Cu_2OSeO_3, starting from the generalized Heisenberg model,

$$H = \sum_{\langle ij \rangle} \mathbf{S}_i^{\dagger} \hat{J}_{ij} \mathbf{S}_j, \tag{6.1}$$

where the interaction tensor between the lattice sites i and j

$$\hat{J}_{ij} = \begin{pmatrix} J_{ij}^x & D_{ij}^z & -D_{ij}^y \\ -D_{ij}^z & J_{ij}^y & D_{ij}^x \\ D_{ij}^y & -D_{ij}^x & J_{ij}^z \end{pmatrix}. \tag{6.2}$$

The interaction tensor $\hat{J}_{ij}$ includes the symmetric exchange $\mathbf{J}_{ij}$ and the antisymmetric off-diagonal DMI terms $\mathbf{D}_{ij}$, caused by the spin-orbit coupling. The DMI vector is defined as $\mathbf{D}_{ij} = (D_{ij}^x, D_{ij}^y, D_{ij}^z)$, and its value is discussed in the next section. Following earlier works [59], we include five Heisenberg exchange interactions shown in Figure 6.1 (b), with their numerical values listed in Table 6.1. As the total magnetization per tetrahedra satisfy $3\langle S_{\mathrm{Cu1}}^z \rangle + \langle S_{\mathrm{Cu2}}^z \rangle = 1$, we set the spin length of $\mathbf{S}_{\mathrm{Cu2}}$ as 0.45 and $\mathbf{S}_{\mathrm{Cu1}}$ as 0.4833 to get the best fitting results. To deal with the ferrimagnetic system, the rotation matrix O_i is used, introduced in Chapter 2.4.2, where O_i determines the magnetic moment direction at the site i.

Based on the LSWT, we first calculate the magnon dispersion without the DMI, and the obtained magnon dispersions are very close to previously published data, as shown in Figure 6.7. The results demonstrate that there are two doubly-degenerate crossing points among the lowest four magnon branches: one at $\mathbf{\Gamma}$ and one at $\mathbf{R}$ high-symmetry points. However, the results of high-resolution INS measurements, presented in Figure 6.2, clearly mark the formation of a 1.6 meV band gap at $\mathbf{R}$ with the eigenvalue around 10 eV. Therefore, the DMI is utilized to the effective spin Hamiltonian to reproduce the experimental results, and the corresponding magnonic topology in Cu_2OSeO_3 is investigated due to the introduction to DMI.

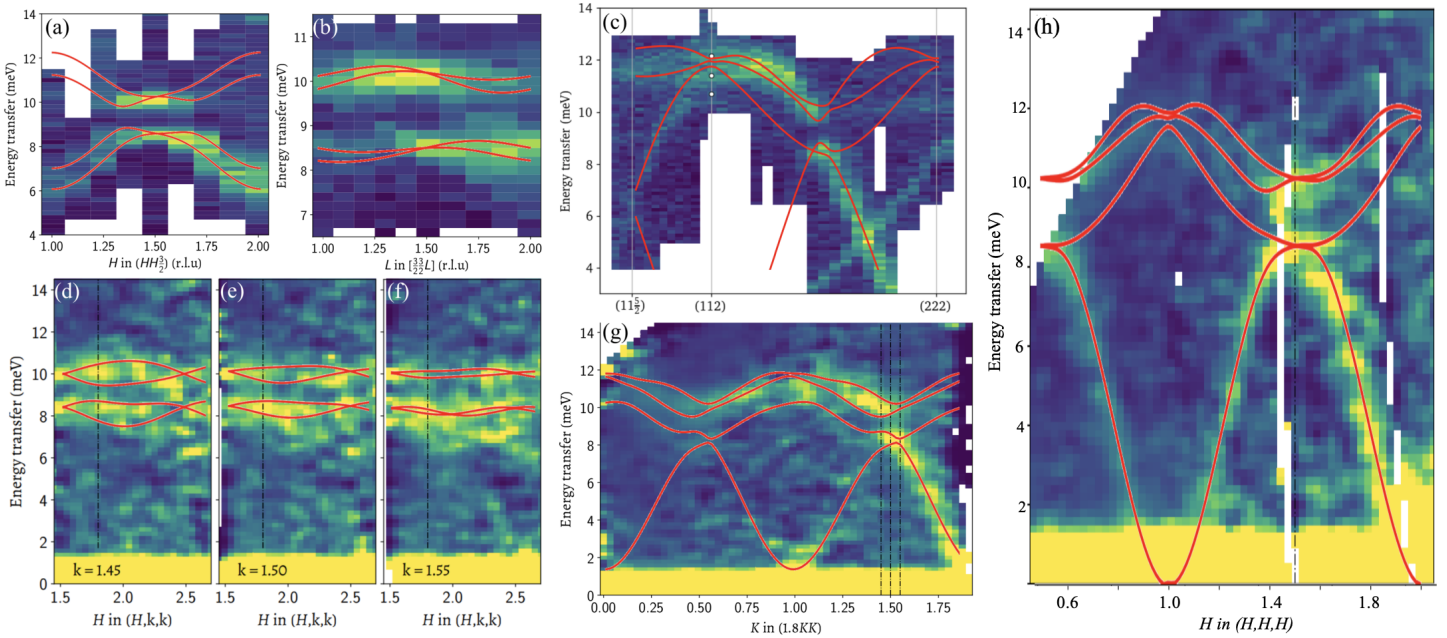

FIGURE 6.2: Momentum-energy cuts along (a) $(H\,H\,\frac{3}{2})$, (b) $(\frac{3}{2}\frac{3}{2}L)$, (c) $(1\,1\,L)-(H\,H\,2)$, (d) $(1.45\,K\,K)$, (e) $(1.5\,K\,K)$, (f) $(1.55\,K\,K)$, (g) $(1.8\,K\,K)$ and (h) $(H\,H\,H)$ directions in reciprocal space. All measurements were done at 2 K without applying magnetic field. Data in panels (a, b, c) were measured at the triple-axis spectrometer, while panels (d-g) are cuts from the TOF dataset, integrated within ± 0.1 r.l.u. in momentum directions orthogonal to the figure plane. The magnon dispersion calculated with the fitted value of the DMI is shown with thin red lines. The straight feature in the bottom-right corner of (c), which is not captured by the spin-wave model, is a spurious peak from nonmagnetic multiple scattering.

6.2.2 The DMI vector

The cubic Cu_2OSeO_3 has the B20 structure with the space group $P2_13$. Employing the symmetry operations, the positions of all Cu^{2+} ions can be obtained from the positions of the Cu(2) (u, u, u) and the Cu(1) (a, b, c) atom, where $u = 0.88557$, $a = 0.13479$, $b = 0.12096$, and $c = 0.87267$. Furthermore, global symmetries are related to the different bond directions of equivalent pairwise interactions. According to the Moriya's symmetry rules [26], the corresponding DMI vectors obey the same respective symmetry relations as the bond directions. The atomic positions, the bond directions, and the corresponding DMI vectors of the nearest neighbor interaction are listed in Table 6.2, the copper structure and the nearest neighbor interaction bonds are additionally visualized in Figure 6.3. Similarly, other kinds of interactions and DMI vectors can be obtained, but they are not listed here.

The DMI vectors can be acquired through *ab initio* calculation and experimental fitting. We tried both methods and the results are shown below.

DMI vector with *ab initio* parameters

As indicated in Eq. (6.1) and Eq. (6.2), considering five antisymmetric DMI vectors in the Hamiltonian, there are 15 additional parameters introduced, which is very hard to accurately fit them. In this section, we use 5 distinct *ab initio* DMI vectors which were reported by O. Janson *et al.* [Nat. Commun. **5**, 5376 (2014)]. As the Heisenberg interaction parameters from the *ab initio* results are similar to the results shown in Table 6.1, we fix the exchange interaction parameters to study the influence of DMI. The comparison between the theoretical result and the experimental data is shown in Figure 6.4, and four Dirac points between band 2 and band 3 were found in the first BZ. The results indicate that two doubly-degenerate crossing points split at $\mathbf{R}$ point, by utilizing the *ab initio* DMI parameters. However, the calculated magnon dispersion is not consistent with experimental results. We attribute this to an inherent flaw in the strong spin-orbit coupling system with *ab initio* calculation.

Parameters	Distance (Å)	J (meV) [59]	**D** (meV)
$J_{\mathrm{w}}^{\mathrm{FM}}$	3.039	-4.2	$(-0.491,\ 2.0,\ -1.41)$
$J_{\mathrm{s}}^{\mathrm{AFM}}$	3.057	12.3	0
$J_{\mathrm{s}}^{\mathrm{FM}}$	3.220	-14.5	0
$J_{\mathrm{w}}^{\mathrm{AFM}}$	3.300	2.33	0
$J_{\mathrm{O..O}}^{\mathrm{AFM}}$	6.350	3.88	0

TABLE 6.1: Values of the parameters entering the Heisenberg Hamiltonian Eq. (6.2). Five exchange interactions are listed together with the corresponding interatomic distances which are very similar to the previous works. The nearest-neighbor DMI vector was chosen so as to reproduce the experimental spin-wave dispersion.

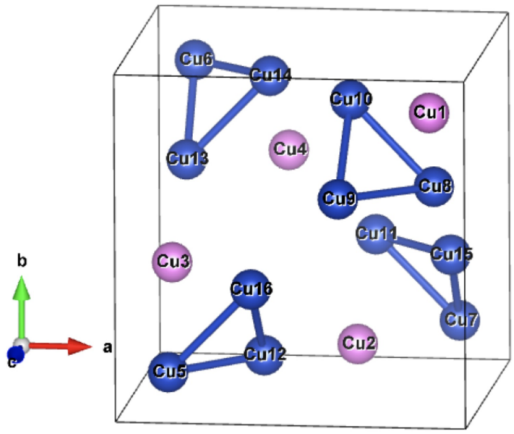

r_5, (a, b, c)
r_6, (b, c, a)
r_7, (c, a, b)
r_8, $(1-a, 0.5+b, 1.5-c)$
r_9, $(0.5+b, 1.5-c, 1-a)$
r_{10}, $(1.5-c, 1-a, 0.5+b)$
r_{11}, $(0.5+a, 0.5-b, 1-c)$
r_{12}, $(0.5-b, 1-c, 0.5+a)$
r_{13}, $(1-c, 0.5+a, 0.5-b)$
r_{14}, $(0.5-a, 1-b, -0.5+c)$
r_{15}, $(1-b, -0.5+c, 0.5-a)$
r_{16}, $(-0.5+c, 0.5-a, 1-b)$

FIGURE 6.3: The atomic positions of copper atoms in the unit cell of Cu_2OSeO_3. The blue lines represent the nearest neighbor bonds of Table 6.2. The position of Cu^{2+} ions are listed in the right side of picture with $a = 0.13479$, $b = 0.12096$, and $c = 0.87267$. The position of Cu1, Cu2, Cu3 and Cu4 are represented as: (u, u, u); $(1.5-u, 1-u, u-0.5)$; $(1-u, u-0.5, 1.5-u)$ and $(u-0.5, 1.5-u, 1-u)$ with $u = 0.88557$.

TABLE 6.2: The bond vector and the DMI vector for the nearest-neighbor interaction in Cu_2OSeO_3.

i	j	$\mathbf{R}_{ij}$	$\mathbf{D}_{ij}$
r_5	r_{12}	$(0.5-b-a, 1-c-b, 0.5+a-c)$	(D_x, D_y, D_z)
r_5	r_{16}	$(-0.5+c-a, 0.5-a-b, 1-b-c)$	$(-D_z, D_x, D_y)$
r_6	r_{13}	$(1-c-b, 0.5+a-c, 0.5-b-a)$	(D_y, D_z, D_x)
r_6	r_{14}	$(0.5-a-b, 1-b-c, -0.5+c-a)$	$(D_x, D_y, -D_z)$
r_7	r_{11}	$(0.5+a-c, 0.5-b-a, 1-c-b)$	(D_z, D_x, D_y)
r_7	r_{15}	$(1-b-c, -0.5+c-a, 0.5-a-b)$	(D_y, D_z, D_x)
r_8	r_9	$(-0.5+b+a, 1-c-b, -0.5-a+c)$	$(-D_x, D_y, -D_z)$
r_8	r_{10}	$(0.5-c+a, 0.5-a-b, -1+b+c)$	$(D_z, D_x, -D_y)$
r_9	r_{10}	$(1-c-b, -0.5-a+c, -0.5+b+a)$	$(D_y, -D_z, -D_x)$
r_{11}	r_{15}	$(0.5-b-a, -1+c+b, -0.5-a+c)$	$(D_x, -D_y, -D_z)$
r_{12}	r_{16}	$(-1+c+b, -0.5-a+c, 0.5-b-a)$	$(-D_y, -D_z, D_x)$
r_{13}	r_{14}	$(-0.5-a+c, 0.5-b-a, -1+c+b)$	$(-D_z, D_x, -D_y)$

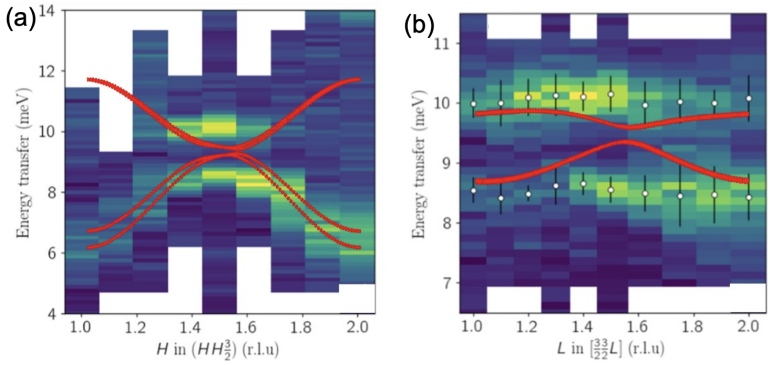

FIGURE 6.4: Momentum-energy cuts along (a) (110) and (b) (001) directions that cross at $(1.5, 1.5, 1.5)$. The red dotted lines represent the theoretical results using the referenced *ab initio* DMI vectors[141].

DMI vector with fitting

Alternatively, the DMI vectors can be obtained by fitting to the experimental magnon dispersion. In this section, we present how to obtain the DMI vector based on the experimental fitting. First, a set of representative points of experimental data are selected as the data base for the fitting. Subsequently, the Broyden-Fletcher-Goldfarb-Shanno (BFGS) Hessian update strategy is employed to converge the considered DMI vector. This procedure is executed separately for each DMI vector of the first 4 nearest neighbors given in Table 6.1. After few iteration steps, the first, second, third and fourth nearest DMI vectors converge to $(-0.458, 2.011, 0.565)$ meV, $(1.505, 6.143, 3.013)$ meV, $(0.262, 4.615, 1.236)$ meV and $(3.976, -2.484, -2.024)$ meV, respectively. The comparison of the magnon dispersion with different DMI vectors are shown in Figure 6.5, which points towards great accuracy when considering the first nearest neighbor DMI. We get the conclusion that including the nearest-neighbor DMI vector obtained from the experimental fitting can reproduce the experimental results.

However, the ground state of the system is the helical spin order, which is not included in the previous fitting. The nearest-neighbour DMI vector is refitted to realize the similar spin-spiral ground state, and the new DMI vector is obtained as $(-0.491, 2.0, -1.41)$ meV. As shown in Figure 6.6, we compare the total energy of different spin spiral states with different DMI vectors, and the minimum energy of the black line is located close to the $q = 0.01\,\text{Å}^{-1}$, which is the wave number observed from the experiment. Therefore, only the nearest-neighbor DMI vector with the fitted value $(-0.491, 2.0, -1.41)$ meV is introduced to the Hamiltonian in Table 6.1.

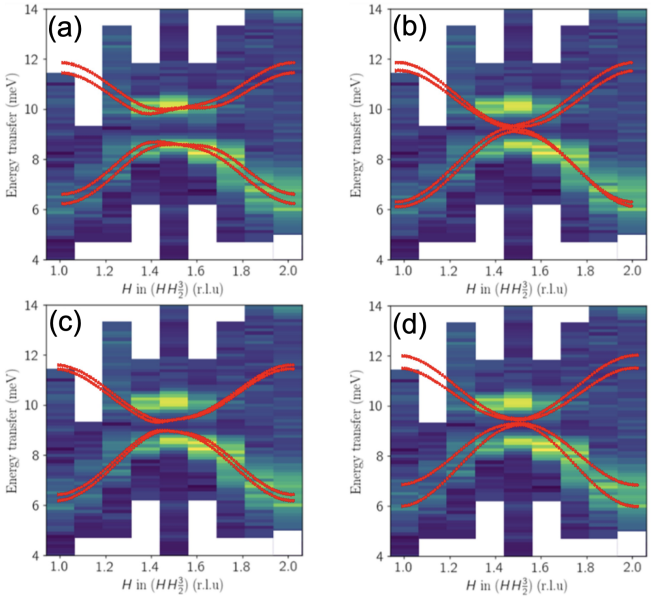

FIGURE 6.5: The comparison of fitted results to the experimental data. Panels (a)–(d) correspond to the results obtained when considering only the first, second, third, and fourth nearest-neighbor DMI vector, respectively.

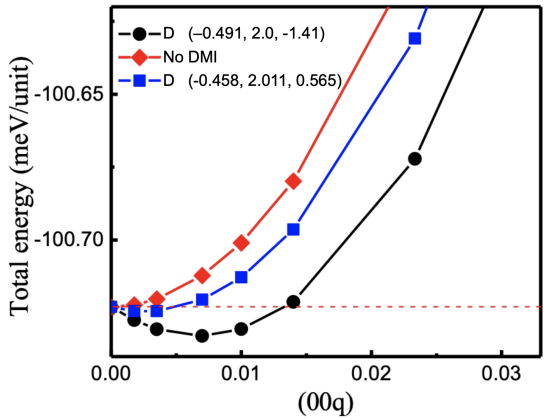

FIGURE 6.6: The comparison of the total energy of the system for the spin spiral calculation. During the simulation, the cone angles is selected as $\pi/2$. The calculation result with the fitted DMI vector $(-0.491, 2.0, -1.41)$ is almost consistent with the experimental result.

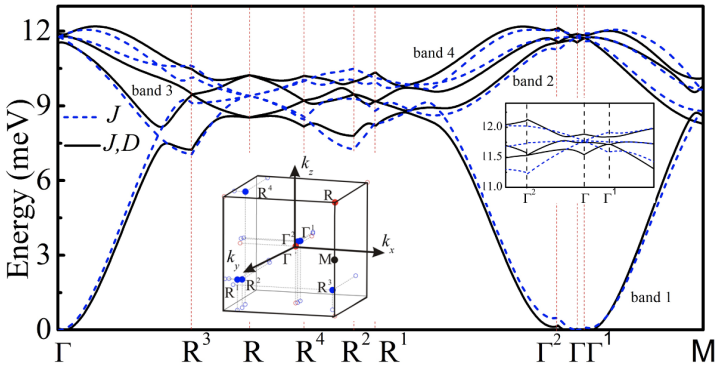

FIGURE 6.7: The magnon dispersion of the lowest four bands of Cu_2OSeO_3. The dotted blue line represents the dispersion without the effect of the DMI, with the Weyl points emerging at $\mathbf{R}$ and at $\mathbf{\Gamma}$. The black line represents the dispersion upon including the DMI, with six Weyl points emerging at $\mathbf{R^1}$, $\mathbf{R^2}$, $\mathbf{R^3}$, $\mathbf{R^4}$, $\mathbf{\Gamma^1}$ and $\mathbf{\Gamma^2}$. The exact positions of the Weyl points are shown in the inset: $\mathbf{R^1} = (-0.39, 0.47, -0.23)$, $\mathbf{R^2} = (-0.38, 0.34, -0.25)$, $\mathbf{R^3} = (0.40, 0.22, -0.33)$, $\mathbf{R^4} = (-0.40, 0.18, 0.49)$, $\mathbf{\Gamma^1} = (0.01, -0.03, 0.04)$, $\mathbf{\Gamma^2} = (0.01, -0.11, 0.03)$.

6.2.3 Magnon dispersion from the LSWT

The magnon dispersion is studied based on the LSWT, and the effect of DMI on the magnon dispersion is explored, shown in Figure 6.7. Irrespective of its exact choice, including the DMI into the picture has a drastic effect on the number and position of the degenerate crossings between bands 2 and 3 in the magnonic band structure, while the position of these degenerate crossings at high symmetry points without the DMI is enforced by the crystal symmetry. The set of DMI parameters we used here (see Table 6.1), splits previously degenerate crossing points at $\mathbf{\Gamma}$ and $\mathbf{R}$, giving rise to overall six crossings: two at $\mathbf{R^3}$ and $\mathbf{R^4}$ (in the vicinity of $\mathbf{R}$), two at $\mathbf{\Gamma^1}$ and $\mathbf{\Gamma^2}$ (in the vicinity of $\mathbf{\Gamma}$) and one additional pair of new crossing points at $\mathbf{R^1}$ and $\mathbf{R^2}$, see Figure 6.7. Given state-of-the-art experimental conditions, it is difficult to obtain the neutron scattering evidence (*e.g.*, in terms of characteristic intensity pattern) for the predicted crossing points from the experiment, which can be partly attributed to their asymmetric positioning in the BZ and the respective necessity of scanning through the directions which contain them. However, given the excellent agreement between theory and experiment in Figure 6.2, we are confident that our theoretical model reproduces the magnonic spectrum of Cu_2OSeO_3 throughout the whole BZ well and that the degeneracy points predicted by the model can be eventually resolved experimentally in the future. In the next subsection, we analyze the topological character of these points.

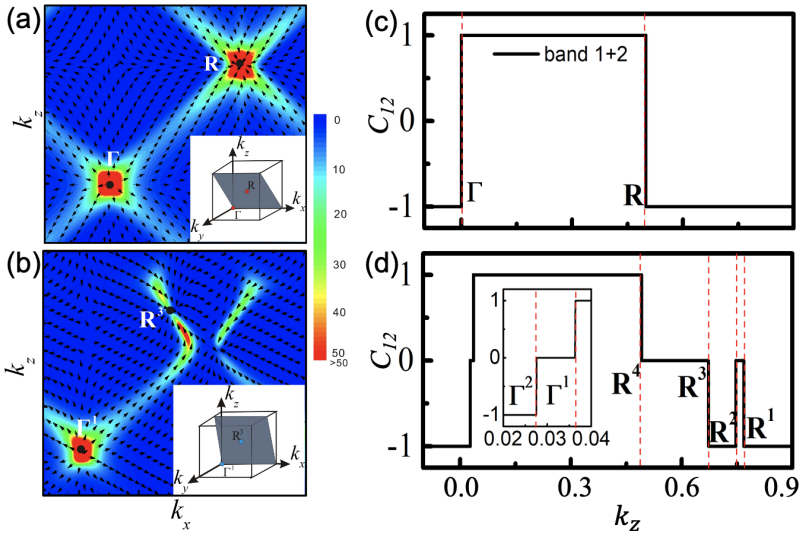

FIGURE 6.8: (a,b) Monopole distribution of the absolute magnitude of the Berry curvature corresponding to two lowest magnon bands in the k-planes marked in the inset. In (a), the DMI was not taken into account, while (b) shows the result with the DMI included. The k-planes are chosen so that they include the Weyl points. (c, d) The evolution of the Chern number as a function of k_z. Here, the Chern number C_{12} refers to the total Chern number of band 1 and band 2. The (c) and (d) panels display the result without and with the DMI effect, respectively. The inset in (d) is the zoom into the region around $k_z = 0.03$.

6.3 Topological properties of Cu_2OSeO_3

6.3.1 Magnonic Weyl states

The magnon berry curvature is calculated to investigate the magnonic topology, based on Eq. (6.3).

$$\mathbf{\Omega}_n(\mathbf{k}) = -\sum_{m\neq n} \frac{\mathrm{Im}\left[\langle V^L_{n\mathbf{k}}|\partial_{\mathbf{k}}\hat{D}(\mathbf{k})|V^R_{m\mathbf{k}}\rangle \times \langle V^L_{m\mathbf{k}}|\partial_{\mathbf{k}}\hat{D}(\mathbf{k})|V^R_{n\mathbf{k}}\rangle\right]}{(\epsilon_{n\mathbf{k}} - \epsilon_{m\mathbf{k}})^2}, \tag{6.3}$$

where $\epsilon_{m\mathbf{k}}$ and $\epsilon_{n\mathbf{k}}$are the magnonic eigenvalues. $\hat{D}$ is the dynamical matrix discussed in Chapter 2 and V_{R} and V_{L} represent the right and left eigenstates. As we mainly focus on the topological nature of the band crossings arising between bands 2 and 3, we analyze the cumulative Berry curvature of the bands 1 and 2. In Figure 6.8 (a) we present the direction of the normalized projected cumulative Berry curvature vector field and its absolute magnitude in the $k_y = k_z$ plane, first for the case without DMI. In the mentioned figure, the color scale represents the absolute value of the Berry curvature vector

field. As apparent from the figure, the Berry curvature distribution exhibits two monopole-like features at $\mathbf{R}$ and $\mathbf{\Gamma}$, where the band crossings occur, with the crossing at $\mathbf{\Gamma}$ serving as a source, and the crossing at $\mathbf{R}$ serving as a sink of the Berry curvature field. The corresponding distribution, obtained after including the DMI, is shown in Figure 6.8 (b) in the plane which includes $\mathbf{\Gamma^1}$ and $\mathbf{R^3}$ points and which is perpendicular to the k_y-k_z plane. In the latter case the distribution of the Berry curvature field, although similar to the previous case, is more complex, owing to the fact that the crossings at $\mathbf{\Gamma^2}$, $\mathbf{R^1}$, $\mathbf{R^2}$ and $\mathbf{R^4}$ are very close to the plane.

Next, we compute the monopole charge of the ith band crossing by evaluating the flux of the cumulative Berry curvature field through an infinitesimal sphere S_i surrounding the crossing:

$$Q_i = \frac{1}{2\pi} \int_{S_i} \mathbf{\Omega}(\mathbf{k}) \cdot \mathbf{n} \, dS_i, \tag{6.4}$$

where $\mathbf{n}$ is the surface normal. According to our calculations, without the DMI, the total topological charge of the two degenerate points at $\mathbf{\Gamma}$ is $+2$, while it constitutes a value of -2 at $\mathbf{R}$. Upon including the effect of the DMI, each of the double degeneracies splits into two nondegenerate points with charges of $+1$ at $\mathbf{\Gamma^1}$ and $\mathbf{\Gamma^2}$, and -1 at $\mathbf{R^3}$ and $\mathbf{R^4}$. Meanwhile, a pair of newly emerging degeneracies have the monopole charge $+1$ and -1 at $\mathbf{R^2}$ and $\mathbf{R^1}$ points, respectively.

The topological analysis is further supported by the BZ evolution of the first Chern number, defined analogously to the charge as: $C(P) = \frac{1}{2\pi} \int_P \mathbf{\Omega}(\mathbf{k}) \cdot \mathbf{n} \, dP$ where P is a two-dimensional slice of the BZ and $\mathbf{n}$ is its normal vector. By defining the plane P as the k_x-k_y plane at a given k_z with $\mathbf{n} = (0, 0, 1)$, we compute the evolution of $C(k_z)$ as a function of k_z, presenting the results in Figure 6.8 (c, d). Without DMI, the Chern number changes by 2 when P passes through the degenerate crossing points, while in the presence of DMI it changes by 1 when P passes through every nondegenerate crossing point. This analysis underlines the main finding of this chapter — the emergence of two doubly degenerate type-I Weyl points [148] in the magnonic structure of Cu_2OSeO_3, located at $\mathbf{R}$ and $\mathbf{\Gamma}$ without DMI, which further split into overall four Weyl points when the symmetry of the system is reduced by including the DMI into consideration, while the latter additionally drives an emergence of a new pair of Weyl points near $\mathbf{R}$.

6.3.2 Surface states

As the emergence of the Weyl points in the magnonic band structure of a three-dimensional crystal is expected to give rise to the surface states of a thin film, here, we analyze the magnon band structure of a 75-layer thick two-dimensional slab of Cu_2OSeO_3 cut along the [001] axis, presenting the results in Figure 6.9. The spin-wave dispersion is shown along the path which includes the projections of the Weyl points onto the (001)-plane, which are further indicated with red and blue small circles in the figure, according to their topological charge. In the magnon band structure, the states are marked

with their weight at the surface of the slab, which is represented by different color scales. Here, the color scale is calculated based on the equation:

$$LW(\mathbf{k}, j) = \sum_i V_{\mathrm{L}}^i(\mathbf{k}, j) V_{\mathrm{R}}^i(\mathbf{k}, j)(R_z^i - 0.5), \tag{6.5}$$

where $\mathbf{k}$ is the reciprocal space vector, j denotes the band index, i numbers the magnetic atom, and R_z^i represents the normalized position for atom i along the z-axis. $V_{\mathrm{L}}^i(\mathbf{k}, j)$ and $V_{\mathrm{R}}^i(\mathbf{k}, j)$ are the components of the left and right eigenstates of jth magnon branches at the magnetic atom i. The Eq. (6.5) provides a reasonable measurement to judge the surface character of each state. However, as shown in Figure 6.9 (a), surface states at about 9.2 meV along $\overline{\Gamma Y}$ and $\overline{YR}$ appear to loose and regain their surface character without contact to bulk states, which is highly unusual. This issue is resolved by Figure 6.9 (d), which shows the real-space decomposition of one of these apparent bulk states at the $\mathbf{Y}$ point. That state exhibits highly localized contributions on both surfaces but none in the bulk, hence the degenerate states are indeed highly localized at the surfaces. Accordingly, Eq. (6.5) is unable to classify such states equally localized on both surfaces. This justifies the assumption that the other apparent bulk states along that high symmetry line are of surface character as well. Numerically, the origin of the surface character concealment is the exact energetic degeneracy which causes unsuitable eigenstate superpositions.

Figure 6.9 (a) corresponds to the situation without the DMI, with projections of the Weyl points positioned at high symmetry points in the two-dimensional BZ. We observe that in this case the Weyl points of opposite chirality are connected by the magnon "arc" surface states, which is in accord with our topological analysis in Section 6.3.1. Additional analysis of the surface magnon arcs with the cut energy 9.25 meV is given in Figure 6.9 (c), visualizing clear arcs connecting the projected Weyl point to bulk states. Upon including the effect of the DMI, the Weyl points split, and their projections move to the $\mathbf{\Gamma^1}$, $\mathbf{R^3}$, $\mathbf{\Gamma^2}$ and $\mathbf{R^4}$ points. Meanwhile, one pair of Weyl points appear in $\mathbf{R^1}$ and $\mathbf{R^2}$ points. Again, this is consistent with the previous analysis of the topological charges: while the points of the same charge are not connected by the surface states, the points of opposite chirality are.

6.4 Thermal Hall conductivity

In Cu_2OSeO_3, the thermal Hall effect of magnons is the generation of a transverse thermal Hall voltage under an applied longitudinal temperature gradient due to the presence of the DMI [6, 149]. The energy-dependent contribution to the ij'th Cartesian component of the thermal Hall conductivity tensor $\hat{\kappa}$ is given by:

$$\kappa^{ij}(\epsilon) = -\frac{k_{\mathrm{B}}^2 T}{(2\pi)^3 \hbar} \sum_n \int_{\mathrm{BZ}} \delta(\epsilon_{n\mathbf{k}} - \epsilon)\, C_2(f_n^{\mathrm{B}})\, \Omega_n^{ij}(\mathbf{k})\, d\mathbf{k}, \tag{6.6}$$

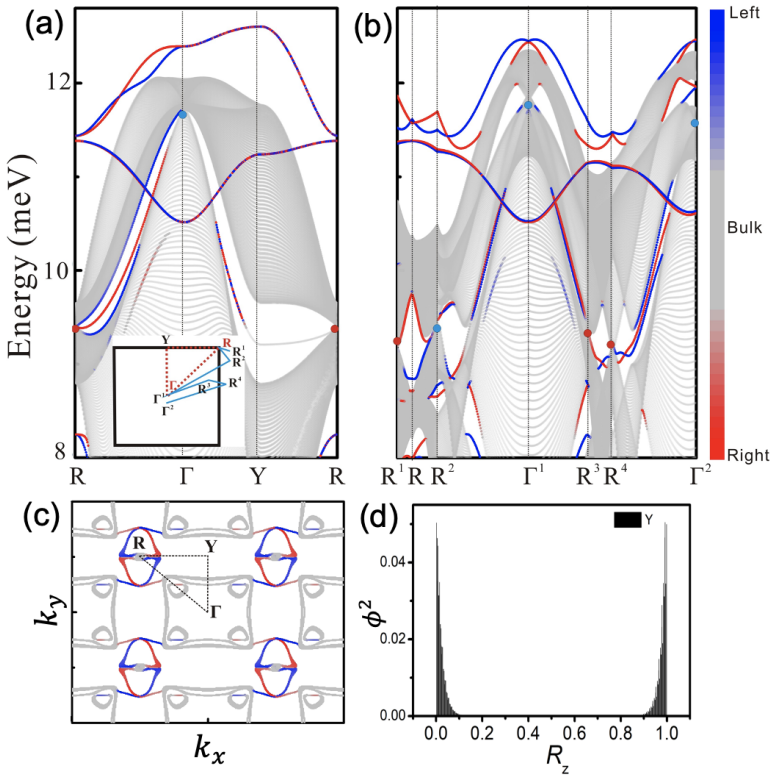

FIGURE 6.9: (a, b) The surface magnon band structure of the 75-layer thick slab of $Cu_2OSeO_3(001)$ along the paths indicated in the inset shown on the (a) without the DMI, and on the (b) including the DMI. The special points $\mathbf{\Gamma}$, $\mathbf{R}$, $\mathbf{\Gamma^1}$, $\mathbf{R^1}$, $\mathbf{\Gamma^2}$, $\mathbf{R^2}$, $\mathbf{R^3}$ and $\mathbf{R^4}$ are the projections of the Weyl points onto the (001) plane, which are indicated with red (positive charge) and blue (negative charge) solid circles. The color scale represents the weight of the magnonic wave function along with the slab. (c) The surface arcs calculated without DMI effect for the selected energy of 9.25 meV. (d) The real-space distribution of the weight of the state at $\mathbf{Y}$-point shown in (a) with the energy of about $9.2\,$meV. Here, the R_z refers to the z-component of the atomic position represented with fractional coordinates.

where n enumerates the magnon bands, f_n^{B} is the Bose distribution function, which can be expressed as $f_n^{\mathrm{B}} = (e^{\epsilon_{n\mathbf{k}}/k_{\mathrm{B}}T} - 1)^{-1}$, and C_2 is given by

$$C_2(x) = (1+x)\left(\ln\frac{1+x}{x}\right)^2 - \ln^2 x - 2\mathrm{Li}_2(-x), \tag{6.7}$$

with Li_2 denoting the dilogarithm function. The thermal Hall conductivity tensor of the system is then defined as $\kappa^{ij} = \lim_{\mu\to\infty}\kappa_\mu^{ij}$, where $\kappa_\mu^{ij} =$

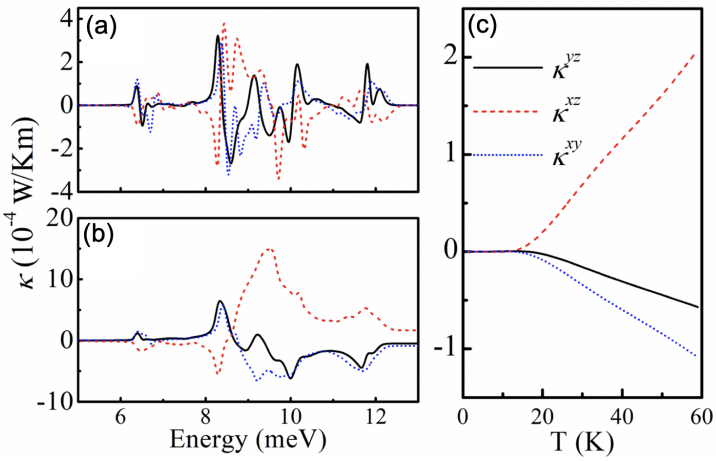

FIGURE 6.10: Components of the thermal Hall conductivity tensor in Cu_2OSeO_3. Energy-dependent (a), and cumulative (b) thermal Hall conductivity computed at 60 K. (c) The temperature dependence of the thermal Hall conductivity.

$\int_0^\mu \kappa^{ij}(\epsilon)\, d\varepsilon$ is the cumulative thermal Hall conductivity.

From the experiment, we know that the Curie temperature of Cu_2OSeO_3 is around $60\,\mathrm{K}$ [141, 58]. The computed energy-dependence and the cumulative components of the thermal Hall conductivity, calculated according to Eq. (6.6) at 60 K, are shown in Figure 6.10 (a, b). In these plots, we observe that there is a significant enhancement especially in the κ^{xz} component of the thermal Hall conductivity in the energy region between 8 and 10 meV. This enhancement can be attributed to the distribution of the Berry curvature around the Weyl points in that energy region, which correspondingly gives rise to the fingerprint of the Weyl points in the energy distribution of the thermal Hall effect. Since the Weyl-point enhancement is most prominent for the κ^{xz} component, the overall value of the thermal Hall conductivity for this component is by far dominant over the other two components at 60 K, see Figure 6.10 (c), where the thermal Hall conductivity as a function of temperature is shown. As magnons obey the Bose distribution, and the low-lying states are thus responsible for the thermal Hall effect at low temperatures, the characteristic zero-plateau in κ observed in Figure 6.10 (c) is the consequence of the vanishing contribution by the "topologically-trivial" low-lying bands which are basically not affected by the DMI, (Figure 6.7). Respectively, the thermal Hall effect "lifts off" once the region of Weyl points is reached by the distribution of magnons. The overall magnitude of the thermal Hall effect that we predict in the region of higher temperatures can reach as much as $2 \times 10^{-4}\,\mathrm{W/Km}$, which is large enough to be observed in experiments [6, 149].

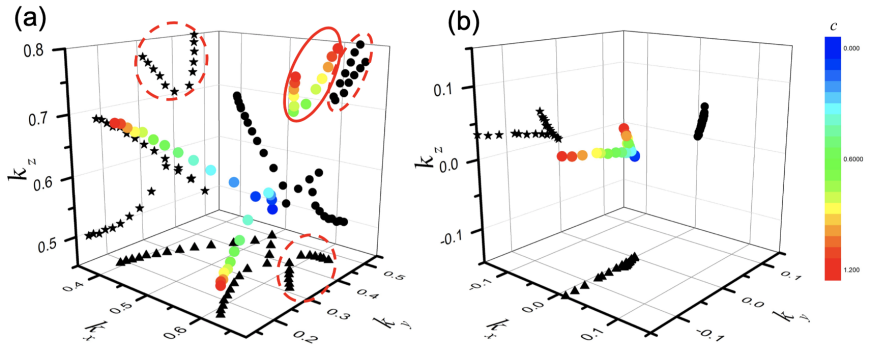

FIGURE 6.11: The evolution of the Weyl points near **R** (a) and **Γ** (b) as a function of the DMI strength, with the DMI vector following $D = c(-0.491, 2.0, -1.41)$ meV, where the coefficient c represented by the color scale is chosen from 0 to 1.2. The red circle marks a new pair of Weyl points, and their projections are circled by red dotted circles.

6.5 Effect of the DMI on Weyl points and thermal Hall conductivity

6.5.1 Effect of DMI on Weyl points position

Given the low structural symmetry of Cu_2OSeO_3, it is reasonable to explore the influence of the DMI vector on the position of the Weyl points in the BZ. While we envisage that the tuning of the DMI parameters can be realized *e.g.*, by pressure, strain, electric field [150, 151, 152, 153], or doping with defects, knowing the correlation between the Weyl point geometry and the DMI provides a unique tool for accessing the details of the DMI in a given sample, which are challenging to extract with other techniques based on *e.g.*, measuring the properties of domain walls [154, 155].

To estimate the influence of the DMI on the Weyl points, we first keep the direction of the DMI along the fitted DMI direction, while scaling its magnitude following $D = c(-0.491, 2.0, -1.41)$ meV, (c is the coefficient represented by the color scale in Figure 6.11 (a,b)). The evolution of the Weyl points around **R** and **Γ** upon increasing the DMI is shown in Figure 6.11 (a) and (b) separately. Notably, upon starting from a degenerate case at zero DMI, the splitting between the two Weyl points is clearly driven by lowering of symmetry upon including the non-vanishing DMI. When the value of the coefficient c continues to increase and eventually approaches 0.5, a new pair of Weyl points appears near the **R** point, which is indicated by the red circle.

Further, after fixing the magnitude of the DMI to the value of 1meV, we rotate the direction of the nearest neighbor DMI vector, as specified by angle θ, about the x, y and z-axis, and track the position of two Weyl points around **Γ** and **R** in Figure 6.12, respectively. The results indicate that the Weyl points

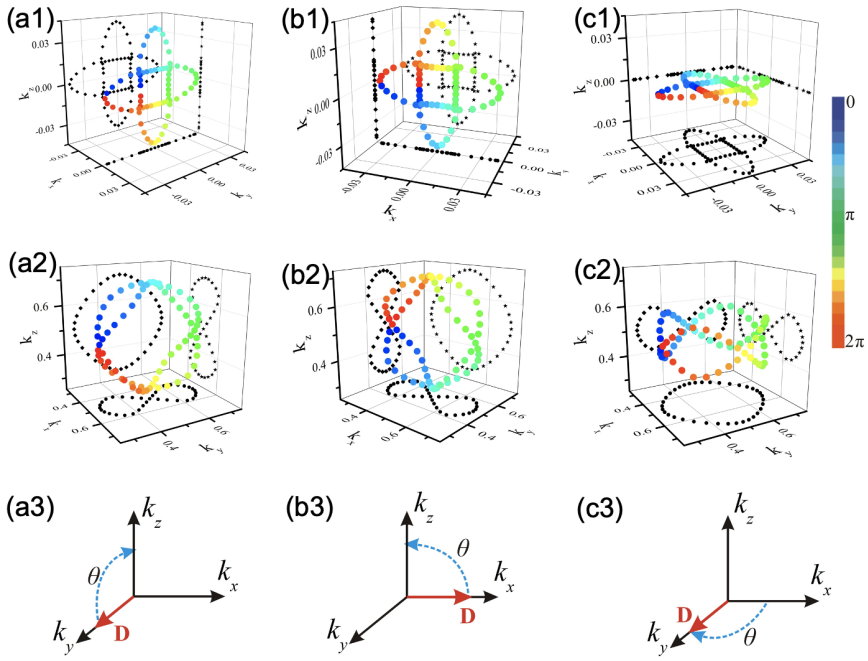

FIGURE 6.12: The effect of the DMI on Weyl point positions. Only the nearest DMI was taken into account and the positions of Weyl points were drawn separately near the **R** (a2, b2, c2) point and **Γ** (a1, b1, c1) points. (a,b,c) corresponds to the rotation of the DMI vector around x, y and z axes with the initial vector along [010] (a3), [100] (b3) and [010] (c3). The projection of each Weyl point onto the k_x-k_y, k_x-k_z and k_y-k_z planes is shown with black symbols in the corresponding planes. The color map represents the value of θ in the range from 0 to 2π.

rotate around the **R** and **Γ** points along specific paths when following the rotation of the DMI vector. The corresponding trajectories, while having a relatively complex shape in the three-dimensional BZ, clearly possess a high degree of symmetry, as apparent from the projections of the trajectories onto the high-symmetry planes, see *e.g.*, Figure 6.12 (a1–c1) and (a2–c2).

6.5.2 Effect of DMI on thermal Hall conductivity

In addition, to systematically investigate the influence of DMI on the magnonic topology, we also address the relationship between the thermal Hall effect and the DMI. To do this, under the premise of ensuring the agreement with the experimental magnon dispersion, the magnon dispersion, and thermal Hall conductivity are calculated for a different choice of the DMI vector, which gives rise to 4 Weyl points. As we show in Figure 6.13, the magnon dispersion can be fitted very well with the DMI vector $(-0.458, 2.011, 0.565)$.

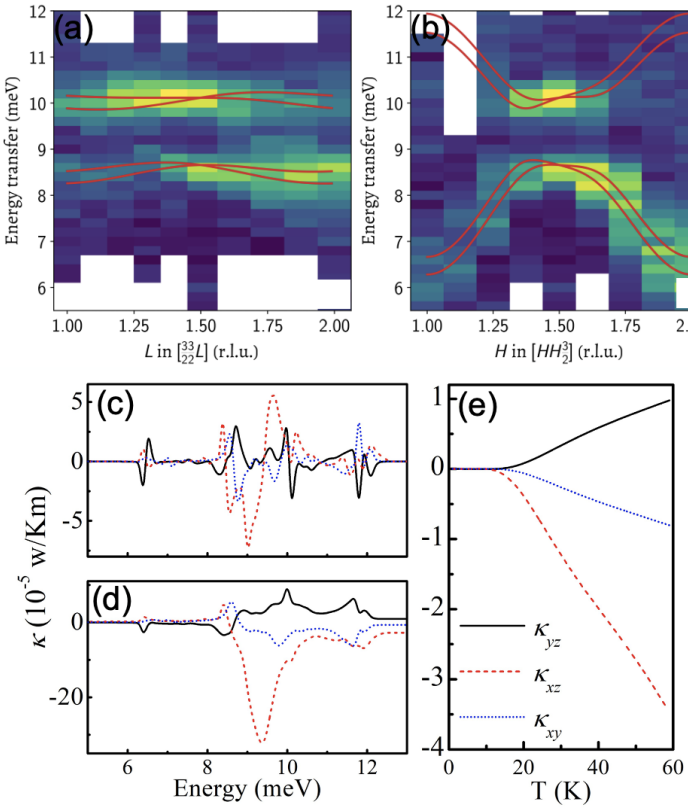

FIGURE 6.13: Momentum-energy cuts along (a) $(HH\frac{3}{2})$, (b) $(\frac{3}{2}\frac{3}{2}L)$, and the first two cuts are centered a the $\mathbf{R}(\frac{3}{2}\frac{3}{2}\frac{3}{2})$ point. The magnon dispersion calculated with the nearest-neighbor DMI vector $(-0.458, 2.011, 0.565)$ meV is shown with thin red lines. The Energy-dependent and cumulative thermal Hall conductivity calculated at 60 K are shown in (c, d), separately. The temperature dependence of the thermal Hall conductivity is shown in (e). During the calculation, the nearest-neighbor DMI is selected as $(-0.458, 2.011, 0.565)$ meV for (c-e).

However, the magnitude of the thermal Hall conductivity is about one order smaller than the one discussed above. These results suggest that the thermal Hall conductivity in this compound is directly related to the Weyl points modulated by the microscopics of the DMI.

6.6 Discussion

In this chapter, based on the LSWT and experiment, several important findings concerning the magnonic properties of Cu_2OSeO_3 are obtained. On the one hand, we can attribute the origin of the experimentally observed

magnon band gap in the spin-wave spectrum at the **R** point to the effect of the DMI, which is chosen so as to provide the best fit to the high-resolution neutron scattering data. On the other hand, after systematically addressing the topological properties of Cu_2OSeO_3, we reveal the emergence of the doubly-degenerate Weyl nodes with topological charge ± 2 at high-symmetry points even without the effect of the DMI. We further predict that not only each Weyl point splits into two but also one pair of Weyl points appears near **R** point, as the symmetry of the system is reduced when bringing the DMI into play. The proximity of several bands makes it difficult to resolve the bands forming the Weyl crossing point from the other two modes, yet from the overall agreement of the calculations with the experimental measurements one can conclude that our proposed fitting parameters must be valid within the present accuracy of the experiment. Moreover, we find that the position and number of the Weyl points can be controlled by changing the details of DMI. We further predict that the emergence of the Weyl points in the system goes hand in hand with the formation of topological magnonic surface states, which can be observed for instance at the (001) surface of Cu_2OSeO_3.

These findings open a quest for experimental observation of the Weyl points in this material, and exploring the influence of such points in the magnon spectrum on various properties of more complex magnetic phases in Cu_2OSeO_3, for example, its skyrmion phase. While we discover that Weyl points play a crucial role in shaping the magnitude and temperature dependence of the thermal Hall effect in its ferrimagnetic phase, we expect that the same holds true also for skyrmions in Cu_2OSeO_3. The observation of the exact position of the Weyl points as well as following their dynamics upon structural reconstructions in Cu_2OSeO_3 can further provide a unique tool for accessing the microscopics of the DMI in this complex compound, which can be of paramount importance for understanding and shaping of chiral dynamics and properties of Cu_2OSeO_3. The latter finding also suggests that in special materials of Cu_2OSeO_3 type one can expect that the topologies in the space of magnons and the real-space of skyrmions can be closely intertwined.

Chapter 7

The interplay of Kitaev interactions and Dzyaloshinskii-Moriya-interactions

In magnets, the Dzyaloshinskii-Moriya interaction and the anisotropic exchange interaction respected by Kitaev interaction can coexist. However, it is a challenge to distinguish their magnitude separately, as both of them may hold similar magnon dispersion. In this chapter, we demonstrate that it can be done by accessing magnonic transport properties and magnetic field response. Based on our proposed strategy, the spin interactions in $CrSiTe_3$ and $CrGeTe_3$ are predicted and their candidate applications in magnonics are explored.

Results presented in this chapter have already been published:
Li-chuan Zhang, et. al., Physical Review B 103, 1344142021, 2021.
Fengfeng Zhu, Li-chuan Zhang, et. al., Science Advance 7(37), eabi7532, 2021.

7.1 The Kitaev interaction in magnets

As presented in Section 2.3.3, the Kitaev interaction has been theoretically investigated in triangle, honeycomb and kagome lattice [43, 42, 44], and the layered magnetic materials with anisotropic Kitaev-type of spin interactions, such as iridates A_2IrO_3 (A=Li; Na) [45, 156, 157, 158], α-$RuCI_3$ [159, 42] or CrI_3 [54], are attracting an ever-increasing attention owing to their potential applications in topological quantum computing and spintronics [160, 73]. Similar to the Dzyaloshinskii-Moriya interaction (DMI) - another pivotal interaction in the realm of magnetic materials – the Kitaev interaction is originated from the spin-orbit coupling, and it has been shown that both interactions can coexist in one material [161, 162, 163].

Practically, one of the natural ways to address the properties of Kitaev interaction in a specific material lies in measuring and analyzing the magnon spectra, which directly reflect the interplay of spin interactions in the system with magnetic anisotropy and an external magnetic field [164, 165, 166]. However, it is known that similar magnon properties in terms of magnon band dispersion can be realized by either Kitaev or DMI in honeycomb ferromagnets such as *e.g.*, CrI_3 [25, 167]. This makes the magnonic detection of the

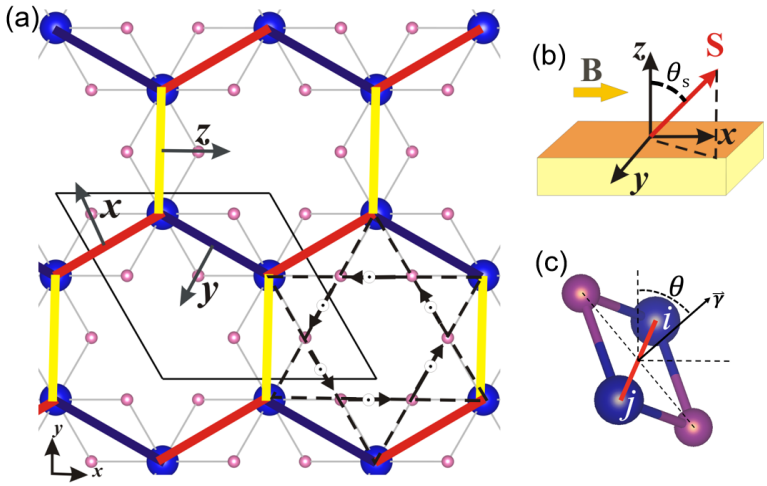

FIGURE 7.1: (a) Sketch of the structure of honeycomb CrI_3 monolayer. The unit cell is outlined with a thin black line, where blue balls represent Cr^{3+} ions and pink balls are iodide ions. The Kitaev bonds x (red), y (dark blue), z (yellow) are indicated with thick colored lines. The arrows mark the second-nearest-neighbor bond orientations along black dotted lines that share a common sign of out-of-plane DM vector. (b) Schematic diagram of the influence of an in-plane magnetic field $\mathbf{B}$ on the spin direction $\mathbf{S}$ whose polar angle is defined as θ_s. (c) The perspective view of Cr_2I_2 plane, where its normal vector is marked as $\hat{\gamma}$ and the Kitaev angle is defined as the polar angle of $\hat{\gamma}$.

Kitaev interaction ambiguous, and calls for refining the measurement protocol for bringing to light the magnitude and symmetry of the exotic Kitaev exchange.

The phase diagram of the Kitaev-DMI model has been studied in the past, and the distinction between the gapped and gapless phases of this model has been shown to be possible to draw by referring to thermal Hall effect measurements [11]. In order to distinguish whether the system is DMI or Kitaev interaction dominated, magnonic properties other than the dispersion have to be investigated in detail.

7.2 Model establishment

To investigate the magnonic properties of honeycomb ferromagnets exhibiting DMI and Kitaev interactions in the presence of Heisenberg exchange and magneto-crystalline anisotropy exposed to a magnetic field, we consider the effective spin Hamiltonian on a two-dimensional ferromagnetic honeycomb

lattice, sketched in Figure 7.1, given by:

$$\begin{aligned} H = &- \sum_{i,j} J_{ij} \mathbf{S}_i \cdot \mathbf{S}_j - K \sum_{\langle ij \rangle^\gamma} S_i^\gamma S_j^\gamma - \sum_{ij} \mathbf{D}_{ij} \cdot (\mathbf{S}_i \times \mathbf{S}_j) \\ &- \sum_i A(\hat{\mathbf{n}}_i \cdot \mathbf{S}_i)^2 - \mathbf{B} \cdot \mu_{\mathrm{B}} g_e \sum_i \mathbf{S}_i, \end{aligned} \tag{7.1}$$

where the first and second terms contribute to the exchange interaction. The J_{ij} coefficients mediate the isotropic Heisenberg exchange interaction between spins $\mathbf{S}_i$ and $\mathbf{S}_j$ on sites i and j, and the second term is the Kitaev interaction, where $S_i^\gamma = \mathbf{S}_i \cdot \hat{\gamma}_{ij}$ with $\hat{\gamma}_{ij}$ being the Kitaev vector determined by the sites i and j. The second-nearest-neighbor DMI is represented by the third term with DMI vectors $\mathbf{D}_{ij}$ pointing out-of-plane, as required by the symmetry of the structure, i.e., $\mathbf{D}_{ij} = (0, 0, D_{ij}^z)$. Additionally, we add a single-ion anisotropy term with respect to the local easy axis $\hat{\mathbf{n}}_i$ (choosing it to be the unit vector along the z-direction), and the energy of Zeeman coupling to the magnetic field $\mathbf{B}$, with μ_{B} as Bohr magneton and g_e-factor of 2.

Figure 7.1 represents the monolayer honeycomb Kitaev materials such as α-$RuCl_3$ [159, 42] and CrI_3 [54], and for simplicity we refer to our studied system as CrI_3 in the following. Referring to experimental data from the Ref [54], we set approximate values for the nearest-neighbor exchange interaction $J = 0.2$ meV, the Kitaev interaction $K = 5.2$ meV, and the spin moment magnitude $S = 1.5$. An easy-axis anisotropy energy of $A = 0.1$ meV is chosen so as to ensure that the ground state is ferromagnetic along the z-axis and reproduce the 0.3 meV band gap in the magnon spectrum at the zone center for the lowest branch. As displayed in Figure 7.1 (c), the Kitaev vector $\hat{\gamma}_{ij}$ is defined as the normal vector to the Cr_2I_2 plane spanned by Cr ions i and j, and the nearby I atoms. Respectively, the Kitaev vector corresponding to the yellow bond in Figure 7.1 (a) and marked with $\boldsymbol{z}$ is chosen as $\hat{\gamma}_{\mathbf{z}}$=(sin$\theta$, 0 cos$\theta$)=($\frac{\sqrt{2}}{\sqrt{3}}$, 0, $\frac{1}{\sqrt{3}}$) [54, 168], where the Kitaev angle θ is about 54.74° for the case of CrI_3. The Kitaev vectors for red and blue bonds are determined analogously, and their value are obtained according to the C_3 symmetry, as discussed in Section 2.4.

7.3 The magnonic properties in Heisenberg-Kitaev model

To study the interplay of DMI and Kitaev interaction, we first ignore the effect of the magnetic field and DMI. Then we can easily study the magnonic transport properties in a simplified Heisenberg-Kitaev model with all spin directions along z direction. As introduced in Section 2.4, the Holstein-Primakoff transformation [51] is employed to rewrite the Hamiltonian in terms of bosonic ladder operators a_i and $a_i^\dagger$, and the linear spin-wave theory (LSWT) [52, 53] is used to obtain the eigenvalue and eigenvector of the system. As the Kitaev angle θ is different in different Kitaev materials [169, 54], we investigate the Heisenberg-Kitaev model by varying the θ angle and the magnitude of

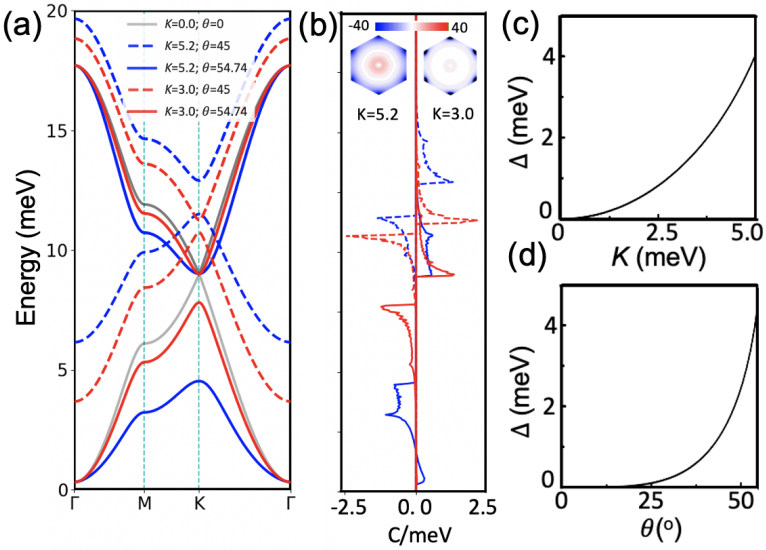

FIGURE 7.2: (a) The comparison of magnon dispersions along high-symmetry lines for different values of the Kitaev parameters. Grey, blue and red lines correspond to the K values of 0, 5.2 and 3 meV. The dashed and solid lines correspond to the Kitaev angles θ of $45°$ and $54.74°$, respectively. The corresponding energy-resolved Chern number is shown in (b). The Berry curvature distribution of the first magnon branch in the first Brillouin zone for different K-values with $\theta = 54.74°$ is shown in the inset of (b). The color map ranges from -40 to 40 in arb. units, and the exceeding values are marked with black. The magnon band gap $\triangle$ as a function of K (at $\theta = 54.74°$) and θ (at $K = 5.2$ meV) is shown in (c) and (d), respectively.

K, assuming that the sign of the latter remains positive. We further keep the value of $J + K/3$ constant so as to ensure that the ground state has the same energy. By comparing the band dispersion for different K and θ values shown in Figure 7.2 (a), we find that the band gap between the two modes $\triangle$ is enlarged as either K or θ increases, see Figure 7.2 (c,d). Meanwhile, a larger K not only decreases the spin stiffness at the Γ point but also opens a larger band gap at **K**, as shown in Figure 7.2 (a, c). As a larger θ enhances the effect of anisotropic exchange interaction, the single-ion anisotropy energy is introduced to ensure the stability of the system. In Figure 7.2 (d), the range of considered angles is limited by $54.75°$ owing to the fact that the system becomes unstable if the single-ion anisotropy energy remains unchanged. The relationship between the θ and the required anisotropy energy A is studied and we show the result in Figure 7.3, indicating that an anisotropy energy is required if the interaction is dominated by the Kitaev interaction with the Kitaev angle larger than $54.74°$.

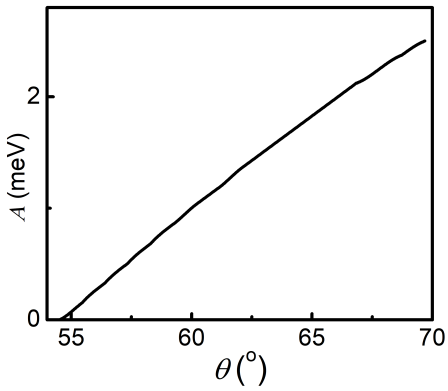

FIGURE 7.3: The relationship between the θ and the required minimum anisotropy energy A in the Heisenberg-Kitaev model with $K = 5.2$ meV and $D = 0$ meV.

The topological character of the magnonic bands is accessed by computing the Chern number C_n, given by $C_n = \frac{1}{2\pi}\int \Omega^{xy}_{n\mathbf{k}}\, dk_x dk_y$, where the $\Omega^{xy}_{n\mathbf{k}}$ is obtained based on the Eq. (4.15) and the integral is performed over the first Brillouin Zone (BZ), and n is the n-th magnon branch. The calculated Chern numbers are -1 and $+1$ for the first and second branches in the Heisenberg-Kitaev model. As shown in Figure 7.2 (b), the energy-dependent Chern number defined as an integral of the Berry curvature at a given energy, as well as the Berry curvature distribution of the first branch indicate that the largest contributions to the Chern number come from around the **K**-point. Besides, the observed Chern number variation and Berry curvature distribution are quite non-trivial in energy and in the reciprocal space (the opposite sign of magnon Berry curvature around $\mathbf{\Gamma}$ point), which brings about the unusual topological transport properties as manifested in the unusual temperature dependence of the thermal Hall conductivity and the magnon Nernst conductivity.

According to Eq. (4.30), we obtain the thermal Hall conductivity $\kappa^{xy}_{\mathrm{TH}}$ and magnon Nernst conductivity κ^{xy}_{N} of the model system. As shown in Figure 7.4 (a-b), a sign change with increasing temperature T of $\kappa^{xy}_{\mathrm{TH}}$ and κ^{xy}_{N} is clearly obtained for the values of $K = 5.2\,\mathrm{meV}$ and $\theta = 54.74°$, which is in line with the observations for Kitaev materials [170, 171]. This can be explained by a variation in the sign of the energy-dependent Chern number in the energy region of 1 to $2\,\mathrm{meV}$ for these specific values of K and θ, which is absent for smaller values of Kitaev parameters. For smaller K and θ, the Berry curvature magnitude rises at much higher energies, which explains the overall suppression of thermal Hall and magnon Nernst conductivity that we observe. To emphasize this effect further, we plot the dependence of $\kappa^{xy}_{\mathrm{TH}}/T$ on temperature T and parameters K and θ separately in Figure 7.4 (c-d). In this figure, we observe that regardless of the sign of $\kappa^{xy}_{\mathrm{TH}}/T$, its absolute

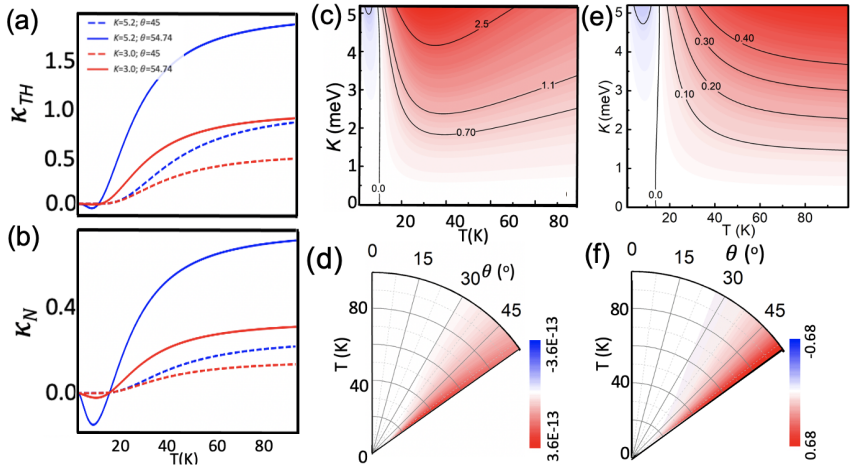

FIGURE 7.4: (a, b) The temperature dependence of thermal Hall conductivity $\kappa_{\mathrm{TH}}^{xy}$ and magnon Nernst conductivity κ_{N}^{xy}, in units of 10^{-11} W/K and $k_{\mathrm{B}}/2\pi$, respectively. Blue and red lines correspond to the K values of 5.2 and 3 meV, separately. The dashed and solid lines correspond to the Kitaev angles θ of 45° and 54.74°, respectively. The map of $\kappa_{\mathrm{TH}}^{xy}/T$ (c) and κ_{N}^{xy} (e) as a function of temperature T and parameter K at the Kitaev angle of $\theta = 54.74°$. The map of $\kappa_{\mathrm{TH}}^{xy}/T$ (d) and κ_{N}^{xy} as a function of T and θ at the constant K-value of 5.2 meV. The unit of the color map in (c, d) is chosen as W/K^2. The unit of the color map in (e, f) is $k_{\mathrm{B}}/(2\pi)$.

value always increases with K and θ at a given temperature. Similar conclusions can be drawn for the magnon Nerst conductivity κ_{N}^{xy}, as shown in Figure 7.4 (e-f).

Utilizing the mean-field-theory (MFT), we can simply estimate the Curie-Weiss temperature in ferromagnetic honeycomb lattice, following the equation:

$$T_{\mathrm{C}} = \frac{2S(S+1)}{k_{\mathrm{B}}}(-A - \frac{3}{2}J_1 - -\frac{1}{2}K), \tag{7.2}$$

and the estimated T_{C} is about 84 K for CrI_3. Even though the MFT cannot distinguish the isotropic and anisotropic interaction and the T_{C} is overestimated, the estimated value is still lower than 100 K.

However, the Curie temperature is not taken into account in our magnonic transport properties calculation. In this chapter, the main target is to reveal the magnonic transport characteristics with the interplay of DMI and Kitaev interaction, whose features are demonstrated up to the high-temperature limit. The 100 K is simply taken as a natural boundary for our simulations, and in fact, all the features in corresponding dependencies which emphasize the influence of two types of interactions are clearly visible and prominent

for temperatures which are well below 100 K. Moreover, the Curie temperature can be easily controlled by the modifications in the Heisenberg exchange strength, magnetic anisotropy, or by the strength of the applied magnetic field [54], which do not necessarily alter the qualitative behavior of the transport characteristics especially with respect to the relative importance of the DMI and Kitaev interactions.

7.4 The Heisenberg-Kitaev model with the influence of DMI

After fully understand the magnonic topology in the FM Heisenberg-Kitaev model, we investigate the impact of DMI on its magnon dispersion and magnonic transport properties. As shown in Figure 7.5 (a), our results indicate that both DMI and Kitaev interaction can modify the magnon dispersion and open a gap at the crossing point **K**. The difference in the impact of DMI and Kitaev interactions is that the latter strongly influences the shape of magnon dispersion, whereas the DMI mainly influences the dispersion around the **K** point. As also visible in Figure 7.5(a-b), a band gap of the same magnitude $\triangle$ can be realised by a combination of different DMI and Kitaev parameters. We can expect that if introducing more exchange interactions, a similar magnon dispersion with different parameter sets for Heisenberg-Kitaev model and Heisenberg-DMI model can be obtained. For instance, the experimental magnon dispersion of CrI_3 can be fitted well with both Heisenberg-Kitaev model or Heisenberg-DMI model [162, 54]. In this context, the relevance of a given model can be probed by accessing its topological transport properties and comparing them to experiments.

The topological thermal Hall conductivity $\kappa_{\mathrm{TH}}^{xy}$ modulated by Kitaev parameters (θ, K) and DMI (D) is shown in Figure 7.6. The topological phase boundary marked with different sets of $(C_1,\ C_2)$ Chern numbers is shown with a white dashed line. As the sign of the Berry curvature generally changes in the BZ for the first branch, shown in Figure 7.5 (c-f), the zero isolines of $\kappa_{\mathrm{TH}}^{xy}$ does not generally coincide with the phase boundary, which is different from the purely DMI-mediated system [76, 18]. Similar to Figure 7.4 (c), in Fig. 7.6 (b-c) the sign change of $\kappa_{\mathrm{TH}}^{xy}$ is observed when increasing T in the topological phase marked as $(-1,\ +1)$. This feature can be explained by the fact that while DMI mainly influences the magnonic states around **K** or **M** points, the Berry curvature around $\mathbf{\Gamma}$ point is mainly determined by the Kitaev interaction, see Figure 7.5 (c-f). The total contribution to $\kappa_{\mathrm{TH}}^{xy}$ thus presents a subtle competition between Berry curvature contributions from around these points, whose overall sign depends on the interplay between the parameters. The phase diagrams of $\kappa_{\mathrm{TH}}^{xy}$ with respect to θ, K and D at $T = 100\,\mathrm{K}$ are shown in Figure 7.6 (a, d). Consistent with the discussion above, the magnitude of $\kappa_{\mathrm{TH}}^{xy}$ is directly determined by the strength of K and the magnitude of θ. Notably, at a given K, the sign of $\kappa_{\mathrm{TH}}^{xy}$ can be adjusted by the sense of DMI. Similar observations can be made also for the

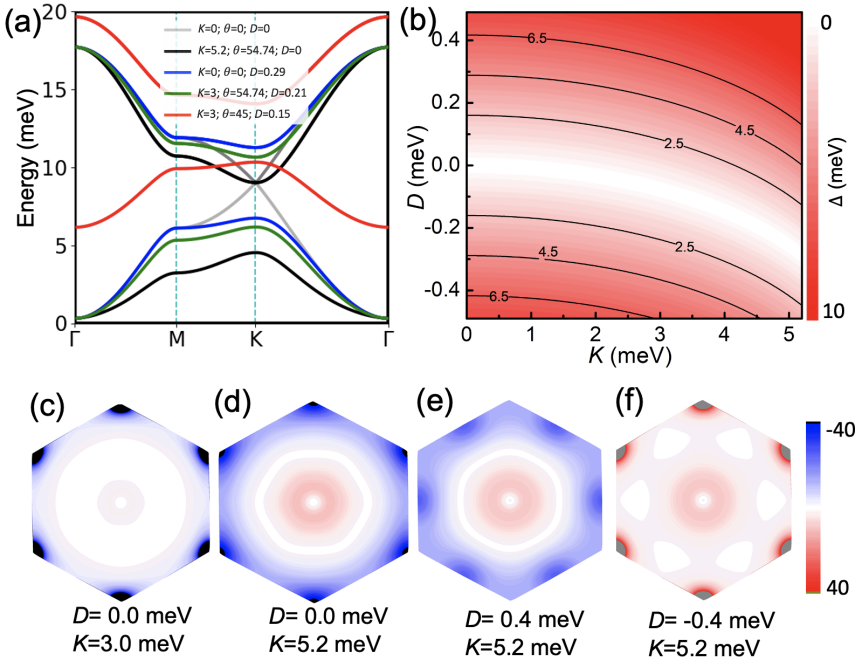

FIGURE 7.5: (a) The comparison of magnon dispersions with different Kitaev and DMI parameters specified in the legend (in the units of meV and degrees). The magnon dispersions represented with black, blue, green and red lines have almost the same band gap $\triangle$ between the two branches. (b) Band gap $\triangle$ at point $\mathbf{K}$ as a function of D and K at $\theta = 54.74°$. (c-f) The comparison of berry curvature distribution in first BZ with different D and K with the Kitaev angle $\theta = 54.7°$. The color map ranges from -40 to 40 arb. units, and the exceeded value is marked as black and grey. During the calculation, the $J + K/3$ is kept as a constant.

magnon Nernst conductivity, and here we don't discuss them again as the phenomenon are very similar to the thermal Hall conductivity of magnon.

7.5 The effect of a magnetic field on the Heisenberg-Kitaev-DMI model

In this section, we explore the effect of an external in-plane magnetic field on magnonic properties in the Heisenberg-Kitaev-DMI model, as shown in Fig. 7.1(b). Under the influence of the magnetic field $\mathbf{B} = \mathrm{B}(\cos\phi_\mathrm{s}, \sin\phi_\mathrm{s}, 0)$ with ϕ_s corresponding to the azimuthal angle of $\mathbf{B}$, spins in the FM magnets incline into the plane. In honeycomb ferromagnetic lattice, the spin vector

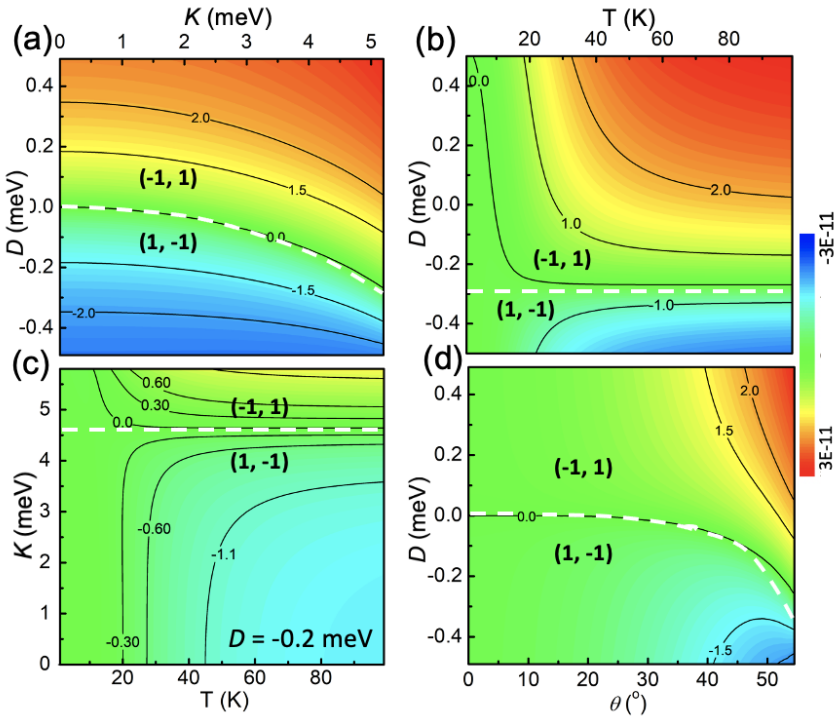

FIGURE 7.6: (a) Dependence of thermal Hall conductivity $\kappa_{\mathrm{TH}}^{xy}$ on K and D at $T = 100\,\mathrm{K}$ and $\theta = 54.74°$. Here, we keep the value of $J + K/3$ constant. The T-dependence of thermal Hall conductivity $\kappa_{\mathrm{TH}}^{xy}$ is shown in (b, c). (b) $\kappa_{\mathrm{TH}}^{xy}$ as a function of T and D, with K and θ corresponding to the case of CrI_3. (c) $\kappa_{\mathrm{TH}}^{xy}$ as a function of T and K for $\theta = 54.74°$ and $D = -0.2\,\mathrm{meV}$. Similar to (a), the $J + K/3$ is a constant. (d) $\kappa_{\mathrm{TH}}^{xy}$ as a function of θ and D at $T = 100\,\mathrm{K}$ and $K = 5.2\,\mathrm{meV}$. The corresponding color map is in the units of W/K.

modulated by the magnetic field is represented as:

$$\mathbf{S}_i = S(\sin\theta_{\mathrm{s}}\cos\phi_{\mathrm{s}}, \sin\theta_{\mathrm{s}}\sin\phi_{\mathrm{s}}, \cos\theta_{\mathrm{s}}), \tag{7.3}$$

where S represents the spin length and θ_{s} donates the polar angle of spin direction. Then, the classical total energy of each unit cell is calculated based on the Hamiltonian Eq. (7.1), which is expressed as below.

$$E_{\mathrm{unit}}(\theta_{\mathrm{s}}) = -2\mu_{\mathrm{B}} g_e B S \sin\theta_{\mathrm{s}} - 2AS^2\cos^2\theta_{\mathrm{s}} + const. \tag{7.4}$$

Obviously, the energy of the Hamiltonian is the function of θ_{s}, the minimum energy of the system is obtained through solving the equation:

$$\frac{\partial E_{unit}(\theta_{\rm s})}{\theta_{\rm s}} = -2\mu_{\rm B} g_e BS\cos\theta_{\rm s} + 4AS^2\sin\theta_{\rm s}\cos\theta_{\rm s} = 0. \tag{7.5}$$

We get the relationship between the applied magnetic field and the $\theta_{\rm s}$:

$$\sin\theta_{\rm s} = g_e\mu_{\rm B}{\rm B}/2A{\rm S}. \tag{7.6}$$

As shown in Figure 7.7, both polar angle $\theta_{\rm s}$ and azimuthal angle $\phi_{\rm s}$ have an influence on the magnon dispersion in the Heisenberg-Kitaev model. Besides, the C_3 symmetry of the magnon dispersion is broken if the polar angle is nonzero assuming non-vanishing Kitaev interaction. To demonstrate this feature from the inelastic neutron scattering (INS) experiment, the spin-spin correlation function of the Heisenberg-Kitaev model in honeycomb lattice is calculated through *spinW* [172] code according to the following equation [52, 173]:

$$S(\omega,\mathbf{k}) = \frac{1}{2\pi}\int_{-\infty}^{\infty} exp^{i\omega t}\langle \mathbf{S}(\mathbf{k},t)\mathbf{S}(\mathbf{k},0)\rangle dt, \tag{7.7}$$

where the $\mathbf{S}(\mathbf{k},t)$ is the lattice Fourier transform of the spin configuration at time t. The calculated results are shown in Figure 7.8, which can be used as a reference for the experiment to distinguish the Heisenberg-Kitaev model and Heisenberg-DMI model. If ignoring the anisotropy energy, the magnon dispersion remains the same when the polar angle is changed in the pure Heisenberg model. In the Heisenberg-DMI model, although the constant energy mapping of the magnon spectra changes with the evolution of polar

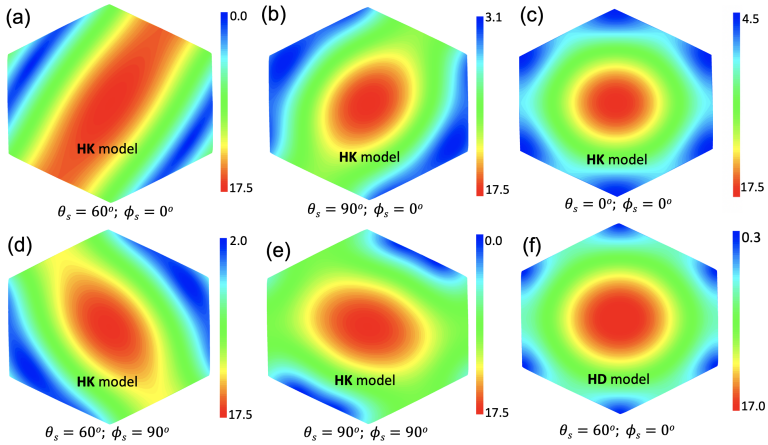

FIGURE 7.7: The distribution of the eigenvalue difference between the second and first branch in the first BZ with different $\theta_{\rm s}$ and $\phi_{\rm s}$. The parameters are chosen as $K = 5.2$ meV, $D = 0$ meV for (a-e) which is marked as Heisenberg-Kitaev model (HK model). The (f) is the result of Heisenberg-DMI model with $K = 0$ meV and $D = 0.29$ meV.

angle, the magnon dispersion still remains the C_3 symmetry. However, the C_3 symmetry of the magnon dispersion is broken in the Heisenberg-Kitaev model, for a given nonzero θ_s.

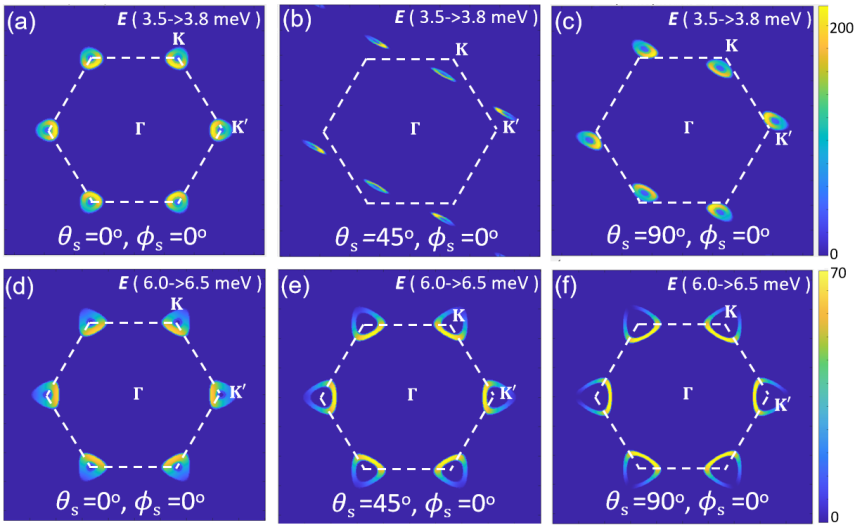

FIGURE 7.8: The constant energy mappings of the magnon spectra in the xy plane with different polar angle θ_s. The first BZ is outlined by the white dotted line and the energy is selected ranging from 3.5 to 3.8 meV for (a-c) and 6.0 to 6.5 meV for (d-f). The (a-c) represent the Heisenberg-Kitaev model and (d-f) denote the Heisenberg-DMI model. The parameters of Kitaev interaction in (a-c) are the same as in CrI_3 mentioned above. In (d-f) the parameters are chosen as $J = 1.933$ meV, $K = 0$ meV, and $D = 0.21$ meV. The calculated magnon spectra is convolved with an energy of 0.1 meV as an estimation of the instrument energy resolution.

Additionally, we systematically studied the evolution of the band gap between the two magnon branches, marked by $\triangle$, with the angles θ_s and ϕ_s in the Heisenberg-DMI model and Heisenberg-Kitaev model. We find ϕ_s has a strong impact on the band gap when θ is larger than 40° with nonzero finite K value, while the band gap is only influenced by the polar angle θ_s in the Heisenberg-DMI model ($K = 0$).

The magnonic transport properties affected by the magnetic field are studied. We draw the topological phase diagram of thermal Hall conductivity as a function of θ_s and ϕ_s in Figure 7.9 (c). When θ_s is smaller than 40°, the system resides in the $(-1, +1)$ phase, and the influence of ϕ_s is suppressed. However, $\kappa_{\mathrm{TH}}^{xy}$ exhibits a very non-trivial dependence on ϕ_s when the system enters the $(+1, -1)$ phase upon increasing θ_s. The strong dependence of $\kappa_{\mathrm{TH}}^{xy}$ on ϕ_s and θ_s is also visible in the temperature-dependence plots shown in Figure 7.10. As indicated in Figure 7.10 (a, b), the C_3 symmetry of the conductivity is preserved, in line with the symmetry of the Kitaev interaction on

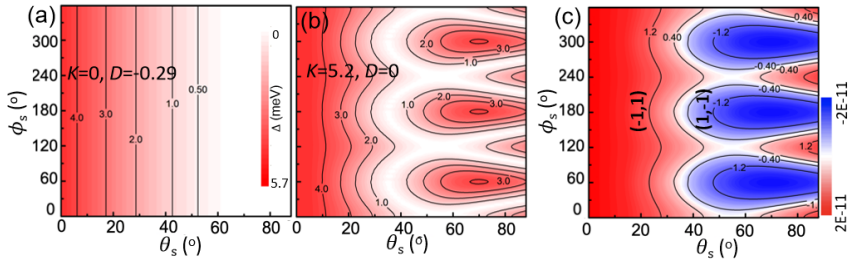

FIGURE 7.9: (a, b) Evolution of the band gap $\triangle$ with the angles θ_s and ϕ_s in the Heisenberg-DMI model ($K = 0$) (a), and Heisenberg-Kitaev model ($D = 0$) (b). (a, b) share the same color map and the units are meV. (c) Thermal Hall conductivity $\kappa_{\mathrm{TH}}^{xy}$ as a function of θ_s and ϕ_s at $T = 100\,\mathrm{K}$ (same parameters as in (b)). The unit of the color map in (c) is chosen as W/T.

a honeycomb lattice. Moreover, from Figure 7.10 (c,d) we observe a strong influence of the DMI on the magnitude and angular dependence of the thermal Hall conductivity. Overall our result reveals a rich landscape of thermal Hall effect of Kitaev ferromagnets exposed to an external magnetic field.

7.6 Summary

In our study, we reveal the magnonic properties of honeycomb ferromagnets with DMI and Kitaev interaction subject to an external magnetic field. On the one hand, we observe intricate magnonic transport characteristics, which have been observed in Kitaev materials [170, 171] that we attribute to the nontrivial Berry phase properties of the system. On the other hand, our results demonstrate a rich magnonic topological phase diagram drawn as a function of Kitaev parameters, DMI and magnetic field strength. Since the magnitude of the DMI and Kitaev interaction can be adjusted through *e.g.*, application of strain [174] or electric field [153], our investigation provides a good reference point for designing the magnonic properties of candidate Kitaev materials. Our findings bare significant relevance given that although several Kitaev materials have been discovered to date (*e.g.*, [45, 156, 157, 158, 159, 42]), it is still not clear how to judge the relative importance of Kitaev interaction with respect to DMI.

From the perspective of magnons, based on the results of our work, we propose several strategies to disentangle the two types of interactions from each other. We claim that one anisotropy energy A have to be introduced to ensure the stability of the system in the Heisenberg-Kitaev model for certain Kitaev angle θ. Besides, if an application of an external in-plane magnetic field brings along a significant modification of the shape of the magnon dispersion and a strong variation of the magnonic properties as a function of the in-plane direction of the field, then the system is dominated by Kitaev

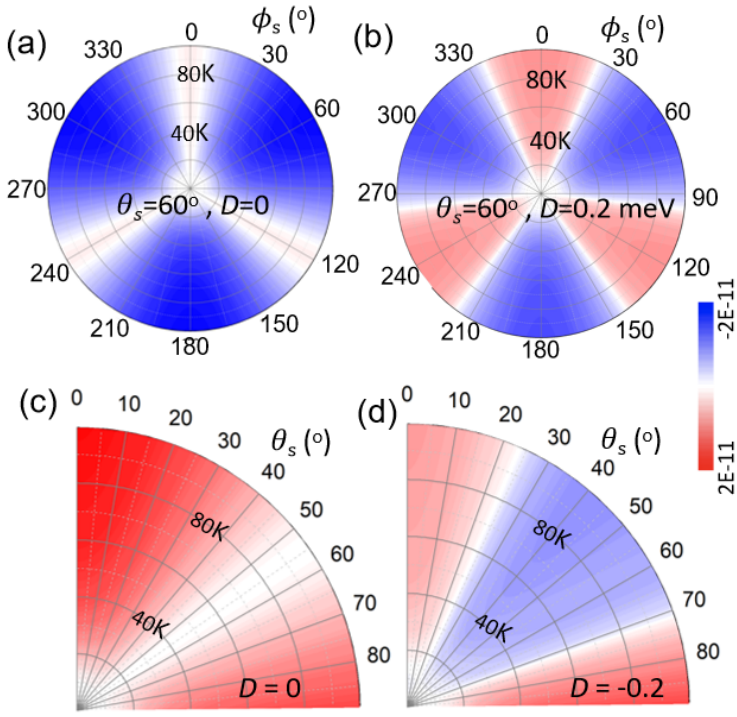

FIGURE 7.10: (a, b) $\kappa_{\mathrm{TH}}^{xy}$ with the function of temperature and the azimuthal angle ϕ_{s}, which ranges from 0^o to 360^o at $\theta_{\mathrm{s}} = 60°$. The D is chosen as 0 meV in (a) and 0.2 meV in (b). (c-d) $\kappa_{\mathrm{TH}}^{xy}$ as a function of temperature and θ_{s} for different values of D assuming $\phi_{\mathrm{s}} = 0°$ and $K = 5.2$ meV. (a-d) share the same color map in the unit of W/T.

interaction rather than DMI. Additionally, the changes of sign in the thermal transverse characteristics as a function of temperature or strength with an external magnetic field can serve as another indication of the prominence of the Kitaev interaction in the system. These simple criteria can potentially enable a magnonic characterization of exchange interactions of Kitaev materials, and pave the way to employing magnonic topology for designing their exotic properties.

7.7 Application in $CrGeTe_3$ and $CrSiTe_3$

According to the theoretical study mentioned above, we investigate the spin interactions in $CrSiTe_3$ and $CrGeTe_3$ cooperated with our experimental collaborates.

7.7.1 Introduction of $CrGeTe_3$ and $CrSiTe_3$

The $CrSiTe_3$ and $CrGeTe_3$ are van der Waals layer materials with the ferromagnetic ground states. As shown in Figure 7.11, $CrXTe_3$ (X=Si, Ge) is an ABC stacked honeycomb lattice with spin length $S = 3/2$ for each Cr^{3+} ions, which is similar to CrI_3 [25, 167]. Some magnetic properties of these materials have been explored in the previous studies. For instance, the *ab initio* calculations predict that in monolayer $CrGeTe_3$ both Kitaev interaction and DMI can exist in monolayer $CrGeTe_3$ except for the ion anisotropy energy, in which the magnitude of Kitaev interaction is predicted about 5% of the Heisenberg exchange interaction [169]. It is already demonstrated that the

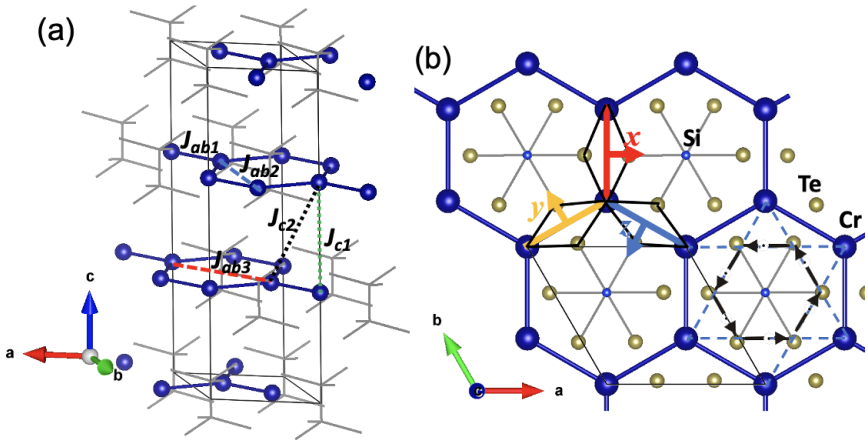

FIGURE 7.11: (a) Magnetic structure of $CrXTe_3$ (X= Si, Ge). The Cr atoms form a honeycomb lattice in xy plane. The first and second nearest-neighbor exchange interactions in intra-plane and inter-planes are marked separately. (b) The top view of monolayer $CrSiTe_3$. We present the Kitaev interaction and DMI in the same plot. The unit cell is outlined with a thin black line, where blue balls represent Cr^{3+} ions. In the Heisenberg-Kitaev model, the Kitaev bonds $\boldsymbol{x}$ (red), $\boldsymbol{y}$ (dark yellow), $\boldsymbol{z}$ (blue) are indicated with thick colored lines. In the Heisenberg-DMI model, the arrows mark the second-nearest-neighbor bond orientations along black dotted lines that share a common sign of an out-of-plane DM vector.

spin interaction of CrI_3 is dominated by the Kitaev interaction [54], and both CrI_3 and $CrXTe_3$ (X=Si, Ge) have very similar magnetic structures. Here, we want to figure out whether the Kitaev interaction plays an important role in $CrXTe_3$ or not.

7.7.2 The parameterization of effective spin Hamiltonian in $CrXTe_3$ (X=Si, Ge)

To explore the spin interaction in $CrXTe_3$ (X=Si, Ge), the magnon spectrum of $CrSiTe_3$ and $CrGeTe_3$ are obtained based on the INS experiment. All the experimental results are offered from our collaborate: Dr. Fengfeng Zhu from Dr. Yixi Su's research group in Jülich Centre for Neutron Science (JCNS) at Heinz Maier-Leibnitz Zentrum (MLZ).

As shown in Figure 7.12 and Figure 7.13, there is a global band gap between the upper three magnonic branches and the lowest three magnonic branches. According to the symmetry of the system, the glob band gap cannot be realized just through the isotropic Heisenberg exchange interaction. To open the band gap, more types of spin interactions need to be considered, such as the DMI or Kitaev interaction. Since $CrXTe_3$ (X=Si, Ge) systems contain heavy element atoms, the spin-orbit coupling (SOC) plays an important role, indicating that the DM and Kitaev interaction may exist in these materials. Based on the LSWT, we separately fit the experimental results with the Heisenberg-DMI model and Heisenberg-Kitaev model:

$$\begin{aligned} H_{\mathrm{H-DMI}} &= -\sum_{i,j} J_{ij}\mathbf{S}_i \cdot \mathbf{S}_j - \sum_{ij} \mathbf{D}_{ij} \cdot (\mathbf{S}_i \times \mathbf{S}_j) - \sum_i A(\hat{\mathbf{n}}_i \cdot \mathbf{S}_i)^2 \\ H_{\mathrm{H-K}} &= -\sum_{i,j} J_{ij}\mathbf{S}_i \cdot \mathbf{S}_j - K\sum_{\langle ij\rangle^\gamma} S_i^\gamma S_j^\gamma - \sum_i A(\mathbf{n}_i \cdot \mathbf{S}_i)^2. \end{aligned} \tag{7.8}$$

The second-nearest-neighbor DMI is considered based on the symmetry of the material in the Heisenberg-DMI model. While in the Heisenberg-Kitaev model, the nearest-neighbor Kitaev interaction is adopted with the setting shown in Figure 7.11. We list the fitted parameters of $CrXTe_3$ (X=Si, Ge) with both models in Table. 7.1.

In Figure 7.12 (c, d) and Figure 7.13 (c, d), we present the fitted results based on the Heisenberg-DMI model. The black solid lines are the calculated magnon spectra by using the Heisenberg-DMI model with LSWT and

Parameters	J_{ab1}	J_{ab2}	J_{c1}	J_{c2}	A	$\mathbf{D}_{ij}$	K	Remark
$CrSiTe_3$	-1.49	-0.15	-0.07	-0.06	-0.01	(0, 0, 0.12)	-	H-DMI
	-0.4	-0.2	-0.08	-0.065	-0.22	-	-3	H-Kitaev
$CrGeTe_3$	-2.73	-0.33	-0.10	-0.08	-0.01	(0, 0, 0.32)	-	H-DMI
	-0.24	-0.42	-0.1	-0.08	-1.9	-	-6.5	H-Kitaev

TABLE 7.1: The exchange interactions including DMI and Kitaev interactions are all listed together for both $CrSiTe_3$ and $CrGeTe_3$. The values of the next nearest-neighbor DMI vector is chosen to reproduce the experimental spin-wave dispersion in the Heisenberg-DMI model, same for Kitaev interaction in the Heisenberg-Kitaev model.

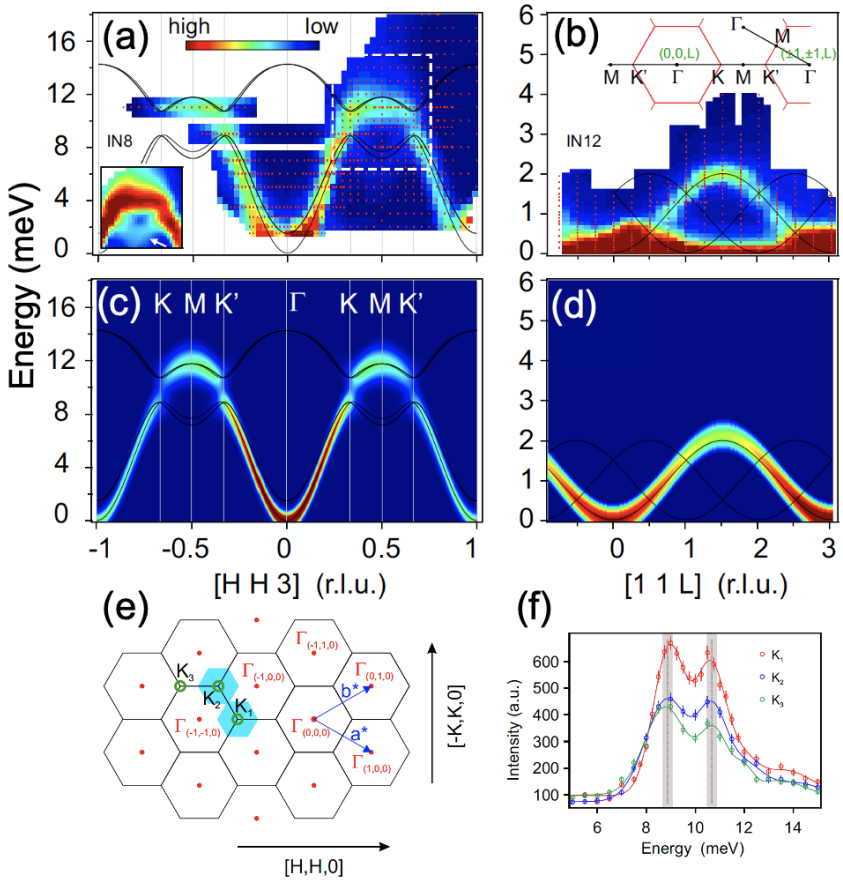

FIGURE 7.12: (a, b) Energy and intensity map of magnons in $CrSiTe_3$ along high symmetry directions measured by thermal neutron triple-axis spectrometer IN8, PUMA and cold neutron triple-axis spectrometer IN12, respectively. The black solid lines are the calculated magnon spectra by using the parameters from the second-nearest-neighbor Heisenberg-DMI models. The inset in (a) is a contrast-adjusted plot for the dashed rectangle part to make the acoustic branch much easier to see. The inset in (b) shows the exact Q-path measured in the reciprocal space. (c-d) Calculated magnon spectra intensity maps for (a-b) respectively with the code *spinW*. The calculated spectra is convolved with an energy resolution of 1 meV to compare with experimental data. The parameters are listed in Table.7.1. (f) Energy scan of magnon Density of states at 3 different K points in (e) The solid lines are the multi-peak Gauss fitting. the gray bars represent the averaged energy position for the magnon bands at different **K** point.

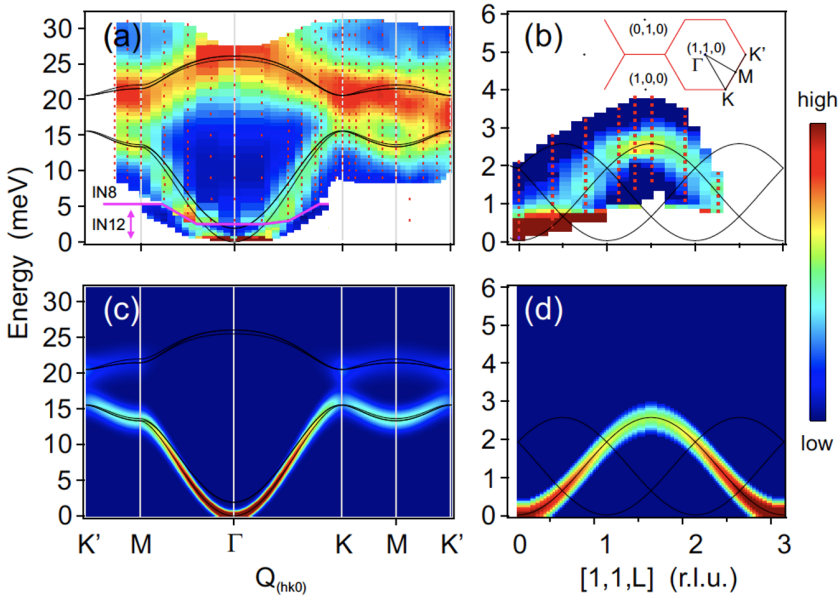

FIGURE 7.13: (a, b) Energy and momentum-resolved neutron scattering intensity map of magnons in $CrGeTe_3$ along high symmetry directions measured by thermal neutron triple-axis spectrometer IN8 and cold neutron triple-axis spectrometer IN12. Black solid lines are the calculated magnon dispersion based on the Heisenberg-DMI model. Inset in (b) shows the projected BZ boundaries with high symmetry points and experimental measured paths. (c,d) The corresponding simulated magnon intensity map for (a,b) by using the *spinW* code. The calculated spectra are convolved with an energy resolution of 1 meV to compare with experimental data.

the simulated magnon spectra intensity maps are obtained with the code *spinW*. Overall, our calculated results are consistent with the experimental results. Although there is a mismatch for the scattering intensity shown in Figure 7.13 (a, c), we suspect that it may lie in the magnon-phonon interaction. The projected phonon density of state for bulk $CrGeTe_3$ is calculated, and we show the result in Figure 7.14. Clearly, the phonon states with the energy of about 6 THz (about 25 meV) are mainly contributed by magnetic Cr ions which are consistent with the previous calculation for monolayer $CrGeTe_3$ [175]. Coincidentally, the optical magnon branches of $CrGeTe_3$ are also located in a similar energy range. The overlap in energy makes the coupling between magnons and phonons favorable. Moreover, both types of excitation are mainly originated in Cr atoms, so the spectral weight transfer from phonon to magnon states is very likely to occur.

In fact, in addition to the Heisenberg-DMI model, the Heisenberg-Kitaev model also fits the experimental result very well. The comparison between

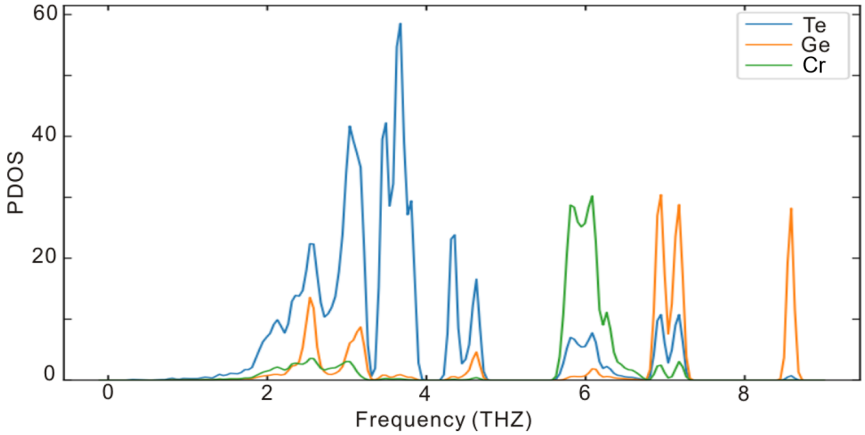

FIGURE 7.14: The projected phonon density of state in $CrGeTe_3$. The result is calculated based on the *ab initio* code *VASP*.

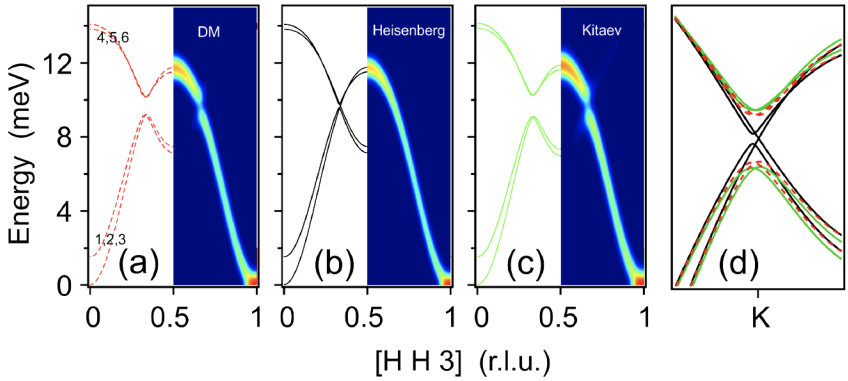

FIGURE 7.15: Comparison of different models in $CrSiTe_3$. (a) Magnon spectra calculated by Heisenberg-DMI model. Dash lines are the calculated magnon spectra and the intensity maps are the result of convolution with energy resolution of 1 meV. (b) Magnon spectra calculated by Pure Heisenberg model. (c) Magnon spectra calculated by Heisenberg-Kitaev model. (d) Comparison of the magnon spectra dispersion near **K** point between all the models in (a-c).

the Heisenberg-DMI model and Heisenberg-Kitaev model are shown in Figure 7.15. In the Heisenberg-Kitaev model, as shown in Table 7.1, a very large magnetic anisotropy energy needs to be introduced to ensure the system stable. This is consistent with the study in Section 7.3, where the Kitaev angle in $CrSiTe_3$ and $CrGeTe_3$ are 57.28° and 62.26°, respectively. However, it is indicated that the magnetic anisotropic energy of both materials are very small

from the experimental investigation. Besides, even if the magnon dispersion can be reproduced well when the bond-dependent Kitaev interactions are assumed to be perfectly orthogonal, it is still difficult to understand the huge difference of the strength of the Kitaev interaction between $CrSiTe_3$ and $CrGeTe_3$, since the Kitaev interaction is mainly caused by the heavy Te atoms of $CrXTe_3$ [169, 174]. Therefore, the conflictive results lead us to believe that the Kitaev interaction is weak in these materials and the magnonic band gap is more likely opened through the DMI rather than the Kitaev interaction.

7.7.3 Topological properties of $CrXTe_3$ (X=Si, Ge)

To investigate the topological nature in $CrXTe_3$, the Berry curvature is calculated based on Eq. (6.3). The Chern number C_n is calculated to characterize the topology of magnonic bands according to $C_n = \frac{1}{2\pi}\int \Omega^{xy}_{n\mathbf{k}} \cdot \mathbf{n}\, dP$, where P is a two-dimensional slice of the Brillouin zone and $\mathbf{n}$ is the normal vector of P. As the intra-face interactions dominate the spin interaction, the lowest three branches cross with each other. Therefore, we use the sum of the lowest three branches to calculate the total Chern number. For bulk $CrXTe_3$, the total Chern number is calculated as $(-3, +3)$ for the lowest three branches and upper three branches, which means that every honeycomb layer will hold one topological edge state inside this nontrivial bulk gap. To indicate this feature, the edge states of monolayer $CrSiTe_3$ are calculated, which is shown in Figure 7.16. The color scale is calculated according to Eq. (6.5), and the edge states are observed clearly in zigzag and armchair nanoribbon with the projections of the bulk states.

The DMI vector can be modulated by the strength of SOC, pressure, strain, electric field [150, 151, 152, 153], or doping with defects. It is promising that we can obtain a stronger DMI effect in $CrSnTe_3$ and $CrPbTe_3$ or $CrXTe_3$ heterojunction. To reveal the influence of DMI strength on magnonic properties, we calculate the magnon dispersion and thermal Hall conductivity, which are shown in Figure 7.17 and Figure 7.18. As shown in Figure 7.17, the magnonic band gap increases linearly with the increase of DMI value, which is very similar to the SOC effect in electronic band structure. From the experimental results, we know that the Curie temperature of $CrSiTe_3$ and $CrGeTe_3$ are around 30 K and 60 K. The calculated temperature-dependent and energy-dependent thermal Hall conductivity are shown in Figure 7.18 (a-d), according to Eq. (4.28). For both materials, the κ^{xy} is significantly enhanced in the energy region close to the band gap, which can be attributed to the distribution of the Berry curvature around the $\mathbf{K}$ point. In low temperature only these "topologically-trivial" states are excited according to the Bose distribution, leading to the zero platform at very low temperature. The effect of DMI on thermal Hall conductivity is shown in Figure 7.18 (e), from which we can observe that the thermal Hall conductivity increases with the enhancement of DMI. The predict value for $CrGeTe_3$ reaches the order of 10^{-4} W/Km, which is large enough to be observed in experiment.

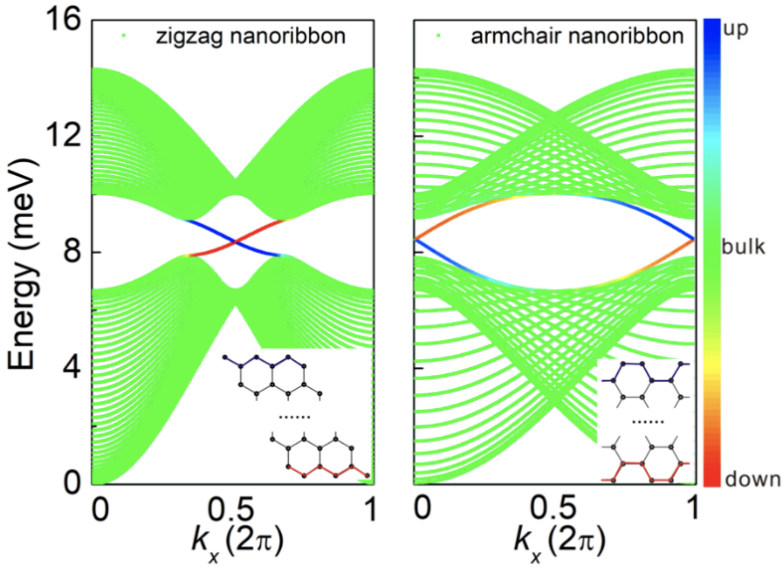

FIGURE 7.16: The edge states of monolayer $CrSiTe_3$ for zigzag and armchair nanoribbon. The color scale represents the weight of the magnonic wave function along with the slab.

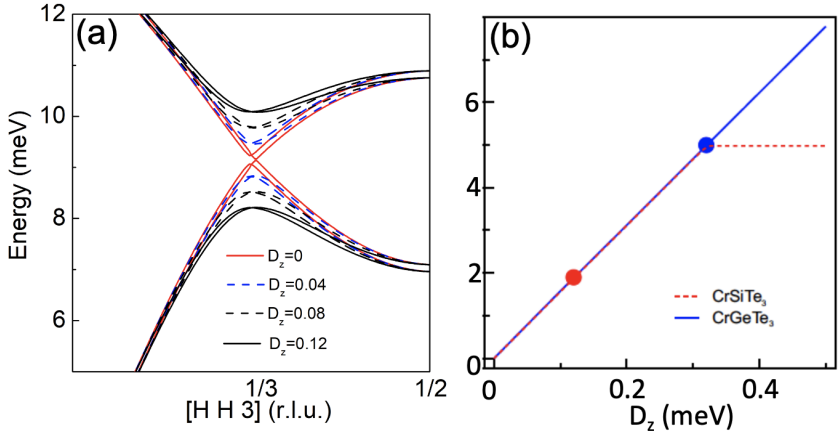

FIGURE 7.17: (a) The impact of the DMI on the magnon dispersion of $CrSiTe_3$. (b) The relationships between the global band gap and the strength of D^z. Red and blue filled circles correspond to the band gap of $CrSiTe_3$ and $CrGeTe_3$, respectively.

7.8 Discussion

In this chapter, we put the DMI and Kitaev interaction to one stage, and

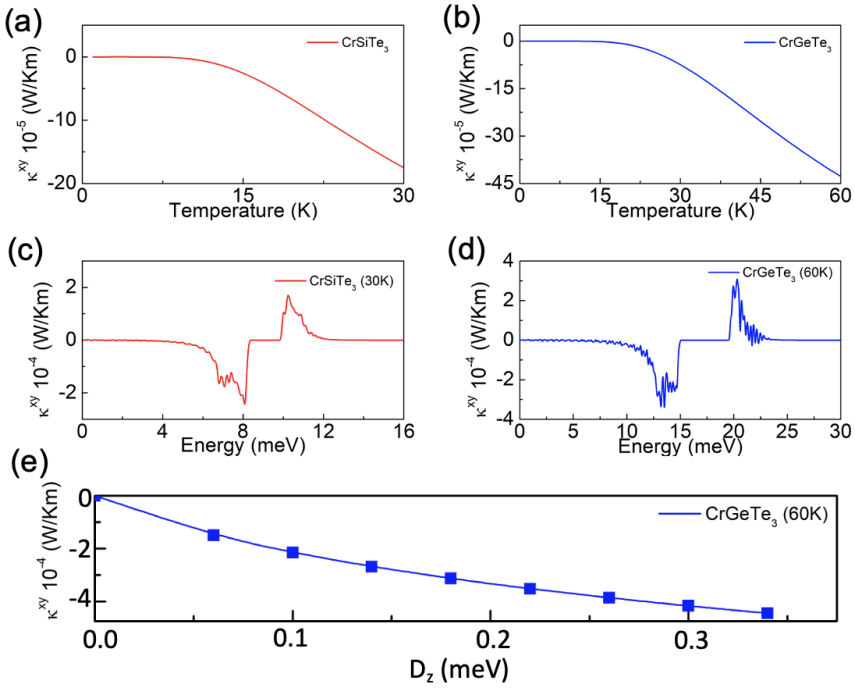

FIGURE 7.18: The transverse thermal Hall conductivity (κ^{xy}) of $CrGeTe_3$ and $CrSiTe_3$. The temperature dependence κ^{xy} is shown in (a, b), and the energy-dependent thermal Hall conductivity of $CrSiTe_3$ at 30 K and $CrGeTe_3$ at 60 K are shown in (c, d). The κ^{xy} with the function of D^z in $CrGeTe_3$ for the given temperature 60K is shown in (e).

systematically study the interplay of them in magnonic aspects from the numerical methods. Several methods are proposed to distinguish whether the DMI or Kitaev interaction is dominant in ferromagnetic honeycomb materials from the perspective of magnons. Moreover, based on the proposed strategy, we investigate the spin interactions in $CrSiTe_3$ and $CrGeTe_3$, and discovered a very promising new class of 2D topological magnon insulators.

Chapter 8

Imprinting and driving electronic orbital magnetism using magnons

Magnons, as the most elementary excitations of magnetic materials, have recently emerged as a prominent tool in electrical and thermal manipulation and transport of spin, and magnonics, as a field is considered as one of the pillars of modern spintronics. On the other hand, orbitronics, which exploits the orbital degree of freedom of electrons rather than their spin, emerges as a powerful platform in efficient design of currents and redistribution of angular momentum in structurally complex materials.

In this chapter, a link between the worlds of magnonics and orbitronics is established, with the example of ferromagnetic kagome lattice, resulting in a unique blend of paradigms which can enrich the respective fields and give rise to novel unexpected functionalities relying on efficient magnon-to-orbital conversion. The so far unknown coupling of magnonic excitations to spin-chirality in generic classes of spin systems is theoretically investigated. By referring to microscopic arguments, a finite spin chirality can be generated by thermally excited magnons even if the former is forbidden in the ground state of a collinear spin system. Besides, it is predicted that the magnonic generation of chirality will lead to a strong orbital response of the spin system via the mechanism of topological orbital magnetism, which promotes the orbital dynamics of electrons in spin systems with chirality. This provides a direct link between magnonic excitations and generation of electronic orbital magnetization. Finally, we demonstrate that driving currents of magnons for example in an applied temperature gradient causes a significant magnon drag of the orbital momentum across the system. The latter discovery reveals the potential of orbital electron-magnon coupling for controlling the magnetization properties via "magnon-orbital" torques and generation of sizeable orbital accumulation which can be probed experimentally. Alternatively, our findings point to a possibility of selected orbital control of magnonic properties and functionalities.

Results presented in this chapter have already been published:
Li-chuan Zhang, et. al., Communications Physics, 3, 227, 2020.

8.1 Electronic topological orbital magnetism

As discussed in Chapter 2, the orbital magnetism is not only influenced by the strength of the spin-orbital coupling (SOC) but also the the scalar spin chirality (SSC). In this chapter, we focus on the orbital magnetism aroused from the SSC, which is called as topological orbital magnetism [1]. We first present the results which concern the generation of electronic orbital magnetism by the mechanism of SSC. The electronic Hamiltonian with *s-d* model is established by making use of the tight-binding (TB) model of a magnet on a two-dimensional (in the xy-plane) kagome lattice without the SOC (Figure 2.1).

In the electronic Hamiltonian shown in Eq. (8.1), hoppings among the atoms and an exchange splitting at each atomic site are considered, which is similar to that of Refs. [176, 177]. The spin-orbit interaction is explicitly not employed to reveal the SSC-mediated mechanism of orbital moment generation. We show the electronic Hamiltonian:

$$\mathcal{H} = t_1 \sum_{\langle i,j \rangle} c_i^\dagger c_j + t_2 \sum_{\langle\langle i,j \rangle\rangle} c_i^\dagger c_j + J \sum_i \hat{\mathbf{m}}_i \cdot \boldsymbol{\sigma}, \tag{8.1}$$

where i and j are site indices, $\langle \cdots \rangle$ and $\langle\langle \cdots \rangle\rangle$ indicate first and second nearest neighbor pairs, respectively, and $\hat{\mathbf{m}}_i$ is the direction of the local magnetic moment at site i. The first and second nearest hopping amplitudes are chosen as $t_1 = 1.0\,\mathrm{eV}$ and $t_2 = 0.15\,\mathrm{eV}$, respectively, and strength of the exchange interaction is set to $J = 1.7\,\mathrm{eV}$.

As shown in the inset of Figure 8.2 (b), three basis atoms in the unit cell, namely A, B and C, are marked. The directions of the local magnetic moments are parameterized by $\hat{\mathbf{m}}_i = (\cos\theta\cos\phi_i, \cos\theta\sin\phi_i, \sin\theta)$, where the azimuthal angles ϕ_i are assumed to be chirally ordered, i.e., $\phi_i = \phi_0$ for $i \in \mathrm{A}$, $\phi_i = \phi_0 + 2\pi/3$ for $i \in \mathrm{B}$, and $\phi_i = \phi_0 + 4\pi/3$ for $i \in \mathrm{C}$. We start with the ferromagnetic state with the spins along z axis (see the corresponding band structure in Figure 8.2 (a)) and then rotate all spins into the plane by an angle θ away from the xy plane, while keeping the azimuthal angles of the three spins at 0°, 120° and 240° (keeping z-axis as the three-fold rotational symmetry axis). Based on the TB model with parameters mentioned above, we obtained the corresponding electronic band structure. We find that the effect of such non-coplanarity on the band structure is most prominent in the vicinity of band degeneracies, shown in Figure 8.2 (a).

Based on Eq. (2.4), we calculate the behavior of electronic orbital moment as a function of angle θ and Fermi level. The calculated result is shown in Figure 8.2 (b), where the red symbols represent the calculated orbital moment for the electron density of $\rho = 1.0\,e(cell)^{-1}$. The result indicates that the orbital moment vanishes for the coplanar and collinear cases, and the largest value of orbital moment is reached for the state with the largest SSC. As the spin-orbit coupling is not considered, the total orbital moment is generated

[1] The so-called chiral, proportional to the vector spin chirality, is not considered. This is because it is expected to arise in the regime of large spin-orbit interaction [15], although it has contribution to the orbital magnetism

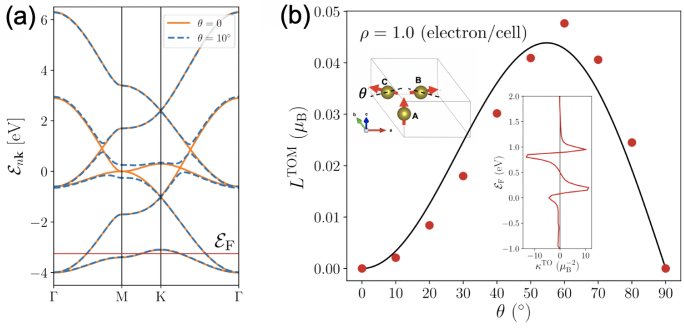

FIGURE 8.1: Microscopics of topological orbital magnetism. (a) The electronic band structure based on the tight-binding model of a kagome ferromagnet. The orange lines represent the bands of the ferromagnetic structure and the blue dotted lines mark the bands of the state canted by a polar angle of $\theta = 10°$. (b) The total topological orbital moment (TOM) as a function of the canting angle for the electron density of $\rho = 1.0\, e(cell)^{-1}$. The red symbols mark the calculated values according to Eq. (2.4), while the black line is a fit according to Eq. (8.2). The inset in the upper left corner indicates the spin direction of the calculated kagome lattice. The inset on the right displays the value of the topological orbital susceptibility κ^{TO} around the ferromagnetic state as a function of Fermi energy of the tight-binding model.

by the topological orbital moment (TOM) $\mathbf{L}^{\mathrm{TOM}}$. From the Eq. (2.6), with the arranged azimuthal angles, we can expand the equation with canting angle θ in kagome lattice:

$$L_z^{\mathrm{TOM}}(\theta) = \kappa^{\mathrm{TO}} \hat{\mathbf{m}}_A \cdot (\hat{\mathbf{m}}_B \times \hat{\mathbf{m}}_C) = \frac{3\sqrt{3}}{2} \kappa^{\mathrm{TO}} \cos\theta \sin^2\theta, \tag{8.2}$$

where we can get the relationship between the TOM and canting angle θ. Then the obtained $\mathbf{L}^{\mathrm{TOM}}$ can be fitted with the function of θ, and overall the explicitly calculated orbital response of the system to canting fits the TOM-picture very well, such as the case with band filling of one electron per unit cell in Figure 8.2 (b). This type of behavior, when κ^{TO} with a good degree of accuracy can be assumed to be independent of θ in the whole range of possible canting, persists over large regions of energies. The deviations from it occur in the vicinity of band crossings where the response of the band structure to canting is very large, and where the orbital response is expected to be pronounced [15].

Regardless, we focus on the interplay of orbital magnetism and magnons which cause small deviations of the magnetization from the ferromagnetic state, thus the value of the topological orbital susceptibility in the vicinity of

$\theta = 0^\circ$ is of primary interest. To extract κ^{TO} near $\theta = 0$, we use

$$\kappa^{\mathrm{TO}} = \frac{2}{3\sqrt{3}} \left. \frac{d^2 L_z^{\mathrm{TOM}}}{d\theta^2} \right|_{\theta=0}, \tag{8.3}$$

where the second derivative is evaluated by a finite difference method. Our calculations, shown in the inset of Figure 8.2 (b) for the entire range of energies of the model, reveal that the magnitude of κ^{TO} in the limit of small canting exceeds the value of 1 μ_{B} over large regions of energy, and sensitively depends on the electronic structure.

Overall, our electronic tight-binding calculations demonstrate that even within the simplest electronic structure considered here it is possible to generate sizable electronic orbital magnetization by the mechanism of SSC, the properties of which can be tuned by electronic structure design.

8.2 Magnonic excitations in ferromagnetic kagome lattice

In this section, the influence of electronic orbital magnetism on magnonic properties are investigated by referring to an effective Hamiltonian of spin-waves of a ferromagnet on a two-dimensional kagome lattice, which is given by

$$\begin{aligned} H = &- \frac{1}{2} \sum_{ij} J_{ij} \mathbf{S}_i \cdot \mathbf{S}_j - \frac{1}{2} \sum_{ij} \mathbf{D}_{ij} \cdot (\mathbf{S}_i \times \mathbf{S}_j) \\ &- \mathbf{B} \cdot \kappa^{\mathrm{TO}} \sum_{ijk} \hat{\mathbf{e}}_{ijk} [\hat{\mathbf{S}}_i \cdot (\hat{\mathbf{S}}_j \times \hat{\mathbf{S}}_k)] - \mu_{\mathrm{B}} \mathbf{B} \cdot \sum_i \mathbf{S}_i, \end{aligned} \tag{8.4}$$

where J_{ij} mediates the Heisenberg exchange between spins $\mathbf{S}_i$ and $\mathbf{S}_j$ on sites i and j, the second term is the antisymmetric DMI quantified by vectors $\mathbf{D}_{ij}$, and the fourth term couples the spins to an external magnetic field $\mathbf{B}$. In addition, we extend the Hamiltonian by the ring-exchange term in Eq. (8.4) to include explicitly the interaction between the magnetic field and the TOM [178, 48, 7]. This term is given by the product of the SSC and the topological orbital susceptibility κ^{TO} [15, 16]. Owing to the symmetry of the planar kagome lattice, the TOM, and the DMI vectors are perpendicular to the film plane (along the z-axis, as shown in Figure 8.2 (a)), along which we also apply the external magnetic field of magnitude B. Theoretically, the topological orbital susceptibility κ^{TO} is $\mathbf{k}$ dependent parameter, but here we treat it as a constant to simplify the calculation and analysis.

In the toy model, we consider in our analysis only nearest-neighbor interactions except for the Heisenberg term, where we include next-nearest neighbors as well. The nearest-neighbor Heisenberg coupling is set as $J_1 = 1meV$, and the next-nearest-neighbor strength amounts to $J_2 = 0.1\, J_1$ unless stated otherwise, and the spin-moment length S is fixed to 1. For the magnitude of topological orbital susceptibility κ^{TO}, we choose a representative value of

$-0.5\,\mu_B$ – a value not only motivated by recent material studies [12, 16, 179], but also corresponding to the lower bound of κ^{TO}-range found in Section 8.1 for small deviations from the ferromagnetic state. As follows from the model considerations, the range of values for κ^{TO} exhibited by the electrons living on a kagome lattice is very large, and one should keep in mind that the effects discussed below can be further enhanced by engineering the electronic structure and the values of κ^{TO}. This route of material design is distinctly different from that associated with the design of the spin-orbit strength, taken routinely in conventional spin-orbitronics.

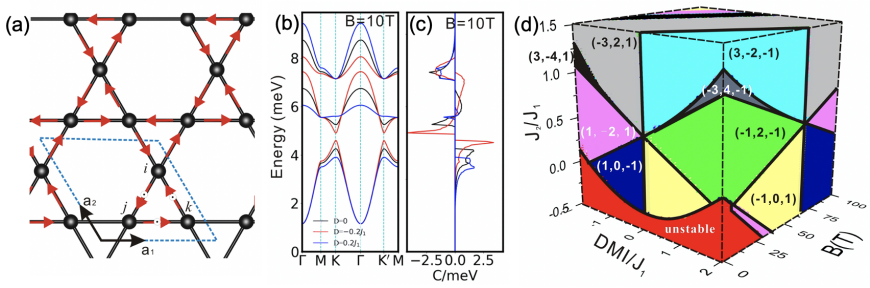

FIGURE 8.2: (a) The unit cell of kagome lattice is indicated by blue dotted line. The directions of DMI are shown in the triangle. (b, c) Magnon dispersion and the corresponding Chern number of isoenergy in a magnetic field of 10 T. Black, blue and red lines correspond to different DMI values of 0 meV, $0.2J_1$, and $-0.2J_1$, respectively. (c) Topological phase diagram of the magnonic bands of a kagome ferromagnet as a function of the second nearest-neighbor Heisenberg coupling J_2 and Dzyaloshinskii-Moriya interaction (DMI) (in units of the nearest-neighbor Heisenberg coupling J_1), as well as external magnetic field B (in Tesla). Colors highlight different phases that are characterized by sets (C_1, C_2, C_3) of Chern numbers. The unstable ferromagnetic phase is shown in red.

To obtain the magnonic bands and the corresponding topology, the linear spin-wave theory [172, 76] is used, which we reformulate first in terms of bosonic ladder operators a_i and $a_i^\dagger$ via the Holstein-Primakoff transformation [51]. Similarly to the previous approximation to treat the effect of chirality [7], only the quadratic terms are kept in the effective spin-wave Hamiltonian. Within the linear theory, the SSC χ_{ijk}, coupling directly to the magnetic field in Eq. (8.4), can be expressed as [7]:

$$\chi_{ijk} = \frac{i}{S}(a_i^\dagger a_j - a_i a_j^\dagger + a_j^\dagger a_k - a_j a_k^\dagger + a_k^\dagger a_i - a_k a_i^\dagger). \tag{8.5}$$

A Fourier transform of the bosonic ladder operators is performed to map from real space to momentum space. Then, the Hamiltonian matrix $H(\mathbf{k})$ at the spin-wave vector $\mathbf{k} = (k_x, k_y)$ is diagonalized to obtain the eigenvectors and the eigenvalue of the spin-waves. We address the topological character

of the magnonic bands by computing the Chern number C_n, given by $C_n = \frac{1}{2\pi}\int \Omega^{xy}_{n\mathbf{k}}\, d\mathbf{k}$, where the integral is performed over the first Brillouin zone (BZ), and $\Omega^{xy}_{n\mathbf{k}}$ represents the magnon Berry curvature of the nth spin-wave branch calculated based on Eq. (4.14).

The magnonic bands and the corresponding Chern number of isoenergy are shown in Figure 8.2. The dispersion of the three spin-wave branches in the presence of an external magnetic field of $10\,\mathrm{T}$ is shown in Figure 8.2 (b). In the absence of DMI, the Chern numbers of magnon bands from lowest to highest exhibit 1, 0, and -1, solely due to the coupling of the magnetic field to the SSC. The distribution of Berry curvature is reflected in Figure 8.2 (c), from which we can see that the maximum berry curvature is located around the $\mathbf{K}$ point. By including the effect of DMI, we find that the coupling to the vector spin chirality modifies the dispersion without changing the topology of the bands for this choice of parameters. While the microscopic origin of interactions with vector and scalar spin chiralities which enter Eq. (8.4) is fundamentally different, their roles for the resulting magnon dispersion are rather similar at the level of linear spin-wave theory. Based on the obtained spin-wave spectra and Berry curvature calculations, we present in Figure 8.2 (d) the complete topological phase diagram as a function of the model parameters entering the Hamiltonian. Sampling the nearest-neighbor coupling J_2, the DMI strength, and the magnitude of the B-field, we identify eight non-trivial phases in addition to an unstable ferromagnetic state. These phases come in pairs with an opposite overall sign in the set of Chern numbers.

8.3 Imprinting topological orbital magnetism by magnons

In this section, the mechanism of TOM generated by magnons excitation through SSC is explored. We refer to this quantity as the local TOM of the n-th magnon branch and access it according to

$$L^{\mathrm{TOM}}_{n\mathbf{k}} = \kappa^{\mathrm{TO}} \langle \Psi_{n\mathbf{k}} | \chi(\mathbf{k}) | \Psi_{n\mathbf{k}} \rangle, \tag{8.6}$$

where $\Psi_{n\mathbf{k}}$ represent the eigenvector of nth branch for $\mathbf{k}$ vector and $\chi(\mathbf{k})$ is the Fourier transform of the SSC. The value of the local TOM for different magnon branches is presented in Figure 8.3 (a–c), where the magnitude of TOM is represented by the line thickness. While either finite DMI or B-field are necessary to activate the local TOM, the Γ point typically hosts the minima and maxima of $L^{\mathrm{TOM}}_{n\mathbf{k}}$ in our model. Specifically, the local TOM of the lowest spin-wave branch reaches its global minimum at Γ whereas the higher magnon bands carry the maximal values as they correspond to precessional modes with an innately larger SSC. Clearly, the complex interplay between DMI and the orbital Zeeman coupling modifies not only the magnon topology but imprints also on the local TOM. In particular, the ordering of the states with the positive and negative sign of $L^{\mathrm{TOM}}_{n\mathbf{k}}$ is inverted during the

topological phase transition, which directly links the nature of electronic orbital magnetism with non-trivial topology of magnonic bands.

Since the local orbital moment carried by magnons depends strongly on the band and position in the Brillouin zone, the effect of finite temperature which results in the excitation of magnons with finite energy, can give rise to a net magnon-mediated electronic orbital magnetization. To show this, we introduce a finite temperature T in our spin system, and calculate the orbital response of the electronic bath. The temperature dependence of the TOM is represented as

$$\langle \mathbf{L}^{\mathrm{TOM}} \rangle_T = \kappa^{\mathrm{TO}} \sum_{ijk} \hat{\mathbf{e}}_{ijk} \langle \chi_{ijk} \rangle_T, \tag{8.7}$$

where $\langle \chi_{ijk} \rangle_T$ denotes the expectation value of the scalar spin chirality.

The Eq. (8.7) is proved as follows. We know that the Hamiltonian in momentum space is quadratic and can thus be written as:

$$H = \sum_{ij} h_{ij} a_i^\dagger a_j = \mathbf{a}^\dagger \hat{h}\, \mathbf{a}, \tag{8.8}$$

where $\mathbf{a}^\dagger$ and $\mathbf{a}$ stand for basis vectors formed by the set of ladder operators, and $\hat{h}$ is the matrix representation of the Hamiltonian. After solving the corresponding eigenvalue problem of $\hat{h}$, we obtain the matrix of eigenvectors $\hat{U}$, and the diagonal matrix $\hat{\epsilon}$ containing the eigenvalues, i.e., $\hat{\epsilon} = \hat{U}^\dagger \hat{h}\, \hat{U}$. This information provides an alternative representation of the Hamiltonian in terms of new basis vectors $\mathbf{b}$ and $\mathbf{b}^\dagger$ (with the identity $\mathbf{a} = \hat{U}\mathbf{b}$):

$$H = \mathbf{b}^\dagger \hat{\epsilon}\, \mathbf{b} = \sum_i \epsilon_i b_i^\dagger b_i. \tag{8.9}$$

To determine the temperature dependence of TOM via the average scalar spin chirality $\langle \chi_{ijk} \rangle_T$, according to Eq. (8.5), we need to evaluate expressions of the form $\frac{\mathrm{i}}{S} \sum_{ij} o_{ij} \langle a_i^\dagger a_j \rangle_T$, where o_{ij} is the matrix element of a general operator $\hat{O}$:

$$\frac{\mathrm{i}}{S} \sum_{ij} o_{ij} \langle a_i^\dagger a_j \rangle_T = \frac{\mathrm{i}}{S} \langle \mathbf{a}^\dagger \hat{O} \mathbf{a} \rangle_T = \frac{\mathrm{i}}{S} \langle \mathbf{b}^\dagger \hat{U}^\dagger \hat{O} \hat{U} \mathbf{b} \rangle_T = \frac{\mathrm{i}}{S} \sum_{ij} \langle b_i^\dagger b_j \rangle_T (\hat{U}^\dagger \hat{O} \hat{U})_{ij}. \tag{8.10}$$

Since magnons are bosons that follow the Bose distribution function $n_{\mathrm{B}}(\epsilon) = [\exp(\beta\epsilon) - 1]^{-1}$ with $\beta = 1/k_{\mathrm{B}}T$, the above equation can be simplified by taking into account the relation

$$\langle b_i^\dagger b_j \rangle_T = \delta_{ij} n_{\mathrm{B}}(\epsilon_i). \tag{8.11}$$

Substituting this result back into the temperature-dependent expectation value of the scalar spin chirality, we arrive at the final expression for the overall

TOM perpendicular to the kagome plane, as used in the main text:

$$\begin{aligned}\langle L^{\mathrm{TOM}}\rangle_T &= \kappa^{\mathrm{TO}} \sum_n \int n_{\mathrm{B}}(\epsilon_{n\mathbf{k}}) \langle \Psi_{n\mathbf{k}}|\chi(\mathbf{k})|\Psi_{n\mathbf{k}}\rangle d\mathbf{k} \\ &= \sum_n \int_{\mathrm{BZ}} n_{\mathrm{B}}(\epsilon_{n\mathbf{k}})\, L^{\mathrm{TOM}}_{n\mathbf{k}}\, d\mathbf{k},\end{aligned} \tag{8.12}$$

where the integral is performed over the two-dimensional BZ, and $\chi(\mathbf{k})$ is the Fourier transform of Eq. (8.5).

In Figure 8.3 (d–g) we analyze the sum of the local TOM weighted by the occupation number of each spin-wave branch at a given temperature, i.e.,

$$\ell(\mathbf{k}) = \sum_n L^{\mathrm{TOM}}_{n\mathbf{k}} n_{\mathrm{B}}(\epsilon_{n\mathbf{k}}). \tag{8.13}$$

Depending on T, the number of excited magnons is different in each branch, which leads to a non-trivial distribution of $\ell(\mathbf{k})$ in momentum space, as shown in Figure 8.3 (d–g) for the model with finite B-field but zero DMI. At low T, as shown in Figure 8.3 (d), only the magnons around the Γ-point from the first branch can be excited, leading to small local contributions around the BZ center. As the temperature is increased, for example, to $T = 25\,\mathrm{K}$, all spin-wave states from the first branch are excited such that $\ell(\mathbf{k})$ peaks in the M point with moderate magnitude as shown in Figure 8.3 (e). If additionally magnons from the higher branches contribute at elevated temperatures, the maximum of $\ell(\mathbf{k})$ occurs at the Γ point, where the local TOM of the corresponding magnon states is the largest.

The total TOM carried by thermally activated magnons per unit cell is calculated based on the Eq. (8.12) and the results are shown in Figure 8.4, illustrating the B, T-dependence of the overall TOM for various DMI coupling strengths. On the one hand, as more magnons become available to carry the TOM, higher temperatures enhance the magnitude of $\langle L^{\mathrm{TOM}}\rangle_T$ in the spin-wave system. On the other hand, the roles of orbital Zeeman coupling and DMI are intertwined in generating TOM. For example, while TOM locally vanishes at zero DMI and B-field, a DMI with positive coupling strength generally counteracts the effect of the magnetic field on TOM if κ^{TO} is negative. Overall, for non-trivial choices of these parameters, as shown in Figure 8.4 (d), at low T the total TOM increases linearly and dependent on the value of κ^{TO}.

The total TOM emerges as a quantity which can be readily measured experimentally by referring to techniques which are sensitive to orbital magnetization in solids [180, 181, 182, 183]. Besides, the different temperature response of spin and TOM for magnetization provides us another option to detect the TOM. The sizeable magnitude of the effect that we predict not only

lends itself to an unambiguous observation, but can also influence significantly the temperature dependence of the overall magnetization in a sample, providing thus an additional "anomalous" orbital channel to the conventional mechanism of magnetization variation mediated by thermally excited magnons [74, 184, 185]. Given the much stronger sensitivity of TOM to electronic structure changes, as compared to the spin, we suggest that the magnon-driven orbital magnetism can serve as a unique tool in tracking the electronic structure dynamics in various types of setups. Besides, as we observe that the sign of $\langle L^{\mathrm{TOM}} \rangle_T$ correlates with the ordering of the topological spin-wave bands and their respective Chern numbers, we suggest to exploit the total topological orbital moment as an indicator of topological dynamics of magnons.

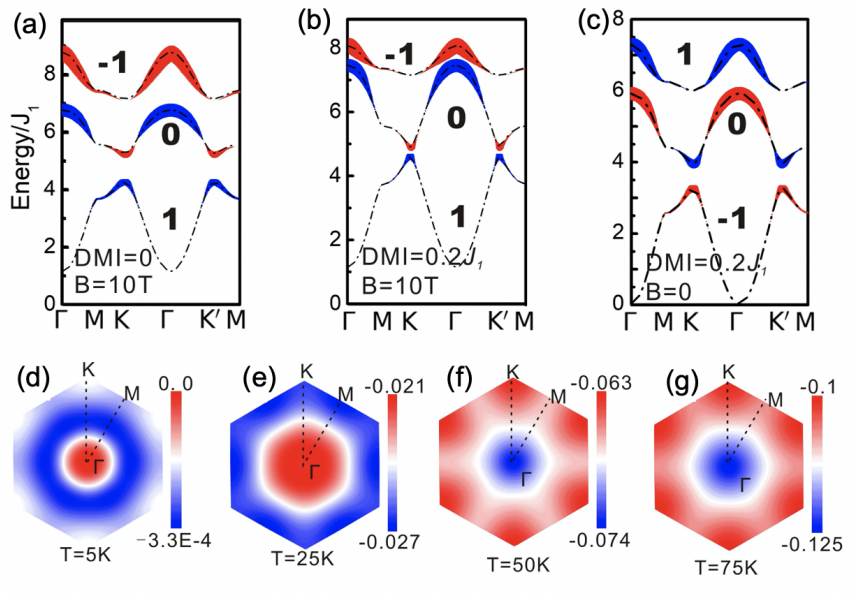

FIGURE 8.3: Imprinting electronic orbital magnetism by magnons in a kagome ferromagnet. (a–c) Fat band analysis for the magnonic bands of the model for the values of the Dzyaloshinskii-Moriya interaction (DMI) (in units of the nearest-neighbor Heisenberg coupling J_1), and magnetic field B specified at the bottom. Red and blue colors represent positive and negative sign of the local topological orbital moment (TOM) $L^{\mathrm{TOM}}_{n\mathbf{k}}$, respectively, and the line thickness denotes the corresponding magnitude. Bold integers indicate the Chern numbers of the spin-wave bands. (d–g) Distribution of the local TOM in the Brillouin zone for different temperatures, after summing over all magnon branches weighted by the Bose distribution. The color map is in units of μ_{B}, and the model parameters of the panel (a) are used.

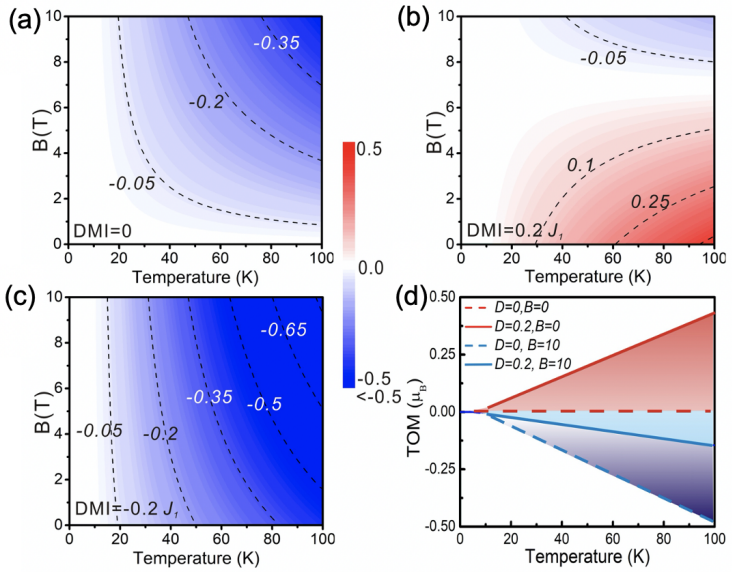

FIGURE 8.4: Overall TOM of the spin-wave system as a function of magnetic field and temperature. The panels (a–c) present phase diagrams for the DMI strengths of 0, $0.2J_1$, and $-0.2J_1$, respectively, with the color map indicating the net TOM in units of μ_B per unit cell. In (d), solid and dotted lines correspond to DMI strengths of 0 and $0.2J_1$, respectively, and the magnetic field is given in Tesla.

8.4 Driving orbital currents by magnons

From the discussion of Section 8.3, we get the conclusion that a finite TOM, stemming from orbital electronic currents, can be triggered by thermally activated magnons. This observation suggests that TOM is intimately linked to thermal spin transport, which is mediated by the coupling of the SSC to the bath of electrons in the system.

8.4.1 Orbital Nernst effect of magnons

Analogy to the well-known magnon Nernst effect, we coin the orbital Nernst effect of magnons, which is illustrated in Figure 8.5. The phenomenon of orbital Nernst effect relates spatial temperature gradients to the emergence of topological orbital currents via $j_x^{\mathrm{TOM}} = \kappa_{\mathrm{ONE}}^{xy}(\nabla T)_y$, where $\kappa_{\mathrm{ONE}}^{xy}$ stands for the topological orbital Nernst conductivity, which within the semiclassical theory reads

$$\kappa_{\mathrm{ONE}}^{xy} = -\frac{k_{\mathrm{B}}}{4\pi^2\mu_{\mathrm{B}}} \sum_n \int_{\mathrm{BZ}} c_1(n_{\mathrm{B}}(\epsilon_{n\mathbf{k}}))\, \Omega_{n\mathbf{k}}^{xy} L_{n\mathbf{k}}^{\mathrm{TOM}}\, d\mathbf{k}\,, \tag{8.14}$$

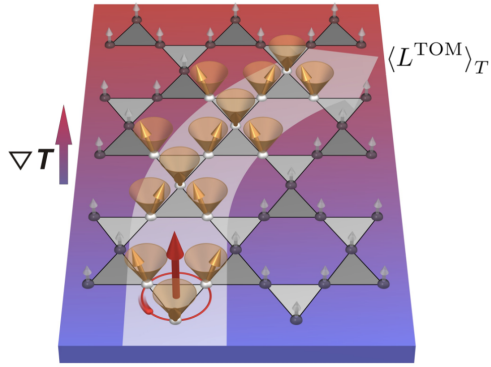

FIGURE 8.5: Sketch of the orbital Nernst effect of magnons for a ferromagnet on an example of the kagome lattice. While the generation of a magnon (orange arrows) imprints an average scalar spin chirality into the system and leads to the generation of electronic TOM (red arrow), the generation of a magnon flow in a temperature gradient ∇T results in a transverse deflection of magnons and corresponding TOM-mediated drag of the orbital angular momentum, denoted by $\langle L^{\mathrm{TOM}} \rangle_T$ – which we refer to as the orbital Nernst effect.

where $c_1(\tau) = \int_0^\tau \ln[(1+t)/t]dt = (1+\tau)\ln(1+\tau) - \tau \ln \tau$. In essence, the latter relation quantifies the fundamental mechanism behind a magnon – which develops a transverse velocity proportional to the Berry curvature in an applied temperature gradient – "dragging" with it the electronic orbital angular momentum which is generated by non-zero SSC inherent to the magnon. In contrast to the usual spin Nernst effect of magnons [96, 186, 77], the conductivity in Eq. (8.14) characterizing the orbital Nernst effect depends explicitly on the local TOM of the magnon branches.

8.4.2 Comparison of the orbital Nernst effect and magnon Nernst effect

Based on Eq. (8.14), we demonstrate the existence of the orbital Nernst effect via explicit calculation. In Figure 8.6 (a, b) and Figure 8.7 (b) the non-trivial dependence of the orbital Nernst effect on T and on the model parameters, as well as its correlation with the topology of the magnon bands are summarized. Although the orbital Nernst effect has a distinct microscopic origin in the orbital electron-magnon coupling, we predict that the corresponding conductivity can reach the order of k_{B}/π. When assuming a distance of 5 Å between two kagome layers, an orbital Nernst conductivity of $(2\pi)^{-1}k_{\mathrm{B}}$ is equivalent to the value 4.394×10^{-15} $\mathrm{Jm^{-1}K^{-1}}$, or 66786 $\hbar \mathrm{e}^{-1}\mu\mathrm{Acm^{-1}K^{-1}}$, which is comparable to the values known as the spin Nernst effect of magnons or spin Nernst effect of electrons [77, 186, 76, 187, 188, 189]. Additionally, we emphasize that the magnitude of the effect can be further enhanced by

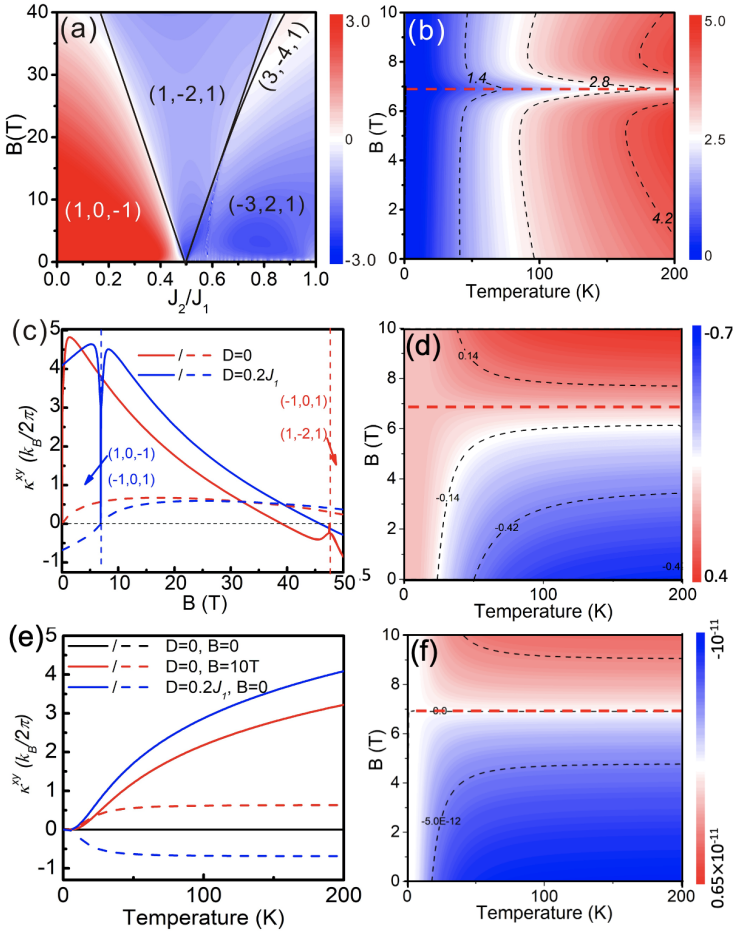

FIGURE 8.6: Driving orbital currents by magnons: the orbital Nernst effect. (a) Phase diagram of the orbital Nernst effect. Dependence of the orbital Nernst conductivity $\kappa^{xy}_{\rm ONE}$ on magnetic field B and second nearest-neighbor Heisenberg coupling J_2 (in units of the nearest-neighbor Heisenberg coupling J_1) at $T = 200\,$K and zero Dzyaloshinskii- Moriya interaction (DMI). Solid black lines are the boundaries between different topological phases characterized by the Chern numbers of the three magnon branches. (b) $\kappa^{xy}_{\rm ONE}$ as a function of B and temperature T for the model with DMI strength of $0.2J_1$. (c,e) Comparison of the $\kappa^{xy}_{\rm ONE}$ (solid lines) and magnon Nernst conductivity $\kappa^{xy}_{\rm N}$ (dashed lines). (c) $\kappa^{xy}_{\rm ONE}$ and $\kappa^{xy}_{\rm N}$ as a function of B for the model at 200 K with DMI strength of 0 (red) and $0.2J_1$ (blue). The different topological phases are distinguished with a thin vertical line. (e) $\kappa^{xy}_{\rm ONE}$ and $\kappa^{xy}_{\rm N}$ as a function of T for different strengths of the DMI and B. (d, f) Magnon Nernst conductivity $\kappa^{xy}_{\rm N}$ and thermal Hall conductivity $\kappa^{xy}_{\rm TH}$ as a function of B and temperature T for the model with DMI strength of $0.2J_1$.

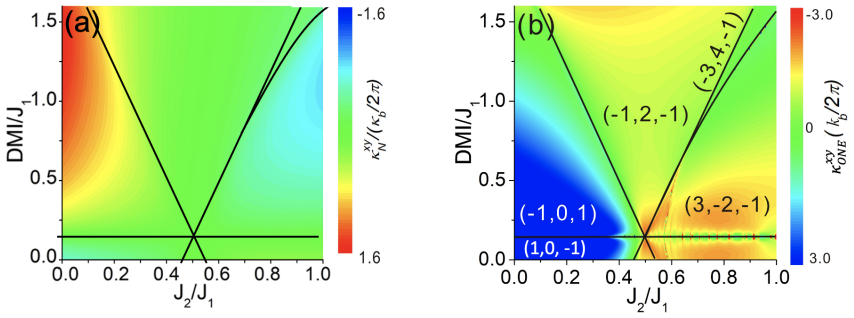

FIGURE 8.7: (a) Phase diagram of the magnon Nernst effect. Dependence of the magnon Nernst conductivity κ_{N}^{xy} on DMI D and second nearest-neighbor Heisenberg coupling J_2 (in units of the nearest-neighbor Heisenberg exchange coupling J_1) at $T = 200\,\mathrm{K}$ and $B = 5\mathrm{T}$. (b) Phase diagram of the orbital Nernst effect of magnon. Dependence of the magnon Nernst conductivity $\kappa_{\mathrm{ONE}}^{xy}$ on DMI D and second nearest-neighbor Heisenberg exchange coupling J_2 at $T = 200\,\mathrm{K}$ and $B = 5\mathrm{T}$. Solid black lines are the boundaries between different topological phases characterized by the Chern numbers of the three magnon branches.

proper electronic structure engineering of the topological orbital susceptibility, which in its nature does not rely on the presence of spin-orbit interaction in the system. As such, our finding underlines the strong potentiality of the orbital Nernst effect for the realm of spincaloritronics and marks this effect as an entry point for ideas evolving around magnon-mediated orbitronics.

Besides, our analysis obtained by the calculation in Figure 8.6 and Figure 8.7, indicates that both DMI and the coupling of the external magnetic field to the SSC can generate a finite orbital Nernst conductivity. Comparing these results in more detail, we note that the sign of $\kappa_{\mathrm{ONE}}^{xy}$ is the same in topological phases in which the sets of Chern numbers differ by a global sign as shown in Figure 8.6 (c) and Figure 8.7 (b). This invariance stems from the product of the two microscopic quantities in Eq. (8.14), each of which changes its individual sign as the Chern numbers are reversed. Still, as exemplified in Figure 8.6 (a-c) and Figure 8.7 (b), the orbital Nernst effect is characteristic to the non-trivial magnon topology of distinct phases. Close to topological phase transitions, the orbital Nernst effect changes abruptly and thus behaves rather differently compared to thermal Hall and magnon Nernst effects, see Figure 8.6 (b–f). As a consequence, the conductivity $\kappa_{\mathrm{ONE}}^{xy}$ can in principle reach very large values near the phase boundary as shown in Figure 8.7 (b). Since the orbital Nernst effect is absent without the B-field and DMI, the peak structure in Figure 8.6 (b,c) for a magnetic field of about $7\,\mathrm{T}$ can be understood as a result of the competition between the effects of orbital Zeeman coupling and DMI, which results in a strongly suppressed

orbital Nernst effect. Besides, Figure 8.6 (b, d, e) reveal the qualitative difference in the temperature dependence of the orbital Nernst effect, conventional Nernst effect and thermal Hall effect of magnon. The peculiar behavior of the orbital Nernst effect in response to an external magnetic field can be used to disentangle it from the magnon Nernst effect experimentally.

8.5 Discussion

In this chapter, we present a new mechanism to build a link between the magnonic and orbitronics. The ferromagnetic kagome lattice is selected as an example to demonstrate the characteristic, among material representatives of which one can name for example Cu(1-3,bdc) [190] or $Nd_3Sb_3Mg_2O_{14}$ [191]. Furthermore, the conclusions drawn from our analysis go well beyond this particular class of materials, and include for instance collinear or non-collinear states on a hexagonal, pyrochlore, B20 and Mn_3Ge quasi-kagome type of lattice [162, 192, 12, 16, 29], as well as their thin films. While in the latter classes the magnon drag of orbital momentum is non-vanishing, a precursor of prominent magnon-driven orbital phenomena is a large topological orbital susceptibility κ^{TO} in a given material of the order of that exhibited, *e.g.*, by MnGe [16], Mn/Cu(111) [12], or Mn_3Ge [179]. The latter quantity can be estimated from microscopic calculations, as well as from experiment, as first approximation κ^{TO} is given by the orbital susceptibility of the system [15].

The uncovered mechanism of magnon-driven chirality accumulation has far-reaching consequences for the transport properties of systems which exhibit such chirality. For example, it will result in the generation of topological Hall or topological spin Hall effect of the underlying electronic bath [193, 194, 195, 194], which will contribute to the temperature dependence of the anomalous Hall conductivity even in nominally collinear magnets [196]. On the other hand, magnon-driven orbital magnetism brings the orbital angular momentum variable into the game of magnon-based spincaloritronics, which is conventionally associated with the generation and transport of spin. Unleashing the orbital channel for the magnon-mediated effects poses a key question of the role of orbital magnetism for the temperature-dependent magnetization dynamics, however, it also opens a number of exciting possibilities for direct applications. Given the sensitivity of the orbital effects to the topology of magnonic bands and generally magnonic properties, we suggest that accessing the magnon-mediated dynamics of orbital properties can serve as a unique tool of tracking the topological dynamics of magnons. Moreover, our findings also point at an exciting possibility of exploiting properly engineered orbital injection for excitation of specific magnonic modes via the inverse orbital Nernst effect. As in topologically-complex materials the electronic topology is directly related to the orbital properties [197], this link can be used for realizing hybrid non-trivial electron-magnon topologies. Overall, the uncovered here orbital electron-magnon coupling bares various prospects for integration of spin-orbitronics schemes into magnonic setups and vice versa, which shall be explored in the future.

In the next chapter, we present the application of the orbital Nernst effect in other systems, where the modulation of orbital magnetism on magnonic properties are also demonstrated.

Chapter 9

Magnon-driven orbitronics in non-collinear systems

In Chapter 8, we introduce a mechanism to generate and transport topological orbital magnetization by magnonic excitations, with a example of ferromagnetic kagome lattice. Except for the ferromagnetic kagome lattice, magnon-meidated topological orbital magnetization also exists in other lattices, *e.g.*, a ferromagnetic honeycomb lattice as well as non-collinear systems. In this chapter, we present the application of magnon-driven orbitronics in non-collinear magnetic systems, *e.g.*, antiferromagnetic kagome lattice and Mn_3Ge.

Results presented in Chapter 9.2 have already been published:
Li-chuan Zhang, et. al., Communications Physics, 3, 227, 2020.

9.1 Magnon-driven orbitronics in antiferromagnetic kagome lattice

9.1.1 Establishing the model

Nowadays, the antiferromagnetic (AFM) kagome magnets are studied intensively and many compounds have already been synthesized in this field, *e.g.*, $YCu_3(OH)_6Cl_3$ [198], $Nd_3Sb_3Mg_2O_{14}$ [191], etc. In this section, we investigate the magnon-mediated electronic topological orbital magnetization and its transport properties in non-collinear AFM kagome lattice with coplanar 120°, shown in Figure 9.1. The effective spin Hamiltonian of the model is given in Eq.(9.1).

$$\begin{aligned} H = &- \sum_{\langle ij \rangle} J_{ij} \mathbf{S}_i \cdot \mathbf{S}_j - \mathbf{B} \cdot \kappa^{\mathrm{TO}} \sum_{ijk} \hat{\mathbf{e}}_{ijk} [\hat{\mathbf{S}}_i \cdot (\hat{\mathbf{S}}_j \times \hat{\mathbf{S}}_k] \\ &- \mu_{\mathrm{B}} g_e \mathbf{B} \sum_i \mathbf{S_i} + \sum_{ij} \mathbf{D}_{ij} \cdot (\mathbf{S}_i \times \mathbf{S}_j) - \sum_i A (\hat{\mathbf{n}}_i \mathbf{S}_i)^2, \end{aligned} \tag{9.1}$$

In Eq.(9.1), the J_{ij} mediates the isotropic Heisenberg exchange interaction between spins $\mathbf{S}_i$ and $\mathbf{S}_j$ on sites i and j. The second and third terms are Zeeman coupling terms, where an external magnetic field $\mathbf{B}$ couples the electronic orbital moment and spin moment separately. The fourth term is the

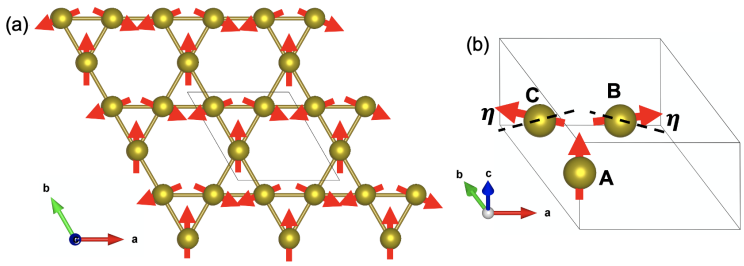

FIGURE 9.1: Schematic structure of monolayer antiferromagnetic kagome lattice. The top view and perspective view are shown in (a) and (b), respectively. The unit cell is outlined with a black line, where the yellow ball represents the magnetic atom and its moment direction is revealed by the red arrow . The canting angle η is marked in (b) aroused by the magnetic field.

antisymmetric Dzyaloshinskii-Moriya interaction (DMI) quantified by vectors $\mathbf{D}_{ij}$, and the last term is the single-ion anisotropy energy with respect to the local in-plane easy axes $\hat{\mathbf{n}}_i$. In Eq. (9.1), the electronic orbital moment is given by the product of the scholar spin chirality (SSC) and free electron coupling, where the coupling strength is characterized by the topological orbital susceptibility κ^{TO} [15, 16]. To simplify the calculation, the topological orbital moment (TOM), DMI vectors, and the external magnetic field are chosen perpendicular to the film plane (along the z-axis).

9.1.2 The canting angle η

Firstly, the spin configuration influenced by the out-of-plane magnetic field in the AFM kagome lattice is explored. As shown in Fig. 9.1, the direction of magnetic moments can be represented with the vector:

$$\hat{\mathbf{S}}_i = (\cos\eta\cos\phi_i, \cos\eta\sin\phi_i, \sin\eta), \tag{9.2}$$

where ϕ_i is the azimuthal angle and η represents the out-of-plane canting angle. In this section, the azimuthal angles ϕ_i are assumed to be chirally ordered, i.e., $\phi_i = \phi_0$ for $i \in \mathrm{A}$, $\phi_i = \phi_0 + 2\pi/3$ for $i \in \mathrm{C}$, and $\phi_i = \phi_0 + 4\pi/3$ for $i \in \mathrm{B}$. In our model, we set $\phi_0 = \pi/2$, and then the the spin vector of each magnetic atoms can be represented as:

$$\begin{aligned}
\mathbf{S}_A &= S(0, \cos\eta, \sin\eta), \\
\mathbf{S}_B &= S(-\frac{\sqrt{3}}{2}\cos\eta, -\frac{1}{2}\cos\eta, \sin\eta), \\
\mathbf{S}_C &= S(\frac{\sqrt{3}}{2}\cos\eta, -\frac{1}{2}\cos\eta, \sin\eta),
\end{aligned} \tag{9.3}$$

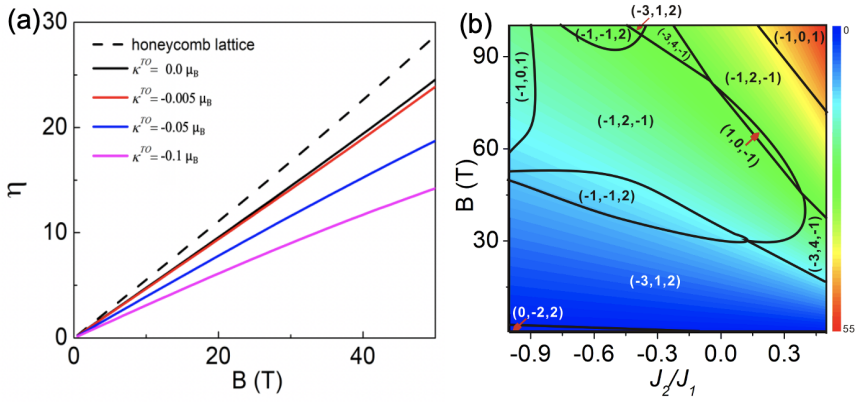

FIGURE 9.2: (a) The relationship between the canting angle η and the out-of-plane magnetic field $\mathbf{B} = (0, 0, B)$ (in Tesla) for different value of topological orbital susceptibility κ^{TO} with $J_1 = -2$ meV, $J_2 = 0.1J_1$ and $A = 0.02J_1$. (b) Topological phase diagram of the magnon bands in a antiferromagnet kagome lattice with a function of J_2 (in units of J_1) and magnetic field value B with parameters $D_z = 0.1J_1$, $\kappa^{\mathrm{TO}} = 0.05\mu_{\mathrm{B}}$ and $A = 0.02J_1$. The colors highlight the canting angle of the ground state with the unit degree. Different phases are outlined by the black line and marked by sets (C_1, C_2, C_3) of Chern numbers.

Here, S is the length of the spin moment. In our model, the exchange interactions are considered only upto the second-nearest-neighbor. From the Hamiltonian Eq. (9.1), the classical total energy of each unit cell is calculated:

$$\begin{aligned} E_{\mathrm{unit}}(\eta) = &-\frac{3J_1S^2}{2} - \frac{3J_2S^2}{2} + \frac{9J_1S^2}{2}\cos 2\eta + \frac{9J_2S^2}{2}\cos 2\eta \\ &- 3\sqrt{3}B\kappa^{\mathrm{TO}}S^3\cos^2\eta\sin\eta - 3BS\sin\eta \\ &+ (3\sqrt{3}DS^2 - 3AS^2)\cos^2\eta, \end{aligned} \tag{9.4}$$

Obviously, the energy of the Hamiltonian is the function of η, and the minimum energy of the system is obtained through solving the Eq. (9.5):

$$\begin{aligned} \frac{\partial E_{\mathrm{unit}}(\eta)}{\eta} = &-9(J_1 + J_2)S^2\sin 2\eta + 6\sqrt{3}B\kappa^{\mathrm{TO}}S^3\cos\eta\sin^2\eta \\ &- 3\sqrt{3}B\kappa^{\mathrm{TO}}S^3\cos^3\eta - 3BS\cos\eta \\ &- 2(3\sqrt{3}DS^2 - 3AS^2)\cos\eta\sin\eta = 0, \end{aligned} \tag{9.5}$$

As the range of $\sin\eta$ and $\cos\eta$ are from -1 to 1, we find that only one solution of η satisfies the condition, which corresponds to the minimum energy.

In this section, we set the model parameters as $S = 0.5$, $J_1 = -2$ meV,

$J_2 = 0.1J_1$, $\kappa^{\mathrm{TO}} = 0.05\mu_{\mathrm{B}}$, $A = 0.02J_1$. Besides, we set the $\mathbf{D} = (0, 0, D_z)$ with $D_z = 0.1J_1$ for the nearest-neighbor interaction. The magnetic field dependent canting angle η for AFM kagome lattice is shown in Fig. 9.2 (a), where the magnetic field effect on the canting angle η is compared by changing the topological orbital susceptibility κ^{TO}. Under the same external magnetic field, the generated η is different with different κ^{TO}, and it is indicated that η and κ^{TO} are negatively correlated in Figure 9.2 (a). The magnetic field effect on a honeycomb lattice is also calculated to make a comparison. The canting angle of the minimum energy in honeycomb lattice fulfills the equation $\sin\eta = \frac{B/S}{-6J_1+2A}$, which is similar to the previous work [199].

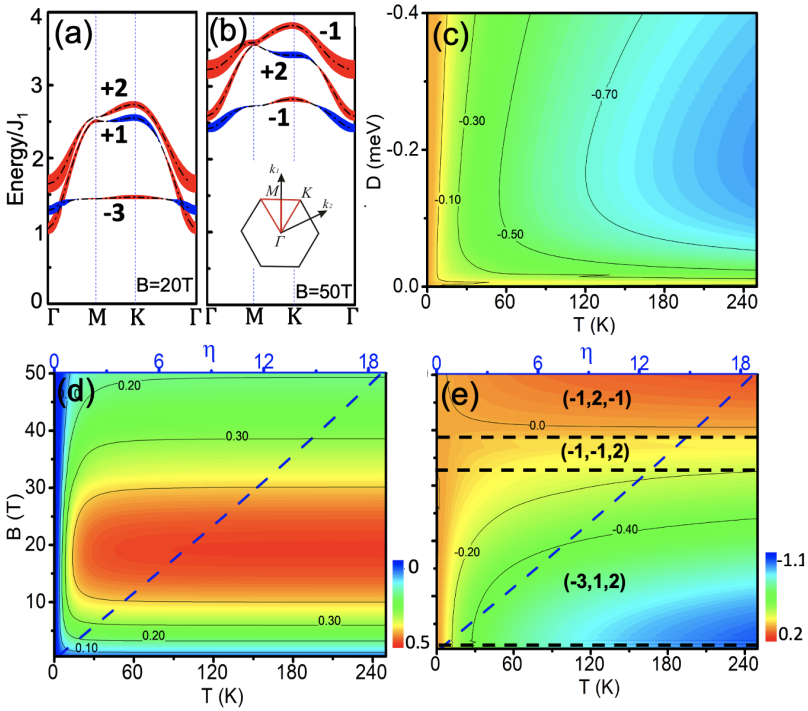

FIGURE 9.3: (a-b) Fat band analysis for the magnonic bands with different B specified at the bottom. Red and blue colors represent positive and negative signs of the local TOM $L^{\mathrm{TOM}}_{n\mathbf{k}}$, respectively, and the line thickness denotes the corresponding magnitude. Bold integers indicate the Chern numbers of the spin-wave bands. (c) Orbital Nernst conductivity $\kappa^{xy}_{\mathrm{ONE}}$ as a function of DMI and temperature with the magnetic field of 10T. (d) Magnon Nernst conductivity κ^{xy}_{N} as a function of B and temperature with DMI strength of $0.1J_1$. (e) $\kappa^{xy}_{\mathrm{ONE}}$ as a function of B and temperature with DMI strength of $0.1J_1$. The blue dotted line for (d, e) represents magnetic field dependent canting angle and the black dotted line indicates the phase boundary. The unit of the color map for (c-e) is chosen as $k_{\mathrm{B}}/2\pi$.

9.1.3 Topological phase diagram and orbital Nernst effect

Based on the linear spin-wave theory (LSWT) [52, 53], we calculate the magnon dispersion and eigenvector of the AFM kagome lattice. To characterize the topology of magnonic bands, the Chern number C_n is calculated, based on $C_n = \frac{1}{2\pi}\int_{BZ}\Omega^{xy}_{n\mathbf{k}}\,d\mathbf{k}$, where the n refers to the nth magnon branch, and $\Omega^{xy}_{n\mathbf{k}}$ is obtained based on Eq. (4.15). Then the topological phase of the system can be marked by sets (C_1, C_2, C_3) of Chern numbers, and the topological phase diagram as the function of J_2 and external out-of plane magnetic field is shown in Figure 9.2 (b). With the increase of magnetic field value B, the canting angle η increases together with the scalar spin chirality and TOM Zeeman coupling, leading to the modulation of topological phase. The complex phase diagram in Figure 9.2 indicates that the noncoplanarity of kagome magnets aroused by the magnetic field has rich topological properties, thus resulting in rich magnonic transport properties in this system.

In order to explore magnonic transport properties, we calculate the topological orbital Nernst conductivity and magnon Nernst conductivity in the presence of an external magnetic field. We first calculate the local TOM of the n-th magnon branch according to $L^{\mathrm{TOM}}_{n\mathbf{k}} = \kappa^{\mathrm{TO}}\langle\Psi_{n\mathbf{k}}|\chi^{\mathrm{noc}}(\mathbf{k})|\Psi_{n\mathbf{k}}\rangle$, where the $\chi^{\mathrm{noc}}(\mathbf{k})$ is the Fourier transform of $\chi^{\mathrm{noc}}_{ijk} = \hat{\mathbf{S}}_i\cdot(\hat{\mathbf{S}}_j\times\hat{\mathbf{S}}_k) = \hat{\mathbf{S}}'_{\mathbf{i}}O_i^{\mathrm{T}}\cdot(O_j\hat{\mathbf{S}}'_{\mathbf{j}}\times O_k\hat{\mathbf{S}}'_{\mathbf{k}})$ between triplets of spins, and the rotation matrix O_i represents the magnetic moment direction at the site i and $\hat{\mathbf{S}}'$ is the unit quasi-spin pointing z direction. The calculated local TOM is shown in Figure 9.3 (a-b).

According to Eq. (8.14) and Eq. (4.29), we calculate the topological orbital Nernst conductivity $\kappa^{xy}_{\mathrm{ONE}}$ and magnon Nernst conductivity κ^{xy}_{N}. The calculated results are shown in Figure 9.3 (c-e), which indicates that the DMI and magnetic field can modulate the value of $\kappa^{xy}_{\mathrm{ONE}}$ and κ^{xy}_{N}, and the value of $\kappa^{xy}_{\mathrm{ONE}}$ is related to the topological phase diagram. Besides, in the calculation, the magnitude of topological orbital susceptibility κ^{TO} is much smaller than the value we chose in Chapter 8 (lower by an order of magnitude) and some noncollinear textures according to the *ab initio* calculation [12, 16, 179], whereas the calculated $\kappa^{xy}_{\mathrm{ONE}}$ is still larger than the calculated κ^{xy}_{N}.

9.2 Orbital Nernst effect in Mn_3Ge

9.2.1 Introduction of Mn_3Ge

In Chapter 8, we select the ferromagnetic kagome lattice as a platform to demonstrate the existence of orbital Nernst effect in collinear systems which do not exhibit chirality in their ground state. Besides, in Section 9.1, we discuss the orbital Nernst effect in non-collinear kagome lattice, and the magnetic field effect on the spin frustration is investigated. In this section, the orbital Nernst effect in realistic material Mn_3Ge is investigated. Mn_3Ge is a compensated noncollinear antiferromagnetic material with a Néel temperature of about 380 K [200], and the spin moment of each Mn atom is about S= 2.5 μ_{B}. The behavior of the TOM with the chirality of spins in Mn_3Ge has

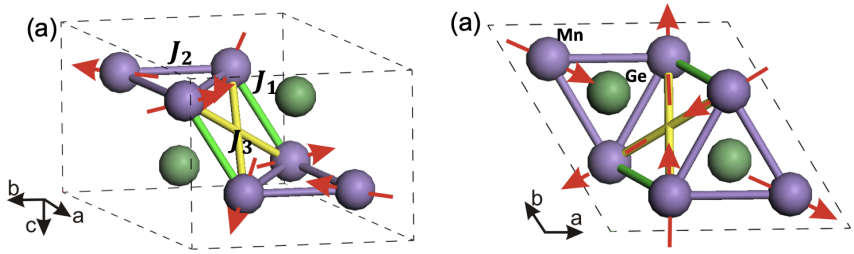

FIGURE 9.4: Perspective view (a) and top view (b) of Mn_3Ge. Three different interaction paths with different colors are marked as J_1, J_2 and J_3. The inter-layer interaction (J_4) is not shown. The Mn atom is represented with the purple ball. The spin direction of each Mn atom is revealed by red arrows.

been studied through *ab initio* calculations [201]. Taking the data for the latter work, the topological orbital susceptibility κ^{TO} is obtained through fitting the TOM as a function of polar angle θ according to Eq. 8.2. We estimate its value, and give a rough value as $-0.1\mu_{\mathrm{B}}$ for this quantity.

9.2.2 Establishing the model for Mn_3Ge

Similar to the method discussed in Section 9.1, the rotation matrix is introduced to deal with the non-collinear antiferromagnetic spin arrangement. Then, the SSC $\chi^{\mathrm{noc}}_{ijk}$ can be represented by the product of rotation matrix and quasi-spin operators. To get the magnon dispersion, the LSWT is used, where the Holstein-Primakoff (HP) transformation [51] is adopted to introduce the quantum spin operators. In the calculation, only the quadratic part of the Hamiltonian (H_2) is kept. After Fourier transformation, the magnon bands are obtained through diagonalizing the dynamical matrix of H_2. More technical details can be seen in Section 2.4.2.

Parameters	J (meV)	**D** (meV)
J_1	-7.5	0
J_2	-6.0	$(0, 0, -0.25)$
J_3	1.2	0
J_4	-1	0
K	0.04	0

TABLE 9.1: Values of the parameters entering the Heisenberg Hamiltonian Eq. 9.6. Four exchange interactions and one single-ion anisotropy parameters are listed. The second nearest-neighbor DMI vector was chosen so as to reproduce the experimental spin-wave dispersion.

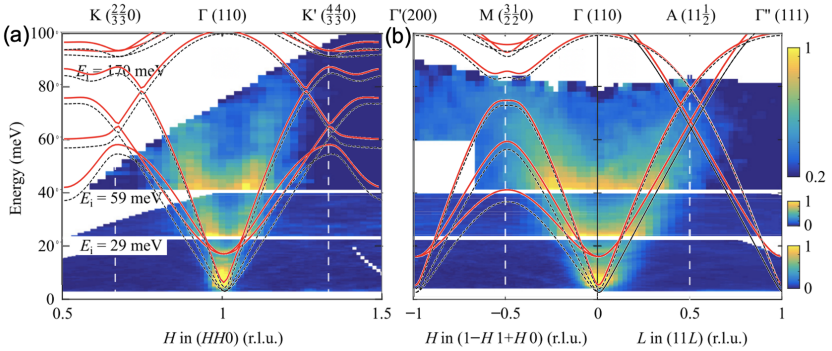

FIGURE 9.5: The comparison between the experimental data and the theoretical calculation of the magnon spectra of Mn_3Ge. The neutron scattering figure is adapted from the Ref. [203], while the red and black dotted lines mark the magnon dispersion calculated with the fitted parameters. The red line is calculated based on the parameters shown in Table. 9.1 and the black dotted line is the calculation performed without DMI. The experimental magnon dispersion at the Γ point exhibits a dispersion of about 17 meV, and the magnitude of the DMI is introduced to reproduce it.

To reproduce the magnonic structure of Mn_3Ge properly, the spin Hamiltonian is modified as:

$$\begin{aligned} H = &- \sum_{\langle ij \rangle} J_{ij} \mathbf{S}_i \cdot \mathbf{S}_j - \sum_{\langle ij \rangle} \mathbf{D}_{ij} \cdot (\mathbf{S}_i \times \mathbf{S}_j) - K \sum_i (\hat{\mathbf{n}}_i \cdot \mathbf{S}_i)^2 \\ &- \mathbf{B} \cdot \kappa^{\mathrm{TO}} \sum_{ijk} \hat{\mathbf{e}}_{ijk} [\hat{\mathbf{S}}_i \cdot (\hat{\mathbf{S}}_j \times \hat{\mathbf{S}}_k)] - \mathbf{B} \cdot \sum_i \mathbf{S}_i, \end{aligned} \tag{9.6}$$

where the third term is introduced to take into account the single-ion anisotropy energy with respect to the local in-plane easy axes $\hat{\mathbf{n}}_i$. The magnon excitation spectrum of Mn_3Ge has been accessed experimentally before [202, 203], and we used the experimental data to estimate the exchange interaction and DMI through the fitting. In our calculation, the exchange interactions are considered up to the fourth nearest neighbor, where different interaction paths are shown in Figure 9.4. To fit the experiment, the second-nearest neighbor DMI is taken into account. The comparison between the calculated and experimental spectra is shown in Figure 9.5, with the parameters listed in Table. 9.1. The comparison in Figure 9.5 indicates that the experimental data can be fit quite well, while including the effect of the DMI is indispensable, with the latter finding being consistent with the situation of Mn_3Sn [204, 205].

Based on the fitted parameters, we calculate the transport properties of Mn_3Ge. In experiments, an external magnetic field is applied to study the transport properties of this material. The applied magnetic field gives rise to

a small out of the plane canting of the spins. From experimental data on the magnetization variation, the canting angle of the order of 1° can be estimated for the magnetic field of the magnitude of several Tesla – *e.g.*, an angle of 0.4° was deduced for the applied magnetic field of 5T [29]. Using the latter estimate, we compute the properties of the system in the canting range of $0.4 - 2^\circ$, adjusting the magnitude of the external field accordingly.

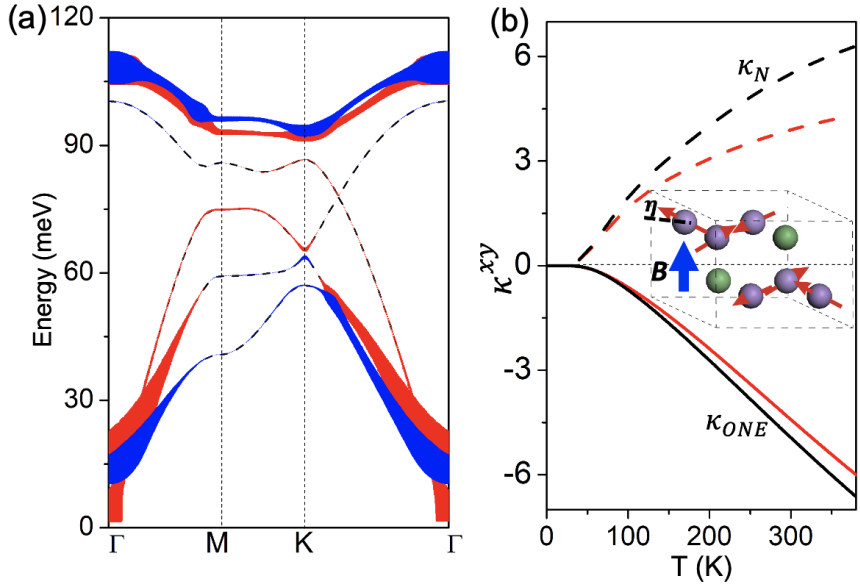

FIGURE 9.6: Orbital Nernst effect in Mn_3Ge. (a) Fat band analysis for the magnonic bands of Mn_3Ge with the canting angle $\eta = 1^\circ$. Red and blue colors represent the positive and negative signs of the local TOM $L^{\mathrm{TOM}}_{n\mathbf{k}}$, respectively, and the line thickness denotes the corresponding magnitude. (b) Comparison between the magnon Nernst conductivity (dotted line) and orbital Nernst conductivity (solid line) as the function of temperature for Mn_3Ge. Different color represents two different canting angles $\eta = 0.4^\circ$ (red color) and $\eta = 1^\circ$ (black color). The unit of Nernst conductivity in (b) is $10^3\hbar e^{-1}\mu\mathrm{A(cm)}^{-1}\mathrm{K}^{-1}$. The schematic sketch of the magnetic structure of Mn_3Ge is shown in the inset.

9.2.3 Orbital Nernst effect in Mn_3Ge

The local TOM of the Mn_3Ge, $L^{\mathrm{TOM}}_{n\mathbf{k}}$ is calculated according to Eq. (8.6). The fat band analysis of Mn_3Ge for $\eta = 1^\circ$ is shown in Figure 9.6 (a). Similar to the antiferromagnetic kagome lattice, the maximum value appears in the vicinity of the Γ point.

Except for the local orbital analysis of the bands, the magnon, κ_{N}^{xy}, and orbital, $\kappa_{\mathrm{ONE}}^{xy}$, Nernst conductivities in this material are estimated as a function of temperature. Our calculations show that in Mn_3Ge the magnitude of magnonic and orbital contributions to the transverse thermal currents is comparable and sizeable. As both contributions are opposite in sign, this potentially gives rise to a non-trivial dependence of the overall current of angular momentum on temperature, which can be accessed experimentally. The comparison between the magnon Nernst conductivity and orbital Nernst conductivity with different canting angles is shown in Figure 9.7 (a). Comparing the values of $\kappa_{\mathrm{ONE}}^{xy}$ and κ_{N}^{xy}, we find that the spin and orbital contributions to the Nernst effect in this material exhibit a similar order of magnitude in a wide range of temperatures. Overall, we find that the scale of $\kappa_{\mathrm{ONE}}^{xy}$ in Mn_3Ge is comparable to the available values for the spin Nernst effect of magnons or spin Nernst effect of electrons [206].

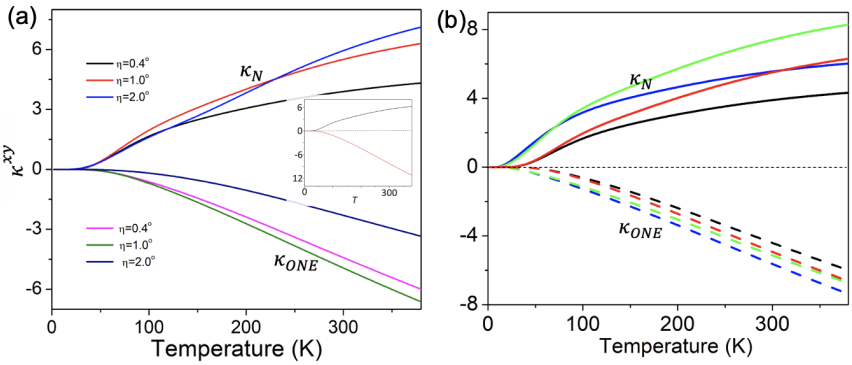

FIGURE 9.7: (a) The comparison between the magnon Nernst conductivity and orbital Nernst conductivity for Mn_3Ge with different canting angle η. The inset is the comparison between the magnon Nernst conductivity and orbital Nernst conductivity for Mn_3Ge at $\eta = 1°$, with the κ^{TO} selected as $-0.2\,\mu_{\mathrm{B}}$. (b) The DMI effect on the magnon Nernst conductivity (represented with a solid line) and orbital Nernst conductivity (represented with a dotted line) in Mn_3Ge. The black and red color correspond to $\eta = 1°$, $\eta = 0.4°$ respectively, while green and blue color of the lines represent the case without the DMI when η is chosen as $1°$ and $0.4°$ respectively. The units of the conductivity are $10^3\ \hbar \mathrm{e}^{-1}\mu\mathrm{A(cm)}^{-1}\mathrm{K}^{-1}$.

The result without DMI is calculated, and the result is shown in Figure 9.7 (b). Expectedly, as shown in Figure 9.7 (b), we find the magnitude of the $\kappa_{\mathrm{ONE}}^{xy}$ and κ_{N}^{xy} of Mn_3Ge are impacted by the DMI. By performing calculations assuming a value of $-0.2\,\mu_{\mathrm{B}}$ for κ^{TO}, we demonstrate that the orbital Nernst effect might be even stronger than the magnon Nernst effect in Mn_3Ge if the coupling of conduction electrons to the SSC is stronger, see the

inset of Figure 9.7 (a). The modulation of κ^{TO} has been discussed in Chapter 8, and stronger coupling between the free electron and SSC can be realized by doping the system or applying strain.

9.3 Summary

In this chapter, we demonstrate the mechanism of orbital Nernst effect in non-collinear systems, such as in material Mn_3Ge. The orbital moment, generated and transported by magnons, is systematically investigated under the influence of the magnetic field.

Chapter 10

Summary and future work

10.1 Summary

This thesis mainly focuses on the magnonic topological properties in magnets.

As shown in Chapter 2, the effective spin Hamiltonian was employed to investigate the properties of magnons in magnets, which is composed of the Heisenberg exchange interaction, Dzyaloshinskii-Moriya interaction, Kitaev interaction, Zeeman coupling, and higher order interactions, etc. In Chapter 3, the parameterization of Hamiltonian was done based on the first-principles calculation and fitting to experiments, separately. Then, by utilizing the linear spin-wave theory, a generalized method was proposed to obtain the magnon dispersion and eigenvector in the adiabatic approximation of the Hamiltonian represented with matrix format (shown in Section 2.4). In addition, the magnon Berry curvature was introduced to describe the magnonic topological phenomenon and explore the magnonic transport properties in Chapter 4. Utilizing these methods, we have implemented research works on magnons presented in Chapter 5-9.

By relying on the first-principles calculation, a family of two-dimensional metal-organic frameworks with Shastry-Sutherland lattice were systematically investigated in the application of spintronics in Chapter 5. Besides, the effective spin Hamiltonian of Mn-PBP was obtained, the magnonic transport properties of which were investigated to explore the candidate application in magnonics.

Via the cooperation with the experiment, the effective spin Hamiltonian was obtained and the magnonic Weyl points were shown in multiferroic ferrimagnet Cu_2OSeO_3 (Chapter 6). It was predicted that the thermal Hall conductivity and Weyl points were strongly influenced by the Dzyaloshinskii-Moriya interactions.

In Chapter 7, we discussed the interplay of the Dzyaloshinskii-Moriya interaction and Kitaev interaction for magnonic properties in a honeycomb lattice. From the perspective of magnons, we proposed several strategies to distinguish the two types of interactions from each other. Importantly, cooperated with experimental collaborators, the proposed strategies were successfully applied to materials $CrSiTe_3$ and $CrGeTe_3$.

In addition to the magnonics, the orbitronics was also discussed in the thesis. As shown in Chapter 8, a theoretical mechanism is proposed, among

which we coupled magnonic excitations to spin-chirality in generic classes of spin systems. Together with the microscopic analysis, we revealed that even in the ground state with a collinear spin system, a finite spin chirality can be generated by thermally excited magnons. Further, this generated chirality led to a strong orbital response of the spin system via the mechanism of topological orbital magnetism, which built the bridge between magnonic excitation and the generation of electronic orbital magnetization. Moreover, we indicated that in an applied temperature gradient, a significant magnon drag of the orbital momentum was driven by currents of magnons. Based on this, we proposed a new transport mechanism, which was named as orbital Nernst effect of magnons.

Finally, we presented the application of orbital Nernst effect of magnons in Chapter 9, where the orbital transport properties driven by magnons were investigated in non-collinear systems (*e.g.*, antiferromagnetic kagome lattice and real material Mn_3Ge).

10.2 Future work

High throughput computing and spin-wave theory

By combining the Monte Carlo, spin-wave theory, and first-principles calculations, the magnonics properties can be investigated in a range of magnets. For instance, we can study the candidate Kitaev materials and explore their corresponding topological magnonic properties through *Fleur-AiiDa*.

Orbital magnetism driven by magnons

In the thesis, we present the electronic orbital moment and its transport character. More works can be done in this field, such as its application in real materials or complex magnetic structures.

Magnon and phonon coupling

Notably, both magnon and phonon are bosons, which have similar energy scales and are easily coupled with each other in momentum space. The topology can be introduced through their coupling.

Appendix A

Publication List

- **Li-chuan Zhang**, Guangzhao Qin, Wu-Zhang Fang, Hui-Juan Cui, Qing-Rong Zheng, Qing-Bo Yan and Gang Su, Tinselenidene: a Two-dimensional Auxetic Material with Ultralow Lattice Thermal Conductivity and Ultrahigh Hole Mobility, *Scientific Reports* **6** (2016), 19830. (DOI: 10.1038/srep19830)
  − Results obtained in this paper are not discussed in this thesis.

- **Li-chuan Zhang**, Lizhi Zhang, Guangzhao Qin, Qing-Rong Zheng, Ming Hu, Qing-Bo Yan, Gang Su, Two-dimensional Magnetic Metal-Organic Frameworks with Shastry-Sutherland Lattice, *Chemical Science* **10**(2019), 10381-10387. (DOI: 10.1039/C9SC03816G)
  − This paper summarizes the computational method and investigates the application of the 2D-MOFs MT-PBP with SS lattices in spintronics. Some results are presented in Chapter 5.

- **Li-chuan Zhang**, Y.A. Onykiienko, P.M. Buhl, Y.V. Tymoshenko, P. Čermák, A. Schneidewind, A. Henschel, M Schmidt, S. Blügel, D.S. Inosov, Y. Mokrousov. Magnonic Weyl states in Cu_2OSeO_3. *Phys. Rev. Research* **2**(2020), 013063. (DOI: 10.1103/PhysRevResearch.2.013063)
  − This paper is cooperated with experimental collaborates to investigate the magnonic Weyl point. I contribute the theoretical part, and some results are discussed in Chapter 6.

- **Li-chuan Zhang**, Dongwook Go, Fabian R Lux, Jan-Philipp Hanke, Patrick M Buhl, Sergii Grytsiuk, Stefan Blügel, Yuriy Mokrousov. Imprinting and driving electronic orbital magnetism by magnons. *Communications Physics* **3**(2020), 227. (DOI: 10.1038/s42005-020-00490-3)
  − This work is done with collaborators. I performed the magnonic part of the calculations and analysis. For a better introduction of the work, both magnonic results and electronic TOM calculation which is calculatted by Dongwook, Go are presented in Chapter 8 and Chapter 9.

- **Li-chuan Zhang**, Fengfeng Zhu, Dongwook, Go, Fabian R Lux, Flaviano José dos Santos, Samir Lounis, Yixi Su, Stefan Blügel, Yuriy Mokrousov. The interplay of Dzyaloshinskii-Moriya and Kitaev interactions for magnonic properties of Heisenberg-Kitaev honeycomb ferromagnets. *Physical Review B* 103(2021), 1344142021. (10.1103/PhysRevB.103.134414)

– This paper discusses the interplay between the DMI, Kitaev interaction and magnetic field in magnetic honeycomb lattice. Some results are presented in Chapter 7.

- Fengfeng Zhu*, **Li-chuan Zhang***, Yao Wang*, Flaviano José dos Santos, Junda Song, Thomas Mueller, *et. al.* Topological magnon insulators in two-dimensional van der Waals ferromagnets $CrSiTe_3$ and $CrGeTe_3$: towards intrinsic gap-tunability. *Science Advance* 7 (37), eabi7532, (2021). (DOI: 10.1126/sciadv.abi7532)
  – This paper is done with experimental collaborators. I performed the magnonic part of the calculations and analysis. Some results are presented in Chapter 7.

- Guangzhao Qin, Zhenzhen Qin, Wu-Zhang Fang, **Li-Chuan Zhang**, Sheng-YingYue, Qing-Bo Yan, Ming Hu, and Gang Su, Diverse anisotropy of phonon transport in two-dimensional group IV-VI compounds: a comparative study. *Nanoscale*, **8**(2016), 11306.
  (DOI: 10.1039/C6NR01349J) – Results obtained in this paper are not discussed in this thesis.

- Chengxiao Peng, Guangzhao Qin, **Li-chuan Zhang**, Guangbiao Zhang, Chao Wang, Yuli Yan, Yuanxu Wang, Ming Hu, Dependence of phonon transport properties with stacking thickness in layered ZnO. *Journal of Physics D: Applied Physics*, **51** (2018), 315303.
  (DOI: 10.1088/1361-6463/aacf19) – Results obtained in this paper are not discussed in this thesis.

- Guanzhao Qin, Zhenzhen Qin, **Li-Chuan Zhang**, Minghu, Giant effect of spin-lattice coupling on the thermal transport in two-dimensional ferromagnetic CrI_3. *J. Mater. Chem. C*, **8**(2020), 3520-3526.
  (DOI: 10.1039/C9TC05928H) – Results obtained in this paper are not discussed in this thesis.

Bibliography

[1] Cosimo Magazzino et al. "Investigating the link among ICT, electricity consumption, air pollution, and economic growth in EU countries". In: *Energy Sources, Part B* (2021), pp. 1–23.

[2] Grünberg Binasch et al. "Enhanced magnetoresistance in layered magnetic structures with antiferromagnetic interlayer exchange". In: *Phys. Rev. B* 39.7 (1989), p. 4828. DOI: 10.1103/PhysRevB.39.4828.

[3] Terunobu Miyazaki and Nobuki Tezuka. "Giant magnetic tunneling effect in Fe/Al_2O_3/Fe junction". In: *J. Magn. Magn. Mater.* 139.3 (1995), pp. L231–L234. DOI: 10.1016/0304-8853(95)90001-2.

[4] Werner Heisenberg. "Zur theorie des ferromagnetismus". In: *Original Scientific Papers Wissenschaftliche Originalarbeiten*. Springer, 1985, pp. 580–597. DOI: 10.1007/BF01328601.

[5] B N Brockhouse. "Scattering of neutrons by spin waves in magnetite". In: *Phys. Rev.* 106.5 (1957), p. 859. DOI: 10.1103/PhysRev.106.859.

[6] Y Onose et al. "Observation of the magnon Hall effect". In: *Science* 329.5989 (2010), pp. 297–299. DOI: 10.1126/science.1188260.

[7] Hosho Katsura, Naoto Nagaosa, and Patrick A Lee. "Theory of the thermal Hall effect in quantum magnets". In: *Phys. Rev. Lett.* 104.6 (2010), p. 066403. DOI: 10.1103/PhysRevLett.104.066403.

[8] Naoto Nagaosa and Yoshinori Tokura. "Topological properties and dynamics of magnetic skyrmions". In: *Nat. Nanotechnol.* 8.12 (2013), p. 899. DOI: 10.1038/nnano.2013.243.

[9] Filipp N Rybakov et al. "New spiral state and skyrmion lattice in 3D model of chiral magnets". In: *New J. Phys.* 18.4 (2016), p. 045002. DOI: 10.1088/1367-2630/18/4/045002.

[10] Y Kasahara et al. "Majorana quantization and half-integer thermal quantum Hall effect in a Kitaev spin liquid". In: *Nature* 559.7713 (2018), pp. 227–231. DOI: 10.1038/s41586-018-0274-0.

[11] Yong Hao Gao et al. "Thermal Hall signatures of non-Kitaev spin liquids in honeycomb Kitaev materials". In: *Phys. Rev. Research* 1.1 (2019), p. 013014. DOI: 10.1103/PhysRevResearch.1.013014.

[12] Jan-Philipp Hanke et al. "Role of Berry phase theory for describing orbital magnetism: From magnetic heterostructures to topological orbital ferromagnets". In: *Phys. Rev. B* 94.12 (2016), p. 121114. DOI: 10.1103/PhysRevB.94.121114.

[13] Jan-Philipp Hanke et al. "Prototypical topological orbital ferromagnet γ-FeMn". In: *Sci. Rep.* 7 (2017), p. 41078. DOI: 10.1038/srep41078.

[14] Manuel dos Santos Dias et al. "Chirality-driven orbital magnetic moments as a new probe for topological magnetic structures". In: *Nat. Commun.* 7 (2016), p. 13613. DOI: 10.1038/ncomms13613.

[15] Fabian R Lux et al. "Engineering chiral and topological orbital magnetism of domain walls and skyrmions". In: *Commun. Phys.* 1.1 (2018), p. 60. DOI: 10.1038/s42005-018-0055-y.

[16] S Grytsiuk et al. "Topological–chiral magnetic interactions driven by emergent orbital magnetism". In: *Nat. Commun.* 11.1 (2020), pp. 1–7. DOI: 10.1038/s41467-019-14030-3.

[17] Li-chuan Zhang et al. "Imprinting and driving electronic orbital magnetism using magnons". In: *Commun. Phys.* 3.1 (2020), pp. 1–8. DOI: 10.1038/s42005-020-00490-3.

[18] L-C Zhang et al. "Magnonic Weyl states in Cu_2OSeO_3". In: *Phys. Rev. Research* 2.1 (2020), p. 013063. DOI: 10.1103/PhysRevResearch.2.013063.

[19] Li-Chuan Zhang et al. "Two-dimensional magnetic metal–organic frameworks with the Shastry-Sutherland lattice". In: *Chem. Sci.* 10.44 (2019), pp. 10381–10387. DOI: 10.1039/C9SC03816G.

[20] Li-Chuan Zhang et al. "Interplay of Dzyaloshinskii-Moriya and Kitaev interactions for magnonic properties of Heisenberg-Kitaev honeycomb ferromagnets". In: *Phys. Rev. B* 103.13 (2021), p. 134414.

[21] Flaviano José Dos Santos. *First-principles study of collective spin excitations in noncollinear magnets*. FZJ-2020-01070. JARA-HPC, 2020.

[22] Di Xiao, Wang Yao, and Qian Niu. "Valley-contrasting physics in graphene: magnetic moment and topological transport". In: *Phys. Rev. Lett.* 99.23 (2007), p. 236809. DOI: 10.1103/PhysRevLett.99.236809.

[23] Shuichi Murakami. "Quantum spin Hall effect and enhanced magnetic response by spin-orbit coupling". In: *Phys. Rev. Lett.* 97.23 (2006), p. 236805. DOI: 10.1103/PhysRevLett.97.236805.

[24] John H van Vleck. "On the anisotropy of cubic ferromagnetic crystals". In: *Phys. Rev.* 52.11 (1937), p. 1178. DOI: 10.1103/PhysRev.52.1178.

[25] Igor Dzyaloshinsky. "A thermodynamic theory of "weak" ferromagnetism of antiferromagnetics". In: *J Phys Chem Solids* 4.4 (1958), pp. 241–255. DOI: 10.1016/0022-3697(58)90076-3.

[26] Tôru Moriya. "Anisotropic superexchange interaction and weak ferromagnetism". In: *Phys. Rew.* 120.1 (1960), p. 91. DOI: 10.1103/PhysRev.120.91.

[27] Di Xiao, Junren Shi, and Qian Niu. "Berry phase correction to electron density of states in solids". In: *Phys. Rev. Lett.* 95.13 (2005), p. 137204. DOI: 10.1103/PhysRevLett.95.137204.

[28] Junren Shi et al. "Quantum theory of orbital magnetization and its generalization to interacting systems". In: *Phys. Rev. Lett.* 99.19 (2007), p. 197202. DOI: 10.1103/PhysRevLett.99.197202.

[29] Ajaya K Nayak et al. "Large anomalous Hall effect driven by a nonvanishing Berry curvature in the noncolinear antiferromagnet Mn_3Ge". In: *Sci. Adv.* 2.4 (2016), e1501870. DOI: 10.1126/sciadv.1501870.

[30] Markus Hoffmann et al. "Topological orbital magnetization and emergent Hall effect of an atomic-scale spin lattice at a surface". In: *Phys. Rev. B* 92.2 (2015), p. 020401. DOI: 10.1103/PhysRevB.92.020401.

[31] Shinichiro Seki et al. "Observation of skyrmions in a multiferroic material". In: *Science* 336.6078 (2012), pp. 198–201. DOI: 10.1126/science.1214143.

[32] M Redies et al. "Distinct magneto transport and orbital fingerprints of chiral bobbers". In: *Phys. Rev. B* 99.14 (2019), p. 140407. DOI: 10.1103/PhysRevB.99.140407.

[33] Y Taguchi et al. "Spin chirality, Berry phase, and anomalous Hall effect in a frustrated ferromagnet". In: *Science* 291.5513 (2001), pp. 2573–2576. DOI: 10.1126/science.1058161.

[34] Satoshi Fujimoto. "Hall effect of spin waves in frustrated magnets". In: *Phys. Rev. Lett.* 103.4 (2009), p. 047203. DOI: 10.1103/PhysRevLett.103.047203.

[35] HT Diep et al. *Frustrated spin systems*. World Scientific, 2013. DOI: 10.1142/8676.

[36] A Neubauer et al. "Topological Hall effect in the A phase of MnSi". In: *Phys. Rev. Lett.* 102.18 (2009), p. 186602. DOI: 10.1103/PhysRevLett.102.186602.

[37] N Kanazawa et al. "Large topological Hall effect in a short-period helimagnet MnGe". In: *Phys. Rev. Lett.* 106.15 (2011), p. 156603. DOI: 10.1103/PhysRevLett.106.156603.

[38] Robert M White, Robert M White, and Bradford Bayne. *Quantum theory of magnetism*. Vol. 1. Springer, 1983.

[39] Jiří Chaloupka, George Jackeli, and Giniyat Khaliullin. "Kitaev-Heisenberg model on a honeycomb lattice: possible exotic phases in iridium oxides A_2IrO_3". In: *Phys. Rev. Lett.* 105.2 (2010), p. 027204. DOI: 10.1103/PhysRevLett.105.027204.

[40] Jiří Chaloupka, George Jackeli, and Giniyat Khaliullin. "Zigzag magnetic order in the iridium oxide Na_2IrO_3". In: *Phys. Rev. Lett.* 110.9 (2013), p. 097204. DOI: 10.1103/PhysRevLett.110.097204.

[41] Lukas Janssen, Eric C Andrade, and Matthias Vojta. "Honeycomb-lattice Heisenberg-Kitaev model in a magnetic field: Spin canting, metamagnetism, and vortex crystals". In: *Phys. Rev. Lett.* 117.27 (2016), p. 277202. DOI: 10.1103/PhysRevLett.117.277202.

[42] A Banerjee et al. "Proximate Kitaev quantum spin liquid behaviour in a honeycomb magnet". In: *Nat. Mater.* 15.7 (2016), pp. 733–740. DOI: 10.1038/nmat4604.

[43] PA Maksimov et al. "Anisotropic-exchange magnets on a triangular lattice: spin waves, accidental degeneracies, and dual spin liquids". In: *Phys. Rev. X* 9.2 (2019), p. 021017. DOI: 10.1103/PhysRevX.9.021017.

[44] Katsuhiro Morita, Masanori Kishimoto, and Takami Tohyama. "Ground-state phase diagram of the Kitaev-Heisenberg model on a kagome lattice". In: *Phys. Rev. B* 98.13 (2018), p. 134437. DOI: 10.1103/PhysRevB.98.134437.

[45] Yogesh Singh et al. "Relevance of the Heisenberg-Kitaev model for the honeycomb lattice iridates A_2IrO_3". In: *Phys. Rev. Lett.* 108.12 (2012), p. 127203. DOI: 10.1103/PhysRevLett.108.127203.

[46] Alexei Kitaev. "Anyons in an exactly solved model and beyond". In: *Ann Phys* 321.1 (2006), pp. 2–111. DOI: 10.1016/j.aop.2005.10.005.

[47] Hong-Chen Jiang et al. "Possible proximity of the Mott insulating iridate Na_2IrO_3 to a topological phase: Phase diagram of the Heisenberg-Kitaev model in a magnetic field". In: *Phys. Rev. B* 83.24 (2011), p. 245104. DOI: 10.1103/PhysRevB.83.245104.

[48] Diptiman Sen and R Chitra. "Large-U limit of a Hubbard model in a magnetic field: Chiral spin interactions and paramagnetism". In: *Phys. Rev. B* 51.3 (1995), p. 1922. DOI: 10.1103/PhysRevB.51.1922. URL: https://doi.org/10.1103/PhysRevB.51.1922.

[49] Vladimir Gritsev, Bruce Normand, and Dionys Baeriswyl. "Phase diagram of the Heisenberg spin ladder with ring exchange". In: *Phys. Rev. B* 69.9 (2004), p. 094431. DOI: 10.1103/PhysRevB.69.094431.

[50] David P Landau and Kurt Binder. *A guide to Monte Carlo simulations in statistical physics*. Cambridge university press, 2014.

[51] T Holstein and Hl Primakoff. "Field dependence of the intrinsic domain magnetization of a ferromagnet". In: *Phys. Rev.* 58.12 (1940), p. 1098. DOI: 10.1103/PhysRev.58.1098.

[52] S. Toth and B. Lake. "Linear spin wave theory for single-Q incommensurate magnetic structures". In: *J. Phys.: Condens. Matter* 27.16 (2015), p. 166002. DOI: 10.1088/0953-8984/27/16/166002.

[53] Kangkang Li et al. "Dirac and Nodal Line Magnons in Three-Dimensional Antiferromagnets". In: *Phys. Rev. Lett.* 119 (24 2017), p. 247202. DOI: 10.1103/PhysRevLett.119.247202.

[54] Inhee Lee et al. "Fundamental Spin Interactions Underlying the Magnetic Anisotropy in the Kitaev Ferromagnet CrI_3". In: *Phys. Rev. Lett.* 124.1 (2020), p. 017201. DOI: 10.1103/PhysRevLett.124.017201.

[55] Naoki Ogawa et al. "Photodrive of magnetic bubbles via magnetoelastic waves". In: *Proc. Natl. Acad. Sci.* 112.29 (2015), pp. 8977–8981. DOI: 10.1073/pnas.1504064112.

[56] Roger Fletcher. *Practical methods of optimization*. John Wiley & Sons, 2013.

[57] Judit Romhányi, Jeroen van den Brink, and Ioannis Rousochatzakis. "Entangled tetrahedron ground state and excitations of the magnetoelectric skyrmion material Cu_2OSeO_3". In: *Phys. Rev. B* 90 (14 2014), p. 140404. DOI: 10.1103/PhysRevB.90.140404.

[58] GS Tucker et al. "Spin excitations in the skyrmion host Cu_2OSeO_3". In: *Phys. Rev. B* 93.5 (2016), p. 054401. DOI: 10.1103/PhysRevB.93.054401.

[59] P. Y. Portnichenko et al. "Magnon spectrum of the helimagnetic insulator Cu_2OSeO_3". In: *Nat. Commun.* 7 (2016), p. 10725. DOI: 10.1038/ncomms10725.

[60] Max Born and Robert Oppenheimer. "Zur quantentheorie der molekeln". In: *Annalen der physik* 389.20 (1927), pp. 457–484. DOI: 10.1002/andp.19273892002.

[61] Pierre Hohenberg and Walter Kohn. "Inhomogeneous electron gas". In: *Phys. Rev.* 136.3B (1964), B864. DOI: 10.1103/PhysRev.136.B864.

[62] Walter Kohn and Lu Jeu Sham. "Self-consistent equations including exchange and correlation effects". In: *Phys. Rev.* 140.4A (1965), A1133. DOI: 10.1103/PhysRev.140.A1133.

[63] John P Perdew, Kieron Burke, and Matthias Ernzerhof. "Generalized gradient approximation made simple". In: *Phys. Rev. Lett.* 77.18 (1996), p. 3865. DOI: 10.1103/PhysRevLett.77.3865.

[64] A Rohrbach, J Hafner, and G Kresse. "Electronic correlation effects in transition-metal sulfides". In: *Journal of Physics: Condensed Matter* 15.6 (2003), p. 979.

[65] Georg Kresse and Jürgen Furthmüller. "Efficient iterative schemes for *ab* initio total-energy calculations using a plane-wave basis set". In: *Phys. Rev. B* 54.16 (1996), p. 11169. DOI: 10.1103/PhysRevB.54.11169.

[66] Paolo Giannozzi et al. "QUANTUM ESPRESSO: a modular and open-source software project for quantum simulations of materials". In: *J. Phys. Condens. Matter* 21.39 (2009), p. 395502.

[67] Heather J Kulik et al. "Density functional theory in transition-metal chemistry: A self-consistent Hubbard U approach". In: *Phys. Rev. Lett.* 97.10 (2006), p. 103001. DOI: 10.1103/PhysRevLett.97.103001.

[68] Michael Springford. *Electrons at the Fermi surface*. Cambridge University Press, 2011.

[69] Jan-Philipp Hanke. *Topological properties of complex magnets from an advanced ab-initio Wannier description*. Forschungszentrum Jülich GmbH, Zentralbibliothek, Verlag, 2018.

[70] Hongjun Xiang et al. "Magnetic properties and energy-mapping analysis". In: *Dalton Trans.* 42.4 (2013), pp. 823–853. DOI: 10.1039/C2DT31662E.

[71] Charles Kittel. "On the theory of ferromagnetic resonance absorption". In: *Phys. Rev.* 73.2 (1948), p. 155. DOI: 10.1103/PhysRev.73.155.

[72] SA Wolf et al. "Spintronics: a spin-based electronics vision for the future". In: *Science* 294.5546 (2001), pp. 1488–1495. DOI: 10.1126/science.1065389.

[73] Igor Žutić, Jaroslav Fabian, and S Das Sarma. "Spintronics: Fundamentals and applications". In: *Rev. Mod. Phys.* 76.2 (2004), p. 323. DOI: 10.1103/RevModPhys.76.323.

[74] Gerrit EW Bauer, Eiji Saitoh, and Bart J Van Wees. "Spin caloritronics". In: *Nat. Mater.* 11.5 (2012), p. 391.

[75] Michael Victor Berry. "Quantal phase factors accompanying adiabatic changes". In: *Proc. Math. Phys. Eng. Sci.* 392.1802 (1984), pp. 45–57. DOI: 10.1098/rspa.1984.0023.

[76] Alexander Mook, Jürgen Henk, and Ingrid Mertig. "Magnon Hall effect and topology in kagome lattices: a theoretical investigation". In: *Phys. Rev. B* 89.13 (2014), p. 134409. DOI: 10.1103/PhysRevB.89.134409.

[77] Alexey A Kovalev and Vladimir Zyuzin. "Spin torque and Nernst effects in Dzyaloshinskii-Moriya ferromagnets". In: *Phys. Rev. B* 93.16 (2016), p. 161106. DOI: 10.1103/PhysRevB.93.161106.

[78] Vladimir A Zyuzin and Alexey A Kovalev. "Magnon spin nernst effect in antiferromagnets". In: *Phys. Rev. Lett.* 117.21 (2016), p. 217203. DOI: 10.1103/PhysRevLett.117.217203.

[79] Charles Kittel and Paul McEuen. *Introduction to solid state physics*. Vol. 8. Wiley New York, 1976.

[80] Xiangang Wan et al. "Topological semimetal and Fermi-arc surface states in the electronic structure of pyrochlore iridates". In: *Phys. Rev. B* 83.20 (2011), p. 205101. DOI: 10.1103/PhysRevB.83.205101.

[81] BQ Lv et al. "Experimental discovery of Weyl semimetal TaAs". In: *Phys. Rev. X* 5.3 (2015), p. 031013. DOI: 10.1103/PhysRevX.5.031013.

[82] L. Lu, J. D. Joannopoulos, and M. Soljačić. "Topological photonics". In: *Nat. Photon.* 8.11 (2014), p. 821. DOI: 10.1038/nphoton.2014.248.

[83] R. Chisnell et al. "Topological Magnon Bands in a Kagome Lattice Ferromagnet". In: *Phys. Rev. Lett.* 115 (14 2015), p. 147201. DOI: 10.1103/PhysRevLett.115.147201.

[84] W. Yao et al. "Topological spin excitations in a three-dimensional antiferromagnet". In: *Nat. Phys.* 14 (2018), p. 1011. DOI: 10.1038/s41567-018-0213-x.

[85] S. Bao et al. In: *Nat. Commun.* 9.1 (2018), p. 2591. DOI: 10.1038/s41467-018-05054-2.

[86] Feng Li et al. "Weyl points and Fermi arcs in a chiral phononic crystal". In: *Nat. Phys.* 14.1 (2018), p. 30. DOI: 10.1038/nphys4275.

[87] Edwin H Hall et al. "On a new action of the magnet on electric currents". In: *Am. J. Math.* 2.3 (1879), pp. 287–292. DOI: 10.2307/2369245.

[88] Tao Qin, Qian Niu, and Junren Shi. "Energy magnetization and the thermal Hall effect". In: *Physical review letters* 107.23 (2011), p. 236601. DOI: https://doi.org/10.1103/PhysRevLett.107.236601.

[89] C Strohm, GLJA Rikken, and P Wyder. "Phenomenological evidence for the phonon Hall effect". In: *Phys. Rev. Lett.* 95.15 (2005), p. 155901. DOI: 10.1103/PhysRevLett.95.155901.

[90] Ganesh Sundaram and Qian Niu. "Wave-packet dynamics in slowly perturbed crystals: Gradient corrections and Berry-phase effects". In: *Phys. Rev. B* 59.23 (1999), p. 14915. DOI: 10.1103/PhysRevB.59.14915.

[91] Robert Karplus and JM Luttinger. "Hall effect in ferromagnetics". In: *Phys. Rev.* 95.5 (1954), p. 1154. DOI: 10.1103/PhysRev.95.1154.

[92] Ming-Che Chang and Qian Niu. "Berry phase, hyperorbits, and the Hofstadter spectrum: Semiclassical dynamics in magnetic Bloch bands". In: *Phys. Rev. B* 53.11 (1996), p. 7010. DOI: 10.1103/PhysRevB.53.7010.

[93] Carlo Cercignani. "The boltzmann equation". In: *The Boltzmann equation and its applications*. Springer, 1988, pp. 40–103. DOI: 10.1007/978-1-4612-1039-9_2.

[94] David J Thouless et al. "Quantized Hall conductance in a two-dimensional periodic potential". In: *Phys. Rev. Lett.* 49.6 (1982), p. 405. DOI: 10.1103/PhysRevLett.49.405.

[95] Shuichi Murakami and Akihiro Okamoto. "Thermal Hall effect of magnons". In: *J. Phys. Soc. Japan* 86.1 (2017), p. 011010. DOI: 10.7566/JPSJ.86.011010.

[96] Ryo Matsumoto and Shuichi Murakami. "Theoretical prediction of a rotating magnon wave packet in ferromagnets". In: *Phys. Rev. Lett.* 106.19 (2011), p. 197202. DOI: 10.1103/PhysRevLett.106.197202.

[97] Doris Grumelli et al. "Bio-inspired nanocatalysts for the oxygen reduction reaction". In: *Nat. commun.* 4.1 (2013), pp. 1–6. DOI: 10.1038/ncomms3904(2013).

[98] Steven L Tait et al. "Assembling Isostructural Metal-Organic Coordination Architectures on Cu (100), Ag (100) and Ag (111) Substrates". In: *ChemPhysChem* 9.17 (2008), pp. 2495–2499. DOI: doi.org/10.1002/cphc.200800575.

[99] Sebastian Stepanow et al. "Surface-Assisted Assembly of 2D Metal–Organic Networks That Exhibit Unusual Threefold Coordination Symmetry". In: *Angew. Chem. Int. Ed. Engl.* 46.5 (2007), pp. 710–713. DOI: 10.1002/anie.200603644.

[100] Uta Schlickum et al. "Metal- organic honeycomb nanomeshes with tunable cavity size". In: *Nano Lett.* 7.12 (2007), pp. 3813–3817. DOI: 10.1021/nl072466m.

[101] Xiaojun Wu and Xiao Cheng Zeng. "Double metallocene nanowires". In: *J. Am. Chem. Soc.* 131.40 (2009), pp. 14246–14248. DOI: 10.1021/ja904912z.

[102] ZF Wang, Ninghai Su, and Feng Liu. "Prediction of a two-dimensional organic topological insulator". In: *Nano Lett.* 13.6 (2013), pp. 2842–2845. DOI: 10.1021/nl401147u.

[103] Elise M Miner et al. "Electrochemical oxygen reduction catalysed by Ni_3(hexaiminotriphenylene)$_2$". In: *Nat. commun.* 7.1 (2016), pp. 1–7. DOI: 10.1038/ncomms10942.

[104] Wenbin Li et al. "High temperature ferromagnetism in π-conjugated two-dimensional metal–organic frameworks". In: *Chem. Sci.* 8.4 (2017), pp. 2859–2867. DOI: 10.1039/C6SC05080H.

[105] Xiaoming Zhang et al. "Theoretical Discovery of a Superconducting Two-Dimensional Metal-Organic Framework". In: *Nano Lett.* 17.10 (2017), pp. 6166–6170. DOI: 10.1021/acs.nanolett.7b02795.

[106] Zheng Liu et al. "Flat Chern band in a two-dimensional organometallic framework". In: *Phys. Rev. Lett.* 110.10 (2013), p. 106804. DOI: 10.1103/PhysRevLett.110.106804.

[107] LZ Zhang et al. "Intrinsic two-dimensional organic topological insulators in metal-dicyanoanthracene lattices". In: *Nano Lett.* 16.3 (2016), pp. 2072–2075. DOI: 10.1021/acs.nanolett.6b00110.

[108] Liang Dong et al. "Two-dimensional π-conjugated covalent-organic frameworks as quantum anomalous Hall topological insulators". In: *Phys. Rev. Lett.* 116.9 (2016), p. 096601. DOI: 10.1103/PhysRevLett.116.096601.

[109] Jin-Hu Dou et al. "Signature of metallic behavior in the metal–organic frameworks M_3(hexaiminobenzene)$_2$ (M= Ni, Cu)". In: *J. Am. Chem. Soc.* 139.39 (2017), pp. 13608–13611. DOI: 10.1021/jacs.7b07234.

[110] B Sriram Shastry and Bill Sutherland. "Exact ground state of a quantum mechanical antiferromagnet". In: *Physica B+ C* 108.1-3 (1981), pp. 1069–1070. DOI: 10.1016/0378-4363(81)90838-X.

[111] H Kageyama et al. "Exact dimer ground state and quantized magnetization plateaus in the two-dimensional spin system $SrCu_2(BO_3)_2$". In: *Phys. Rev. Lett.* 82.15 (1999), p. 3168. DOI: 10.1103/PhysRevLett.82.3168.

[112] K Kodama et al. "Magnetic superstructure in the two-dimensional quantum antiferromagnet $SrCu_2(BO_3)_2$". In: *Science* 298.5592 (2002), pp. 395–399. DOI: 10.1126/science.1075045.

[113] Andreas Abendschein and Sylvain Capponi. "Effective theory of magnetization plateaux in the Shastry-Sutherland lattice". In: *Phys. Rev. Lett.* 101.22 (2008), p. 227201. DOI: 10.1103/PhysRevLett.101.227201.

[114] Yu I Dublenych. "Ground states of the Ising model on the Shastry-Sutherland lattice and the origin of the fractional magnetization plateaus in rare-earth-metal tetraborides". In: *Phys. Rev. Lett.* 109.16 (2012), p. 167202. DOI: 10.1103/PhysRevLett.109.167202.

[115] Shin Miyahara and Kazuo Ueda. "Theory of the orthogonal dimer Heisenberg spin model for $SrCu_2(BO_3)_2$". In: *J. Phys. Condens. Matter* 15.9 (2003), R327.

[116] Georg Kresse and Daniel Joubert. "From ultrasoft pseudopotentials to the projector augmented-wave method". In: *Phys. Rev. B* 59.3 (1999), p. 1758. DOI: 10.1103/PhysRevB.59.1758.

[117] Hendrik J Monkhorst and James D Pack. "Special points for Brillouin-zone integrations". In: *Phys. Rev. B* 13.12 (1976), p. 5188. DOI: 10.1103/PhysRevB.13.5188.

[118] Engin Torun et al. "Stable half-metallic monolayers of $FeCl_2$". In: *Appl. Phys. Lett.* 106.19 (2015), p. 192404. DOI: 10.1063/1.4921096.

[119] Junjie He et al. "Unusual Dirac half-metallicity with intrinsic ferromagnetism in vanadium trihalide monolayers". In: *J. Mater. Chem. C* 4.13 (2016), pp. 2518–2526. DOI: 10.1039/C6TC00409A.

[120] Renhao Dong et al. "A coronene-based semiconducting two-dimensional metal-organic framework with ferromagnetic behavior". In: *Nat. Commun.* 9.1 (2018), pp. 1–9. DOI: 10.1038/s41467-018-05141-4.

[121] Bevin Huang et al. "Layer-dependent ferromagnetism in a van der Waals crystal down to the monolayer limit". In: *Nature* 546.7657 (2017), pp. 270–273. DOI: 10.1038/nature22391.

[122] SL Dudarev et al. "Electron-energy-loss spectra and the structural stability of nickel oxide: An LSDA+U study". In: *Phys. Rev. B* 57.3 (1998), p. 1505. DOI: 10.1103/PhysRevB.57.1505.

[123] Vladimir I Anisimov, Ferdi Aryasetiawan, and AI Lichtenstein. "First-principles calculations of the electronic structure and spectra of strongly correlated systems: the LDA+U method". In: *J. Phys. Condens. Matter* 9.4 (1997), p. 767.

[124] M Bernien et al. "Tailoring the nature of magnetic coupling of Fe-porphyrin molecules to ferromagnetic substrates". In: *Phys. Rev. Lett.* 102.4 (2009), p. 047202.

[125] Arrigo Calzolari, Andrea Ferretti, and Marco Buongiorno Nardelli. "*Ab* initio correlation effects on the electronic and transport properties of metal (II)-phthalocyanine-based devices". In: *Nanotechnology* 18.42 (2007), p. 424013.

[126] W Tang, E Sanville, and G Henkelman. "A grid-based Bader analysis algorithm without lattice bias". In: *J. Phys. Condens. Matter* 21.8 (2009), p. 084204.

[127] Min Yu and Dallas R Trinkle. "Accurate and efficient algorithm for Bader charge integration". In: *J. Chem. Phys.* 134.6 (2011), p. 064111. DOI: 10.1063/1.3553716.

[128] Andreas Savin et al. "Electron localization in solid-state structures of the elements: the diamond structure". In: *Angew. Chem. Int. Ed. Engl.* 31.2 (1992), pp. 187–188. DOI: 10.1002/anie.199201871.

[129] Kei Yosida. "Magnetic properties of Cu-Mn alloys". In: *Phys. Rev.* 106.5 (1957), p. 893. DOI: 10.1103/PhysRev.106.893.

[130] Andrew J Clough et al. "Metallic conductivity in a two-dimensional cobalt dithiolene metal-organic framework". In: *J. Am. Chem. Soc.* 139.31 (2017), pp. 10863–10867. DOI: 10.1021/jacs.7b05742.

[131] Supriyo Datta and Biswajit Das. "Electronic analog of the electro-optic modulator". In: *Appl. Phys. Lett.* 56.7 (1990), pp. 665–667. DOI: 10.1063/1.102730.

[132] M Malki and GS Uhrig. "Topological magnon bands for magnonics". In: *Phys. Rev. B* 99.17 (2019), p. 174412. DOI: 10.1103/PhysRevB.99.174412.

[133] Paul A McClarty et al. "Topological triplon modes and bound states in a Shastry-Sutherland magnet". In: *Nat. Phys.* 13.8 (2017), pp. 736–741. DOI: 10.1038/nphys4117.

[134] Shinichiro Seki et al. "Observation of Skyrmions in a Multiferroic Material". In: *Science* 336.6078 (2012), pp. 198–201. DOI: 10.1126/science.1214143.

[135] S. Seki et al. "Formation and rotation of skyrmion crystal in the chiral-lattice insulator Cu_2OSeO_3". In: *Phys. Rev. B* 85 (22 2012), p. 220406. DOI: 10.1103/PhysRevB.85.220406.

[136] M. C. Langner et al. "Coupled Skyrmion Sublattices in Cu_2OSeO_3". In: *Phys. Rev. Lett.* 112 (16 2014), p. 167202. DOI: 10.1103/PhysRevLett.112.167202.

[137] M. C. Langner et al. "Nonlinear Ultrafast Spin Scattering in the Skyrmion Phase of Cu_2OSeO_3". In: *Phys. Rev. Lett.* 119 (10 2017), p. 107204. DOI: 10.1103/PhysRevLett.119.107204.

[138] Jan Müller et al. "Nonlinear Ultrafast Spin Scattering in the Skyrmion Phase of Cu_2OSeO_3". In: *Phys. Rev. Lett.* 119.13 (2017), p. 137201. DOI: 10.1103/PhysRevLett.119.137201.

[139] H. Effenberger and F. Pertlik. "Die Kristallstrukturen der Kupfer(II)-oxo-selenite Cu2O(SeO_3) (kubisch und monoklin) und $Cu_4O(SeO_3)_3$ (monoklin und triklin)". In: *Monatsh. Chem.* 117 (1986), pp. 887–896. DOI: 10.1007/BF00811258.

[140] J. H. Yang et al. "Strong Dzyaloshinskii-Moriya Interaction and Origin of Ferroelectricity in Cu_2OSeO_3". In: *Phys. Rev. Lett.* 109 (10 2012), p. 107203. DOI: 10.1103/PhysRevLett.109.107203.

[141] Oleg Janson et al. "The quantum nature of skyrmions and half-skyrmions in Cu_2OSeO_3". In: *Nat. Commun.* 5 (2014), p. 5376. DOI: 10.1038/ncomms6376.

[142] Jan-Willem G. Bos, Claire V. Colin, and Thomas T. M. Palstra. "Magnetoelectric coupling in the cubic ferrimagnet Cu_2OSeO_3". In: *Phys. Rev. B* 78 (9 2008), p. 094416. DOI: 10.1103/PhysRevB.78.094416.

[143] V. A. Chizhikov and V. E. Dmitrienko. "Microscopic description of twisted magnet Cu_2OSeO_3". In: *J. Magn. Magn. Mater.* 382 (2015), pp. 142–151. DOI: 10.1016/j.jmmm.2015.01.032.

[144] M. Ozerov et al. "Establishing the Fundamental Magnetic Interactions in the Chiral Skyrmionic Mott Insulator Cu_2OSeO_3 by Terahertz Electron Spin Resonance". In: *Phys. Rev. Lett.* 113 (15 2014), p. 157205. DOI: 10.1103/PhysRevLett.113.157205.

[145] M. Belesi et al. "Ferrimagnetism of the magnetoelectric compound Cu_2OSeO_3 probed by ^{77}Se NMR". In: *Phys. Rev. B* 82 (9 2010), p. 094422. DOI: 10.1103/PhysRevB.82.094422.

[146] A. Schneidewind and P. Čermák. "*PANDA: Cold three axes spectrometer*". In: *J. Large-Scale Res. Facilities* 1 (2015), A12. DOI: 10.17815/jlsrf-1-35.

[147] R. A. Ewings et al. "Upgrade to the MAPS neutron time-of-flight chopper spectrometer". In: *Rev. Sci. Instrum.* 90 (2019), p. 035110. DOI: 10.1063/1.5086255.

[148] A. A. Soluyanov et al. "Type-II Weyl semimetals". In: *Nature* 527.7579 (2015), p. 495. DOI: 10.1038/nature15768.

[149] Max Hirschberger et al. "Thermal Hall Effect of Spin Excitations in a Kagome Magnet". In: *Phys. Rev. Lett.* 115 (10 2015), p. 106603. DOI: 10.1103/PhysRevLett.115.106603.

[150] Adam WJ Wells et al. "Effect of interfacial intermixing on the Dzyaloshinskii-Moriya interaction in Pt/Co/Pt". In: *Phys. Rev. B* 95.5 (2017), p. 054428. DOI: 10.1103/PhysRevB.95.054428.

[151] Y Nii et al. "Uniaxial stress control of skyrmion phase". In: *Nat. Commun.* 6 (2015), p. 8539. DOI: 10.1038/ncomms9539.

[152] Titiksha Srivastava et al. "Large voltage tuning of Dzyaloshinskii-Moriya Interaction: a route towards dynamic control of skyrmion chirality". In: *Nano Lett.* 18.8 (2018), pp. 4871–4877. DOI: 10.1021/acs.nanolett.8b01502.

[153] Tomohiro Koyama et al. "Electric field control of magnetic domain wall motion via modulation of the Dzyaloshinskii-Moriya interaction". In: *Sci. Adv.* 4.12 (2018), eaav0265. DOI: 10.1126/sciadv.aav0265.

[154] Kwang-Su Ryu et al. "Chiral spin torque at magnetic domain walls". In: *Nat. Nanotechnol.* 8.7 (2013), p. 527. DOI: 10.1038/nnano.2013.102.

[155] Satoru Emori et al. "Current-driven dynamics of chiral ferromagnetic domain walls". In: *Nat. Mater.* 12.7 (2013), p. 611. DOI: 10.1038/nmat3675.

[156] SK Choi et al. "Spin waves and revised crystal structure of honeycomb iridate Na_2IrO_3". In: *Phys. Rev. Lett.* 108.12 (2012), p. 127204. DOI: 10.1103/PhysRevLett.108.127204.

[157] Feng Ye et al. "Direct evidence of a zigzag spin-chain structure in the honeycomb lattice: A neutron and x-ray diffraction investigation of single-crystal Na_2IrO_3". In: *Phys. Rev. B* 85.18 (2012), p. 180403. DOI: 10.1103/PhysRevB.85.180403.

[158] Sae Hwan Chun et al. "Direct evidence for dominant bond-directional interactions in a honeycomb lattice iridate Na_2IrO_3". In: *Nat. Phys.* 11.6 (2015), pp. 462–466. DOI: 10.1038/nphys3322.

[159] JA Sears et al. "Magnetic order in α- $RuCl_3$: A honeycomb-lattice quantum magnet with strong spin-orbit coupling". In: *Phys. Rev. B* 91.14 (2015), p. 144420. DOI: 10.1103/PhysRevB.91.144420.

[160] Chetan Nayak et al. "Non-Abelian anyons and topological quantum computation". In: *Rev. Mod. Phys.* 80.3 (2008), p. 1083. DOI: 10.1103/RevModPhys.80.1083.

[161] Se Kwon Kim et al. "Realization of the haldane-kane-mele model in a system of localized spins". In: *Phys. Rev. Lett.* 117.22 (2016), p. 227201. DOI: 10.1103/PhysRevLett.117.227201.

[162] Lebing Chen et al. "Topological spin excitations in honeycomb ferromagnet CrI_3". In: *Phys. Rev. X* 8.4 (2018), p. 041028. DOI: 10.1103/PhysRevX.8.041028.

[163] Changsong Xu et al. "Topological spin texture in Janus monolayers of the chromium trihalides $Cr(I, X)_3$". In: *Phys. Rev. B* 101.6 (2020), p. 060404. DOI: 10.1103/PhysRevB.101.060404.

[164] Liang Wu et al. "Field evolution of magnons in α- $RuCl_3$ by high-resolution polarized terahertz spectroscopy". In: *Phys. Rev. B* 98.9 (2018), p. 094425. DOI: 10.1103/PhysRevB.98.094425.

[165] Nejc Janša et al. "Observation of two types of fractional excitation in the Kitaev honeycomb magnet". In: *Nat. Phys.* 14.8 (2018), pp. 786–790. DOI: 10.1038/s41567-018-0129-5.

[166] John Cenker et al. "Direct observation of two-dimensional magnons in atomically thin CrI_3". In: *Nat. Phys.* (2020). DOI: 10.1038/s41567-020-0999-1.

[167] T. Moriya. In: *Phys. Rev.* 120 (1960), p. 91. DOI: 10.1103/PhysRev.120.91.

[168] Esteban Aguilera et al. "Topological magnonics in the two-dimensional van der Waals magnet CrI_3". In: *Phys. Rev. B* 102 (2020), p. 024409. DOI: 10.1103/PhysRevB.102.024409.

[169] Changsong Xu et al. "Interplay between Kitaev interaction and single ion anisotropy in ferromagnetic CrI_3 and $CrGeTe_3$ monolayers". In: *NPJ Comput. Mater.* 4.1 (2018), pp. 1–6. DOI: 10.1038/s41524-018-0115-6.

[170] Y Kasahara et al. "Unusual thermal Hall effect in a Kitaev spin liquid candidate α- $RuCl_3$". In: *Phys. Rev. Lett.* 120.21 (2018), p. 217205. DOI: 10.1103/PhysRevLett.120.217205.

[171] Richard Hentrich et al. "Large thermal hall effect in α- $RuCl_3$: Evidence for heat transport by Kitaev-Heisenberg paramagnons". In: *Phys. Rev. B* 99.8 (2019), p. 085136. DOI: 10.1103/PhysRevB.99.085136.

[172] S Toth and B Lake. "Linear spin wave theory for single-Q incommensurate magnetic structures". In: *J. Phys. Condens. Matter* 27.16 (2015), p. 166002.

[173] Alexander Mook, Jürgen Henk, and Ingrid Mertig. "Spin dynamics simulations of topological magnon insulators: From transverse current correlation functions to the family of magnon Hall effects". In: *Phys. Rev. B* 94.17 (2016), p. 174444. DOI: 10.1103/PhysRevB.94.174444.

[174] Changsong Xu et al. "Possible Kitaev Quantum Spin Liquid State in 2D Materials with S= 3/2". In: *Phy. Rev. Lett.* 124.8 (2020), p. 087205. DOI: 10.1103/PhysRevLett.124.087205.

[175] Ke Wang et al. "Magnon relaxation time in ferromagnetic Cr2Ge2Te6 monolayer governed by magnon-phonon interaction". In: *Appl. Phys. Lett.* 118.2 (2021), p. 023102.

[176] Hua Chen, Qian Niu, and Allan H MacDonald. "Anomalous Hall effect arising from noncollinear antiferromagnetism". In: *Phys. Rev. Lett.* 112.1 (2014), p. 017205. DOI: 10.1103/PhysRevLett.112.017205.

[177] Yang Zhang et al. "Spin Hall effect emerging from a noncollinear magnetic lattice without spin–orbit coupling". In: *New J. Phys.* 20.7 (2018), p. 073028. DOI: 10.1088/1367-2630/aad1eb.

[178] Olexei I. Motrunich. "Orbital magnetic field effects in spin liquid with spinon Fermi sea: Possible application to $\kappa-(ET)_2Cu_2(CN)_3$". In: *Phys. Rev. B* 73 (15 2006), p. 155115. DOI: 10.1103/PhysRevB.73.155115.

[179] Sebastian Wimmer, Sergiy Mankovsky, and Hubert Ebert. "Chirality-induced linear response properties in non-coplanar Mn_3 Ge". In: *arXiv preprint arXiv:1912.05211* (2019).

[180] Dongwook Go et al. "Intrinsic spin and orbital Hall effects from orbital texture". In: *Phys. Rev. Lett.* 121.8 (2018), p. 086602. DOI: 10.1103/PhysRevLett.121.086602.

[181] Dongwook Go and Hyun-Woo Lee. "Orbital torque: Torque generation by orbital current injection". In: *Phys. Rev. Research* 2.1 (2020), p. 013177. DOI: 10.1103/PhysRevResearch.2.013177.

[182] Si-Yu Li et al. "Experimental evidence for orbital magnetic moments generated by moir\'e-scale current loops in twisted bilayer graphene". In: *arXiv preprint arXiv:1912.13133* (2019).

[183] Shilei Ding et al. "Harnessing non-local orbital-to-spin conversion of interfacial orbital currents for efficient spin-orbit torques". In: *arXiv preprint arXiv:2006.03649* (2020). URL: https://arxiv.org/pdf/2006.03649.pdf.

[184] Stephen R Boona, Roberto C Myers, and Joseph P Heremans. "Spin caloritronics". In: *Energy Environ. Sci.* 7.3 (2014), pp. 885–910. DOI: 10.1039/C3EE43299H.

[185] AV Chumak et al. "Magnon spintronics". In: *Nat. Phys.* 11.6 (2015), p. 453. DOI: 10.1038/nphys3347.

[186] Ran Cheng, Satoshi Okamoto, and Di Xiao. "Spin Nernst effect of magnons in collinear antiferromagnets". In: *Phys. Rev. Lett.* 117.21 (2016), p. 217202. DOI: 10.1103/PhysRevLett.117.217202.

[187] Alexander Mook, Jürgen Henk, and Ingrid Mertig. "Thermal Hall effect in noncollinear coplanar insulating antiferromagnets". In: *Phys. Rev. B* 99.1 (2019), p. 014427. DOI: 10.1103/PhysRevB.99.014427.

[188] Guillaume Géranton et al. "Spin-orbit torques in $L1_0$- FePt/Pt thin films driven by electrical and thermal currents". In: *Phys. Rev. B* 91.1 (2015), p. 014417. DOI: 10.1103/PhysRevB.91.014417.

[189] Nguyen H Long et al. "Giant spin Nernst effect induced by resonant scattering at surfaces of metallic films". In: *Phys. Rev. B* 93.18 (2016), p. 180406. DOI: 10.1103/PhysRevB.93.180406.

[190] R Chisnell et al. "Topological magnon bands in a kagome lattice ferromagnet". In: *Phys. Rev. Lett.* 115.14 (2015), p. 147201. DOI: 10.1103/PhysRevLett.115.147201.

[191] A Scheie et al. "Effective spin-$\frac{1}{2}$ scalar chiral order on kagome lattices in $Nd_3Sb_3Mg_2O_{14}$". In: *Phys. Rev. B* 93.18 (2016), p. 180407. DOI: 10.1103/PhysRevB.93.180407.

[192] Max Hirschberger et al. "Large thermal Hall conductivity of neutral spin excitations in a frustrated quantum magnet". In: *Science* 348.6230 (2015), pp. 106–109. DOI: 10.1126/science.1257340.

[193] P Bruno, VK Dugaev, and M Taillefumier. "Topological Hall effect and Berry phase in magnetic nanostructures". In: *Phys. Rev. Lett.* 93.9 (2004), p. 096806. DOI: 10.1103/PhysRevLett.93.096806.

[194] Patrick M Buhl et al. "Topological spin Hall effect in antiferromagnetic skyrmions". In: *Phys. Status Solidi RRL* 11.4 (2017), p. 1700007. DOI: 10.1002/pssr.201700007.

[195] C Franz et al. "Real-space and reciprocal-space Berry phases in the Hall effect of $Mn_{1-x}Fe_xSi$". In: *Phys. Rev. Lett.* 112.18 (2014), p. 186601. DOI: 10.1103/PhysRevLett.112.186601.

[196] Hiroaki Ishizuka and Naoto Nagaosa. "Spin chirality induced skew scattering and anomalous Hall effect in chiral magnets". In: *Sci. Adv.* 4.2 (2018), eaap9962. DOI: 10.1126/sciadv.aap9962.

[197] Chengwang Niu et al. "Mixed topological semimetals driven by orbital complexity in two-dimensional ferromagnets". In: *Nat. Commun.* 10.1 (2019), pp. 1–10. DOI: 10.1038/s41467-019-10930-6.

[198] Imran Khan and Jisang Hong. "High Curie temperature and strain-induced semiconductor-metal transition with spin reorientation transition in 2D $CrPbTe_3$ monolayer". In: *Nanotechnology* 31.19 (2020), p. 195704. DOI: 10.1103/PhysRevB.100.144420.

[199] SA Owerre. "Noncollinear antiferromagnetic Haldane magnon insulator". In: *J. Appl. Phys.* 121.22 (2017), p. 223904. DOI: 10.1063/1.4985615.

[200] AS Sukhanov et al. "Gradual pressure-induced change in the magnetic structure of the noncollinear antiferromagnet Mn_3Ge". In: *Phys. Rev. B* 97.21 (2018), p. 214402. DOI: 10.1103/PhysRevB.97.214402.

[201] Sebastian Wimmer, Sergiy Mankovsky, and Hubert Ebert. "Chirality-induced linear response properties in noncoplanar Mn_3Ge". In: *Phys. Rev. B* 103.2 (2021), p. 024437. DOI: 10.1103/PhysRevB.103.024437.

[202] JW Cable, N Wakabayashi, and P Radhakrishna. "Magnetic excitations in the triangular antiferromagnets Mn_3Sn and Mn_3Ge". In: *Phys. Rev. B* 48.9 (1993), p. 6159. DOI: 10.1103/PhysRevB.48.6159.

[203] AS Sukhanov et al. "Magnon-polaron excitations in the noncollinear antiferromagnet Mn_3Ge". In: *Phys. Rev. B* 99.21 (2019), p. 214445. DOI: 10.1103/PhysRevB.99.214445.

[204] Pyeongjae Park et al. "Magnetic excitations in non-collinear antiferromagnetic Weyl semimetal Mn_3Sn". In: *npj Quantum Mater.* 3.1 (2018), pp. 1–8. DOI: 10.1038/s41535-018-0137-9.

[205] Ramon Cardias et al. "Dzyaloshinskii-Moriya interaction in absence of spin-orbit coupling". In: *arXiv preprint arXiv:2003.04680* (2020).

[206] Guang-Yu Guo and Tzu-Cheng Wang. "Large anomalous Nernst and spin Nernst effects in the noncollinear antiferromagnets $Mn_3X(X = Sn, Ge, Ga)$". In: *Phys. Rev. B* 96.22 (2017), p. 224415. DOI: 10.1103/PhysRevB.96.224415.

Acknowledgements

It was an enjoyable journey for me in Germany to finish this thesis. On the way, I could count on the help and support of many people. Here, I would like to thank all of them!

First of all, I would like to thank Prof. Dr. Stefan Blügel for giving me the opportunity to conduct my Ph.D. studies in the renowned PGI-1/IAS-1 institute at Forschungszentrum Jülich. I benefited a lot from his sagacious thoughts and rigorous attitude towards science. Especially, I would like to appreciate him for improving the quality of this thesis. Besides, I would thank in particular my supervisor Prof. Yuriy Mokrousov, who is a wise and friendly mentor. He offered constructive help and encouragement when I was in trouble. His way of thinking influenced me a lot on scientific research. I am very fortunate to have had him as a mentor and collaborator during these years. Without his insightful advice, this work would not have been possible. Also, thanks to my previous supervisor Prof. Ming Hu (now at the University of South Carolina) for receiving me into RWTH and offer guidance in the research work. I would like to thank Prof. Dr. Matthias Wuttig for accepting to read and report on this dissertation. Moreover, I would like to thank China Scholarship Council (CSC) for the financial support granted through my predoctoral fellowship.

Next, I would like to thank all the members of "Topological Nanoelectronics Group". In particular, I would like to thank Dr. Patrick M. Buhl (now at University of Mainz) for his guidance and help on my PhD study. Special thanks to my other colleagues, Dr. Jan-Philipp Hanke, Fabian Lux, Dr. Dongwook Go, Prof. Dr. Chengwang Niu (at Shandong University, China), and Prof. Dr. Wanxiang Feng (at Beijing Institute of Technology) for the kind help and discussion both in life and work. I also want to show my gratitude to Jonathan Kipp, Maximilian Merte, Dr. Sumit Ghosh, and Dr. Frank Freimuth. I wish current and future members of Yuriy's group having good luck and hope you can continue to make the group to be an exciting and fruitful place. Moreover, I want to thank my experimental collaborators: Prof. Dmytro Inosov and Y. A. Onykiienko from TU Dresden and Dr. Yixi Su, Dr. Fengfeng Zhu from Jülich Centre for Neutron Science (JCNS).

I wish to thank all the members of the PGI-1/IAS-1 who have helped me over the years, especially my office mate Matthias Redies, who made life and work much more enjoyable. I want to thank Flaviano José dos Santos (now at MARVEL, Switzerland) for helping me in my work. I also want to thank Dr. Hongying Jia, Zhewen Xu, Dr. Marjana Ležaić, Prof. Dr. Samir Lounis, Dr. Gustav Bihlmayer, Dr. Sergii Grytsiuk, Ute Winkler, et.al. They offer a lot of help for my work and life, hope they are happy and safe every day.

Finally, I would like to thank my family and friends from China. I wish to express my gratitude to my parents for their unconditional love and support through these years. I want to show my thanks to my brother Dr. Lizhi Zhang (now at ORNL, USA) and my sister-in-law Qiuhui Zhou for their encouragement and understanding. I would like to give my greatest thanks to

my fiancée: Lingling Ding. You have always been there for me, no matter how hard a time it is! I look forward to our upcoming daughter!

Band / Volume 239
Single crystal growth and neutron scattering studies of novel quantum materials
X. Wang (2021), VI, 145 pp
ISBN: 978-3-95806-546-8

Band / Volume 240
Structure and Dynamics of Magnetocaloric Materials
N. A. Maraytta (2021), vii, 146 pp
ISBN: 978-3-95806-557-4

Band / Volume 241
Novel insights into the transcriptional regulation of cell division in *Corynebacterium glutamicum*
K. J. Kraxner (2021), V, 83 pp
ISBN: 978-3-95806-560-4

Band / Volume 242
Interplay of proximity effects in superconductor/ferromagnet heterostructures
A. Stellhorn (2021), ix, 219 pp
ISBN: 978-3-95806-562-8

Band / Volume 243
Silencing and counter-silencing of the Lsr2-like protein CgpS in *Corynebacterium glutamicum*
J. Wiechert (2021), IV, 265 pp
ISBN: 978-3-95806-569-7

Band / Volume 244
Molecular Layer Functionalized Neuroelectronic Interfaces:
From Sub-Nanometer Molecular Surface Functionalization to Improved Mechanical and Electronic Cell-Chip Coupling
N. R. Wolf (2021), IV, 101, xx pp
ISBN: 978-3-95806-570-3

Band / Volume 245
Surface Acoustic Waves in Strain-Engineered Thin (K,Na)NbO_3 Films:
From Basic Research to Application in Molecular Sensing
S. Liang (2021), VI, 125 pp
ISBN: 978-3-95806-571-0

Band / Volume 246
Tailoring neuroelectronic interfaces via combinations of oxides and molecular layers
X. Yuan (2021), 113 pp
ISBN: 978-3-95806-572-7

Band / Volume 247
Stoichiometric control and magnetoelectric coupling in artificial multiferroic heterostructures
P. Schöffmann (2021), vii, 176 pp
ISBN: 978-3-95806-575-8

Band / Volume 248
A Unified Framework for Functional Renormalisation Group Calculations and its Application to Three Dimensional Hubbard Models
J. Ehrlich (2021), xvi, 213 pp
ISBN: 978-3-95806-582-6

Band / Volume 249
Photoemission electron microscopy of magneto-ionic effects in $La_{0.7}Sr_{0.3}MnO_3$
M. Wilhelm (2021), 134 pp
ISBN: 978-3-95806-592-5

Band / Volume 250
Development of a Multiplexer System and Measurement of the Neutron Yield for a Low-Energy Accelerator-Driven Neutron Source
M. Rimmler (2021), v, 200 pp
ISBN: 978-3-95806-600-7

Band / Volume 251
Resolving interface effects in voltage controlled magnetic heterostructures using advanced neutron scattering and electron microscopy methods
T. Bhatnagar-Schöffmann (2021), ix, 171 pp
ISBN: 978-3-95806-604-5

Band / Volume 252
Strain development of *Gluconobacter oxydans* and *Pseudomonas putida* for production of the sweetener 5-ketofructose
K. Wohlers (2022), VI, 118 pp
ISBN: 978-3-95806-612-0

Band / Volume 253
Topological magnonic properties of two-dimensional magnetic materials
L. Zhang (2022), xx, 154 pp
ISBN: 978-3-95806-621-2

Schlüsseltechnologien / Key Technologies
Band / Volume 253
ISBN 978-3-95806-621-2

Mitglied der Helmholtz-Gemeinschaft

JÜLICH
Forschungszentrum